



The  
University  
Of  
Sheffield.

# **Evaluation of Solid Oxide Fuel Cells Operating on Hydrogen Sulfide Contaminated Fuel**

**by:**

**Abdolkarim Sheikhansari**

**Supervisors:**

**Dr. Simon Blakey**

**Dr. Jonathan Paragreen**

**A thesis submitted in partial fulfilment of the  
degree of Doctor of Philosophy**

**in the  
Faculty of Engineering  
Department of Mechanical Engineering  
University of Sheffield**

**February 2017**

## Abstract

This research was conducted to investigate the effect of hydrogen sulfide on the performance of single solid oxide fuel cells. A test rig was designed and commissioned to test 5x5 cm<sup>2</sup> cells (active area: 4x4 cm<sup>2</sup>). The test rig consists of a gas blender, a humidifier, a high temperature furnace, fuel and air manifolds and a control/data logging system. The characterisation techniques used in this project, include v-i measurement, EIS and SEM/EDX analysis.

The first series of experiments were carried out to investigate the effect of time, hydrogen partial pressure and temperature on the performance of the cells operating on clean fuel. The results showed that the current of lowest resistance is independent of the operating temperature, however, depends on partial pressure of H<sub>2</sub> and tends to increase as P<sub>H<sub>2</sub></sub> rises. The lowest resistance of the cell occurs at almost constant fuel utilization which was equal to 17 % in this research.

In the second series of tests, the cells were exposed to a range of H<sub>2</sub>S concentrations i.e. 50, 100, 150 and 200 ppm. The composition of the fuel mixture was 0.1 nl/min (14.5 %) of H<sub>2</sub>, 0.567 nl/min (82.5 %) of N<sub>2</sub> and 0.020 nl/min (3 %) of H<sub>2</sub>O (steam). All the contamination tests were carried out at 700 °C. The cells were exposed to H<sub>2</sub>S for 12 hours followed by a recovery period for 24 hours. The results revealed that the voltage drop at the end of the exposure period was similar for all degrees of poisoning. However, the performance at the end of the recovery, was different. The degree of recovery tended to decrease as the concentration of H<sub>2</sub>S increased. The SEM analysis of samples showed that H<sub>2</sub>S has caused the anode structure to change. This change occurred at the interface of anode functioning and support layers and was more severe at higher concentrations of H<sub>2</sub>S.

In addition, two contamination models were developed based on the H<sub>2</sub>S degradation mechanism. The models considered the effects of time and H<sub>2</sub>S concentration. However, they could not predict the performance of the poisoned cells as the voltage drop at the end of exposure time was independent of the H<sub>2</sub>S concentration for the tested range.

## Table of Contents

1	Introduction .....	1
1.1	Fuel cell technology .....	1
1.1.1	Types of fuel cells.....	2
1.1.2	Fuel cells features .....	4
1.1.3	Reversibility of fuel cells .....	7
1.2	Contamination sources .....	9
1.3	Problem statement .....	10
1.4	Aims and objectives .....	10
1.5	Structure of thesis.....	11
2	Literature review.....	13
2.1	Fuel cell theory.....	13
2.1.1	Ideal performance.....	13
2.1.2	Actual performance .....	17
2.2	Solid oxide fuel cells (SOFCs).....	19
2.3	SOFC components, materials and configurations.....	22
2.3.1	Anode .....	23
2.3.2	Electrolyte .....	30
2.3.3	Cathode.....	32
2.3.4	SOFC configurations .....	33
2.4	SOFC mathematical model.....	34
2.5	SOFC degradation .....	36
2.6	Fuel and impurity sources.....	39
2.7	SOFC poisoning .....	41
2.8	Fuel cells characterisation methods .....	49
2.8.1	In-situ techniques.....	50
2.8.2	Ex-situ techniques.....	55
2.9	Summary .....	56
3	Methodology.....	57
3.1	Operating conditions .....	57
3.1.1	Fuel composition.....	57
3.1.2	Temperature and pressure .....	58
3.1.3	Current density .....	58

3.2	Selection of H <sub>2</sub> S as contaminant .....	58
3.3	Test matrix .....	63
3.4	Applied characterization techniques .....	63
4	Contamination model .....	65
4.1	Basic assumptions .....	65
4.2	H <sub>2</sub> S damage model.....	66
4.2.1	Damage model 1 .....	67
4.2.2	Damage model 2 .....	68
4.3	Procedure to calculate damage factor.....	69
4.4	Fit of models with synthetic data .....	70
4.4.1	Damage model modification.....	70
4.4.2	Generating synthetic data.....	71
4.4.3	Curve fitting.....	73
4.4.4	Comparison of the damage models .....	76
5	Initial test apparatus .....	79
5.1	Test set up.....	79
5.1.1	Gas blender .....	79
5.1.2	Humidifier .....	81
5.1.3	High temperature furnace .....	83
5.1.4	Gas delivery manifold .....	84
5.1.5	Single cell.....	85
5.1.6	Load bank.....	87
5.1.7	Water trap.....	88
5.1.8	Controlling and data logging system.....	88
5.1.9	Recording the v-i curve .....	91
5.2	Results.....	92
5.2.1	Cell 01.....	93
5.2.2	Cell 02.....	100
5.2.3	Cell 03.....	106
5.2.1	50 ppm test (cell 04) .....	106
5.2.2	Tests failure (cells 05, 06 and 07).....	112
5.3	Problem investigation (cell 08) .....	115
5.4	Conclusions .....	118
6	Commercial test apparatus.....	119

6.1	Commercial set up .....	119
6.2	Installation tests.....	121
6.2.1	Cell 09.....	121
6.2.2	Cell 10.....	125
6.2.3	Cell 11.....	128
6.2.4	Cell 12.....	131
7	Results.....	137
7.1	Baseline tests (Cell 13) .....	137
7.1.1	Effect of time (run 1).....	137
7.1.2	Effect of hydrogen partial pressure (run 2) .....	140
7.1.3	Effect of temperature (run 3).....	148
7.2	Contamination tests.....	154
7.2.1	50 ppm (cell 14) .....	155
7.2.2	100 ppm (cell 15) .....	158
7.2.3	150 ppm (cell 13 run 4).....	161
7.2.4	200 ppm (cell 16) .....	164
7.2.5	Comparison of v-i and EIS curves before H <sub>2</sub> S exposure .....	167
8	Analysis and discussion .....	171
8.1	Baseline tests .....	171
8.1.1	Effect of time (cell 13 run 1) .....	171
8.1.2	Effect of H <sub>2</sub> partial pressure (cell 13 run 2).....	175
8.1.3	Effect of temperature (cell 13 run 3) .....	177
8.2	Contamination tests.....	179
8.2.1	50 ppm test .....	179
8.2.2	100 ppm test .....	182
8.2.3	150 ppm test .....	185
8.2.4	200 ppm test .....	187
8.2.5	Comparison of contamination tests.....	190
8.3	SEM/EDX analysis.....	195
8.3.1	Clean cells.....	195
8.3.2	Contaminated cells .....	198
8.3.3	Comparison of cells.....	202
9	Conclusion and future work.....	207
9.1	Conclusions .....	207

9.1.1	Test rig commissioning.....	207
9.1.2	Clean fuel tests.....	208
9.1.3	Contamination tests.....	209
9.2	Recommendations and future work.....	211
Appendix 1	Operating Faults.....	213
Appendix 2	Risk Assessment and COSHH Forms.....	217
Appendix 3	LabVIEW Hardware and Channels .....	223
Appendix 4	Test Procedure .....	225
Appendix 5	Electrical Drawing of SOFC Test Rig .....	241
Appendix 6	Test Sheet.....	243
References	.....	245

## List of Figures

Figure 1.1: Cross sectional SEM image of solid oxide fuel cell.....	2
Figure 1.2: Summary of different types of fuel cell [10].....	4
Figure 1.3: Schematic of PEMFC (left) and SOFC (right) [9].....	4
Figure 1.4: Assembly of cell with edge seals [9] .....	7
Figure 1.5: Proton exchange membrane electrolysis cell (top) and solid oxide electrolysis cell (bottom) [12].....	8
Figure 1.6: Solid oxide fuel/electrolysis cell [13] .....	9
Figure 2.1: Inputs and outputs of fuel cell [14].....	13
Figure 2.2: Schematic of change in Gibbs free energy [15] .....	14
Figure 2.3: Voltage/current density graph of low temperature (left) and high temperature (right) cells [9].....	19
Figure 2.4: Cross section of tubular SOFC [8, 9].....	20
Figure 2.5: Planar SOFC [31] .....	21
Figure 2.6: Schematic of a planar SOFC [34].....	23
Figure 2.7: TPB regions for an electronically conducting cermet (left) and a MEIC (right) [9] .....	24
Figure 2.8: Microstructural modification due to redox cycle [60] .....	29
Figure 2.9: YSZ structure [64].....	31
Figure 2.10: Schematic of cathode/electrolyte interface [69].....	32
Figure 2.11: Schematic of different configurations of single SOFCs [20].....	33
Figure 2.12: Cracks and delamination in cathode.....	37
Figure 2.13: Example of secondary phase formation at anode - Nickel is red, YSZ is green and nickel phosphide phases are blue [82] .....	38
Figure 2.14: Phase equilibrium of the Ni-O-S system at different temperatures, a: 673 K, b: 873 K, c: 1073 K and d: 1273 K [128] .....	46
Figure 2.15: Phase equilibrium of the Ni-O-S system at different partial pressures of H <sub>2</sub> and levels of steam content [128] .....	47
Figure 2.16: Dependence of performance loss on temperature and H <sub>2</sub> S concentration [135] .....	48
Figure 2.17: Charge double layer [9].....	51
Figure 2.18: Typical voltage profile in current interruption method [9] .....	52

Figure 2.19: Example of resistor/capacitor circuit and corresponding Nyquist plot [141].....	54
Figure 2.20: Typical EIS curve for a single electrode [141] .....	55
Figure 3.1: Composition of sulfur-containing compounds in fuel .....	61
Figure 3.2: Composition of nitrogen-containing compounds in fuel.....	62
Figure 4.1: Typical voltage degradation profile .....	72
Figure 4.2: Voltage profile of the experimental and synthetic data.....	73
Figure 4.3: Results of model 1 curve fitting .....	74
Figure 4.4: Results of model 2 curve fitting – variable <b>A</b> , constant <b>k2</b> .....	75
Figure 4.5: Results of model 2 curve fitting – variable <b>A</b> and <b>k2</b> .....	76
Figure 4.6: Comparison of the data and model 1 .....	77
Figure 4.7: Comparison of the data and model 2 .....	77
Figure 5.1: Schematic of test rig .....	79
Figure 5.2: Schematic of gas blender .....	80
Figure 5.3: SOFC gas blender .....	81
Figure 5.4: Humidifier .....	82
Figure 5.5: Schematic of humidifier .....	82
Figure 5.6: High temperature furnace .....	84
Figure 5.7: Gas delivery manifold .....	84
Figure 5.8: Drawing of gas delivery manifold (all dimensions are in mm).....	85
Figure 5.9: Drawing of layers of a single cell [151] .....	86
Figure 5.10: Schematic of housing/cell assembly .....	86
Figure 5.11: Schematic of load bank.....	87
Figure 5.12: Front (left) and back (right) views of load bank.....	88
Figure 5.13: LabVIEW code front panel .....	90
Figure 5.14: LabVIEW code block diagram-part 1.....	90
Figure 5.15: LabVIEW code block diagram-part 2.....	91
Figure 5.16: Schematic of v-i measurement circuit .....	92
Figure 5.17: Cell/current collector/manifold assembly .....	93
Figure 5.18: Configuration of cell inside furnace.....	93
Figure 5.19: Voltage and temperature against time – cell 01.....	95
Figure 5.20: Voltage and fuel flow rate – cell 01 .....	96
Figure 5.21: Characteristic curves - first test .....	97
Figure 5.22: Cell assembly after cooling – cell 01 .....	97

Figure 5.23: Voltage and temperature against time – cell 01 run 2 .....	98
Figure 5.24: Voltage and flow rates against time - cell 01 run 2 .....	99
Figure 5.25: Samples: without cap (left), with cap (right) .....	100
Figure 5.26: Ceramic cap.....	100
Figure 5.27: Profiles of voltage and temperature against time – cell 02.....	102
Figure 5.28: Profiles of voltage and fuel flow rate against time – cell 02.....	102
Figure 5.29: Initial characteristic curves – cell 02 .....	103
Figure 5.30: First and second characteristic curves – cell 02.....	104
Figure 5.31: Characteristic curves during durability test at 700 °C – cell 02.....	105
Figure 5.32: Comparison of the v-i curves taken with and without DC power supply .....	106
Figure 5.33: Profiles of voltage and temperature - cell 03 .....	107
Figure 5.34: Profiles of voltage and flow rates - cell 03.....	107
Figure 5.35: Profiles of voltage and temperature - 50 ppm test cell 04.....	109
Figure 5.36: Profiles of voltage and flow rates - 50 ppm test cell 04 .....	109
Figure 5.37: Initial characteristic curve - 50 ppm test cell 04 .....	110
Figure 5.38: Profiles of voltage and temperature – cell 05 .....	113
Figure 5.39: Profiles of voltage and temperature – cell 06 .....	113
Figure 5.40: Profiles of voltage and temperature – cell 07 .....	114
Figure 5.41: Comparison of v-i curves at 600 °C.....	114
Figure 5.42: Comparison of v-i curves at 700 °C.....	115
Figure 5.43: Cathode current collector .....	117
Figure 5.44: v-i curve at 600 °C – problem investigation test.....	117
Figure 5.45: v-i curve at 700 °C – problem investigation test.....	118
Figure 6.1: Open flange set up.....	120
Figure 6.2: Commercial set up diffuser [154] .....	120
Figure 6.3: Electrical insulation of set up.....	120
Figure 6.4: High temperature furnace for commercial set up.....	121
Figure 6.5: Profiles of voltage and temperature - cell 09 .....	122
Figure 6.6: Profiles of voltage and flow rates - cell 09.....	123
Figure 6.7: v-i curves at 600 °C - cell 09.....	124
Figure 6.8: v-i curves at 700 °C - cell 09 .....	124
Figure 6.9: Profiles of voltage and temperature - cell 10 .....	125
Figure 6.10: Profiles of voltage and flow rates - cell 10.....	126

Figure 6.11: Profiles of voltage and temperature - cell 10 run 2.....	127
Figure 6.12: Profiles of voltage and flow rates - cell 10 run 2 .....	127
Figure 6.13: Profiles of voltage and temperature - cell 11 .....	129
Figure 6.14: Profiles of voltage and flow rates - cell 11.....	129
Figure 6.15: Profiles of voltage and temperature - cell 11 run 2.....	130
Figure 6.16: Profiles of voltage and flow rates - cell 11 run 2 .....	130
Figure 6.17: Profiles of voltage and temperature - cell 12 50 ppm.....	132
Figure 6.18: Profiles of voltage and flow rates - cell 12 50 ppm.....	134
Figure 6.19: Comparison of last V-i curves at 700 °C - cells 09, 10, 11 & 12.....	134
Figure 6.20: Comparison of durability tests at 700 °C - cells 09, 10, 11 & 12.....	135
Figure 7.1: Profiles of voltage and temperature - cell 13 run 1.....	138
Figure 7.2: Profiles of voltage and flow rates - cell 13 run 1 .....	138
Figure 7.3: Profiles of v-i curves – cell 13 run 1 .....	139
Figure 7.4: EIS curves at OCV over durability period - cell 13 run 1 .....	139
Figure 7.5: EIS curves at 200 mA/cm <sup>2</sup> over durability period - cell 13 run 1 .....	140
Figure 7.6: Profiles of voltage and temperature - cell 13 run 2.....	141
Figure 7.7: Profiles of voltage and flow rates - cell 13 run 2 .....	141
Figure 7.8: Profiles of v-i curves – cell 13 run 2 .....	142
Figure 7.9: EIS curves at different current densities (A/cm <sup>2</sup> ) for P <sub>H2</sub> = 0.145 bar.	143
Figure 7.10: EIS curves at different current densities (A/cm <sup>2</sup> ) for P <sub>H2</sub> = 0.291 bar .....	143
Figure 7.11: EIS curves at different current densities (A/cm <sup>2</sup> ) for P <sub>H2</sub> = 0.436 bar .....	144
Figure 7.12: 3D plot of EIS curves – A: 0.145 bar, B: 0.291 bar, C: 0.436 bar .....	145
Figure 7.13: EIS curves at 1 A (0.0625 A/cm <sup>2</sup> ) for P <sub>H2</sub> of 0.145, 0.291 and 0.436 bar .....	146
Figure 7.14: EIS curves at 3 A (0.1875 A/cm <sup>2</sup> ) for P <sub>H2</sub> of 0.145, 0.291 and 0.436 bar .....	147
Figure 7.15: EIS curves at 6 A (0.375 A/cm <sup>2</sup> ) for P <sub>H2</sub> of 0.145, 0.291 and 0.436 bar .....	147
Figure 7.16: Profiles of voltage and temperature - cell 13 run 3.....	148
Figure 7.17: Profiles of voltage and flow rates - cell 13 run 3 .....	149
Figure 7.18: Profiles of v-i curves – cell 13 run 3 .....	150
Figure 7.19: EIS curves at different current densities (A/cm <sup>2</sup> ) for 600 °C.....	150

Figure 7.20: EIS curves at different current densities (A/cm <sup>2</sup> ) for 650 °C.....	151
Figure 7.21: EIS curves at different current densities (A/cm <sup>2</sup> ) for 700 °C.....	151
Figure 7.22: EIS curves at different current densities (A/cm <sup>2</sup> ) for 750 °C.....	151
Figure 7.23: EIS curves at 1 A (0.0625 A/cm <sup>2</sup> ) for 600, 650, 700 and 750 °C.....	153
Figure 7.24: EIS curves at 3 A (0.1875 A/cm <sup>2</sup> ) for 600, 650, 700 and 750 °C.....	153
Figure 7.25: EIS curves at 5 A (0.3125 A/cm <sup>2</sup> ) for 600, 650, 700 and 750 °C.....	153
Figure 7.26: 3D plot of EIS curves – A: 600 °C, B: 650 °C, C: 700 °C, D: 750 °C.....	154
Figure 7.27: Profiles of voltage and temperature - cell 14 .....	156
Figure 7.28: Profiles of voltage and flow rates - cell 14.....	156
Figure 7.29: Profiles of v-i curves during stabilisation period – cell 14 .....	157
Figure 7.30: Profiles of EIS curves at OCV during durability period - cell 14 .....	157
Figure 7.31: Profiles of EIS curves at 0.2 A/cm <sup>2</sup> during durability period - cell 14	158
Figure 7.32: Profiles of voltage and temperature - cell 15 .....	159
Figure 7.33: Profiles of voltage and flow rates - cell 15.....	159
Figure 7.34: Profiles of v-i curves during stabilisation period – cell 15 .....	160
Figure 7.35: Profiles of EIS curves at OCV during durability period - cell 15 .....	160
Figure 7.36: Profiles of EIS curves at 0.2 A/cm <sup>2</sup> during durability period - cell 15	161
Figure 7.37: Profiles of voltage and temperature – cell 13 run 4 .....	162
Figure 7.38: Profiles of voltage and flow rates - cell 13 run 4 .....	162
Figure 7.39: Profiles of v-i curves during stabilisation period – cell 13 run 4.....	163
Figure 7.40: Profiles of EIS curves at OCV during durability period - cell 13 run 4 .....	163
Figure 7.41: Profiles of EIS curves at 0.2 A/cm <sup>2</sup> during durability period – cell 13 run 4.....	164
Figure 7.42: Profiles of voltage and temperature - cell 16 .....	165
Figure 7.43: Profiles of voltage and flow rates - cell 16.....	165
Figure 7.44: Profiles of v-i curves during stabilisation period – cell 16 .....	166
Figure 7.45: Profiles of EIS curves at OCV during durability period – cell 16 .....	166
Figure 7.46: Profiles of EIS curves at 0.2 A/cm <sup>2</sup> during durability period – cell 16 .....	167
Figure 7.47: Comparison of the v-i curves before exposure to H <sub>2</sub> S.....	168
Figure 7.48: Comparison of the EIS curves at OCV before exposure to H <sub>2</sub> S.....	168
Figure 7.49: Comparison of the EIS curves at 0.2 A/cm <sup>2</sup> before exposure to H <sub>2</sub> S	169
Figure 8.1: The equivalent electrical circuit used for curve fitting .....	171

Figure 8.2: Comparison of curve fit and experiment at 0.2 A/cm <sup>2</sup> – cell 13 run 1172	
Figure 8.3: Comparison of experimental data and OD model - cell 13 run 1 - 85 hrs	
.....	175
Figure 8.4: Comparison of curve fit and experiment at 2 A – cell 13 run 2 .....	178
Figure 8.5: Plot of ohmic resistance vs temperature .....	179
Figure 8.6: Profiles of v-i curves during H <sub>2</sub> S exposure and recovery periods - 50 ppm	
.....	180
Figure 8.7: Profiles of EIS curves at 0.2 A/cm <sup>2</sup> during H <sub>2</sub> S exposure and recovery periods - 50 ppm	
.....	181
Figure 8.8: Profiles of v-i curves during H <sub>2</sub> S exposure and recovery periods - 100 ppm	
.....	182
Figure 8.9: Profiles of EIS curves at 0.2 A/cm <sup>2</sup> during H <sub>2</sub> S exposure and recovery periods - 100 ppm	
.....	183
Figure 8.10: Equivalent electrical circuit for 100 ppm test.....	184
Figure 8.11: Comparison of EIS experimental data and curve fit at 0.2 A/cm <sup>2</sup> – before exposure to 100 ppm of H <sub>2</sub> S.....	185
Figure 8.12: Profiles of v-i curves during H <sub>2</sub> S exposure and recovery periods - 150 ppm	
.....	185
Figure 8.13: Profiles of EIS curves at 0.2 A/cm <sup>2</sup> during H <sub>2</sub> S exposure and recovery periods - 150 ppm	
.....	186
Figure 8.14: Profiles of v-i curves during H <sub>2</sub> S exposure and recovery periods - 200 ppm	
.....	188
Figure 8.15: Profiles of EIS curves at 0.2 A/cm <sup>2</sup> during H <sub>2</sub> S exposure and recovery periods - 200 ppm	
.....	189
Figure 8.16: Normalised ASR at different stages of contamination tests.....	191
Figure 8.17: Normalised voltage at different stages of contamination tests .....	193
Figure 8.18: Normalised voltage during exposure period .....	193
Figure 8.19: Voltage drop of contaminated cells.....	194
Figure 8.20: Layers of anode supported cells .....	196
Figure 8.21: SEM pictures of cell 07 (top) and cell 08 (bottom) .....	197
Figure 8.22: SEM picture of cell 11 .....	198
Figure 8.23: Anode functioning layer – 50 ppm test .....	199
Figure 8.24: Anode functioning and supports layer – 50 ppm test .....	199
Figure 8.25: SEM picture of cell – 100 ppm test .....	200

Figure 8.26: SEM picture and EDX analysis of cell – 150 ppm test .....	201
Figure 8.27: SEM picture and EDX analysis of cell – 200 ppm test .....	202
Figure 8.28: Comparison of SEM pictures of contaminated cells .....	204
Figure 01: connection of lead wires to terminals .....	226
Figure 02: gas panel ball valves .....	227
Figure 03: emergency buttons .....	227
Figure 04: manual fuel line .....	237
Figure 05: solenoid valves power supply .....	228
Figure 06: solenoid air supply valve and pressure regulator .....	228
Figure 07: controlling program .....	229
Figure 08: operation mode-power switch .....	229
Figure 09: flow controllers set point .....	229
Figure 10: check the float switch alarm .....	230
Figure 11: humidifier controller .....	230
Figure 12: heating tape/wire to cover fuel inlet and outlet tubes .....	231
Figure 13: heating tape & controller .....	231
Figure 14: load bank .....	232
Figure 15: 3-way valves – 1st mode .....	232
Figure 16: 3-way valve - 2nd mode .....	232
Figure 17: humidifier check valve .....	233
Figure 18: ball valves on N <sub>2</sub> and H <sub>2</sub> line .....	234
Figure 19: set N <sub>2</sub> and H <sub>2</sub> set points in LabVIEW to purge .....	234
Figure 20: air flow valve, pressure regulator and rotameter .....	234
Figure 21: set N <sub>2</sub> and H <sub>2</sub> set points in LabVIEW .....	234
Figure 22: time target and data auto save .....	235
Figure 23: voltage graph in LabVIEW .....	235
Figure 24: Power supply in series to the cell .....	236
Figure 25: V-I curve button .....	236

## List of tables

Table 1.1: Applications and power range of different types of fuel cell.....	6
Table 2.1: Features of single cell configurations.....	34
Table 2.2: Typical composition of biomass derived syngas .....	41
Table 2.3: Maximum concentration of BDS contaminants.....	41
Table 2.4: Summary of studies on effect of H <sub>2</sub> S on SOFCs performance.....	44
Table 3.1: Calculation of mole fraction - COS hydrolysis .....	60
Table 3.2: Conditions at which the EIS curves are taken .....	64
Table 4.1: Model 1 parameters.....	73
Table 4.2: Model 2 parameters – variable <b>A</b> , constant <b>k2</b> .....	74
Table 4.3: Model 2 parameters – variable <b>A</b> and <b>k2</b> .....	75
Table 5.1: Characteristics of individual cells .....	85
Table 5.2: Summary of control & monitor devices .....	89
Table 5.3: Characteristics of the first test.....	94
Table 5.4: Test plan of second cell.....	101
Table 5.5: Characteristics of 50 ppm test (cell 04).....	107
Table 5.6: Test plan of 50 ppm test .....	108
Table 5.7: Summary of stages of test interruption.....	112
Table 6.1: Steps of commercial set up initial test - cell 09 .....	122
Table 8.1: Values of model parameters – cell 13 run 1 – effect of time.....	172
Table 8.2: Operating condition and cell parameters for SOFC 0D model.....	174
Table 8.3: Values of model parameters – cell 13 run 2 – effect of hydrogen partial pressure .....	175
Table 8.4: Fuel utilization for different P <sub>H2</sub> .....	177
Table 8.5: Values of model parameters – cell 13 run 3 – effect of temperature .	178
Table 8.6: ARS of cell - 50 ppm test .....	180
Table 8.7: Equivalent circuit parameters - 50 ppm test.....	181
Table 8.8: ARS of cell - 100 ppm test .....	182
Table 8.9: Equivalent circuit parameters - 100 ppm test.....	183
Table 8.10: ARS of cell - 150 ppm test .....	186
Table 8.11: Equivalent circuit parameters - 150 ppm test.....	187
Table 8.12: ARS of cell - 200 ppm test .....	188
Table 8.13: Equivalent circuit parameters - 200 ppm test.....	190
Table 01: steps to decrease the resistance on load bank .....	237

## Nomenclature

Label	Description
Latin	
$A$	Active sites
$A, B, C, D$	Constants in damage model
$c$	Integration constant in damage model
$C_{H_2S}$	Concentration of hydrogen sulfide
$D$	Damaged sites
$D_{eff}$	Electrode effective diffusion coefficient
$E$	Activation energy , Reversible voltage (Nernst voltage)
$e$	Cell component thickness
$F$	Faraday constant
$f$	Damage factor
$\bar{g}_f$	Gibbs free energy
$\bar{h}_f$	Enthalpy
$I$	Current
$i$	Current density
$i_0$	Exchange current density
$K$	Pre-exponential factor
$k$	Time dependent constant in damage model
$k_p$	Equilibrium constant
$k_1$	Rate constant of cell degradation without sulfur
$k_2$	Rate constant of sulfur poisoning reaction
$l_{TPB}$	Length of triple phase boundaries
$M$	Molar weight
$m$	Mass
$\dot{m}$	Mass flow rate
$n$	Number of moles
$\dot{n}$	Molar flow rate
$P$	Pressure
$R$	Resistance
$R$	Universal gas constant

$T$	Temperature
$t$	Time
$U_f$	Fuel utilisation
$V$	Voltage
$X$	Mole fraction of vapour
$y$	Mole fraction
$Z$	Change in number of moles
$z$	Number of electrons

#### Greek

$\alpha$	Charge transfer coefficient
$\beta$	Constant in electrolyte conductivity equation
$\gamma$	Constant in cathode conductivity equation
$\varepsilon$	Constant in anode conductivity equation
$\theta$	Arbitrary parameter to generate synthetic data
$\eta$	Overpotential (loss)
$\sigma$	Cell component conductivity
$\emptyset$	Relative humidity
$\omega$	Specific humidity

#### Superscripts

0	Standard condition
---	--------------------

#### Subscripts

0	Initial value
a	Air channel
act	Activation
<i>ads</i>	Adsorption
an	Anode
c	Cell
ca	Cathode
conc	Concentration
<i>ele</i>	Electrolyte
<i>f</i>	Fuel channel
<i>g</i>	Gaseous state - Vapour saturation condition

$i, j$	Index
ohm	Ohmic
s	Solid state
$v$	Vapour

#### Acronyms

ASC	Anode supported cell
AFC	Alkaline fuel cell
BDS	Biomass derived syngas
CSC	Cathode supported cell
CTE	coefficient of thermal expansion
EIS	Electrochemical impedance spectroscopy
EDX	Energy Dispersive X-ray
EMF	Electro motive force
ESC	Electrolyte supported cell
FC	Fuel cell
GDC	Gadolinium doped ceria
HHV	Higher heating value
LHV	Lower heating value
MCFC	Molten carbon
MEIC	Mixed electronic and ionic conductor
OCV	Open circuit voltage
PAFC	Phosphoric acid fuel cell
PEMEC	Proton exchange membrane electrolysis cell
PEMFC	Proton exchange membrane fuel cell
SEM	Scanning Electron Microscopy
SOEC	Solid oxide electrolysis cell
SOFC	Solid oxide fuel cell
TPB	Triple phase boundary
WGS	Water gas shift
YSZ	Yttria stabilised zirconia

## Acknowledgement

Firstly, I would like to remember the late Professor Chris Wilson who provided me an opportunity to pursue my doctoral studies at the University of Sheffield. His incredible encouragement, patience and knowledge helped me at several stages in this research project.

I would like to express my sincere gratitude to my supervisors Dr Simon Blakey and Dr Jonathan Paragreen for taking up the tough task of filling in the late Chris Wilson's shoes and supervising me during the last years of my PhD. I will never forget their valuable support, guidance and knowledge without which it would never have been possible for me to complete this work.

Besides my supervisory team, I would like to thank all the staff from the Low Carbon Combustion Centre, specifically Mr Andrew Delorenzi, for their support and assistance with the technical tasks through my studies.

I would also like to thank Dr Mohammed Ismail for several meetings and discussions from which I benefited greatly at several stages of my PhD.

Last but not least, I would like to thank my family: my parents and my brothers, for their immense support, patience and love throughout writing this thesis and my life in general.

# 1 Introduction

## 1.1 Fuel cell technology

Fuel cells (FCs) are electrochemical devices which generate electrical power through electrochemical reactions. FCs are similar to batteries in which they convert the chemical energy into electricity. However, they are different as a constant source of fuel and oxidant is required for FCs to carry on the reactions, whereas, the batteries rely on the available chemicals which are consumed and run out during the operation period. As long as fuel and oxidant are supplied, a FC can sustain the electrochemical reactions and deliver electricity.

Fuel cells avoid combustion and convert the chemical energy of a fuel directly into electrical energy through a chemical reaction with an oxidizing agent which is generally oxygen or air. Fuel cell technology has the potential to be a more efficient method of converting fuel to electrical power and is therefore, considered to be one of the main greening technologies for 21<sup>st</sup> century. Fuel cells can be used with renewable energy sources in a similar manner to how a combustion engine may also be used with biofuels. The primary motivation for fuel cell examination, development and commercialization is the growing concern about global pollution arising from energy emissions, in particular from industry and transportation and the potential efficiency savings [1]. The Climate Change Bill, published in draft in March 2007, has proposed an aim of at least 60 % decrease in carbon dioxide emissions by 2050 [2] and fuel cell systems have been considered to have an important role in order to achieve this goal.

Relying on electrochemistry instead of combustion to oxidize fuel and generate electricity, fuel cell technology is characterized by, especially, low emissions and high efficiencies [3] and therefore, demonstrates considerable economic and environmental potential in the next generation power sources i.e. renewable energies [4-6].

Generally, fuel cells consist of three main layers; an anode (which generates negative electrical charge) fed with fuel, a cathode (which generates positive electrical charge) fed with oxidant and an electrolyte which is sandwiched between the electrodes. Figure 1.1 demonstrates a cross sectional image of a solid oxide fuel cell. Fuel is oxidized at the anode through an oxidation reaction, while oxidant, by contrast, is reduced at the cathode through a reduction reaction. Electrolyte is a

dense ion-conducting, non-porous material which allows ions to transfer from one electrode to the other.

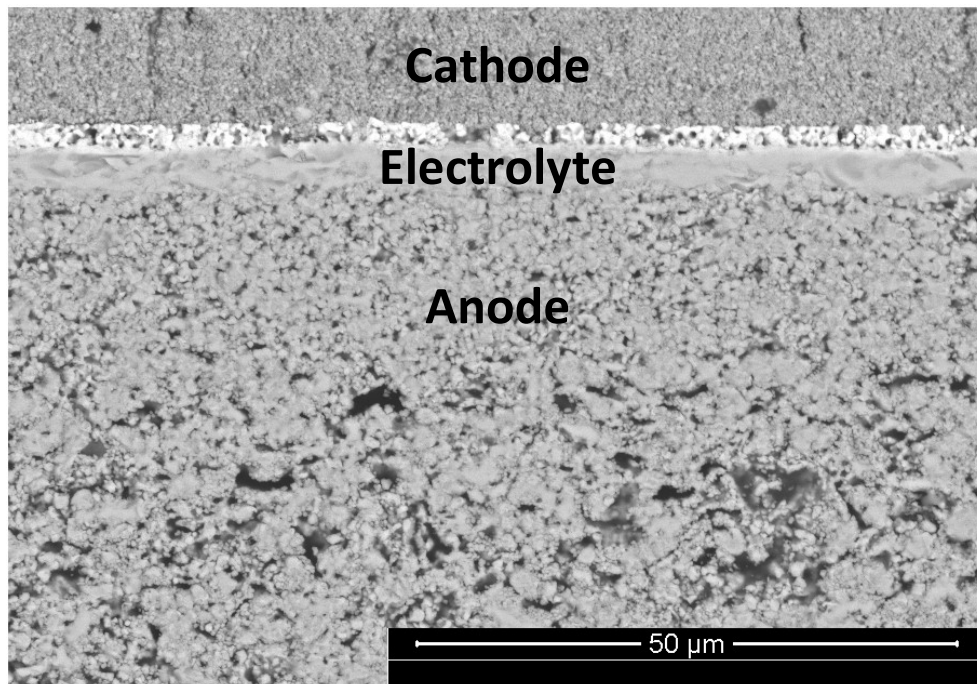


Figure 1.1: Cross sectional SEM image of solid oxide fuel cell

### 1.1.1 Types of fuel cells

At the present time, fuel cells are manufactured in different types and models. Although there are a large number of variables among fuel cells, such as fuel type, method used to produce hydrogen for the cell reaction and operating temperature, the main difference lies in the material used for electrolyte. Over the last four decades, some general agreement has been reached to characterize and name fuel cell systems by the type of electrolyte; solid polymer, alkaline, phosphoric acid, molten carbonate, and solid oxide [7]. In each type, the details of reaction at electrodes, moving ion and direction of motion of ions are different. Fuel cell types can be categorized as [5, 8, 9]:

- Proton Exchange Membrane Fuel Cells (PEMFC): a solid and immobile polymer is used as the electrolyte and protons are the mobile ions. The electrodes are carbon-based and a platinum catalyst is used in order to increase the rate of reaction at electrodes. The operating temperature of this type is quite low (80-100 °C) and the efficiency is in the range of 45 to 50 %. Hydrogen is considered as the main fuel for PEMFCs; however methanol can also be used. In case of methanol the cell is called direct

methanol fuel cell and produces a very lower power for a given size since the rate of oxidation of methanol is slower than that of hydrogen.

- Alkaline fuel cells (AFC): the electrolyte is an alkaline solution such as sodium or potassium hydroxide solution and the  $\text{OH}^-$  is the mobile ion. A variety of non-precious metals such as nickel can be used as electrode. Also platinum or carbon-supported catalysts are used with the electrodes to promote the reduction and oxidation reactions. AFCs operate at temperatures between  $100\text{ }^\circ\text{C}$  and  $250\text{ }^\circ\text{C}$  with an efficiency of 50-60 %.
- Phosphoric Acid Fuel Cells (PAFC): liquid phosphoric acid is used as the electrolyte in this type of cell and the protons are the mobile ions. The electrodes are made of porous carbon (graphite) and a Platinum catalyst. They operate at temperatures around  $200\text{ }^\circ\text{C}$  and efficiency is in the range of 40-45 %.
- Molten Carbonate Fuel Cells (MCFC): This type of cell uses a molten mixture of alkali metal carbonates (usually a mixture of lithium and potassium or lithium and sodium carbonates) retained in a ceramic matrix of Lithium aluminate. The alkali carbonates tend to form a highly conductive molten salt for  $\text{CO}_3^{2-}$  ions at the operating temperatures as high as  $600\text{-}700\text{ }^\circ\text{C}$ . Currently Ni-Cr or Ni-Al, and nickel oxide are used as anode and cathode, respectively. At these elevated temperatures the efficiency of cells is about 50-55 %.
- Solid Oxide Fuel Cells (SOFC): in this type of cell the electrolyte is an impermeable solid ceramic usually Yttria stabilized Zirconia (YSZ) or Gadolinia doped Ceria (GDC). The anode and cathode are typically made of a Ni- $\text{ZrO}_2$  cermet and Lanthanum Strontium Manganite (LSM), respectively. The SOFCs work at temperatures between 600 and  $1000\text{ }^\circ\text{C}$ , with an efficiency of 50-60 %.

A summary of different types of fuel cells has been presented in figure 1.2. While the ions pass through the electrolyte from one electrode to the other, the electrons travel through an external circuit to generate direct current electricity. The schematic of two different types of fuel cell has been shown in figure 1.3.

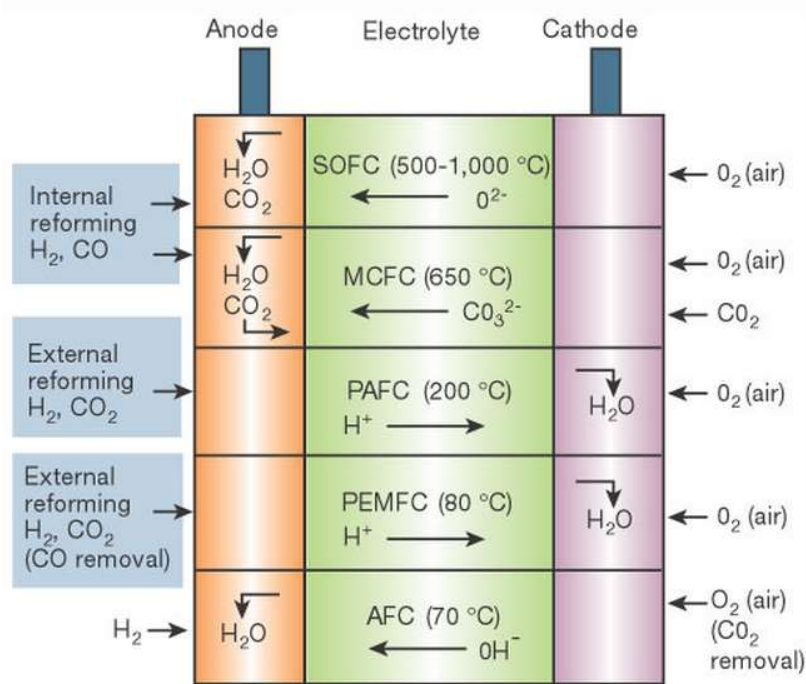


Figure 1.2: Summary of different types of fuel cell [10]

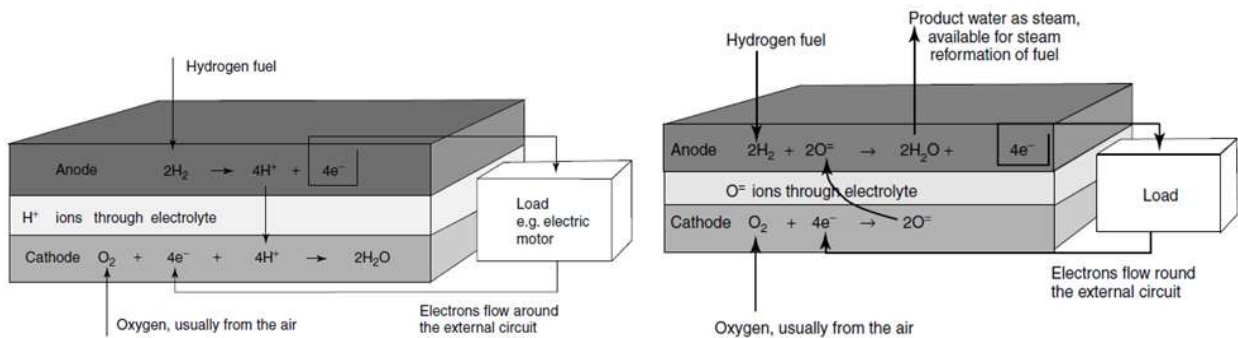


Figure 1.3: Schematic of PEMFC (left) and SOFC (right) [9]

### 1.1.2 Fuel cells features

The most substantial drawback of fuel cell systems at the moment, which is the same for all types and impedes their widespread use, is cost. Nevertheless, there are several advantages which make them promising and beneficial as energy conversion devices. These can be listed as [7-9, 11]:

- High efficiency
- Low chemical, acoustic and thermal emissions
- No combustion in energy conversion process
- No moving parts
- Low maintenance
- Reliability

- Fuel flexibility
- Good performance at off-design load operation
- Modular installations to match load and increase reliability
- Remote/unattended operation
- Size flexibility

Apart from the practical problems associated with fuel cells such as manufacturing and costs, there are two more issues [9]:

- Low power arising from slow reaction rate: the oxidation reaction in fuel cells is exothermic; however it does not mean that the reaction will take place at a high rate. In all the chemical reactions there is an activation barrier which should be overcome, thus some energy should be supplied to the system so that the reaction can proceed. This is the case for fuel cells operating at low temperatures. However this issue can be solved by using a catalyst, increasing the operating temperature or expanding the surface area of the electrodes.
- Relying on hydrogen as the primary fuel: Some types of fuel cell have been developed to operate on other fuels such as methanol, natural gas and carbon monoxide to solve this issue. For instance, SOFCs can use carbon monoxide as a direct fuel. In addition, the high operating temperature of cells can favour the reforming of heavier hydrocarbons such as methane. As a result of this process the methane is reformed to hydrogen which is the principal fuel for all cells.

The benefits of the fuel cells which vary for different types, lead to a wide range of applications including combined heat and power systems, stationary electric power plants, and portable power systems, specifically for electronic equipment such as mobile telephones, portable computers, and military communications devices. Furthermore, they are widely used as motive power for vehicles such as automobiles, buses, motorcycles, boats, and ships; as on-board electric power for space vehicles; and as primary, auxiliary and backup power for industrial units and residential buildings. As a key point, it should be noted that the fuel cell energy output covers a broad domain of power, ranging from a few watts to megawatts, which results in a variety of small-scale and large-scale applications. The power and application range of different types of fuel cell, has been illustrated in table 1.1 [9, 11].

Fuel cell type	Applications	Power range
Proton exchange Membrane (PEMFC)	Vehicles and mobile applications, for lower power CHP systems, residential/commercial power generation, small and/or portable generators and battery replacements	A few watts to 100 kW
Alkaline (AFC)	Used in space vehicles, e.g. Apollo, Shuttle.	500 W to 10 kW
Phosphoric acid (PAFC)	CHP systems, commercial sector applications such as hospitals, hotels, schools, and high value commercial buildings	10 kW to 5 MW
Molten carbonate (MCFC)	Suitable for medium- to large-scale CHP Systems, suitable for industrial, electrical utility, and military applications	100 kW to 15 MW
Solid oxide (SOFC)	Suitable for all sizes of CHP systems, up to multi-MW	5 kW to 15 MW

**Table 1.1: Applications and power range of different types of fuel cell**

A fuel cell system can produce as much power as required, however, a single cell generally produces around 0.7 volts at design current densities [9]. The current which can be drawn from a cell is dependent upon the cell area which is in turn limited by the manufacturing process. Also, high currents will result in greater ohmic losses which is defined as the voltage drop due to the internal resistance of the cell to flow of ions and electrons. Therefore, separate fuel cells are placed in series or parallel circuits, to get the voltage or current output up to an appropriate level, in order to fulfil application's power requirements. This collection of fuel cells combined in series, is known as a stack. The method of such a combination, is to join individual cells – anode/electrolyte/cathode assemblies – by interconnects or bipolar plates. A bipolar plate connects the cathode of one cell to the anode of next cell in a stack (hence bipolar) and makes a connection all over the surfaces of electrodes.

In a fuel cell stack, two tasks are considered for bipolar plates. First, they should provide an electrical contact between electrodes of adjacent cells, and second, they function as means of feeding gas and oxidant to electrodes. In order to do these functions, bipolar plates should have a high electrical conductivity and also, should be grooved to allow gases to flow over the face of anodes and cathodes. Furthermore, they should strictly separate two gas supplies and be impermeable to gases to prevent any fuel and oxidant mixing [8]. Currently, the materials which are used for bipolar plates are metal-based or graphite-based. The choice of material

to produce bipolar plates is dictated by several properties such as permeability to gases, electrical conductivity, thermal conductivity (to remove the heat of reactions), corrosion resistance (the by-product of corrosion can degrade fuel cell performance), and machining [5].

Since the electrodes are porous (to permit the gases to transport) the gases would leak out of the electrode edges. Therefore, all the edges should be sealed properly. In the case of single cells, glass or other sealing pastes are used to seal the edges. In a stack the electrolyte of cells can be made larger than the electrodes and a sealing gasket is fitted around each electrode to seal the edges. These assemblies, as shown in figure 1.4, are put in series to form a stack [9].

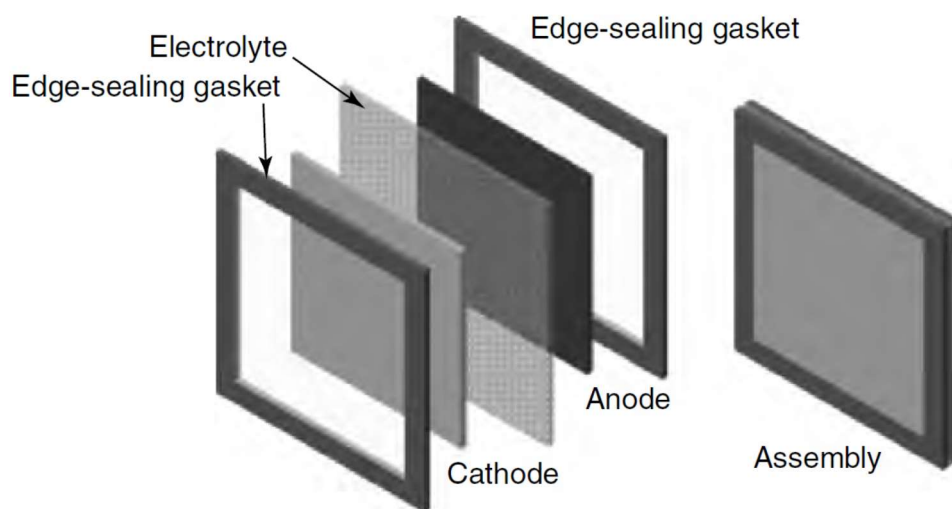


Figure 1.4: Assembly of cell with edge seals [9]

Hydrogen is considered as the basic source of fuel for the FCs although other types of chemicals and fuels e.g. hydrocarbons can be directly used depending on the type of the FC. There are several processes of hydrogen production such as thermochemical methods (steam reforming and gasification), electrolysis and solar energy methods, through which hydrogen is released from the chemical structure of the source.

### 1.1.3 Reversibility of fuel cells

Theoretically, the reactions in fuel cell electrodes can be reversed to achieve electrolysis i.e. the decomposition of water into hydrogen and oxygen. In such process, the cell consumes electricity and  $H_2O$ , and generates  $H_2$  and  $O_2$  at the electrodes. Figure 1.5 illustrates the schematics of PEMECs and SOECs. As can be seen, in electrolysis mode, the direction of motion of ions, electrons and gases is

opposite to that of the fuel cell mode. The required electricity for the process is provided by an external power supply such as solar cells, wind turbines and power plants.

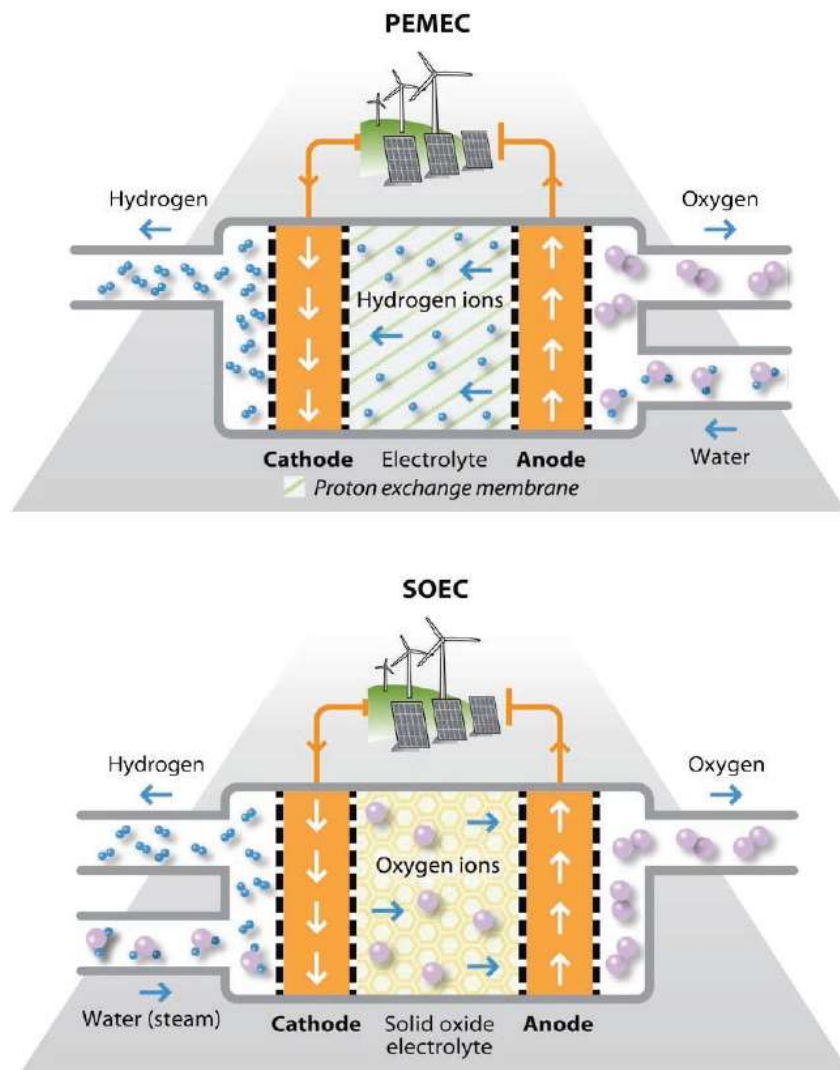
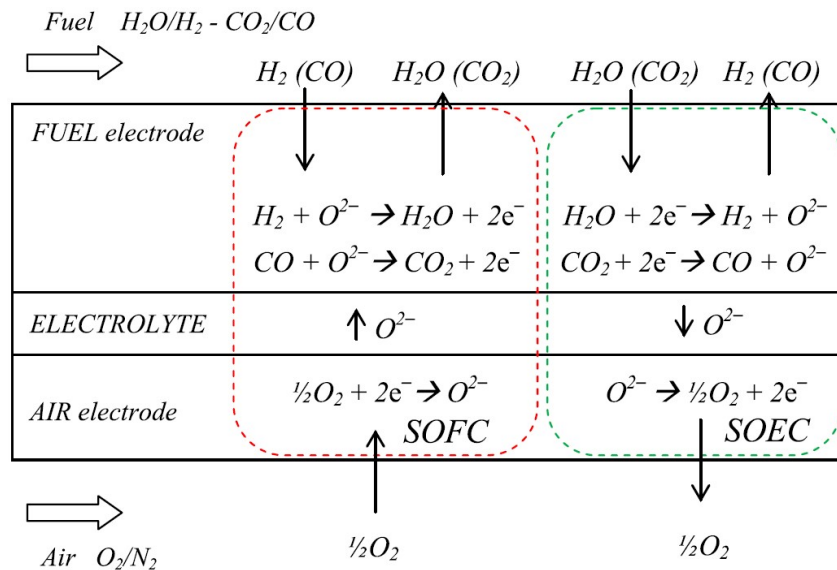


Figure 1.5: Proton exchange membrane electrolysis cell (top) and solid oxide electrolysis cell (bottom) [12]

In addition to  $H_2O$ , carbon dioxide can be used in electrolysis process to produce carbon monoxide. Figure 1.6 shows the schematic of a solid oxide cell which can be operated in both fuel cell and electrolysis modes. The corresponding reactions for the modes are also presented in the figure. In the fuel cell mode, CO can be used as fuel to generate electricity, whereas, in electrolysis, it is produced at the fuel electrode as a result of the  $CO_2$  electrolysis process.



**Figure 1.6: Solid oxide fuel/electrolysis cell [13]**

## 1.2 Contamination sources

In order for the cell to constantly deliver electrical power it is essential for the fuel and oxidant to reach the active sites through the electrodes. In case the active sites are blocked, or their catalytic characteristics deteriorate, the fuel cell will not be able to generate the expected electricity. This can happen due to the presence of contaminants in the fuel or oxidant, and lead to partial or full deactivation of the cell.

Gasification of biomass and coal is one the common methods to produce synthetic gas (syngas). Syngas can then be used as a fuel source in gas turbines and fuel cells to generate electricity. However, in addition to hydrogen, different compounds of sulfur and chlorine are released through the process, as they are present in the feedstocks. These contaminants can take part in the cell's reactions and degrade the performance if not separated from the fuel.

In addition to unavoidable sources of contaminants due to the hydrogen production methods, contaminants can be found in the air or oxidant supplied to the cell. They can also originate from corrosion or evaporation of the elements and compounds within the system components. All types of the contaminants tend to affect the cell performance and degrade it from the optimum operating conditions. Thus, it is important to investigate the effects of impurities and decrease their concentration to the values below the acceptable levels.

There are two main mechanisms through which the performance of a cell can be degraded by impurities: the surface adsorption of the contaminant on the layers of

cell and bulk reaction of the contaminant with the cell compounds. The former tends to block the reactive sites of electrodes and the latter leads to the formation of secondary phases. In either case, the electrochemical characteristics of the cell can be diminished causing the performance to drop.

### **1.3 Problem statement**

Solid Oxide Fuel Cells (SOFCs) are one of the fuel cell types broadly studied in recent years. A large number of scientists have put lots of effort into developing of this technology due to its unique characteristics such as high efficiency, high tolerance to impurities and potential of use in combined heat and power systems. One of the outstanding features of the SOFCs is the ability to promote the internal reforming of hydrocarbons, as a result of the high operating temperature. This characteristic gives the cell the potential to operate on a broad variety of fuels such as methane, methanol and syngas.

Biomass is a renewable source of energy and widely used to produce syngas. Biomass-derived syngas (BDS) consists of hydrogen, carbon monoxide, carbon dioxide, methane, nitrogen, water vapour and sulfur-, nitrogen- and chlorine-containing compounds. In order to remove the impurities, purification techniques should be applied before introducing the fuel to cells. However, these methods will increase the costs. Consequently, there will be a trade off between the cost of purifying the fuel and the damage to the cells, e.g. a small amount of degradation in the cell performance may be preferable to the cost of producing very pure hydrogen.

Hydrogen sulfide is one of the major impurities present in coal- and biomass-derived syngas and profoundly detrimental to the performance of the SOFCs. In this research H<sub>2</sub>S has been selected as the contaminant present in the fuel mixture and its effect on the SOFC performance is experimentally investigated.

### **1.4 Aims and objectives**

The main aim of this project is to evaluate the performance of a single Solid Oxide Fuel Cell operating on hydrogen sulfide contaminated fuel. The composition of the fuel mixture and concentration of H<sub>2</sub>S mimic those of the biomass-derived syngas. The objectives of the research are listed as follows.

- To design and commission a SOFC test set up to carry out durability and contamination tests with single cells
- To test single SOFCs running on clean fuel and investigation of the operating conditions on the cells performance (baseline tests)
- To Investigate the performance of SOFCs operating on a range of H<sub>2</sub>S concentrations (contamination tests)
- To analyze the cells using in-situ (during the test) and ex-situ (after the test) techniques such as Electrochemical Impedance Spectroscopy (EIS), Scanning Electron Microscopy (SEM) and Energy Dispersive X-ray (EDX)
- To develop a mathematical damage model for H<sub>2</sub>S contamination based on the mechanism through which the cells are degraded.

## **1.5 Structure of thesis**

Chapter1 includes the introduction to this research. It summarises the FCs technology as well as the fuel contamination sources. It also outlines the main reasons and objectives of this project. Finally, it covers a brief overview of the chapters included in the thesis.

Chapter 2 reviews FC technology, different types and applications. It focuses on SOFC systems and explains their structure and requirements. The chapter also includes the sources of impurity and their effect on SOFCs' performance.

Chapter 3 explains the methodology of the research project. The motives of H<sub>2</sub>S selection as the contaminant of interest as well as the experimental approach/procedure are presented in this chapter.

A mathematical damage model has been developed in chapter 4 based on the contamination mechanism through which the cell is poisoned by H<sub>2</sub>S. In order to derive the damage models, two different strategies have been considered in the chapter.

The design and commissioning of the experimental set up has been explained in chapter 5. Different components and subsystems of the test rig, tests procedure and initial results have also been included in this chapter.

Due to the drawbacks and problems associated with the initial set up, a part of the test rig was re-designed and replaced with a commercial system. The test rig modification has been described in chapter 6. It also presents the initial results of the tests carried out with the new set up.

Chapter 0 presents the results of the main tests including the baseline (clean fuel) and contamination ( $H_2S$ -contaminated fuel) tests. In the baseline tests section, the effects of several operating conditions on the performance of SOFCs have been investigated, and in the contamination tests section, the results of the tests with different levels of contamination ( $H_2S$  concentrations) have been explained. In this chapter, the v-i and EIS curves, obtained at different operating conditions and contamination levels, are demonstrated.

All the results of the base line and contamination tests are discussed and analysed in chapter 0. The analysis includes curve fitting of the results on an electrical equivalent model which represents the performance of the single cells. Also, the obtained v-i and EIS curves are discussed in detail to study the performance of the cells. In addition, the results of SEM and EDX analyses of the contaminated cells are presented.

Finally, chapter 0 summarises the work carried out in this research and gives a review of the information determined throughout the commissioning and experiments stages. It also covers a series of suggestions for future work, made in accordance with the conclusions.

## 2 Literature review

### 2.1 Fuel cell theory

The approach to understand the operation of a fuel cell is to describe the ideal performance at the first step, and then to define losses. Once both quantities are determined, losses would be subtracted from the ideal performance to calculate the actual operation. The ideal performance of fuel cells cannot be analysed using the thermodynamic system defined for heat engines. In terms of thermodynamics, a heat engine is typically defined by three requirements [5]:

- Receiving heat from a high-temperature source
- Converting part of this heat to work
- Rejecting the remaining heat to a low-temperature sink

Since none of these requirements is satisfied, the Carnot cycle efficiency, which defines the maximum possible efficiency for a heat engine, cannot be applied to electrochemical cells.

#### 2.1.1 Ideal performance

In figure 2.1 the inputs and outputs of a basic fuel cell have been illustrated. At a basic level, it can be said that it is the chemical energy of reactants (hydrogen and oxygen) and product (water) that should be considered. But the problem is that, it is not easy to define the chemical energy. Generally, there are several terms to describe chemical energy such as enthalpy, Helmholtz function, calorific value, and Gibbs free energy. For fuel cells, it is the Gibbs free energy which is of most importance and should be considered to analyse the thermodynamic system of the cell. Gibbs free energy is defined as the “energy available to do external (non-mechanical) work, neglecting any work done by changes in pressure and/or volume” [9].

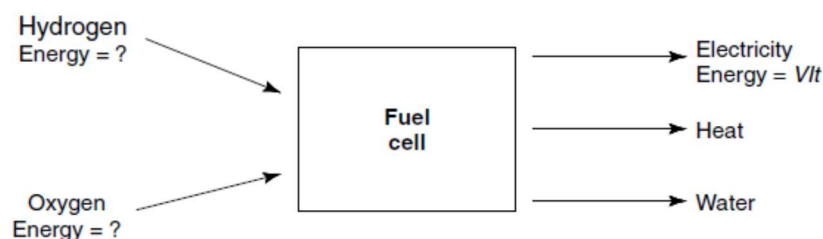


Figure 2.1: Inputs and outputs of fuel cell [14]

One can make a simple analogy between potential energy and chemical energy since both of them describe the maximum available work of their corresponding system. Similar to mechanical potential energy, chemical energy can change. In fuel cells, it is the change in Gibbs free energy which determines the energy released in the electrochemical process [14]. This change is the difference between Gibbs free energy of inputs (reactants) and outputs (products) of cell. Figure 2.2 illustrates a schematic for the change in Gibbs free energy for a typical reaction.

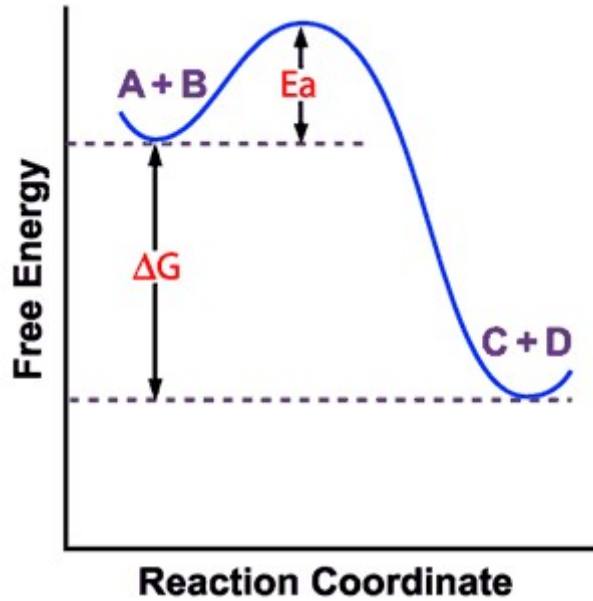


Figure 2.2: Schematic of change in Gibbs free energy [15]

Considering a basic hydrogen/oxygen fuel cell, the chemical reaction will be:



Therefore, the change in Gibbs free energy can be written as

$$\Delta \bar{g}_f = (\bar{g}_f)_{\text{H}_2\text{O}} - (\bar{g}_f)_{\text{H}_2} - \frac{1}{2} (\bar{g}_f)_{\text{O}_2} \quad (2.2)$$

All the quantities are in 'per mole' form for more simplicity.

The ideal performance (or maximum electrical work attainable from fuel cells at a constant operation point i.e. constant temperature and pressure) is described by a fundamental equation which calculates the open circuit voltage (OCV) or electromotive force (EMF) of the cell [9]. This equation is written as:

$$E = \frac{-\Delta \bar{g}_f}{zF} \quad (2.3)$$

where  $E$  is the reversible OCV,  $z$  is the number of electrons passing through external circuit for each molecule of fuel, and  $F$  is the Faraday constant. The Faraday constant is the charge of one mole of electrons, i.e. the product of

Avogadro's number and electrical charge of an electron. Equation 2.3 implies that the ideal performance or OCV depends on the reaction which occurs in fuel oxidation process in the fuel cell. For instance, if the cell operates on carbon monoxide as fuel the overall reaction of cell would be:



and in the case of methane the reaction is:



Considering equation 2.3 the ideal potential of cell operating at standard condition (25 °C and 1 bar) for hydrogen, carbon monoxide and methane is 1.23, 1.33 and 1.04 volts, respectively. The difference in the voltage is due to the change in Gibbs free energy, which is different for reactions 2.1, 2.4 and 2.5 [9, 16]. The information provided by National Institute of Standards and Technology [17] can be used to calculate the quantities such as enthalpy, entropy and Gibbs free energy

Not only is the performance of a fuel cell affected by operational temperature, but also by pressure and concentration of reactants and products. In order to take into account the effects of these parameters for a basic hydrogen/oxygen reaction, the change in Gibbs free energy, using thermodynamic arguments [9, 16, 18] and assuming the fuel and oxidiser as ideal gases, can be re-written as:

$$\Delta \bar{g}_f = \Delta \bar{g}_f^\circ - RT \ln \left( \left( \frac{P_{\text{H}_2}}{P^0} \right) \left( \frac{P_{\text{O}_2}}{P^0} \right)^{1/2} / \left( \frac{P_{\text{H}_2\text{O}}}{P^0} \right) \right) \quad (2.6)$$

in which  $P$  and  $P^0$  are the partial pressure of the gas and standard pressure, 0.1 MPa, respectively. The first term on the right-hand side of equation,  $\Delta \bar{g}_f^\circ$ , accounts for the change in molar specific Gibbs free energy at standard pressure and the second term considers the effect of other parameters. Considering all the pressures in bar,  $P^0$  would be equal to 1. By combining equations 2.3 and 2.6, the OCV would be written as:

$$E = \frac{-\Delta \bar{g}_f^\circ}{zF} + \frac{RT}{zF} \ln \left( \frac{P_{\text{H}_2} (P_{\text{O}_2})^{1/2}}{P_{\text{H}_2\text{O}}} \right) \quad (2.7)$$

Equation 2.7 which gives OCV or EMF of a cell is called the Nernst equation and the amount of calculated OCV is known as Nernst voltage. This equation correlates the ideal standard potential of the cell ( $E^0 = \frac{-\Delta \bar{g}_f^\circ}{zF}$ ) to the ideal voltage ( $E$ ) at other partial pressures and temperatures of reacting and produced gases. Using the Nernst equation, the maximum possible OCV of a cell working at 25 °C with

hydrogen, would be calculated to 1.23 V, as mentioned before. In practice, the operational voltage of a fuel cell is less than the Nernst voltage due to different types of losses which will be discussed later. From equations 2.6 and 2.7 it can be observed that any increase in system pressure or partial pressures, or any decrease in temperature will lead to an increase in OCV.

The effect of system parameters such as partial pressure of hydrogen (as fuel), system pressure, and temperature can be investigated using the Nernst equation. The result of this equation for hydrogen partial pressure changes compares well with what has been experimentally investigated for a phosphoric acid fuel cell operating at 200 °C [8]. Also, the result of experimental studying of system pressure agrees well with what Nernst equation predicts for high temperature fuel cells [8, 19]. The results of the same study for lower temperature cells show a qualitatively similar trend although they are not the same as the values of the Nernst equation. At 200 °C, the actual change in OCV has been reported to be 6.3 times greater than the value predicted by the Nernst equation [8].

It has been mentioned that the Gibbs free energy is converted into electrical energy, within the cell. One definition for the efficiency of fuel cells could be the ratio of the produced electrical energy to the change in Gibbs free energy. However, this definition is rarely used since the efficiency limit is 100 % whatever conditions are used [9]. Another definition of efficiency would be the ratio of produced electricity per mole of fuel to the enthalpy of formation of water (hydrogen oxidation reaction results in water formation). Assuming that all the Gibbs free energy change is converted to electrical energy, the efficiency limit is given by equation 2.8:

$$\text{Maximum possible efficiency} = \frac{\Delta\bar{g}_f}{\Delta\bar{h}_f} \times 100 \quad (2.8)$$

This efficiency is a function of temperature due to the dependency of Gibbs free energy change on temperature. The maximum efficiency limit is 83 % and is calculated from equation 2.8 at 25 °C with liquid products [9]. Any increase in temperature leads to a decrease in the efficiency limit. Although the efficiency limit is higher at lower temperatures it should be noted that the losses at high temperatures are less, thus in practice the voltage of cell will be higher at elevated temperatures which will be discussed in the next sections.

Assuming that all the energy of oxidation reaction of fuel is converted to electricity, the EMF would be calculated by:

$$E = \frac{-\Delta\bar{h}_f}{2F} = \begin{cases} 1.48 \text{ volts if the higher heating value is used} \\ \text{or} \\ 1.25 \text{ volts if the lower heating value is used} \end{cases} \quad (2.9)$$

Higher heating value (HHV) is the enthalpy of formation of water in liquid form and lower heating value (LHV) is the same quantity when the water is in gaseous form. Thus, the actual efficiency of cell can be defined as:

$$\text{Cell efficiency} = \frac{V_c}{1.48} \times 100 \% \text{ (with reference to HHV)} \quad (2.10)$$

Equation 2.10 which can also be re-written with reference to LHV, can be used to calculate the efficiency of a fuel cell directly using the voltage of the cell [9].

### 2.1.2 Actual performance

The Nernst voltage is approximately 1.2 V for a low temperature cell (below 100 °C) and about 1 V for a high temperature cell (800 °C). When fuel cells are manufactured and put to use, the operational voltage is less than Nernst voltage. This lower voltage is due to several operational losses which are referred to by terms such as irreversibility, overpotential, overvoltage, polarization, or voltage drop. If the occurring process in the fuel cell is reversible all the Gibbs free energy will be converted to electricity, however, because of overpotential the performance of fuel cell would be degraded. These voltage drops can be categorized in 4 major groups [8, 9]:

- Activation losses: this type of overpotential is due to slowness of electrochemical reactions occurring in the cell. This means that a portion of generated voltage is lost to drive the reactions to completion and overcome the activation barrier of chemical and electrochemical reactions. The effect of activation losses is less important for high temperature cells since the high operating temperature will increase the rate of reactions and facilitate the splitting and combining process of species. Increasing the cell temperature, using more effective catalysts, increasing the roughness of the electrodes (to increase the real surface area), and increasing reactant concentration/pressure (to increase catalyst site occupancy) would result in a decrease in activation losses.
- Fuel crossover and internal current: although the electrolyte should only allow the conduction of ions, in practice it may permit the fuel and electrons to diffuse from one electrode to the other one. Another proportion of voltage is wasted when un-reacted fuel and electrons pass

through the electrolyte. Usually, these types of losses are low and could be neglected, except in low temperature cells.

- Ohmic losses: this type of polarization is mainly due to electrolyte resistance to flow of ions and, to a lesser extent, due to resistance to flow of electrons in electrodes and bipolar plates. Ohmic voltage drop, which is also known as resistive losses, is proportional to the current and is equal to the product of current and total resistance of cell.
- Mass transport or concentration losses: these drops are due to mass transport problems and change in concentration of species in reacting flow and are related to pressure changes. Slow transport of reactants to reaction sites and products from electrodes surface is a major contributor to mass transport losses which are also known as Nernstian since the effect of concentration (and therefore pressure) is modelled by the Nernst equation.

Because of the losses in cells, the operational voltage is less than the OCV predicted by the Nernst equation and is generally controlled at about 0.7 V, but is dependent upon the current being drawn from the cell. All types of fuel cell losses contribute to entropy generation, thus, exergy destruction.

In order to compare fuel cells performance, the current is considered in per unit of area which is known as current density. For characterizing fuel cells, usually a graph is drawn which shows the change of voltage vs. current density. Since the losses feature more and less severely for different operating temperature of cells, this characteristic graph will be different at different temperatures. This graph has been illustrated for low and high temperature cells in figure 2.3.

From these characteristic graphs, also known as v-i curves, it can be seen that in the case of low operating temperature the OCV of cell is smaller than the theoretical value, whereas, it is very close to the theoretical value in the high temperature cells. Also, there is a rapid initial drop in voltage once the current densities starts to have non-zero values for low temperature cells whereas this drop is quite small at high temperatures. This initial fall is due to the activation loss. The second drop in voltage, which is fairly linear with current density and less rapid, is associated with the ohmic losses of cell. The third drop in voltage results from the concentration losses. This drop is steeper than the ohmic losses and takes place at high current densities.

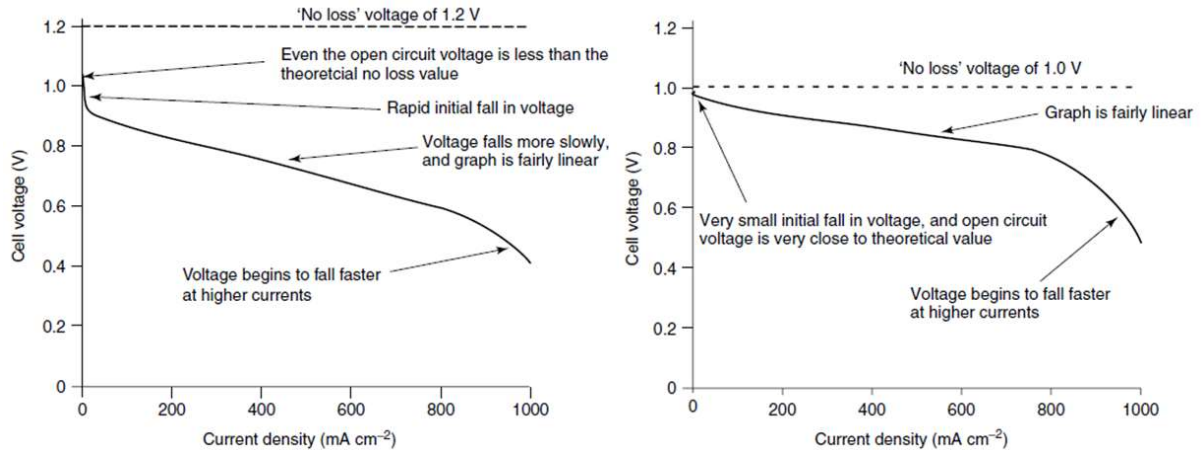


**Figure 2.3: Voltage/current density graph of low temperature (left) and high temperature (right) cells [9]**

## 2.2 Solid oxide fuel cells (SOFCs)

In recent years, solid oxide fuel cells have been widely studied and a lot of effort has been put into developing this technology. The main physical characteristics of the SOFCs are solid state construction and high operating temperature (600-1000 °C) which result in a number of unique features for this type of fuel cell [20, 21]. In addition to general advantages of fuel cells such as flexibility and low emissions, the main benefits of SOFCs over other types are:

- The ability to attain nearly theoretical power generation efficiency [22-24]
- Internal reforming of hydrocarbons [25] which leads to the ability to operate on a wide range of fuels such as natural gas, methanol, ethanol, and biogas [22, 26]
- High tolerance to pollution and impurities [27, 28]
- The potential of use in combined and hybrid systems such as gas turbines due to high operating temperature and hot exhaust gas [28]. The efficiency of SOFCs is about 50-60 %, however, if integrated in cogeneration systems, the efficiency would be more than 80 % [26, 29].

SOFCs are manufactured in different shapes depending on the stack design. Most common shapes are tubular and planar (or flat-plate). In addition to these two shapes, they are made into bell-and-spigot, banded and corrugated structures and as a result, they differ in gas flow configuration, individual cell design and electrical connection of neighboring cells [20].

- Tubular design: in this configuration the cells are designed as a tube and a stack is made of a bundle single cells. Figure 2.4 illustrates a schematic of a

tubular SOFC. In this design the inner layer is the air electrode (cathode) and the electrolyte is deposited on top of it. The anode is deposited on external surface of the electrolyte and would be the outer layer. The advantage of this type of configuration is the elimination of sealing problem of adjacent cells in a stack. In addition they are fairly stable against thermal stress cycle and stress [9, 30]. However, the manufacturing costs are high and also the power density is low which is due to the long path for electrical power through each cell [9]. The diameter of tubular SOFCs may vary from 0.1 mm to a few centimeters and their length may be up to 1.5 meters [8].

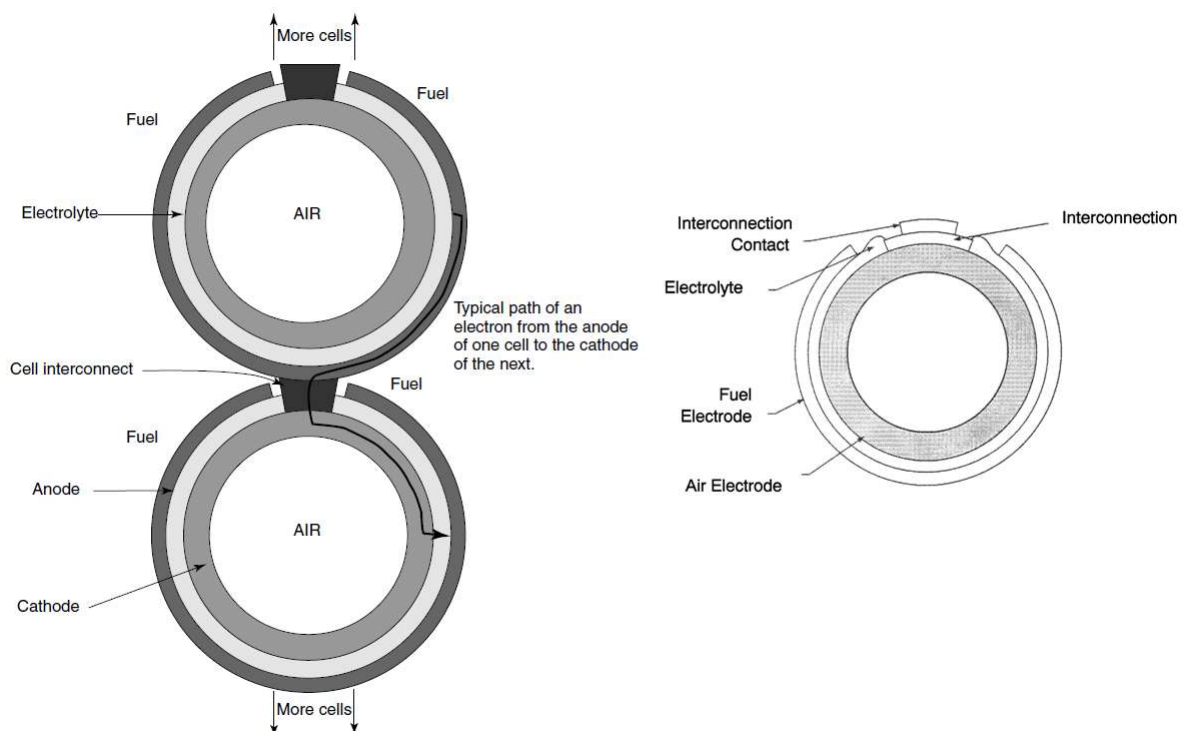


**Figure 2.4: Cross section of tubular SOFC [8, 9]**

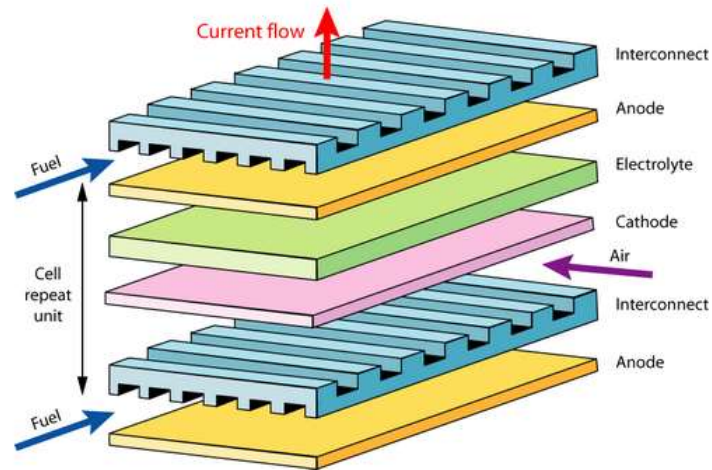


Figure 2.5: Planar SOFC [31]

- Planar design: single cells are designed as flat plates in this configuration which are connected in series to form a stack, as seen in figure 2.5. Using bipolar plates results in a lower ohmic resistance and thus a higher power density. Also the fabrication costs of this design are less than the tubular configuration. However, sealing the cells in a stack can be an issue. As mentioned before the edges of individual cells need to be sealed properly. The other issue associated with this design is the low thermal stability. Thermal stress at the interface of neighboring cells and also the stack material may lead to degradation in the performance of the system.

In order to fulfill the SOFC operating conditions there are some key requirements which should be met by the stack configuration, especially for the planar design [16]:

- The ohmic resistance of the stack should be minimized to obtain a higher performance. Therefore all the electrical conductive materials used in the cell and stack including the electrodes and interconnects should be highly conductive. Also there should be a sufficient contact area between the stack components to make the current path as short as possible.
- In order to achieve a high electrochemical performance the configuration should provide a minimum polarisation. Thus, all the gas and cross leakages as well as electrical shortcuts must be avoided carefully. In addition all the reactants should be distributed evenly over the surface of electrodes as also across the cells in stack. It is of great importance that the gases can

reach the reaction sites as rapidly as possible to minimize the concentration losses.

- The design should be able to manage and withstand thermal stresses. This means that a cooling system as well as a uniform temperature distribution during operation should be provided for the stack.
- The final requirement is the mechanical and structural integrity. This means that the stack should be designed to have high mechanical strength during operation and minimize mechanical and thermal stresses to prevent loss of integrity, cracking or delamination of components at normal and off-design operating conditions.

However, degradation over time remains as an issue and should be understood before the widespread use of the fuel cells at industrial level. In order to rectify this drawback, it is necessary to identify the characteristics, operating conditions and materials of SOFCs. Currently, lots of companies and research groups are involved in SOFCs industrial development and commercialisation, to find the solutions and broaden the range of the applications. In the next section a brief description of the components of SOFCs is presented.

### **2.3 SOFC components, materials and configurations**

Similar to other types of fuel cell, solid oxide fuel cells consist of three main layers: anode, electrolyte and cathode. The electrodes (anode and cathode) are separated by electrolyte made of a dense solid cermet (ceramic/metal) and sandwiched in between. The mobile ion is  $O^{2-}$ . Oxygen gas is reduced to oxygen ions at cathode and passes through the electrolyte to the anode. These ions, then, react with hydrogen at anode producing water. Figure 2.6 shows a schematic of the planar SOFCs. As a result of hydrogen reaction with oxygen ions, two electrons are released which travel through an external circuit producing a DC current.

Considering the high operating temperature and solid nature of cell components, in order to minimise the thermal stresses and avoid any potential crack or delamination the thermal expansion coefficient of material should be in the same range. A reduction in the operating temperature may result in a number of advantages such as [32]:

- The possibility of replacing expensive ceramic interconnects and separators with low cost metallic ones

- Longer life time and performance stability
- Compactness of SOFC system due to reduced thickness of heat insulator

However, it should be considered that temperature reduction may degrade the resistance of cells against the different impurities especially sulfur which exists primarily as H<sub>2</sub>S in potential fuels, such as those derived from natural gas, oil, coal, and biofuels [32, 33].

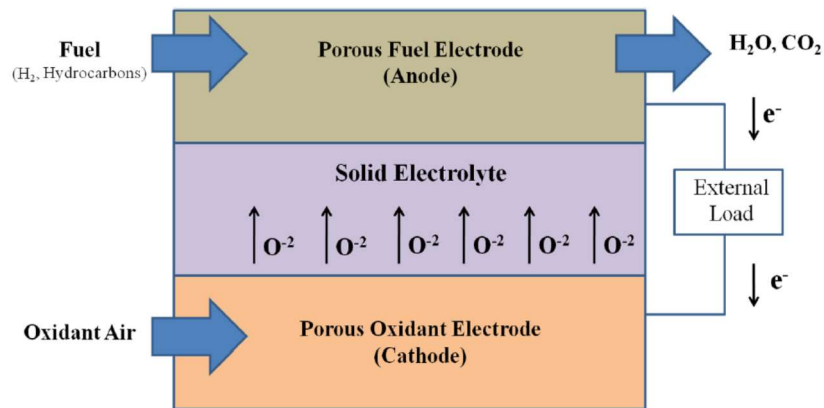


Figure 2.6: Schematic of a planar SOFC [34]

### 2.3.1 Anode

Hydrogen (or other possible fuels) is electrochemically oxidized at anode of the cell. In the case of hydrogen the oxidation reaction would be:



Due to the high operating temperature the water appears as vapour in this reaction.

The material for the anode should be able to satisfy different requirements such as high electrical conductivity to minimize the ohmic losses, chemical stability in a reducing environment, high electrochemical activity to promote the kinetics of oxidation reaction, high porosity (20-40 %) to permit the reactants/product to transport to/from reaction site, chemical compatibility with neighbouring components, high resistance to coke deposition, tolerance to impurities and ability to reform other fuels such as methane and carbon monoxide [9, 35].

All the electrochemical reactions at electrodes occur around Triple Phase Boundaries (TPBs). TPBs are defined as the points where gas, electrode (electron conducting phase), and electrolyte (ion conducting phase) meet [9, 36]. In SOFCs, the TPBs which are next to the electrode/electrolyte interface support the reduction and oxidation reactions at cathode and anode respectively. Therefore, an

active layer for reaction exists. The rest of electrode above this layer does not contribute to reaction and only acts as gas diffusion layer [37]. In order to extend TPBs at anodes, novel materials have been developed such as TiO<sub>2</sub>-based systems. These materials function as mixed electronic and ionic conductors (MEIC) which will result in an increase in number of reaction sites [7, 9, 38]. Three phase boundary regions in the anode for both pure electronic conductor and MEIC have been illustrated in figure 2.7.

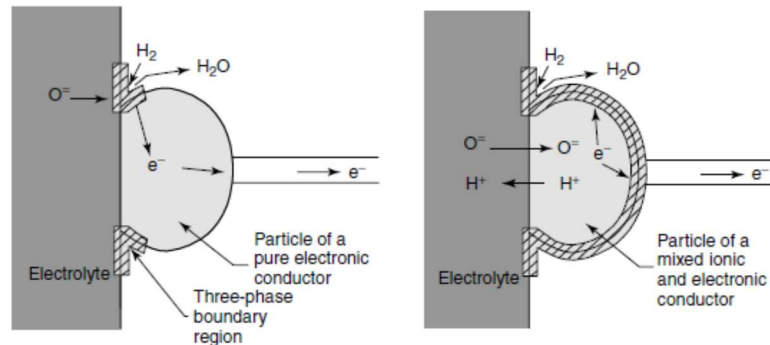


Figure 2.7: TPB regions for an electronically conducting cermet (left) and a MEIC (right) [9]

The most common material for the anode is a porous cermet consisting of metallic nickel and an YSZ skeleton. Such an anode is electrically conductive due to its nickel content. The YSZ skeleton serves different tasks in the anode [39]:

- To inhibit sintering of the metal particles – Once sintered at high temperatures, nickel particles tend to aggregate. Addition of YSZ helps improve the dispersion of nickel as well as the porosity of electrode.
- To provide a coefficient of thermal expansion (CTE) comparable to that of the electrolyte – The average CTE of pure nickel is different from that of YSZ [40]. Addition of YSZ to the nickel anode minimizes the CTE mismatches between anode and electrolyte. The average CTE of pure nickel, YSZ and Ni-YSZ in the range of 0-1000 °C is around 17, 10 and 13 ppm/K, respectively [41].
- To form an extended region of three-phase boundary (TPB) – Addition of YSZ (which is an oxygen ion conductor) results in mixed electronic and ionic conductivity of anode and increases the number of reaction sites.

In recent years many alternative materials based on perovskite-type (ABO<sub>3</sub>) or related structures such as copper-based, lanthanum-based, titanium-based, cobalt-based, platinum-based and cerium-based cermets have been developed to increase the performance of the anode which can be found in literature [9, 21, 35,

42, 43]. Other candidate materials include manganese, vanadium, chromium/vanadium, chromium/manganese and manganese/molybdenum. Although these materials have shown higher resistance to coke deposition and sulphur poisoning they are either less electrically conductive or electrochemically active as compared to Ni-YSZ. Therefore, among the options, Ni-YSZ is considered a very stable and active material for anode [43].

### 2.3.1.1 Internal reforming

One of the outstanding features of SOFCs is the ability to run on different fuels, as mentioned before. Being considered as diluents or poisons for most of the fuel cell types, carbon monoxide and methane can be used as fuel in SOFC anode. In such situations, the anode reactions would be:



Although these reactions in SOFCs, which work at high temperature, are feasible without catalyst, in reality, small amounts of CO and CH<sub>4</sub> are directly oxidized in the cell. Over the last decades, the nickel-based catalysts have been investigated by many researchers and their ability to reform hydrocarbons at elevated temperatures has been proved [44, 45]. Since the most common material used for the anode is nickel-based, a significant portion of CO and CH<sub>4</sub> will undergo reaction with water at the high operating temperature of SOFCs. The basic endothermic reforming reaction for methane, which normally takes place over nickel catalysts at temperatures above 500 °C, is:



Other heavier hydrocarbons can also be reformed through a reaction with water and thus, similar reactions can be written. In such a favorable situation for methane reforming, reaction 2.14 is nearly always followed by another reaction which is exothermic and known as water gas shift (WGS):



Both of these reactions are reversible and finally reach equilibrium. Therefore, hydrogen, carbon monoxide, and methane are present in mixture [9]. In SOFCs, because of the high temperature environment and also the presence of nickel, reactions 2.14 and 2.15 are faster and more favored than direct oxidation of CO and CH<sub>4</sub>. The total amount of H<sub>2</sub> produced from reactions 2.14 and 2.15 along with any

available hydrogen in fuel, which is called equivalent hydrogen, is involved in anode reaction [8].

Direct oxidation of methane in SOFCs is less feasible than that of carbon monoxide, thus, the electrochemical conversion of methane is usually approximated by the reforming reaction [46], whereas, CO can be directly oxidized in the anode [27]. However, the assumption that CO is also reformed with H<sub>2</sub>O to H<sub>2</sub> can simplify the accurate analysis of cell behavior [8].

One of the key points in internal reforming of hydrocarbons in SOFCs is the risk of carbon deposition, known as coking. In the absence of steam, hydrocarbons are prone to decompose and form carbon when the temperature is high, as in SOFCs. Also CO can be another source of carbon deposition through disproportionation in anode [47]. The carbon formation reactions over catalysts such as nickel, cobalt and platinum are reversible and can be listed as [48]:



Reaction 2.16 is called CO dissociation or CO disproportionation or the Roudouard reaction. Reaction 2.17 is named CH<sub>4</sub> cracking or decomposition which is favored at temperature above 650 °C in the absence of air and steam. Up to 650-700 °C, WGS is favored which results in more hydrogen production. Above these temperatures reverse WGS takes place which leads to a decrease in hydrogen concentration in the mixture. Also at temperatures above 700-750 °C the methane is completely reformed to hydrogen and no longer exist in the mixture [9, 45].

The formed carbon can block the pores and prevent gas transfer, and also cover the active sites of the anode which results in cell deactivation and performance degradation. Lots of studies have been conducted to investigate the carbon formation mechanisms and also preventive methods. The general and simplest way to prevent coking is to add steam to the fuel flow, which promotes the reforming reaction and water gas shift. However, adding steam to fuel will dilute the gas, which leads to a decrease in fuel conversion efficiency [45].

Based on the thermodynamic calculations, in order to prevent coke deposition over anode material of SOFCs, the steam to carbon ratio (H<sub>2</sub>O/C ratio) should be kept above 1.5, however, this ratio should be higher in practice [25]. H<sub>2</sub>O/C ratio is defined as the number of moles of steam per mole of carbon in fuel fed to the

anode [9]. Although some other thermodynamic analyses have shown that the  $H_2O/C$  ratio of 1 at 800 °C is enough to prevent coking in methane reforming [49], the optimum conditions has been thermodynamically identified within  $H_2O/C$  ratios of 2-3 and temperatures between 700-800 °C [48]. Rapid deactivation has been shown at  $H_2O/C$  ratios less than 1 in steam reforming of methane over Ni based catalysts [50]. It has been reported by many researchers that, considering a safety margin,  $H_2O/C$  ratios of 2-3 should be employed in order to avoid carbon deposition in conventional steam reforming catalysis [9, 28, 51]. However, novel cermets such as nickel-gadolinium doped ceria (Ni-GDC), which is known for its high resistance to coking, have been tested successfully at  $H_2O /C$  ratio of 0.5 [51].

In the direct reforming process of methane over nickel cermet, it has been reported that the rate of steam reforming is a function of steam content of fuel, operating temperature, and fuel gas composition [52]. In contrast, some studies show that the partial pressure of steam does not influence the steam reforming rate [27]. In addition to methane, other hydrocarbons such as methanol and ethanol could be considered as fuel in SOFCs. Experimental results [53] show that in case of ethanol, the amount of carbon deposited on the anode is much greater than two other fuels. Also it is observed that carbon deposition from methane and methanol decreases with increasing steam content and operating temperature, whereas, coking in ethanol reforming process is slightly improved by increasing steam content and temperature. It has been showed that some parts of carbon deposited at or near TPBs would be reversible, but another portion of carbon, mainly deposited on Ni surface, is irreversible [54].

### **2.3.1.2 Redox cycle**

As mentioned before nickel is the most common material for the anode of SOFCs, however, it may cause two problems during the operation; the first one is the possibility of coke deposition in case of using hydrocarbon as fuel, and the second is the tendency for oxidation which leads to dimensional instabilities [39].

In case of large fuel utilisation factor, leakage of oxygen from cathode to anode or fuel shortage/dilution in presence of current, the nickel phase of anode tends to be oxidised [55]. Fuel utilisation factor is defined as [56]:

$$U_f = \frac{I}{2 \cdot F \cdot \dot{n}_f (X_{H_2} + X_{CO} + 4 \cdot X_{CH_4})} \quad (2.20)$$

where  $\dot{n}_f$  is the molar flow rate of fuel,  $I$  is the drawn current,  $F$  is the Faraday's number, and  $X_i$  is the mole fraction of fuel gases, considering that each mole of carbon monoxide can produce another mole of hydrogen through the water gas shift (reaction 2.15) and each mole of methane produces four extra moles of hydrogen through steam reforming reaction (reaction 2.14) and water gas shift of the produced CO (reaction 2.15). A large fuel utilisation factor results in a large oxygen ion flux reaching the anode which can oxidise the nickel. The oxidation reaction of nickel is:



The general oxidation reaction is [55]:



According to this reaction an oxidised layer is initiated which grows at the interface of anode and electrolyte. The thickness of this layer is a function of time of exposure to oxidation conditions (high temperature and presence of oxygen) as well as material properties [57].

The anode is initially made of a sintered mixture of nickel oxide powders and an oxygen ion conducting phase such as YSZ or GDC. At the first operation of the cell, the NiO is reduced to Ni at high temperatures in the presence of hydrogen through reaction 2.23:



Reaction 2.23 is considered as the first component of redox (reduction and oxidation) cycle. Through this reaction the bulk dimension of anode changes very slightly which can be neglected. However, the decrease in solid volume results in an increase in the porosity of anode. On the contrary, the oxidation of solid Ni to NiO (the second component of redox cycle) leads to an increase of about 70 % in solid volume and expansion of anode. Any further reduction will not recover the initial state of the anode and as a result a dimensional change will be built up as the cell goes through redox cycles [39]. This change in dimensions of the cell can generate mechanical stresses in the anode which may lead to performance degradation or even cell cracking or delamination. Figure 2.8 illustrates the microstructural modification due to redox cycle. The grey particles in this figure show metallic nickel.

Figure 2.8a shows the initial state of anode. As seen from figure 2.8b, reduction of NiO to Ni leads to an increase in porosity of anode. At high operating temperatures metallic Ni particles tend to aggregate (figure 2.8c). Re-oxidation of Ni to NiO is accompanied by a volumetric expansion which may lead to loss of integrity of cell. As a matter of fact the size of NiO particles grows through redox cycles and degrades the performance of cell [39, 58, 59].

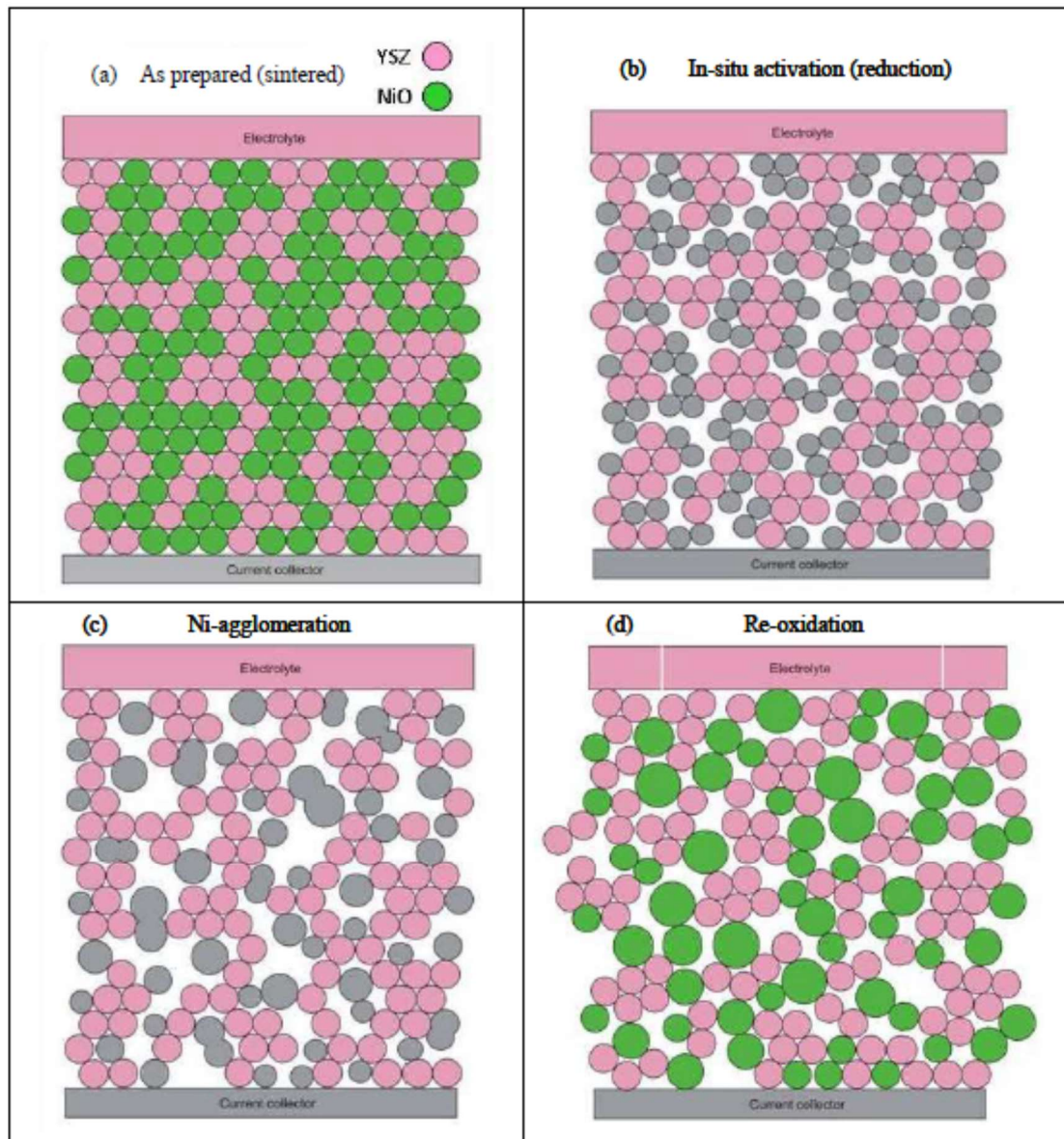


Figure 2.8: Microstructural modification due to redox cycle [60]

The addition of YSZ to anode will affect the redox behaviour of NiO and Ni. The presence of YSZ tends to retard the reduction of NiO to Ni (i.e. the reduction of NiO powder starts at lower temperature compared to NiO-YSZ) and accelerate the oxidation of Ni to NiO (i.e. the oxidation of Ni powder is slower than that of Ni-YSZ). Also it has been shown that the size of particles of NiO and YSZ does not affect the

reduction process. This is due to the sintering of NiO particles and forming an equal surface area at a given temperature. On the contrary, the sintering temperature of anode changes the reduction process of NiO-YSZ cermet i.e. the reduction reaction takes place at lower temperatures for the lower sintering temperatures [61].

In order to prevent the redox cycle and its potential damage to cell performance the anode should be kept at reducing condition during the operation. Generally the reduction of Ni-YSZ cermet takes place at temperatures about 300 °C and above [62]. Also, Ni tends to react with oxygen at the same range of temperatures. Therefore, it is essential to keep the flow of hydrogen during the cooling down process to inhibit the oxidation of Ni. In addition, in order for the anode to be kept at reducing conditions, hydrogen should be fed to the cell, during the heating step of the following test.

### **2.3.2 Electrolyte**

In SOFCs, electrolyte is made of a dense oxygen ion conducting ceramic and sandwiched between two electrodes consisting of porous ceramic materials. The solid oxide electrolyte should permit the transport of oxygen ions from cathode to anode. The electrolyte should exhibit several characteristics in SOFCs [9, 21, 35]:

- ionic conductivity – to pass the oxygen ions
- electronic insulation – to prevent internal currents
- chemical stability at high temperatures and in reducing and oxidizing environments;
- impermeability – to prevent fuel cross over losses
- production as a uniformly thin layer – (to minimize ohmic losses)
- thermal expansion coefficient close to that of electrodes
- inexpensive materials

Historically zirconia was the first material used as the electrolyte in SOFCs due to its ionic conductivity and until recently, it has been the most common material for electrolyte [9]. Due to the cubic fluorite structure, stabilised zirconia and ceria have been considered as the most recommended materials for the electrolyte [16]. In addition to them, some other electrolytes have been developed using materials such as lanthanum, bismuth and barium [35]. Among the alternatives, zirconia is fairly cheap and has been the most common material over previous decades.

Pure zirconia can adopt different types of crystal structure depending on the temperature [63]. Below a temperature of 1446 K it possesses a monoclinic structure. In the range of 1446 to 2643 K the structure changes to tetragonal and above 2643 K it adopts a cubic structure. The cubic structure can be partially or fully stabilised even at room temperatures by replacing tetravalent  $Zr^{4+}$  with di- or trivalent (lower valency) ions such as  $Ca^{2+}$ ,  $Mg^{+2}$ ,  $Y^{3+}$  or  $Sc^{3+}$  [9, 63]. Once the zirconia is doped with yttria, for instance, some oxygen vacancies will be generated to keep the charge neutrality of the structure. Thus it can be said that yttria doping serves two functions: stabilising the cubic structure in zirconia and also generating oxygen vacancies both increasing the ionic conductivity of zirconia [21, 63]. Figure 2.9 illustrates the structure of YSZ.

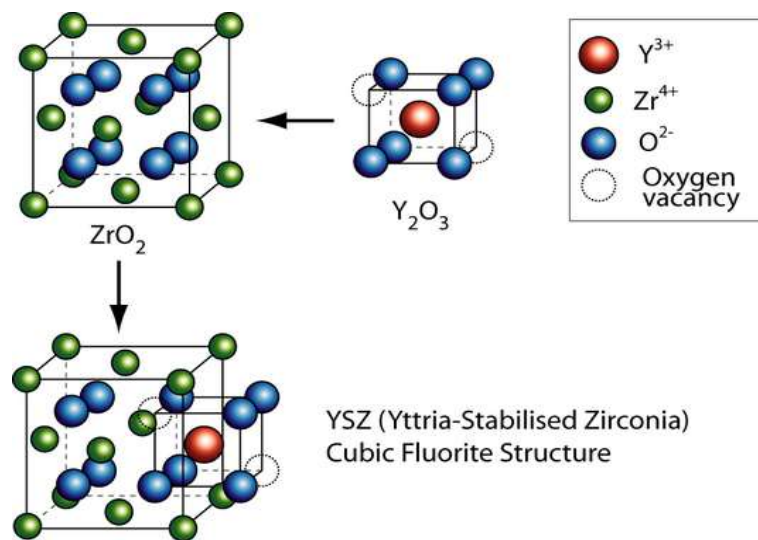


Figure 2.9: YSZ structure [64]

Once a number of the  $Zr^{4+}$  ions are replaced with  $Y^{3+}$  ions some oxygen vacancy will be generated due to three  $O^{2-}$  substituting four  $O^{2-}$  in the lattice as can be seen in figure 2.9.

Another material for electrolyte and ceramic part of anode, which has been widely used in the last few years, is gadolinium doped ceria or GDC. Because of its high performance in lowered temperature and also high resistance to carbon deposition, GDC has received much attention and is used by many SOFC manufacturers. It has been shown that the ceria content of GDC increases the anode resistance to carbon formation [50, 51, 65]. However GDC is considered a costly material which is not as mechanically stable as YSZ [66, 67].

### 2.3.3 Cathode

The cathode is the air or oxidant electrode in SOFCs where oxygen gas is reduced to ions within the cell through the reaction 2.24.



Two released electrons at anode travel through an external circuit and reach the cathode where they react with oxygen to produce  $O^{2-}$  ions.

Similar to the anode, every cathode material should be able to satisfy a number of requirements as follows [9, 21, 35, 68]:

- high electronic conductivity to minimize the resistance against electrons motion
- high catalytic activity to reduce oxygen
- high porosity to permit the transport of gas to avoid concentration losses (30-40 %)
- comparable thermal expansion to other components
- minimum reactivity and compatibility with adjacent components
- mixed electronic and ionic conductivity to increase the number of TPBs
- stable in oxidizing environment
- simple fabrication
- inexpensive materials

Figure 2.10 shows a schematic of a SOFC and cathode/electrolyte interface.

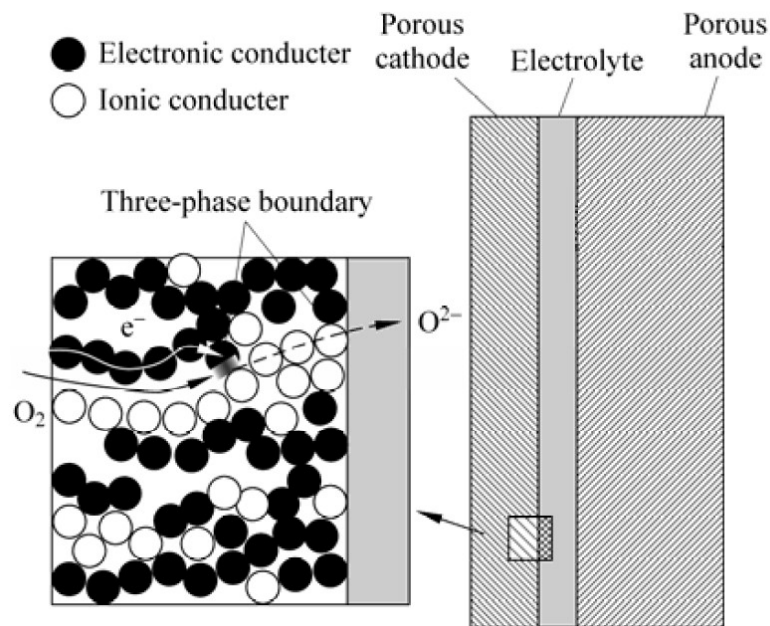


Figure 2.10: Schematic of cathode/electrolyte interface [69]

Traditionally strontium-doped lanthanum manganite (LSM) has been used for the cathode. The perovskite  $\text{LaMnO}_3$  is usually doped with calcium or strontium to improve the electronic conductivity and matches the CTE of  $\text{LaMnO}_3$  to that of other components within the cell [68].

Over recent years many other cathodes have been developed to improve the performance of SOFCs and lower the operating temperature. These include a variety of other lanthanum-based cathodes, gadolinium-, yttria- and strontium-based materials [35, 66]. Among them is  $\text{La}_x\text{Sr}_{(1-x)}\text{CoO}_3$  ( $x:0.6-0.8$ ) or LSC which is a good candidate for lower operating temperatures and mixed electronic and ionic conductor[70]. However, it is known that cobalt-based cathode tends to react with YSZ electrolyte at the interface, thus they are either used with a GDC electrolyte or separated from YSZ with a barrier layer made of DGC [35, 38].

### 2.3.4 SOFC configurations

At the moment single solid oxide fuel cells are fabricated and configured in two ways: self-supporting and external supporting. In self-supporting configuration, one of the layers of cell – anode, electrolyte or cathode – is much thicker than others and acts as the cell support. However, in external-supporting design an external component such as interconnect or a porous substrate tends to support the single cells manufactured as a thin layer. According to this classification, self-supporting design is divided to anode- (ASC), electrolyte- (ESC) and cathode-supported (CSC) configurations. The external-supported design is also categorised in interconnect- and porous substrate-supported configurations. The schematic of each configuration has been illustrated in figure 2.11. These configurations and their key features have been presented in table 2.1 [20, 68].

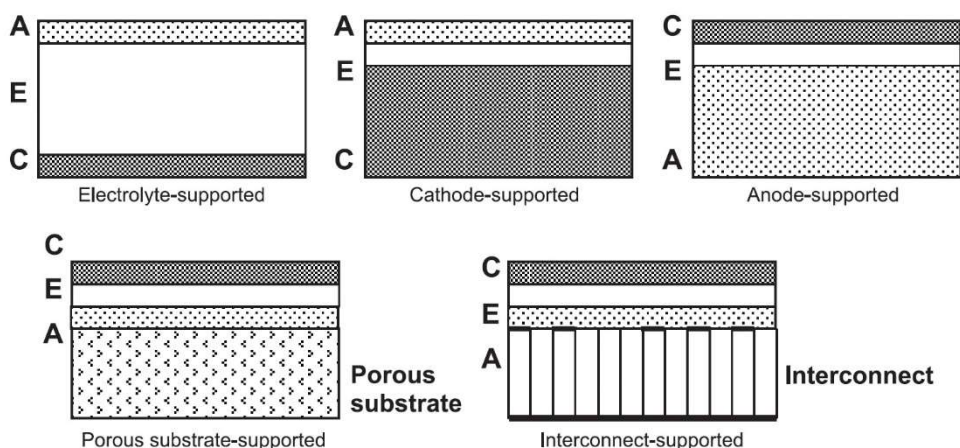


Figure 2.11: Schematic of different configurations of single SOFCs [20]

Cell configuration		Advantage	Disadvantage
<b>Self-supporting</b>	Electrolyte-supported	Relatively strong structural support from dense electrolyte, less susceptible to failure due to anode re-oxidation, (Ni/YSZ anode) and cathode reduction (LSM cathode)	Higher resistance due to low electrolyte conductivity, higher operating temperatures required to minimize electrolyte ohmic losses
	Anode-supported	Highly conductive anode, lower operating temperature via use of thin electrolytes, high potential of reforming, longer cell life, reduced thermal stress	Potential slow electrode reaction kinetics, mass transport limitation due to thick anodes
	Cathode-supported	No oxidation issues but potential cathode reduction, lower operating temperature via use of thin electrolyte	Lower conductivity, mass transport limitation due to thick cathodes
<b>External supporting</b>	Interconnect-supported	Thin cell components for lower operating temperature, stronger structures from metallic interconnects	Interconnect oxidation, flow field design limitation due to cell support requirement
	Porous substrate	Thin cell components for lower operating temperature, potential for use of non-cell material for support to improve properties	Increased complexity due to addition of new materials, potential electrical shorts with porous metallic substrate due to uneven surface

Table 2.1: Features of single cell configurations

## 2.4 SOFC mathematical model

The general approach to model fuel cells is to determine the ideal performance and then, deduct the losses from that. The Nernst voltage (equation 2.7) is used to calculate the maximum possible voltage of the cell once the partial pressure of all reactants is known. The operating voltage of the SOFCs is given by:

$$V = E - \eta_{act} - \eta_{ohm} - \eta_{conc} \quad (2.25)$$

where  $E$  is Nernst voltage,  $\eta_{act}$  is the activation losses (at anode and cathode),  $\eta_{ohm}$  is the ohmic loss (anode, electrolyte and cathode) and  $\eta_{conc}$  is the concentration overpotential (at both electrodes).

Generally, at low current densities activation overpotentials are dominant. Once the current is increased both activation and ohmic losses are present and tend to decrease the voltage of the cell. At high current densities the concentration loss highly affects the performance of the cell leading to a further decrease in the operating voltage.

- Activation losses at anode and cathode are described by Butler-Volmer relation [71, 72] and can be expressed as [73]:

$$\eta_{act,an}(i) = \frac{RT}{\alpha zF} \sinh^{-1} \left( \frac{i}{2i_{0,an}} \right) \quad (2.26)$$

$$\eta_{act,ca}(i) = \frac{RT}{\alpha zF} \sinh^{-1} \left( \frac{i}{2i_{0,ca}} \right) \quad (2.27)$$

where  $\alpha$  is the charge transfer coefficient,  $z$  is the number of electrons,  $R$  is the universal gas constant,  $T$  is the operating temperature,  $F$  is the Faraday number,  $i$  is the current density at which the cell is loaded and  $i_0$  is the exchange current density. Exchange current density is a measure of the electrochemical (catalytic) activity of the cell [9, 74] and strongly depends on the electrode properties i.e. material, metal content and porosity, and operating conditions such as temperature, pressure and fuel composition and can be expressed as [73]:

$$i_{0,an} = \frac{RT}{zF} K_{an} \exp \left( \frac{-E_{an}}{RT} \right) \quad (2.28)$$

$$i_{0,ca} = \frac{RT}{zF} K_{ca} \exp \left( \frac{-E_{ca}}{RT} \right) \quad (2.29)$$

where  $K$  is the pre-exponential factor and  $E$  is the activation energy of the exchange current density.

In addition to equations 2.28 and 2.29, there are other expressions for  $i_0$  taking into account the effects of the partial pressure of species at electrodes [75, 76]. Due to the variation of the presented expressions it is necessary to experimentally measure the correct value of  $i_0$  at the operating conditions of interest [74].

- Ohmic loss is described as [73, 77]:

$$\eta_{ohm} = Ri \quad (2.30)$$

$$R = \sum R_j = \sum \frac{e_j}{\sigma_j} \quad (2.31)$$

where  $R$  is the resistance,  $e$  is the cell component thickness,  $\sigma$  is the cell component conductivity and  $j$  is the index for cell components i.e. anode, cathode and electrolyte. The conductivity of the cell layers is expressed as:

$$\sigma_{ele} = \beta_1 \exp \left( \frac{\beta_2}{T} \right) \quad (2.32)$$

$$\sigma_{an} = \frac{\varepsilon_1}{T} \exp \left( \frac{\varepsilon_2}{T} \right) \quad (2.33)$$

$$\sigma_{ca} = \frac{\gamma_1}{T} \exp \left( \frac{\gamma_2}{T} \right) \quad (2.34)$$

$T$  is the operating temperature and  $\beta_1, \beta_2, \varepsilon_1, \varepsilon_2, \gamma_1, \gamma_2$  are constant values.

- Concentration losses emerge when mass transport effects hinder the electrochemical reactions at the electrodes. Due to the pressure distribution of reactants/products across anode/cathode the Nernst voltage is calculated as [71]:

$$E = \frac{-\Delta g_f^\circ}{zF} + \frac{RT}{zF} \ln \left( \frac{P_{H_2,TPB} (P_{O_2,TPB})^{1/2}}{P_{H_2O,TPB}} \right) \quad (2.35)$$

The difference between equations (2.7) and (2.35) accounts for the concentration overpotential which gives the deviation from the theoretical value of the voltage. Comparing equations (2.7) and (2.35), the concentration losses can be written as:

$$\eta_{conc,an} = \frac{RT}{2F} \ln \left( \frac{P_{H_2O,TPB} P_{H_2,f}}{P_{H_2O,f} P_{H_2,TPB}} \right) \quad (2.36)$$

$$\eta_{conc,ca} = \frac{RT}{4F} \ln \left( \frac{P_{O_2,a}}{P_{O_2,TPB}} \right) \quad (2.37)$$

where  $f$  and  $a$  denote fuel and air channels, respectively.

The relation between the partial pressure of species at TPBs and channel is expressed as:

$$P_{H_2,TPB} = P_{H_2,f} - \frac{RTe_{an}}{2FD_{eff,an}} i \quad (2.38)$$

$$P_{H_2O,TPB} = P_{H_2O,f} + \frac{RTe_{an}}{2FD_{eff,an}} j \quad (2.39)$$

$$P_{O_2,TPB} = P - (P - P_{O_2,a}) \exp \left( \frac{RTe_{ca}}{4FD_{eff,ca}P} i \right) \quad (2.40)$$

where  $e$  is the electrode thickness,  $D_{eff}$  is the electrode effective diffusion coefficient,  $R$  is the universal gas constant,  $T$  is the temperature,  $F$  is the Faraday number and  $i$  is the current density.

## 2.5 SOFC degradation

In order to commercialise the applications of SOFCs it is important to study the performance over long periods of time. To date, a large degree of effort has been put into broadening the knowledge in this area and identifying the degradation mechanisms through which fuel cells can be damaged. Several parameters can contribute to the fuel cell degradation [26, 57, 78-80]:

- Operating conditions (current density, temperature, gas composition and water partial pressure)
- Thermal and redox cycles
- Mismatched properties of components
- Contamination

Generally, the effects of degradation are divided into 2 broad categories: structural and chemical [81]. The structural category includes:

- Flow blockage (when pores of the electrodes are clogged)
- Delamination (when different layers of cell separate)
- Particle formation/coarsening (when formation of a new phase at anode changes the volume of a component of the electrode)
- Structural collapse (formation of cracks or/and loss of integrity).

Parameters such as electrode microstructure, porosity, tortuosity, permeability and pore diameter can be affected by the structural damage group. Figure 2.12 illustrates an example of crack and delamination in the cathode of a SOFC.

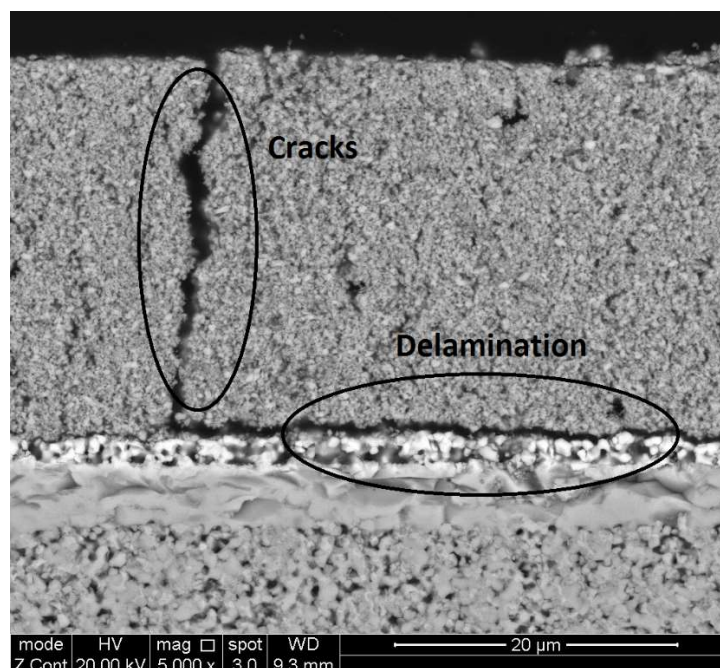


**Figure 2.12: Cracks and delamination in cathode**

There are also, several subcategories in the chemical group:

- Adsorption of contaminant is one of the main degradation mechanisms affecting the number of the reactive sites (length of TPB), surface diffusion, ionic and electrical conductivity, thermal conductivity, reaction rate and charge transfer reaction rate.
- Migration of Ni from anode to react with the contaminant and form secondary phases which affect the electrochemical properties of the electrode such as length of TPB, ionic and electrical conductivity, thermal conductivity and volume fraction.

- Composition change which refers to the reaction of the contaminant with the components of the electrode microstructure and formation of a new material. This mechanism tends to affect the thermal conductivity, length of TPB, ionic and electrical conductivity, reaction rate and charge transfer reaction rate.
- Electrochemical reaction of the electrode with the contaminant resulting in blockage of TPB sites and reduction in the number of the electrons available for the main electrochemical reaction of the cell. This mechanism affects the TPB length, thermal conductivity, charge transfer reaction rate and ionic and electrical conductivity.

An example of secondary phase formation at anode has been shown in figure 2.13. The anode of the cell was exposed to 1 ppm of phosphorous and as a result, phosphide phases were formed during the exposure period.

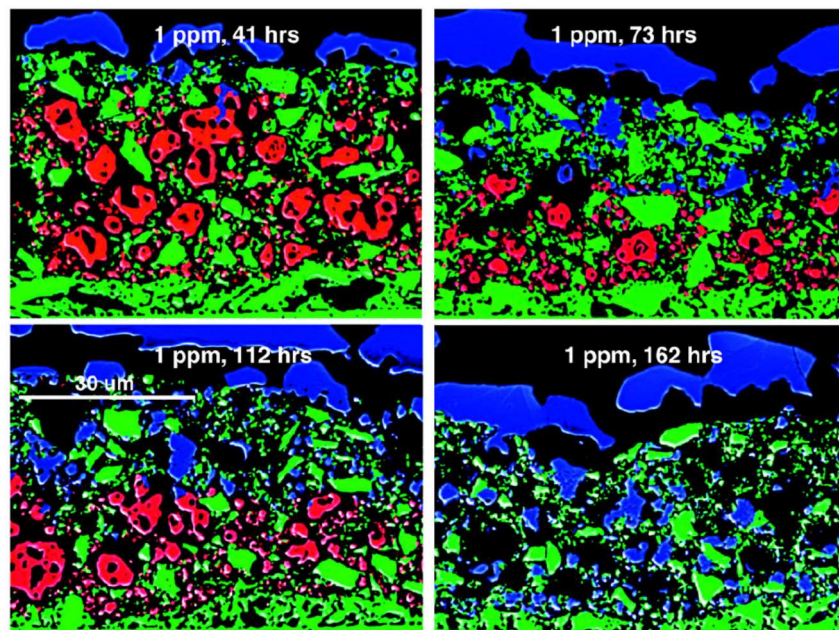


Figure 2.13: Example of secondary phase formation at anode - Nickel is red, YSZ is green and nickel phosphide phases are blue [82]

SOFC performance loss can be caused by intrinsic or extrinsic factors, depending on the source of the degradation. Intrinsic degradation factors are sourced from within the cell such as microstructural change/coarsening, decomposition/interdiffusion of components and impurities present in raw materials. Conversely, extrinsic factors have root causes which have originated from outside of the cell. Unsafe operating procedures, leading to redox of anode or coke deposition, and contaminants present in fuel are examples of the extrinsic group.

Unsafe operation refers to a series of procedures which can cause redox cycles, thermal cycles, coke formation, external physical damage, etc. Under safe operation and clean fuel, cells tend to degrade in long term. The degradation is due to increase in nickel particle size, thus, decrease in TPB's length. The physical change can be modeled as [83]:

$$\frac{l_{TPB} - l_{TPB}^{infinity}}{l_{TPB}^{initial} - l_{TPB}^{infinity}} = e^{-kt} \quad (2.41)$$

The exchange current density of electrodes is proportional to TPB's length [81, 83]:

$$\frac{i_0}{i_0^{initial}} = \frac{l_{TPB}}{l_{TPB}^{initial}} \quad (2.42)$$

Therefore, it can be stated that the exchange current density of electrodes tends to decrease over long periods of time and cause the cell voltage to drop.

As an example of the extrinsic degradation, Ryan et al. [81] proposed a damage model for H<sub>2</sub>S poisoning, based on the H<sub>2</sub>S degradation mechanism:

$$l_{TPB} = l_{TPB}^{initial}(1 - f) \quad (2.43)$$

where  $f$  is the damage factor.

Curve fitting of the experimental data of H<sub>2</sub>S poisoning yielded a relation for  $f$  as:

$$A(T) \ln\left(\frac{P_{H_2S}}{P_{H_2}}\right) + B(T) \quad (2.44)$$

where  $A(T)$  and  $B(T)$  are temperature dependent constants.

## 2.6 Fuel and impurity sources

It is clear that the operation of fuel cells relies on the effective delivery of fuel and oxygen to reactive sites (TPBs) through the porous electrodes and thus permitting the reactions to take place. In situations that no reactant can reach TPBs, such as when the pores of anode and cathode are plugged by the presence of an excessive amount of water, the cell performance will be obviously degraded. Similarly, poisoning of electrodes -especially anode- as a result of the presence of contamination in fuel or oxidant streams, may cause the cell to lose its function which it referred to as fuel cell poisoning. Contamination sources can be divided into three categories: fuel contamination, oxidant contamination and system contamination [1]. Currently, the hydrogen used in fuel cells comes from the sources which are commercially available. These sources include the steam reforming of fossil hydrocarbons (such as natural gas, oil, and coal) and biomass-derived hydrocarbons, electrolysis, and oxidative (or autothermal [48]) reforming

of hydrocarbons. In addition, a variety of solar energy methods for hydrogen production have been developed which are not economical at the current stage of technology. However, the hydrocarbons reforming process - as the main industrial source of hydrogen production - leads to unavoidable impurities such as sulfur compounds and ammonia [84] which will result in cell degradation.

The second source of contamination is air which is widely used in fuel cell stacks as the oxidant. The present pollutants such as nitrogen and sulfur oxides and other chemical species may contaminate the cell and prevent it from operation at optimum condition. Besides fuel and oxidant contaminants, some other contaminants from corrosion or evaporation of system components in high temperature cells such as interconnects and seals may also cause some loss in cell performance. For instance, iron-chromium ferritic stainless steel is widely used as interconnect in SOFC stacks. At the high operating temperature of SOFCs chromium particles are prone to migrate onto the cathode which leads to performance degradation of cell [70, 85, 86].

Biomass as a green and renewable energy source is considered to play an important role in reducing the amount of industrial emissions [87] and is widely used to produce synthesis gas. The term "biomass" refers to a wide range of materials which can be used as fuel through conversion processes. The common feature among all types of biomass is that they are all derived from recently living plants [88]. There are a large number of biomass types, conversion options and techniques, and end-use applications. Biomass can be derived from the cultivation of dedicated energy crops and biomass wastes. Once sourced, thermochemical conversion of biomass can take place to derive heat and power using combustion, pyrolysis or gasification [89].

Gasification, which consists of a series of thermochemical reactions in a high temperature oxygen-poor environment, is considered as an up and coming technology to extract energy from a carbon source such as coal and biomass and convert the solid carbon to a fuel gas. The resulting fuel gas is called producer gas or syngas. Biomass derived syngas can be either burnt directly in boilers, turbines and internal combustion engines to produce heat and power or used as fuel in fuel cell systems. Generally, the gasification derived syngas is composed of hydrogen, carbon monoxide, carbon dioxide, nitrogen, water vapor, traces of heavier hydrocarbons and various contaminants. The composition of syngas is remarkably

changeable and is a function of feedstock properties (type of biomass or coal, ash and water content, and size of fuel particles), the type of process and gasifier, the operating conditions including pressure, temperature and type of catalyst, the gasifying agent (air, oxygen, steam or a mixture of different agents) and the ratio of fuel to gasifying agent [88-93]. Typical composition of Biomass derived syngas (BDS) has been described in table 2.2 [89, 94-97].

Compound	H <sub>2</sub>	CO	CO <sub>2</sub>	CH <sub>4</sub>	N <sub>2</sub>
Typical volume % (dry basis)	15	24	11	3	47

**Table 2.2: Typical composition of biomass derived syngas**

The contaminants available in BDS can be listed as follows [88, 98-101]:

- Particulates, Ashes such as CaO, MgO, Na<sub>2</sub>O, K<sub>2</sub>O
- Alkali metal compounds such as Na and K compounds
- Halides such as HCl and KCl
- Sulfur-containing compounds such as H<sub>2</sub>S and COS
- Nitrogen containing compounds such as NH<sub>3</sub>, HCN
- Tars

The maximum concentration of these compounds reported by different researchers has been presented in table 2.3 [88, 98, 100, 102].

Contaminant		Concentration in BDS	Consideration
S-containing compounds	H <sub>2</sub> S	Up to 200 ppm	93–98 % of the sulfur in BDS is in form of H <sub>2</sub> S and the rest is COS
	COS	4-15 ppm	
N-containing compounds	NH <sub>3</sub>	Up to 4000 ppm	
	HCN	Up to 21 ppm	
HCl		Up to 200/90 ppm	Thermodynamic calculations/experiment
Tars		Up to 150 g/Nm <sup>3</sup>	depending on gasifier type

**Table 2.3: Maximum concentration of BDS contaminants**

## 2.7 SOFC poisoning

As mentioned before, the presence of contaminants in fuel may lead to degradation of the cell through blocking the pores/active sites and prevents the reactants from

reaching the TPBs. In worst cases the contaminants may react with cell material and deactivate the cell. Many studies have investigated the poisoning effect of various trace contaminants available in coal and biomass derived syngas on the performance of SOFCs. It has been indicated that particulates of char and ash could deposit on anodes and block the gas diffusion paths or active sites resulting in performance decline [28]. Tars have been also investigated by many researchers and it has been shown that they may degrade the cells due to carbon deposition. Lorente et al [103] have reported that 15 g/Nm<sup>3</sup> of tars (real or model) can degrade both Ni/DGC and Ni/YSZ anodes and cause coking. They have also shown that the amount of carbon deposited on anode in case of real tar is less as compared to the model tar (toluene was used as the model tar). However, Hofmann et al [56] have reported on the safe operation of Ni/GDC anode loaded with tar levels as high as 10-40 g/Nm<sup>3</sup>. The difference between the results lies in the fact that in the latter study a large amount of steam (~73 %) was employed, whereas in former the water content was 2.5 %. Naphthalene as the model tar has been investigated by Aravind et al [102] and did not affect the performance of Ni/GDC anode up to 110ppm. Mermelstein et al [104] have also reported that 15 g/Nm<sup>3</sup> of benzene (as model tar) leads to cell degradation with Ni/GDC and Ni/YSZ anodes. This effect can be reduced through introducing steam to fuel, which results in steam reforming of tar, and operating the cell at higher current densities, which result in larger flux of oxygen ions traveling to anode and thus partial oxidation of benzene. Another study reported that 2-15 g/Nm<sup>3</sup> of benzene does not affect the performance of a cell with Ni/GDC anode operating on humidified fuel at 765 °C (thermodynamic calculation showed that above 750 °C no carbon deposits on Ni/DGC anodes) and 300 mA/cm<sup>2</sup> although very small amounts of carbon deposited on anode [105]. Also, it has been experimentally proven that 15 g/Nm<sup>3</sup> of benzene or toluene degrades the performance of Ni-YSZ anode loaded with a dry fuel at 775 °C [106].

Other contaminants have been also investigated by many research groups. The results of tests on fuels contaminated with Hg, Zn, Si, and NH<sub>3</sub> show no or slight degradation in cell performance whereas presence of trace elements such as Cl, As, P, Sb, Cd, and Se leads to moderate or severe losses in SOFC operation [107-109]. The degradation of cell performance can be due to two different mechanisms: surface adsorption by which the reactive sites of anode are blocked and bulk reaction which results in a secondary phase formation. Elements such as S and Cl

affect the performance via the first mechanism and other elements such as As, P, and Sb are known to react with Ni in the anode and form a secondary phase [108]. Furthermore, it has been shown that compounds such as AsH<sub>3</sub>, PH<sub>3</sub>, CH<sub>3</sub>Cl and HCl are present in syngas and can lead to cell performance decline. Experimental results indicate that AsH<sub>3</sub> can cause slight degradation in performance [107, 110], whereas the presence of PH<sub>3</sub> in fuel results in an immediate and significant cell decline which is irreversible [107, 111]. Cl compounds such as CH<sub>3</sub>Cl and HCl can also cause some performance losses which in case of HCl, the degradation is recoverable after removal of contaminant and operating on clean fuel [107, 112].

Among all the contaminants H<sub>2</sub>S has received much attention due to its relatively high concentration in different types of fuel source (biomass- or coal-derived syngas) as well as its highly detrimental effect on the performance of SOFCs. Although the typical concentration of NH<sub>3</sub> is much larger than that of H<sub>2</sub>S it is known that NH<sub>3</sub> can be used as a fuel – due to its cracking to 3H<sub>2</sub> and N<sub>2</sub> – in SOFCs at temperatures around 800-1000 °C without any degradation over a long period of time [113, 114]. A number of studies on the effect of H<sub>2</sub>S have been summarised in table 2.4.

From all these studies it can be concluded that the presence of H<sub>2</sub>S in fuel even at concentrations as low as 1ppm can immediately degrade the cell performance. The most important trend which can be drawn is that the degradation of cell increases as the operating temperature decreases or the concentration of H<sub>2</sub>S increases. This loss would be irreversible for cells operating at intermediate temperatures while it is considered to be recoverable after removal of H<sub>2</sub>S for high temperature cells [107, 115-118].

Also, it has been reported by many researchers that the H<sub>2</sub>S degrades the performance through two steps: an immediate drop (within a few minutes or hours) and a slow loss. The initial drop in power which is sharp and immediate is attributed to the adsorption of S onto the nickel surface at the anode functional layer and the formation of nickel sulphide. This step may be fully or partially reversible depending on the concentration of H<sub>2</sub>S and operating condition such as temperature and current. The secondary drop which is sluggish and may end up in a steady state in the long term is due to nickel reconstruction and decomposition of H<sub>2</sub>S at the anode support layer leading to a decrease in electrical conductivity [107, 117, 119-122].

Ref.	Anode material	Concentration (ppm)	Exposure time (hr)	Degradation (%)	Temp. (°C)	Considerations
[32]	Ni-YSZ	0 to 16	Up to 10		750, 900, 1000	Critical concentration for 750, 900 and 1000 °C: 0.05, 0.5 and 2, respectively
[102]	Ni-GDC	9	1.5	0	850	No degradation observed
[107]	Ni-YSZ	1	100	3.5 (@ t=6 hr)	750	Degradation in power started after 45min
[117]	Ni-GDC	119~120	400	12 %/500 hr	850	An immediate degradation of 10 % in power was observed
[118]	Ni-GDC	200~240	570	10~12.5 % (in voltage)	850	An immediate degradation of 6 % in power was observed, mostly recovered on removal of H <sub>2</sub> S
[123]	Ni-Zirconia Co-Zirconia	50	800	5	1000	Immediate drop in voltage was observed
[124]	Ni-YSZ	100			500 to 800	XRD, EDX and SEM analysis Adsorption of sulphur at surface of anode
[125]	Ni-YSZ	- 100 - 100000	5 days		- 727 - 950	- No Ni-S compound detected - Formation of NiS
[115]	Ni-GDC	0.5, 1, 3	1.5		700 to 750	Recoverable degradation suggesting dissolution of sulphur at the surface
[116]	Ni-YSZ	100000	Up to 16		850	Formation of NiS
[126]	Ni-YSZ	0.2-10	5 min	3-14 % (cell relative resistance)	800	Fully recoverable degradation due to short exposure time
[127]	Ni-YSZ	1	35		750	Partially recoverable, both cell performance and internal reforming of methane degraded
[120]	Ni-YSZ	2000	1.5		800	An abrupt increase in cell resistance, followed by a secondary sluggish degradation
[121]	Ni-GDC	1, 3	24		557, 600	A rapid increase in cell resistance, followed by a slow performance loss
[122]	Ni-YSZ	2 to 100	24		850	2 steps of degradation

Table 2.4: Summary of studies on effect of H<sub>2</sub>S on SOFCs performance

In addition it has been shown that the degree of cell poisoning by H<sub>2</sub>S would be lower for higher current densities. This would be due to the reaction of adsorbed sulfur with oxygen ions (reaction 2.45) [115, 126].



Any increase in current of the cell results in an increase in number of oxygen ions reaching the anode which in turn leads to higher rate of desorption.

The thermodynamic analysis for the interaction between Ni, O and S predicts that eight phases can be present in the system, depending on the conditions. The predicted phases are Ni, Ni<sub>3</sub>S<sub>2</sub>, NiS<sub>0.84</sub>, NiS, Ni<sub>3</sub>S<sub>4</sub>, NiS<sub>2</sub>, NiSO<sub>4</sub> and NiO [128, 129], however, NiS<sub>0.84</sub>, NiS and Ni<sub>3</sub>S<sub>4</sub> are not stable at all temperatures. NiS<sub>0.84</sub> tends to be stable at 400 and 600 °C while NiS is stable at 600 and 800 °C [128]. Lin et al have reported that Ni<sub>3</sub>S<sub>2</sub> changes to Ni<sub>3</sub>S<sub>4</sub> at temperature above 572 °C [130], as a result Ni<sub>3</sub>S<sub>4</sub> can be present in the Ni-O-S system at the typical operating temperature of the SOFCs i.e. 600 to 1000 °C.

Lohsoontorn et al [128] has carried out a series of the thermodynamic analyses to study the effect of the SOFC operating conditions such as temperature, H<sub>2</sub>S concentration, partial pressure of H<sub>2</sub> and steam content on the phase equilibrium of the Ni-O-S system. The bounds of the fuel composition were defined as 97 % H<sub>2</sub>/3 % H<sub>2</sub>O at the inlet and 10 % H<sub>2</sub>/90 % H<sub>2</sub>O at the outlet of the cell, representing 90 % fuel utilisation. The range of the H<sub>2</sub>S concentration was set to be 1 to 1000 ppm to mimic the realistic H<sub>2</sub>S content in the various fuel types.

The phase equilibrium of the Ni-O-S system for the above mentioned range of fuel composition and H<sub>2</sub>S concentration, at different operating temperatures is illustrated in figure 2.14. It can be seen in the figure that the tendency of Ni to react with S increases as the concentration of H<sub>2</sub>S is elevated. The results also show that the reaction of Ni with S tends to be favoured as the temperature and/or P<sub>H<sub>2</sub></sub> decrease. The latter is in agreement with the study by Sasaki et al. [131] which suggests that Ni<sub>3</sub>S<sub>2</sub> is more stable in hydrogen-depleted atmospheres.

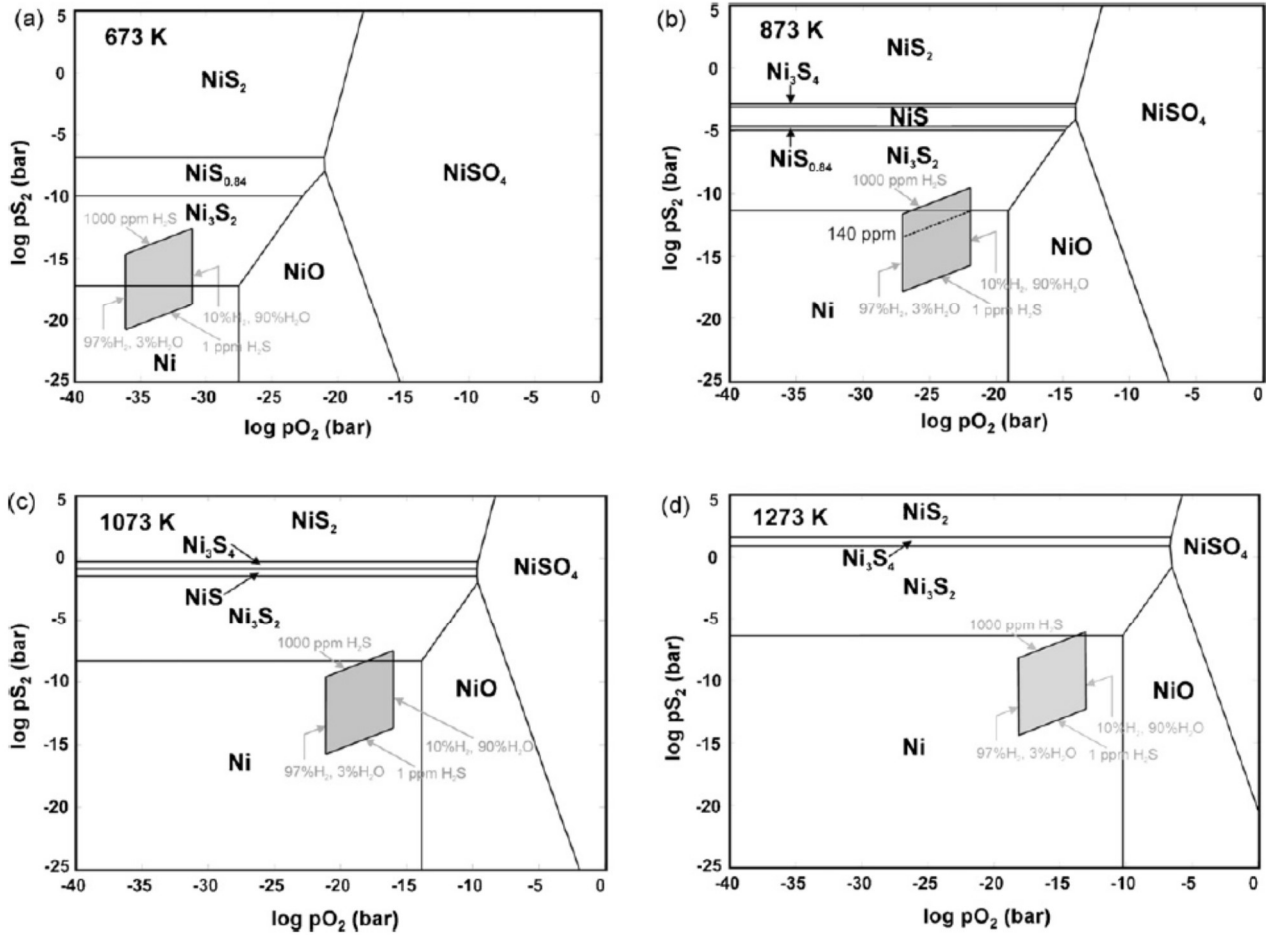


Figure 2.14: Phase equilibrium of the Ni-O-S system at different temperatures, a: 673 K, b: 873 K, c: 1073 K and d: 1273 K [128]

Figure 2.15 compares the phase equilibrium for two cases: different partial pressures of  $H_2$  with the same steam content and the same partial pressure of  $H_2$  with different levels of steam content. The shaded area shown in the figure shows the formed phases of Ni exposed to humidified hydrogen ranging between 97 %  $H_2$  - 3 %  $H_2O$  and 10 %  $H_2$  - 90 %  $H_2O$ , which contains 1 to 1000 ppm of  $H_2S$ , similar to figure 2.14. The left hand side boundary of the area surrounded by the solid lines, corresponds to the phases of Ni fed with 20 %  $H_2$ , 3 %  $H_2O$  and 77 %  $N_2$ , containing 1-1000 ppm of  $H_2S$ . The area bounded by the dotted lines shows the formed phases of Ni exposed to a fuel mixture of 97 %  $H_2$ , 1 %  $H_2O$  and 2 %  $N_2$ . Similar to the previous cases, the fuel mixture contains 1 to 1000 ppm of  $H_2S$ .

The results show that the decrease in  $P_{H_2}$  tends to increase the partial pressure of  $S_2$ , implying that the formation of  $Ni_3S_2$  can occur at lower levels of  $H_2S$  concentration. It was also revealed that the change in the steam content (1 to 3 %) does not affect the reaction of Ni and S significantly.

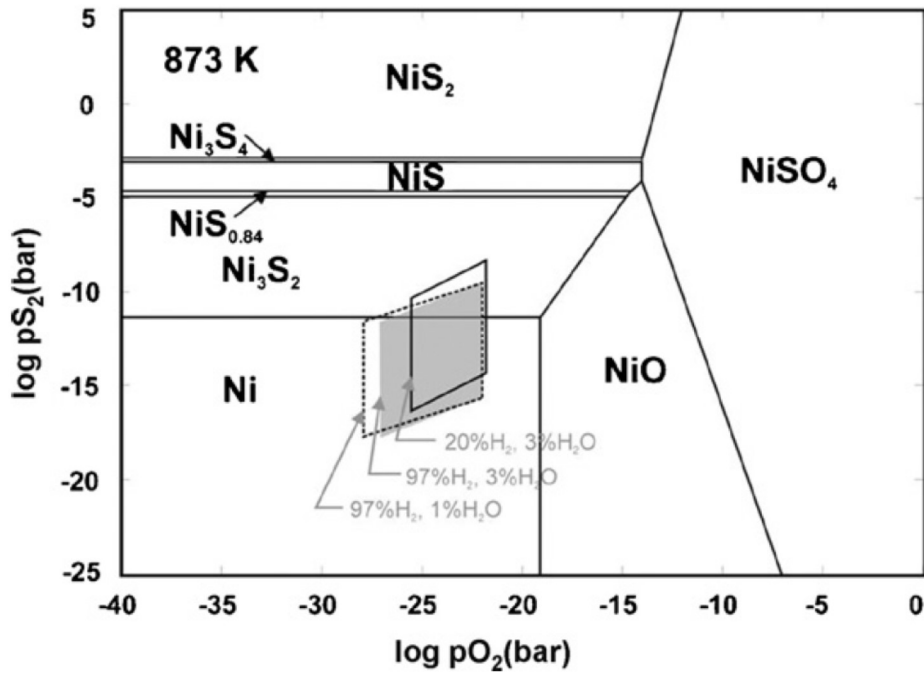
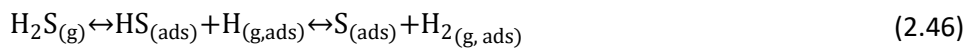


Figure 2.15: Phase equilibrium of the Ni-O-S system at different partial pressures of H<sub>2</sub> and levels of steam content [128]

In agreement with the thermodynamic calculations, a large number of experimental studies suggest that the Ni-S bond for the surface adsorption of sulfur on Ni is more stable than that of nickel sulfide. The results show that the chemisorption of sulfur on Ni is 50 to 100 kJ/mol more exothermic than the bulk reaction of sulfur with Ni, depending on the conditions [132]. Thus, it can be stated that the bulk reaction of S with Ni is less expected to occur at the typical operating conditions of the SOFCs.

It has been reported by many researchers, that at low concentrations of H<sub>2</sub>S (below 100 ppm) the cell degradation would be due to the surface adsorption of sulphur on nickel (reaction 2.46), whereas, at high concentrations (above 100 ppm) the performance loss is caused by the formation of bulk Ni-S species (reactions 2.47 and 2.48) [32, 43, 117, 118, 122, 125, 133]. However, the results of a previous study showed that there is no NiS or Ni<sub>3</sub>S<sub>2</sub> in the anode (Ni-YSZ-GDC) after exposure to 200-500 ppm of H<sub>2</sub>S [134].



In general it can be stated that the interaction of sulfur and nickel is quite complex and significantly depends upon the operating conditions such as temperature,

current density, concentration of  $\text{H}_2\text{S}$ , anode material, exposure time and fuel composition [43, 121].

The results of both experimental and thermodynamic studies show that strategies such as adding steam to the fuel stream and increasing cell operating temperature can increase the critical concentration (the minimum concentration to cause performance loss) of trace contaminants and diminish their poisoning effects [29, 32, 33, 115, 121].

Zha et al. [135] experimentally investigated the performance of SOFCs exposed to a range of  $\text{H}_2\text{S}$  concentrations (0.18 to 10 ppm) at 600, 700 and 800 °C. The results of this study, as shown in figure 2.16, state that the degree of the cell poisoning increased as:

- The temperature was reduced (lower desorption rate of sulfur),
- The  $\text{H}_2\text{S}$  concentration was increased (higher absorption of sulfur on nickel), or
- The exposure time was increased.

Also, they showed that, for 50 ppm of  $\text{H}_2\text{S}$ , the poisoning and recovery effects are influenced by the operating voltage (or current), i.e. at higher operating voltage (lower current) the poisoning is more severe and the degree of recovery is smaller [135]. This is in agreement with the result of other studies in which the large current tends to increase the rate of sulfur desorption (reaction 2.45).

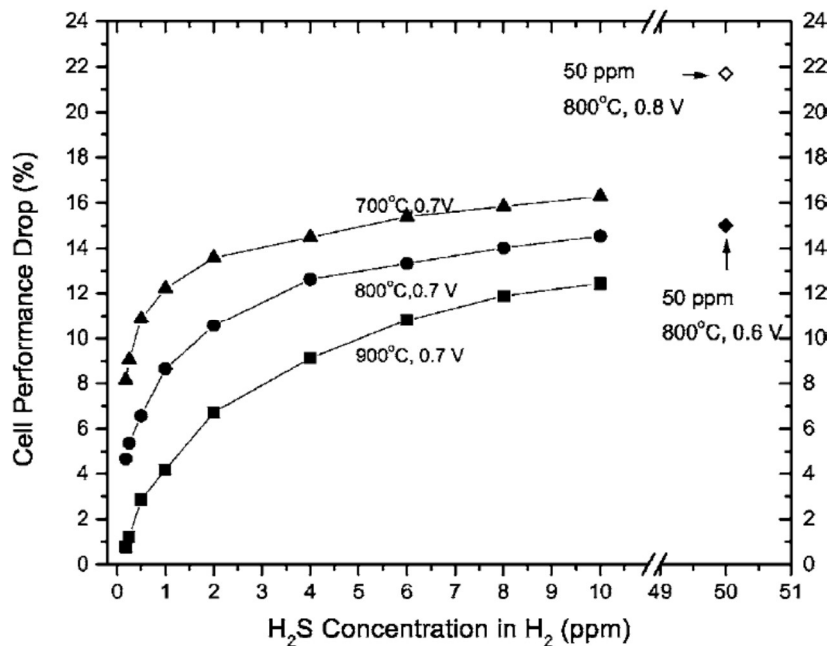


Figure 2.16: Dependence of performance loss on temperature and  $\text{H}_2\text{S}$  concentration [135]

The profiles of the voltage drop for Ni/YSZ and Ni/GDC anodes (half cells) exposed to a wide range of the H<sub>2</sub>S concentrations at 800 °C have been reported by Zhang et al. [136]. The results show that in both cases the drop in the voltage tends to increase as the H<sub>2</sub>S concentration is increased. However, it remains the same for higher levels of the H<sub>2</sub>S concentration. It has also been shown that the resistance of the Ni/GDC anode to H<sub>2</sub>S poisoning is higher than that of Ni/YSZ.

In addition to H<sub>2</sub>S, sulfur is present in the form of COS in the biomass derived syngas. However, COS can convert to H<sub>2</sub>S through hydrolysis (reaction 2.49). COS hydrolysis is reversible and takes place over catalysts such as activated alumina, titania and zirconia [88, 137].



Haga et al. set out the poisoning effects of COS and H<sub>2</sub>S on a Ni-ScSZ anode at 800, 900 and 1000 °C and reported almost the same initial voltage drop for each respective temperature. Consequently, the analysis implied that sulfur was almost entirely present in the form of H<sub>2</sub>S at the mentioned operating conditions [119].

As presented in table 2.3, NH<sub>3</sub> and HCN are the nitrogen containing compounds available in biomass derived syngas. Ammonia has been shown to be functioning as fuel for SOFCs, as discussed before. Similar to COS, HCN can react with water and form ammonia and carbon monoxide according to reaction 2.50.



Hydrolysis of HCN can be accomplished over catalysts such as TiO<sub>2</sub>, Al<sub>2</sub>O<sub>3</sub>, ZrO<sub>2</sub> and SiO<sub>2</sub> [138]. Thus, it can be articulated that HCN has a potential to convert to NH<sub>3</sub> at SOFC operating conditions and function as fuel.

## 2.8 Fuel cells characterisation methods

In order to develop fuel cell technology it is necessary to characterise the performance of the cell once fabricated and tested. The information obtained from fuel cell characterisation techniques can be used to improve the fabrication processes. This also serves to widen the researcher's understanding of electrochemical activity of a cell.

There are a wide range of structural and electrochemical properties which should be characterised in the development of a fuel cell. A non-exhaustive list of fuel cell properties which should be considered during research and assessment of cells includes the following:

- Overall performance: voltage-current density curve
- Electrochemical properties: activation overpotential, charge transfer coefficient, exchange current density
- Ohmic characteristics: ohmic resistance, electrical conductivity of components
- Mass transport parameters: effective diffusion coefficient, pressure drop
- Parasitic overpotential: fuel cross over, leakage
- Electrode structure and properties: porosity, particle size, electrical resistance, TPBs, electrochemical activity
- Flow field: pressure, temperature and species distribution
- Long term performance: degradation, thermal/redox cycles, corrosion of components

The characterisation techniques are generally divided into two categories: in-situ and ex-situ. The former refers to a series of analyses carried out during the operation of cells and the latter includes the methods to inspect fuel cells in the absence of voltage and current i.e. after the cell testing is finished.

### **2.8.1 In-situ techniques**

Some of the in-situ characterisation techniques are as follows:

- Voltage-current measurement: in this method either voltage or current is kept constant and the other is monitored over the operation period. In the case that the voltage is kept constant the process is called potentiostatic mode and in the case of current being kept constant it is referred to as galvanostatic.

In addition to these operation modes, either current or voltage can be changed over a range of values and the corresponding value of the other is measured. In this method a series of voltage and current data points are obtained, which can be plotted as the characteristic or v-i curve. In order to change the current or voltage a variable external resistor is connected to the cell terminals. Once the resistance of the circuit varies a different amount of current is drawn from the cell, causing the voltage to change accordingly.

Voltage-current curves are widely used to compare the performance of different cells as well as the performance of a particular cell at different

stages of a single test. Besides the direct comparison of the v-i curves, the values of current and voltage can be used to calculate the area specific resistance of cells (ASR) for any given operating point [16]:

$$ASR = \frac{OCV - V}{i} \quad (2.51)$$

where OCV, V and i are the open circuit voltage, operating voltage and current density, respectively. ASR is another measure to effectively compare the performance of different cells and performance change over the test periods.

- Current interruption method: in this technique cells are loaded at a small current at which the concentration losses are insignificant. In such case the cell overpotential is due to the ohmic and activation losses. In case the cell is suddenly unloaded the voltage will increase to OCV. The ohmic overpotential will instantly decrease to zero, however, the activation loss will reduce to zero in a slower trend. The latter is due to the presence of a charge double layer at the interface of the electrodes and electrolyte in fuel cells.

Charge double layer phenomenon occurs owing to the accumulation of charges and ions at the electrode/electrolyte interface, as shown in figure 2.17. Differently charged layers at the interface, will provide a place to store electricity and energy, thus, behaving as an electrical capacitor [9].

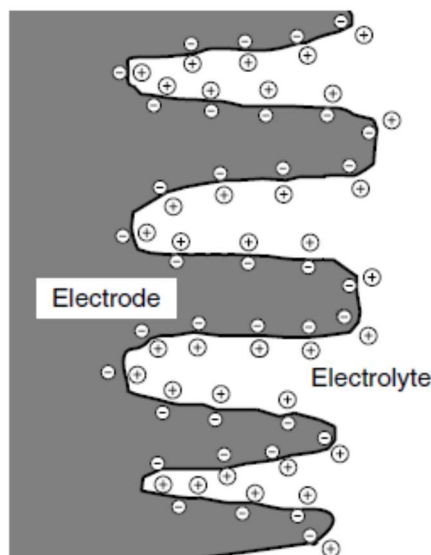
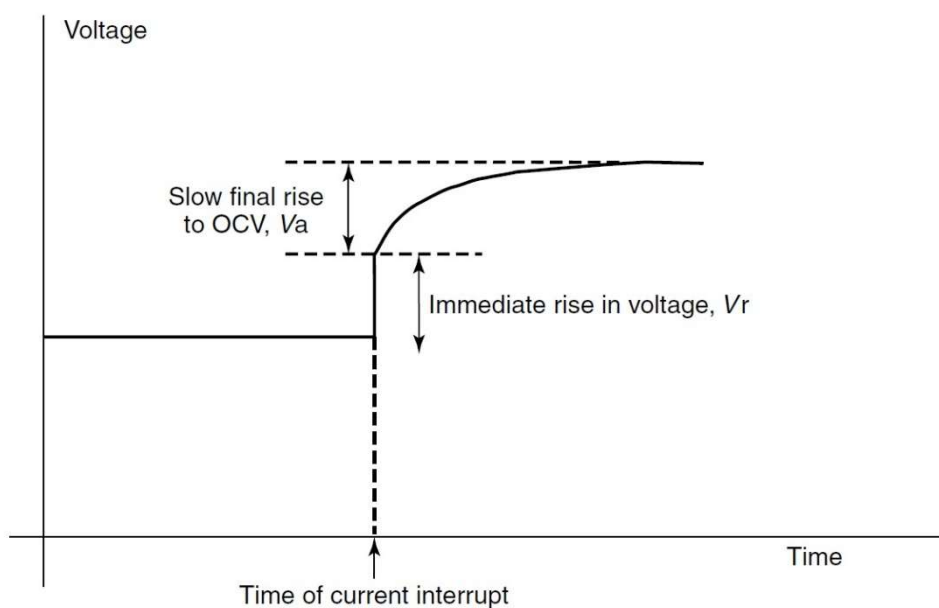


Figure 2.17: Charge double layer [9]

This phenomenon can be modelled by a capacitor in parallel to a resistor simulating the electrochemical resistance of the electrode. However, the capacitors are generally replaced by constant phase elements which represent an imperfect capacitance. The imperfect behaviour of capacitors can be due to several causes such as distributed reactivity and inhomogeneous properties [139].

Once the current drawn from the cell is interrupted the capacitor starts to unload. However, the unloading process will take some time causing the activation loss to decrease slowly. As a result, the voltage rise to OCV tends to be slower.

In the current interruption method it is important to record the voltage at high frequencies to capture the fast change of the cell voltage. Figure 2.18 illustrates a typical profile of voltage during the current interruption method. The first immediate jump in the voltage is due to the ohmic loss and the final rise, which is slower than the first one, represents the activation overpotential.



**Figure 2.18: Typical voltage profile in current interruption method [9]**

Current interruption technique can be applied to a fuel cell i.e. the terminals of the voltage measurement device are connected to the anode and cathode. In this arrangement the total ohmic loss of the cell and total

activation of both electrodes can be characterised. Conversely, the method can measure the voltage difference between reference and working electrodes. In this case the jump in the voltage will be due to the activation loss of the working electrode and a part of the ohmic loss, which has been included in the circuit.

Reference electrodes are generally connected to the electrolyte. The arrangement of the reference and working electrodes play an important role in the implementation of current interruption technique, which can introduce inaccuracy into measurement results. In general, it can be stated that the application of the reference electrode is a complex process and its performance depends on the position of the electrode and geometry of the cell [140].

- Electrochemical impedance spectroscopy (EIS): in this method a sinusoidal voltage or current is applied to cells and the other parameter is measured. The applied perturbation is small so that the system response is pseudo-linear. As a result, the frequency of the applied excitation signal and response will be the same, however, the phase and amplitude will be different. The impedance of the cell, then, can be calculated by dividing the voltage to the current. As both voltage and current are sinusoidal, the impedance of the cell will be a complex number.

Figure 2.19(a) shows an electrical circuit consisting of two resistors ( $R_s$  and  $R_p$ ) and a capacitor ( $C$ ) parallel to one of the resistors ( $R_p$ ) and figure 2.19(b) illustrates the Nyquist plot of the circuit. Once a very high frequency sinusoidal current is applied to the circuit terminals,  $R_p$  is by-passed as the capacitor shorts out. In this case the impedance of the circuit will be equal to  $R_s$ , thus, a real number. At very low frequency, the top path is blocked since the capacitor does not allow the current to pass. As a result, the whole of the applied current passes through  $R_p$ , yielding value of  $R_s+R_p$  for the impedance. These two extreme cases (very high and very low frequencies) correspond to the x-intercepts in the Nyquist plot. For any frequency between the two extreme cases, the current is divided between top and bottom paths, which yields a complex number for the impedance of the circuit.

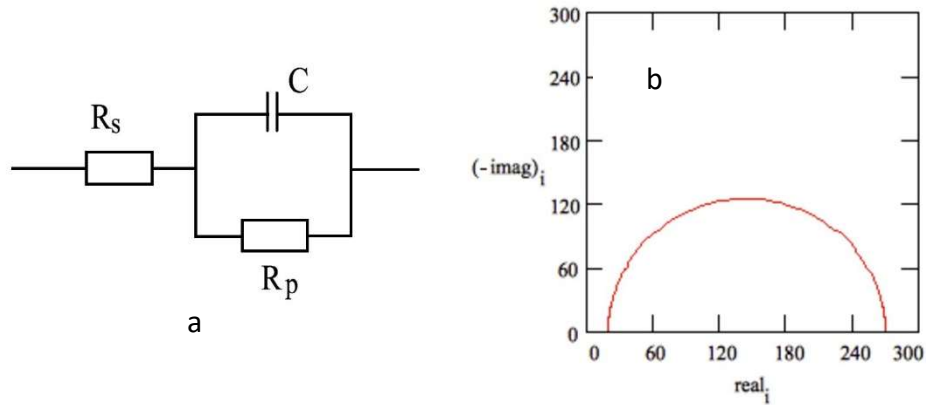


**Figure 2.19: Example of resistor/capacitor circuit and corresponding Nyquist plot [141]**

EIS is a powerful technique widely used to analyse the performance of fuel cells and measure the internal resistance. EIS can also be used to determine the different types of resistance such as ohmic and activation/concentration. The latter is also referred to as the electrode resistance. Based on the electrochemical performance of cells, an equivalent electrical circuit can be used to represent the cell behaviour. The results of the EIS method can then be fitted on to the representative model, to calculate the model parameters. This approach is widely applied to compare different cells or the performance of a cell at different operating conditions.

A typical EIS curve for a single electrode of fuel cells can consist of two semi-circles as shown in figure 2.20. The left hand side semi-circle is the response of the system at high frequencies and the right hand side one is obtained at lower frequencies. The electrochemical processes can be divided to two categories: bulk related and electrode related. The bulk related processes such as bulk resistance and dissociation/combination reactions are associated with the response effects at higher frequencies, whereas the diffusion occurs at lower frequencies [142].

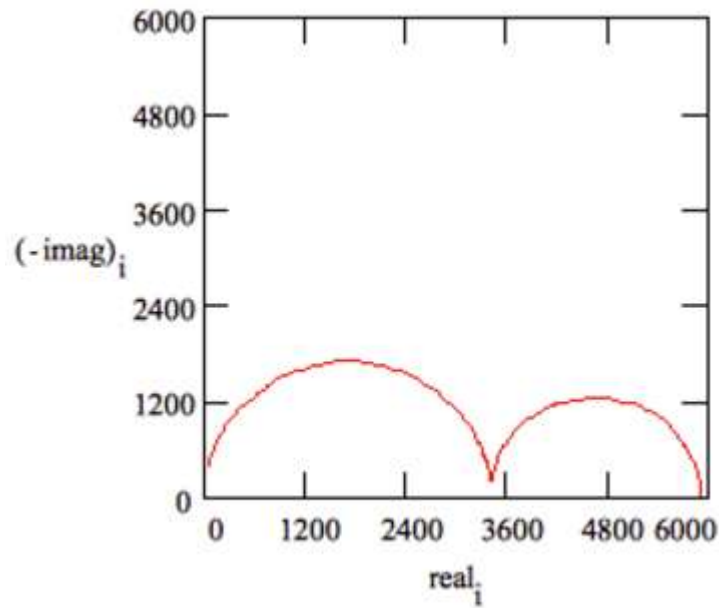


Figure 2.20: Typical EIS curve for a single electrode [141]

In fuel cells the dominant phenomena include charge transfer reactions and diffusion of species and mobile charges. The left semi-circle obtained at higher frequencies is associated with the kinetics of the electrode (charge transfer) which is fast, while the other, obtained at lower frequencies, represents diffusion effects which are slow compared to the charge transfer reactions.

For a full fuel cell the EIS curves includes both charge transfer and diffusion processes at both electrodes. Each process tends to occur at a particular range of frequency which results in a complex curve when put together.

In accordance with a  $v-i$  curve, it can be seen that the cell overpotentials (activation, ohmic and concentration) become larger as the current density rises. However, the resistance obtained from EIS technique, shows a different trend i.e. a decrease followed by an increase. This will result in an optimum point at which the resistance of cell is minimum. The corresponding current is called “current of lowest resistance” and can be used as a basis to compare cells’ performance [143].

### 2.8.2 Ex-situ techniques

The ex-situ characterisation category includes a series of methods such as:

- Porosity determination
- Particle size determination

- Structure determination e.g. scanning electron microscopy (SEM), energy Dispersive X-ray (EDX), X-ray diffraction (XRD): these techniques provide information about the morphology and elements present in cell layers

In SEM method, a beam of electrons is focused on the sample. As the electrons collide with the atoms of the sample, the emitted electrons are attracted by a detector to create an image of the sample.

The EDX process could be elucidated through X-ray characteristics of the atoms present in the solid specimen, which are generated in an event of bombardment through high-energy electrons. Use is made of the X-ray characteristics to identify the elements present in the sample and generally chemical composition of the sample for which this method has been aimed. The minimum detectable concentration by EDX method is about 0.1 % (1000 ppm) by weight [144].

## **2.9 Summary**

In this chapter several aspects of SOFCs such as components, materials, mathematical models and characterisation methods were summarised. In addition, different sources of contamination and degradation, with a focus on H<sub>2</sub>S poisoning, were explained. The information provided in this chapter are used as a basis to study the poisoning effect of H<sub>2</sub>S in the current research. In the following chapter the methodology of the current work, including the operating conditions, motives of H<sub>2</sub>S selection and concentrations of interest, is presented.

## 3 Methodology

Over the last decade, many researchers have investigated the effects of contamination on solid oxide fuel cell performance; however, gaps in the knowledge still remain. One such gap is that contamination results in the literature vary from one cell to another. This could be due to the fact that the tested cells were manufactured from different materials and with a variety of production processes. Conversely, the operating conditions may have been different, generating different degrees of cell damage. In order to compare the results of the contamination tests effectively, in this work, identical cells are used and exposed to a wide range of hydrogen sulfide concentrations. During these tests all other operating conditions remain the same. The following sections presents the operating conditions, motives of selection of H<sub>2</sub>S, test matrix and characterisation methods applied in this work.

### 3.1 Operating conditions

Generally, the operating conditions of fuel cells include fuel composition, temperature, pressure and current density.

#### 3.1.1 Fuel composition

The fuel composition in this research is selected to simulate that of BDS. The typical concentration of hydrogen in BDS has been reported to be 15 % (table 2.2) by many researchers. In addition to hydrogen, there are other components such as CO, CO<sub>2</sub> and CH<sub>4</sub> in BDS. These compounds can change the performance of cells due to their tendency to participate in several reactions such as direct oxidation, internal reforming and coke deposition. As mentioned in the literature review chapter, the typical operating conditions of SOFCs can provide a proper environment to promote these reactions. In order to focus on the effects of H<sub>2</sub>S on the general performance of the single cells, other compounds are replaced by N<sub>2</sub>, in the experiments of this research. Therefore, the fuel mixture will consist of 15 % H<sub>2</sub> (100 ml/min) and 85 % N<sub>2</sub> (566.67 ml/min). In addition to H<sub>2</sub> and N<sub>2</sub>, 3 % of water is added to the fuel mixture, giving a final composition of 14.5 % H<sub>2</sub>, 82.5 % N<sub>2</sub> and 3 % H<sub>2</sub>O.

### **3.1.2 Temperature and pressure**

Temperature: in general, solid oxide fuel cells are considered as high temperature cells as the different layers i.e. anode, electrolyte and cathode, become active and promote the charge/ion transfer reactions at elevated temperatures. The operating temperature should be selected based on the cells type and characteristics. For instance, electrolyte supported cells generally operate at higher temperatures rather than anode supported cells due to the high thickness of the electrolyte which has larger ohmic resistance. Based on the configuration of the cells used in this research, 700 °C is selected as the operating temperature. This is within the temperature range for which the cells have been designed and manufactured. In addition, as stated in the previous chapter, most of the researches have been done at higher operating temperatures (above 750 °C), therefore, lower temperature cells are chosen in this work. Lower temperature SOFCs have recently attracted more attention due to better mechanical integrity, which results from smaller CTE mismatch between the layers.

Pressure: the operating pressure of the test rig/cells will be atmospheric during the experiments.

### **3.1.3 Current density**

Fuel cells can be run at different current densities ranging from very small values to about 1 A/cm<sup>2</sup>. There are several parameters to choose the current drawn for the cell such as microstructure and internal resistance. The maximum current density is dictated by the concentration losses which tend to prevent the species to transfer to/from the active sites. In case of drawing large currents the voltage of the cell drops rapidly yielding low power. It has been also known that the internal resistance of cells changes with the current density. In this research the current density of 0.2 A/cm<sup>2</sup> has been selected, since the corresponding cell resistance is minimal.

## **3.2 Selection of H<sub>2</sub>S as contaminant**

As explained in the previous chapter the gaseous contaminants available in biomass derived syngas (BDS) are H<sub>2</sub>S, COS, NH<sub>3</sub>, HCN and HCl. Hydrogen sulfide is recognised as one of the most detrimental contaminants which can fully deactivate

the cell. Carbonyl sulfide (COS) is prone to react with water and produce hydrogen sulfide and carbon dioxide through reaction 2.49.



In this section, a thermodynamic analysis based on the Gibbs free energy minimization is carried out to find the composition of sulfur-containing compounds in the fuel mixture presuming that COS is present in the fuel as the only contaminant. This analysis has been done for a typical fuel composition with 3 vol% H<sub>2</sub>O, over a range of SOFCs typical operating temperatures.

Considering a mixture of ideal gases, the Gibbs free energy of each component can be written as:

$$\bar{g}_i = \bar{g}_i^0 + RT \ln p_i \quad (3.1)$$

where  $\bar{g}$ ,  $R$ ,  $T$  and  $p$  are Gibbs free energy, universal gas constant, temperature and pressure, respectively.

Considering that all the stoichiometric coefficients in reaction 2.47 are equal to 1, the criterion for chemical equilibrium is:

$$\bar{g}_{\text{H}_2\text{S}} + \bar{g}_{\text{CO}_2} - \bar{g}_{\text{COS}} - \bar{g}_{\text{H}_2\text{O}} = 0 \quad (3.2)$$

The relation in equation 3.1 can now be substituted into equation 3.2:

$$\Delta \bar{g}_i^0 + RT \ln \left( \frac{p_{\text{H}_2\text{S}} p_{\text{CO}_2}}{p_{\text{COS}} p_{\text{H}_2\text{O}}} \right) = 0 \quad (3.3)$$

The equilibrium constant for COS hydrolysis can be written as:

$$k_p = \frac{p_{\text{H}_2\text{S}} p_{\text{CO}_2}}{p_{\text{COS}} p_{\text{H}_2\text{O}}} \quad (3.4)$$

Substituting equation 3.4 into equation 3.3 and rearranging:

$$k_p = e^{-\Delta \bar{g}_i^0 / RT} \quad (3.5)$$

Using the thermodynamic tables, as mentioned in the literature review chapter, the value of  $\Delta \bar{g}_i^0$  can be calculated. Then, equation 3.5 yields the value of  $k_p$ .

Since the stoichiometric coefficients are equal to 1, the equilibrium constant can be re-written as:

$$k_p = \frac{y_{\text{H}_2\text{S}} y_{\text{CO}_2}}{y_{\text{COS}} y_{\text{H}_2\text{O}}} \quad (3.6)$$

where  $y$  is the mole fraction of components.

In order to run the analysis, it is assumed that the initial number of moles in a COS/H<sub>2</sub>O mixture is  $n_{\text{COS}}^0$  and  $n_{\text{H}_2\text{O}}^0$  for COS and H<sub>2</sub>O, respectively. The initial values

will be assumed to change by Z moles, through reaction 2.49. The final number of moles and mole fraction of the components have been shown in table 3.1.

Replacing the final mole fraction of the components (data in table 3.1) into equation 3.6, a new equation is obtained for Z. Consequently, the value of Z can be calculated for given values of initial number of moles.

	COS	H <sub>2</sub> O	H <sub>2</sub> S	CO <sub>2</sub>
Initial value	$n_{\text{COS}}^0$	$n_{\text{H}_2\text{O}}^0$	0	0
Change	-Z	-Z	+Z	+Z
Final value	$n_{\text{COS}}^0 - Z$	$n_{\text{H}_2\text{O}}^0 - Z$	+Z	+Z
Total	$n_{\text{COS}}^0 + n_{\text{H}_2\text{O}}^0$			
Final mole fraction	$\frac{n_{\text{COS}}^0 - Z}{n_{\text{COS}}^0 + n_{\text{H}_2\text{O}}^0}$	$\frac{n_{\text{H}_2\text{O}}^0 - Z}{n_{\text{COS}}^0 + n_{\text{H}_2\text{O}}^0}$	$\frac{+Z}{n_{\text{COS}}^0 + n_{\text{H}_2\text{O}}^0}$	$\frac{+Z}{n_{\text{COS}}^0 + n_{\text{H}_2\text{O}}^0}$

**Table 3.1: Calculation of mole fraction - COS hydrolysis**

Figure 3.1 illustrates the mole fractions of H<sub>2</sub>S and COS at equilibrium for a range of initial COS concentrations. The results of the analyses performed at 500, 600, 700 and 800 °C show that all COS is almost converted into H<sub>2</sub>S as the mole fraction of COS, at equilibrium, is somehow 4 orders of magnitude smaller than that of H<sub>2</sub>S for all respective mentioned temperatures at which the analyses were performed. Also, it can be seen that increasing the temperature raises the mole fraction of COS. This indicates that higher temperatures tend to favour the backward hydrolysis reaction. However, it should be noted that the mole fraction of COS at equilibrium and its variation due to the temperature change is so small that the mole fraction of H<sub>2</sub>S is not affected. As can be seen in the figure 3.1, the 4 interpolated lines of the H<sub>2</sub>S concentration are overlapping and hence seen as a single line. Therefore, care must be taken in analysing the diagram.

With regard to the thermodynamic analyses result, it can be articulated that the cell will mostly be exposed to H<sub>2</sub>S rather than COS owing to the fact that the COS shifts to a quantity several orders of magnitude less than that of H<sub>2</sub>S in case of COS being the only contaminant available in the anode gas. This argument is consistent

with the result of the experimental investigation of COS- and H<sub>2</sub>S-poisoned cells as mentioned in the literature review chapter.

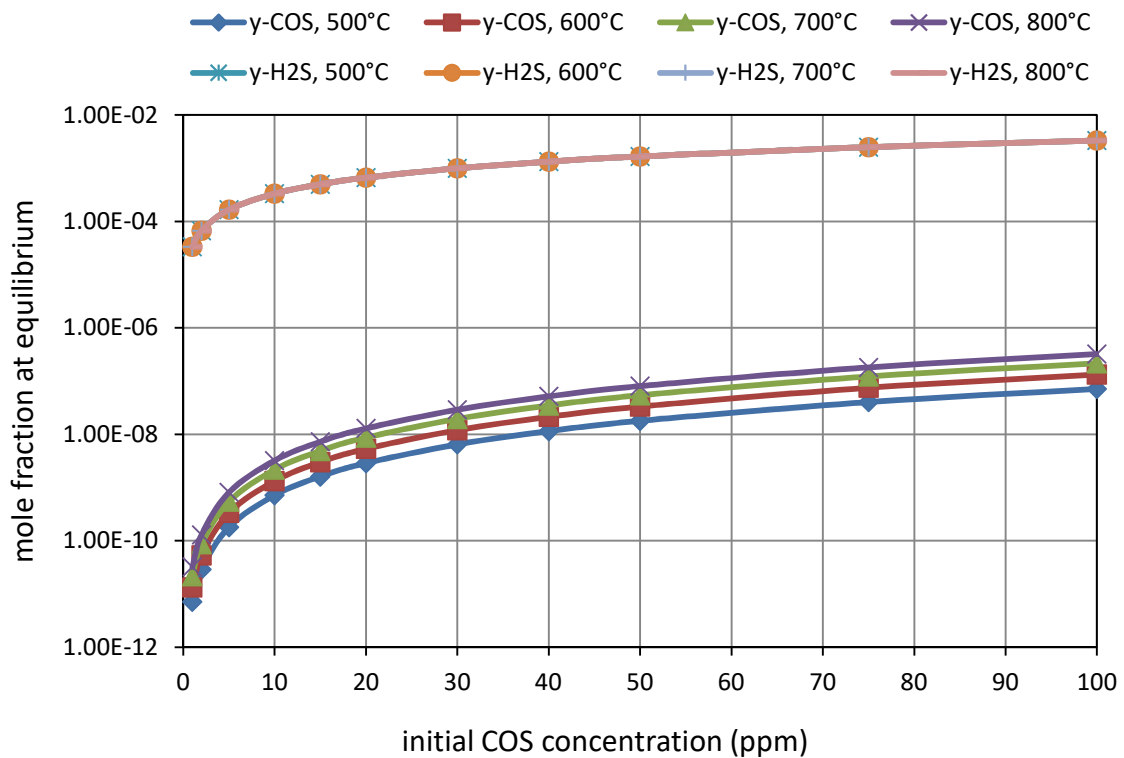
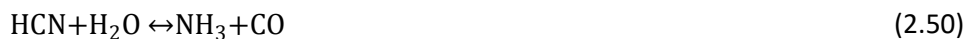


Figure 3.1: Composition of sulfur-containing compounds in fuel

As presented in chapter two, HCN is also available in biomass derived syngas. HCN can react with water and convert to NH<sub>3</sub> through reaction 2.50.



In order to calculate the concentrations of HCN and NH<sub>3</sub>, a thermodynamic analysis is carried out with 3 vol% H<sub>2</sub>O. The approach to calculate the concentrations at equilibrium for HCN/H<sub>2</sub>O mixture is similar to that of COS/H<sub>2</sub>O mixture, as explained above.

Figure 3.2 shows the results of the thermodynamic analysis of HCN hydrolysis accomplished for the initial concentrations of 1 to 100 ppm at 500 to 800 °C. As illustrated in the figure, the concentration of NH<sub>3</sub> is approximately 5 orders of magnitude larger than that of HCN, indicating that almost all HCN converts into NH<sub>3</sub> and only a trivial amount of HCN will remain in the fuel mixture at equilibrium. Therefore, it is appreciated that the cell is mostly exposed to NH<sub>3</sub> which is formed through hydrolysis reaction taking place at the cell operating temperatures. This

process tends to drastically decrease the concentration of HCN to small amounts provided that HCN is the only contaminant available in the fuel mixture.

Moreover, the results show that the effect of temperature on the concentrations of HCN and NH<sub>3</sub> at equilibrium is insignificant. Although increasing the temperature favours the reverse reaction which results in a very slight rise in HCN concentration, the concentration of NH<sub>3</sub> remains approximately unchanged. Concerning the 4 interpolated lines of H<sub>2</sub>S depicted in figure 3.2, it must be noted that they are overlapped, thus, care should be taken to analyse the figure.

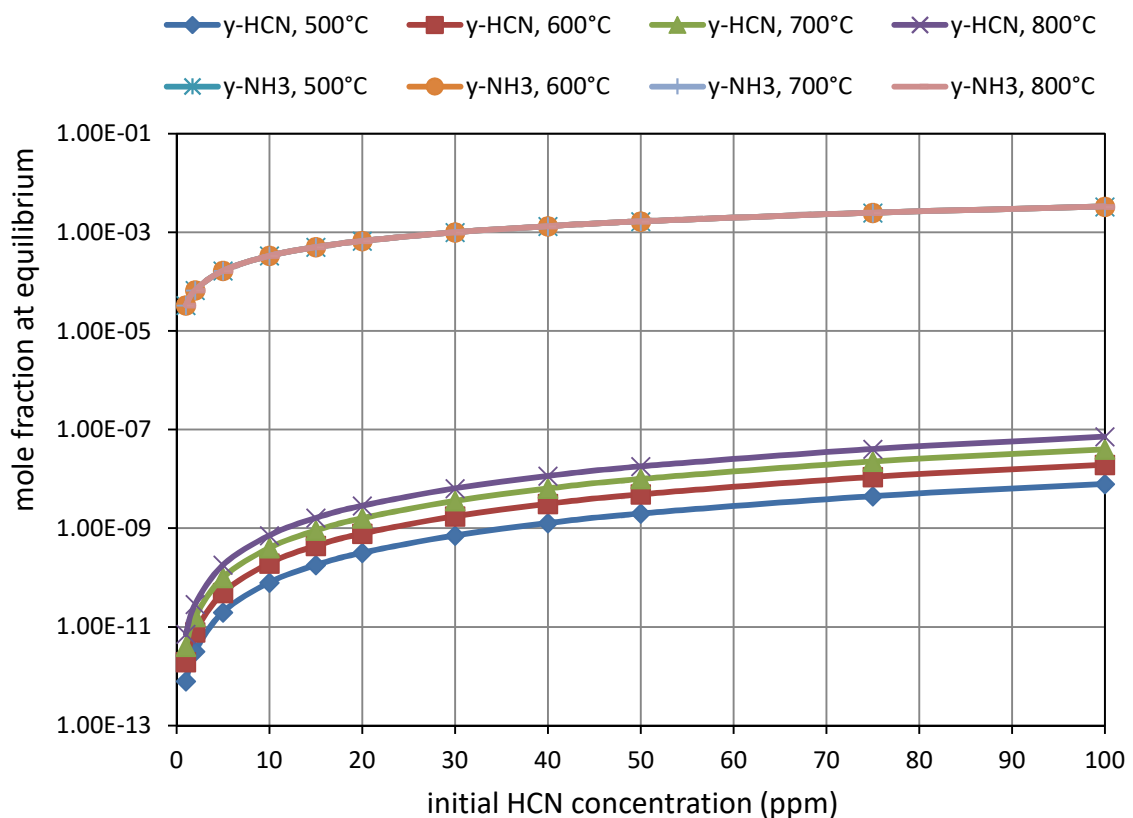


Figure 3.2: Composition of nitrogen-containing compounds in fuel

The thermodynamic analyses revealed a rather low content of the initial contaminants at the typical operating temperatures of SOFCs i.e. 10<sup>-5</sup> to 10<sup>-2</sup> ppm of COS and 10<sup>-6</sup> to 10<sup>-3</sup> ppm of HCN at equilibrium. Considering these results it can be stated that theoretically it will be difficult to expose the cell to COS or HCN only and study their direct effect on the performance of the cell. Thus, these two contaminants are excluded from the list of gaseous impurities which can be practically tested. Ammonia is also ruled out owing to its performance as a potential fuel for SOFCs. Consequently H<sub>2</sub>S and HCl are the contaminants left on the list. Due

to the large concentration in syngas and highly detrimental effect on the performance of cells H<sub>2</sub>S has been chosen as the contaminant for this research.

### 3.3 Test matrix

A baseline test with clean fuel will be carried out to identify the characteristics of cells and investigate the effect of the operating conditions such as fuel composition and temperature on the performance. Upon completion of this section, tests with the contaminated fuel will be carried out. As mentioned in the previous chapter, table 2.3, the maximum amount of available H<sub>2</sub>S in BDS has been reported to be 200 ppm. Thus, four levels of H<sub>2</sub>S concentration are considered in this research: 50, 100, 150 and 200 ppm.

In the literature, there are several studies of these levels of contamination separately, i.e. under different operating conditions, meaning that comparative performance assessment is not possible. Mimicking the concentrations, this work explores concentrations under the same operating conditions.

The desired composition of the fuel mixture is achieved by mixing a pre-set mixture of N<sub>2</sub>/H<sub>2</sub>S (500 ppm of H<sub>2</sub>S), clean H<sub>2</sub> and clean N<sub>2</sub>. By controlling the flow rate of these three lines the composition of the mixture can be adjusted. The accuracy of the pre-set mixture is  $\pm 2\%$ , as advised by the supplier (BOC [145]) and the accuracy of the flow meters (Brooks mass flow meters and controller, model no.: 5850TR/DA1B2B1) is 1% of full scale [146]. Considering the required flow rates for H<sub>2</sub>S concentrations of 50, 100, 150 and 200 ppm, the uncertainty of the H<sub>2</sub>S concentration in the final mixture will be 15, 8, 6 and 5%, respectively.

### 3.4 Applied characterization techniques

In this research a series of characterisation methods are used:

- Voltage and current measurement including:
  - o Galvanostatic mode (for durability tests)
  - o v-i curves
  - o ASR calculation
- SEM and XRD to identify the structure and chemical elements
- EIS analysis to identify the resistance of cells at a wide range of operating conditions such as different temperatures, current densities, fuel compositions and poisoning levels

The EIS and v-i curves are taken using a Gamry reference 3000 potentiostat [147].

In this research all the EIS curves were taken under the galvanostatic mode in which the current is set. The range of frequency and amplitude of the current wave have been summarised in table 3.2.

Minimum frequency (Hz)	0.2
Maximum frequency (Hz)	6500
Current amplitude (A rms)	0.3

**Table 3.2: Conditions at which the EIS curves are taken**

In the durability tests, all the cells are loaded at 0.2 A/cm<sup>2</sup> (3.2 A) and the EIS curves are taken at the conditions shown in the above table.

Once the EIS data are obtained, they can be fitted on a mathematical model to calculate the rough estimates of the fuel cell parameters. The obtained estimates, then, can be used to characterise the materials and properties of the system.

The curve fitting procedure is carried out by the Gamry Echem Analyst software. The software produces the fits by minimising the weighted sum of the residuals using the Simplex method. The residual is defined as the difference between the measured and calculated values at a given frequency. The weighting parameter for each point is the inverse of the measured impedance of the point. The weighted sum of the residuals ( $X^2$ ) and weighting parameter ( $w_i$ ) are mathematically defined as [148]:

$$X^2 = \sum_{i=1}^N w_i \left[ (Z_{meas_{real}} - Z_{fit_{real}})^2 + (Z_{meas_{imag}} - Z_{fit_{imag}})^2 \right] \quad (3.7)$$

$$w_i = \frac{1}{\sqrt{Z_{meas_{i,real}}^2 + Z_{meas_{i,imag}}^2}} \quad (3.8)$$

where  $Z_{meas}$  and  $Z_{fit}$  are measured and calculated impedance, respectively.  $N$  is the number of the data points and  $i$  is the point index.

## 4 Contamination model

### 4.1 Basic assumptions

The operating voltage of the fuel cells is generally given by equation 2.25, as explained in chapter two. In this chapter, this equation is used to develop a contamination model for the cells exposed to H<sub>2</sub>S. In view of the operating conditions and SOFC performance and structure, a few basic assumptions are considered in order to develop the model:

- As mentioned before, the concentration losses are significant at the high current densities. Considering the operating conditions in this research (low currents drawn from the cells), this type of loss will be negligible. However, in case of the high current densities and thus presence of the concentration losses it can be said that any contaminant may dissociate or decompose at the electrode leading to changes in topology of the anode i.e. the size of pores as well as changes in the effective mass transfer coefficient which is affected by tortuosity and porosity.
- Hydrogen sulfide, as the contaminant, is introduced to the fuel mixture, thus, the anode will be the only component of the cell subjected to poisoning.
- Considering the fact that the electrolyte of SOFCs is an impermeable solid oxide it can be assumed that H<sub>2</sub>S will not be able to penetrate into the electrolyte and reach the cathode.

In accordance with the previous studies, the H<sub>2</sub>S degradation mechanism can be divided into 2 steps:

- The initial drop in power which is sharp and immediate and attributed to the adsorption of S onto the nickel surface at the anode functional layer and/or formation of nickel sulfide. This step may be fully or partially reversible depending on the H<sub>2</sub>S concentration and operating conditions such as temperature and current density.
- The secondary drop which is sluggish and may end up in a steady state in the long term run. This step is due to the nickel reconstruction and decomposition of H<sub>2</sub>S at the anode support layer leading to a decrease in the electrical conductivity.

As explained in the literature review chapter, the level of degradation depends on the cell materials and operating conditions. The operating conditions include:

- Temperature: any increase in the operating temperature of the cell results in a decrease in the degree of degradation.
- Concentration of H<sub>2</sub>S: the higher the concentration of contaminant, the higher the performance losses.
- Time: there is an initial sharp drop followed by a sluggish drop which may establish a steady state in the long term performance.
- Operating current density/voltage: it has been shown that the higher operating current density (lower operating voltage) leads to a lower performance loss over time.

## 4.2 H<sub>2</sub>S damage model

In order to develop a mathematical degradation model for H<sub>2</sub>S poisoning of the cells a few assumptions are made at this point:

- The degradation mechanism includes the adsorption of H<sub>2</sub>S on the nickel surface and formation of nickel sulfide. Considering the amount of H<sub>2</sub>S present in the fuel mixture in this work, the former is assumed to be the major cause of the performance loss and the latter is considered to have a smaller impact according to the previous studies. It should be noted that whatever the case is the degradation trend (2-step performance loss) is the same. Also, it should be noted that in either case the same properties of the anode including length of TPB, ionic and electrical conductivity and thermal conductivity are affected and subjected to change by H<sub>2</sub>S.
- It has been shown that the initial drop in the cell performance (associated with the deactivation of the anode reactive sites) is much larger than the secondary loss (attributed to the decreased electrical conductivity of the anode). In accordance with this argument it can be assumed that the most important phenomenon is the deactivation or blockage of the reactive sites which can be represented the best by the TPB length. Thus, a further assumption will be that only  $\eta_{act,an}$  is affected by the contaminant.
- Due to the complexity of the degradation mechanism and presence of a wide range of the affecting parameters the independent variables chosen in this model are concentration, temperature and time. As the current drawn from the cells is low it is assumed that there is no reaction between

oxygen ions and adsorbed sulfur at anode. Thus, the current is excluded from the list of the affecting (independent) parameters.

All the assumptions made for the damage model development can be summarised as:

- Activation losses are considered at both electrodes
- Ohmic losses are taken into account only for the electrolyte
- Concentration losses are ignored due to the fairly small current density
- Only  $\eta_{act,an}$  is affected by H<sub>2</sub>S
- The TPBs length is assumed to be the only parameter reflecting the change in  $\eta_{act,an}$
- Effects of the temperature, contaminant concentration and time are considered

The mathematical model for the SOFCs performance, as presented in chapter 2, can be written as:

$$V = E - \eta_{act,an} - \eta_{act,ca} - \eta_{ohm,ele} \quad (2.25)$$

The damage model can be developed by different approaches, as explained below.

#### 4.2.1 Damage model 1

Combining equations 2.42 and 2.43 a relation for the exchange current density damage can be derived as:

$$i_0 = i_0^{initial}(1 - f) \quad (4.1)$$

The damage factor ( $f$ ) would be a function of temperature (T), concentration of H<sub>2</sub>S ( $C_{H_2S}$ ) and time (t).

$f$  is now assumed to be the product of two functions:  $f1$ , taking into consideration the effects of temperature and H<sub>2</sub>S concentration, and  $f2$ , accounting for time.

$$f = f1(T, C_{H_2S}) \cdot f2(t) \quad (4.2)$$

The relation in equation 2.44 ([81]) can be used for  $f1$ .

As explained in chapter 2, the performance of SOFCs tends to degrade in long run, even operated on the clean fuel. It has been shown that TPBs length (hence exchange current density) can be assumed to represent these types of the performance loss.

In this damage model, the relation in equation 2.41 ([83]) is adopted to model  $f2$ .

Thus,  $f2$  can be written as:

$$f_2(t) = C(T)e^{-kt} + D(T) \quad (4.3)$$

where  $C(T)$ ,  $D(T)$  and  $k$  are temperature dependent constants.

Considering the relations for  $f_1$  and  $f_2$ , the damage factor will be:

$$f = \left( A(T) \ln \left( \frac{P_{H_2S}}{P_{H_2}} \right) + B(T) \right) \cdot (C(T)e^{-kt} + D(T)) \quad (4.4)$$

#### 4.2.2 Damage model 2

In this model it is assumed that the active sites are damaged through a system of two parallel mechanisms: long term degradation (4.5) and  $H_2S$  poisoning (4.6).



where  $A$  and  $D$  represent active and damaged sites, respectively.

A damage factor ( $f$ ) is introduced as:

$$A = A_0(1 - f) \quad (4.7)$$

where  $A_0$  is the initial number of the active sites.

Active sites ( $A$ ) can be represented by the TPBs length as:

$$\frac{A}{A_0} = \frac{l_{TPB}}{l_{TPB}^{initial}} \quad (4.8)$$

Combining equations 2.42, 4.7 and 4.8:

$$\frac{i_0}{i_0^{initial}} = \frac{A}{A_0} = (1 - f) \quad (4.9)$$

The rate of the reactions 4.5 and 4.6, can be written as:

$$-\frac{d[A]}{dt} = \frac{d[D]}{dt} = k_1[A] + k_2[A][H_2S] = [A](k_1 + k_2[H_2S]) \quad (4.10)$$

Rearranging the above equation:

$$\frac{1}{[A]} d[A] = - (k_1 + k_2[H_2S]) dt \Rightarrow \ln[A] = - (k_1 + k_2[H_2S])t + c \quad (4.11)$$

At  $t=0$  the number of the active sites are  $A_0$ . Applying this boundary condition to equation 4.11,  $c$  can be calculated as:

$$at \ t = 0 : c = \ln[A_0] \quad (4.12)$$

Combining equations 4.11 and 4.12:

$$\ln \left( \frac{[A]}{[A_0]} \right) = - (k_1 + k_2[H_2S])t \Rightarrow \frac{[A]}{[A_0]} = e^{- (k_1 + k_2[H_2S])t} \quad (4.13)$$

Comparing equations 4.9 and 4.13, the damage factor can be written as:

$$f = 1 - e^{-(k_1 + k_2[\text{H}_2\text{S}])t} \quad (4.14)$$

$k_1$  is the rate constant of the cell degradation over time without any contaminant. As this degradation is very slow compared to that of  $\text{H}_2\text{S}$  poisoning,  $k_1$  can be neglected. Thus, the damage factor is simplified to:

$$f = 1 - e^{-k_2[\text{H}_2\text{S}]t} \quad (4.15)$$

This model takes into account the concentration of  $\text{H}_2\text{S}$  ( $[\text{H}_2\text{S}]$ ) and time ( $t$ ).  $k_2$  is the rate constant of  $\text{H}_2\text{S}$  poisoning reaction and will depend on the operating temperature.

### 4.3 Procedure to calculate damage factor

The model adopted for the analysis is equation 4.1, as explained before. The key assumption for modelling was only  $i_{0,an}$  is affected by  $\text{H}_2\text{S}$ , thus  $\eta_{act,an}$  will be the only parameter subjected to change and other parameters will remain the same.

There are 5 tests according to the level of  $\text{H}_2\text{S}$  concentration:

Step0: baseline test – no contaminants ( $V_0$ )

Step1: 50 ppm of  $\text{H}_2\text{S}$  ( $V_1$ )

Step2: 100 ppm of  $\text{H}_2\text{S}$  ( $V_2$ )

Step3: 150 ppm of  $\text{H}_2\text{S}$  ( $V_3$ )

Step4: 200 ppm of  $\text{H}_2\text{S}$  ( $V_4$ )

The equation for the cell operating voltage for the baseline test can be written as:

$$V_0 = E - \frac{RT}{\alpha z F} \sinh^{-1} \left( \frac{i}{2i_{0,an}^{initial}} \right) - \eta_{act,ca} - \eta_{ohm,ele} \quad (4.16)$$

For contamination tests the voltage is written as:

$$V_j = E - \frac{RT}{\alpha z F} \sinh^{-1} \left( \frac{i}{2i_{0,an}^j} \right) - \eta_{act,ca} - \eta_{ohm,ele} \quad (4.17)$$

where  $j$  is the index for the level of contamination.

Subtracting equation 4.17 from 4.16:

$$V_0 - V_j = \frac{RT}{\alpha z F} \sinh^{-1} \left( \frac{i}{2i_{0,an}^j} \right) - \frac{RT}{\alpha z F} \sinh^{-1} \left( \frac{i}{2i_{0,an}^{initial}} \right) =$$

$$\frac{RT}{\alpha z F} \ln \left( \frac{\frac{i}{2i_{0,an}^j} + \sqrt{1 + \left( \frac{i}{2i_{0,an}^j} \right)^2}}{\frac{i}{2i_{0,an}^{initial}} + \sqrt{1 + \left( \frac{i}{2i_{0,an}^{initial}} \right)^2}} \right) = \frac{RT}{\alpha z F} \ln \left( \frac{\frac{i}{2i_{0,an}^{initial}(1-f_j)} + \sqrt{1 + \left( \frac{i}{2i_{0,an}^{initial}(1-f_j)} \right)^2}}{\frac{i}{2i_{0,an}^{initial}} + \sqrt{1 + \left( \frac{i}{2i_{0,an}^{initial}} \right)^2}} \right) =$$

$$\frac{RT}{\alpha z F} \ln \left( \frac{\frac{i}{2(1-f_j)} + \sqrt{(i_{0,an}^{initial})^2 + \left(\frac{i}{2(1-f_j)}\right)^2}}{\frac{i}{2} + \sqrt{(i_{0,an}^{initial})^2 + \left(\frac{i}{2}\right)^2}} \right) \quad (4.18)$$

The value of the damage factor ( $f_j$ ) can be calculated from equation 4.18 at each step. The damage factor has a particular value at different times, temperatures and H<sub>2</sub>S concentrations. However, the initial value of  $i_{0,an}$  is required for calculation. Having known the initial value of  $i_{0,an}$  and  $f$  at different levels of contamination, a curve can be fitted to calculate the constants of the damage factor.

#### 4.4 Fit of models with synthetic data

In this section, it is aimed to compare and test the models for their fit to generalised data. The first step for the model evaluation is to find experimental data on which the models can be fitted.

The voltage drop of the cells after 5 minutes of exposure to 0.18 to 10 ppm of H<sub>2</sub>S have been reported in reference [135]. These experimental results were obtained under potentiostatic mode, however, the profile of current during the exposure period is not provided. The damage models proposed above were developed under galvanostatic mode and include the effect of time on the voltage drop. As the profile of the voltage during the contamination period is not provided in the paper, it is not possible to evaluate the damage models. In another study [136], the profiles of the voltage drop for a wide range of the H<sub>2</sub>S concentrations have been reported. However, this data cannot be used directly because the same cell was used for multiple concentrations. This caused the starting point of the voltage profile to vary for each level of the concentration. As a result, they cannot be used for model fitting.

Due to the lack of the experimental data, synthetic data is used for the curve fitting. The synthetic data is generated using the experimental data obtained from the test with 50 ppm of H<sub>2</sub>S in this research.

##### 4.4.1 Damage model modification

Prior to the curve fitting and comparison of the models, the developed models are modified as follows:

- Model 1

Due to the large number of the constants in model 1 ( $A, B, C$  and  $D$ ), the equation yields infinite solutions. In order to have a unique solution, coefficient  $C$  is mathematically removed from the model i.e. it is separated and the equation is re-written with new constants. In addition to constant  $C$ ,  $P_{H_2}$  can also be removed since it has the same value for all cases. Thus, model 1 is simplified and can be re-written as equation 4.19:

$$f = (A \ln(P_{H_2S}) + B) \cdot (e^{-kt} + D) \quad (4.19)$$

- Model 2

Model 2 suggests that the damage factor increases to 1 as the time reaches a large value. This results from reaction 4.6 which implies that all the active sites are damaged due to the exposure to sulfur, i.e. the reaction goes to completion. However, it is known from the literature that the contaminated cells are partially deactivated, thus, only a number of the active sites are damaged. The number of the damaged sites and in turn the final value of the voltage depend on the  $H_2S$  concentration. In order to take into account this effect, the damage model 2 should be modified as:

$$f = A - e^{-k_2[H_2S]t} \quad (4.20)$$

where  $A$  is a constant depending on temperature and  $H_2S$  concentration. Thus, it should be noted that parameter  $A$  will not have the same value for different levels of the  $H_2S$  contamination.

#### 4.4.2 Generating synthetic data

A typical voltage degradation profile is demonstrated in figure 4.1. The degradation curve can be divided into 3 phases: phase 1 is the period between the  $H_2S$  line switch on and start of the voltage drop, phase 2 includes the effects of the active sites blockage (sharp initial drop in voltage) and phase 3 consists of the anode reconstruction (secondary sluggish drop).

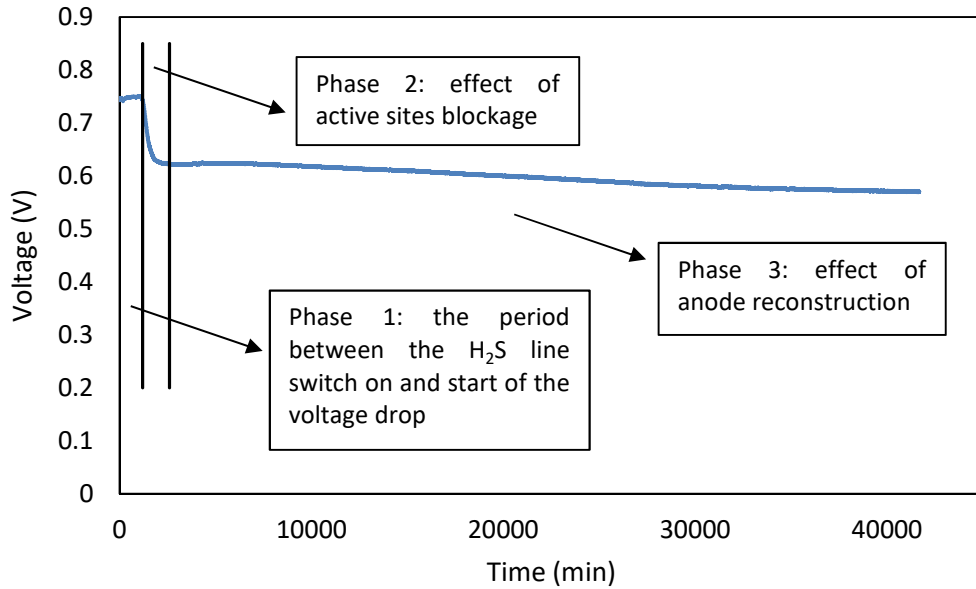


**Figure 4.1: Typical voltage degradation profile**

The proposed models include the effects of the active sites blockage and change in the exchange current density, thus, can only be applied to phase 2.

In order to compare the models synthetic data should be generated in the first step. The experimental results for 50 ppm of H<sub>2</sub>S, obtained in chapter 7, are used as the reference to generate the synthetic data through equation 4.21 where  $\theta$  is an arbitrary parameter.

$$V_j = V_0 - (V_0 - V_{50 \text{ ppm}})\theta \quad (4.21)$$

In the case of  $\theta = 1$ , the equation returns the actual data for 50 ppm. For  $\theta > 1$  a series of smaller values are obtained which can be attributed to a higher H<sub>2</sub>S concentration. On contrary, for  $\theta < 1$  the equation yields larger values for the voltage, representing a lower H<sub>2</sub>S concentration. In this study  $\theta$  is assumed to have values of 0.75 and 1.25 to generate the data for lower and higher H<sub>2</sub>S concentrations. It is presumed that the calculated data correspond to 25 and 75 ppm of H<sub>2</sub>S, respectively. The profiles of the actual data (50 ppm) and synthetic data (25 and 75 ppm) is shown in figure 4.2.

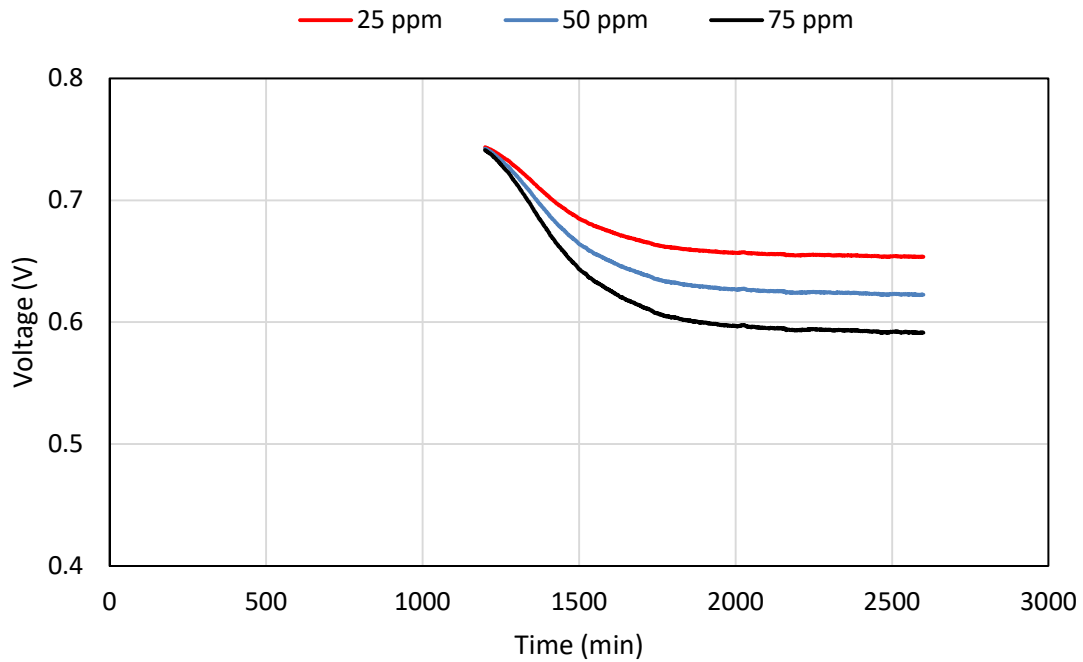


Figure 4.2: Voltage profile of the experimental and synthetic data

#### 4.4.3 Curve fitting

The first step of the curve fitting procedure is to calculate the values of the damage factor for each series of the experimental/synthetic data using equation 4.18. The initial value for the anode exchange current density is assumed to be  $0.134 \text{ A/cm}^2$  as calculated in chapter 8 (table 8.2).  $V_0$  is the cell voltage before exposure to  $\text{H}_2\text{S}$  and equals  $0.747 \text{ V}$  as obtained in the 50 ppm test carries out in chapter 7. Equation 4.18 is solved by the GRG nonlinear engine built in Microsoft Excel.

The curve fitting approach includes the least square (minimisation of the squared sum of the difference between the model and experimental/synthetic data points) and GRG nonlinear methods.

- Model 1:

The calculated constants for model 1 are summarised in table 4.1. Figure 4.3 illustrates the results of the curve fitting for experimental/synthetic data. As the model is well fitted on the results, it can be stated that the proposed model can predict the behaviour of the voltage drop accurately.

A	B	D	k
-0.28113	-0.1319	-1.03941	0.006077

Table 4.1: Model 1 parameters

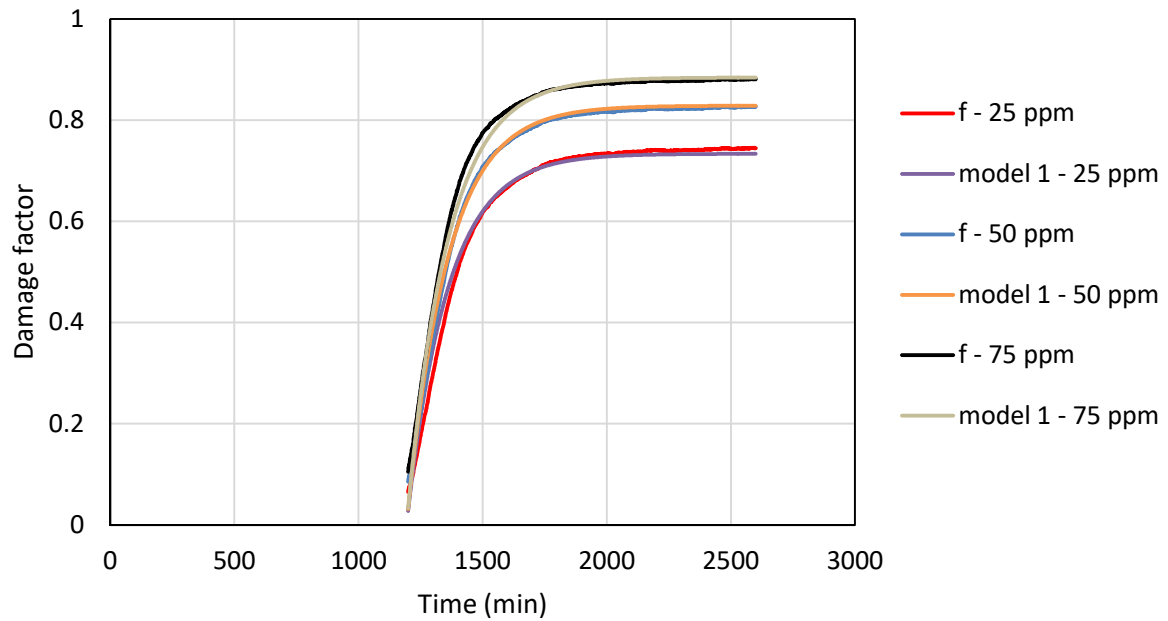


Figure 4.3: Results of model 1 curve fitting

- Model 2:

As mentioned earlier in this section, parameter  $A$  is a function of  $H_2S$  concentration. Therefore, for each series of the experimental/synthetic data the value of  $A$  is different. This implies that the curve fitting procedure should be carried out individually for each set of the data point to calculate the corresponding value of  $A$ . In this approach parameter  $k_2$  remains the same for all sets of data/model (25, 50 and 75 ppm). The calculated parameters are tabulated in table 4.2. As shown in figure 4.4, the model yields a poor fit, thus predicting the change in the damage factor inaccurately.

[H <sub>2</sub> S]	$A$	$k_2$
25	0.810119	0.000178
50	0.811513	0.000178
75	0.842548	0.000178

Table 4.2: Model 2 parameters – variable  $A$ , constant  $k_2$

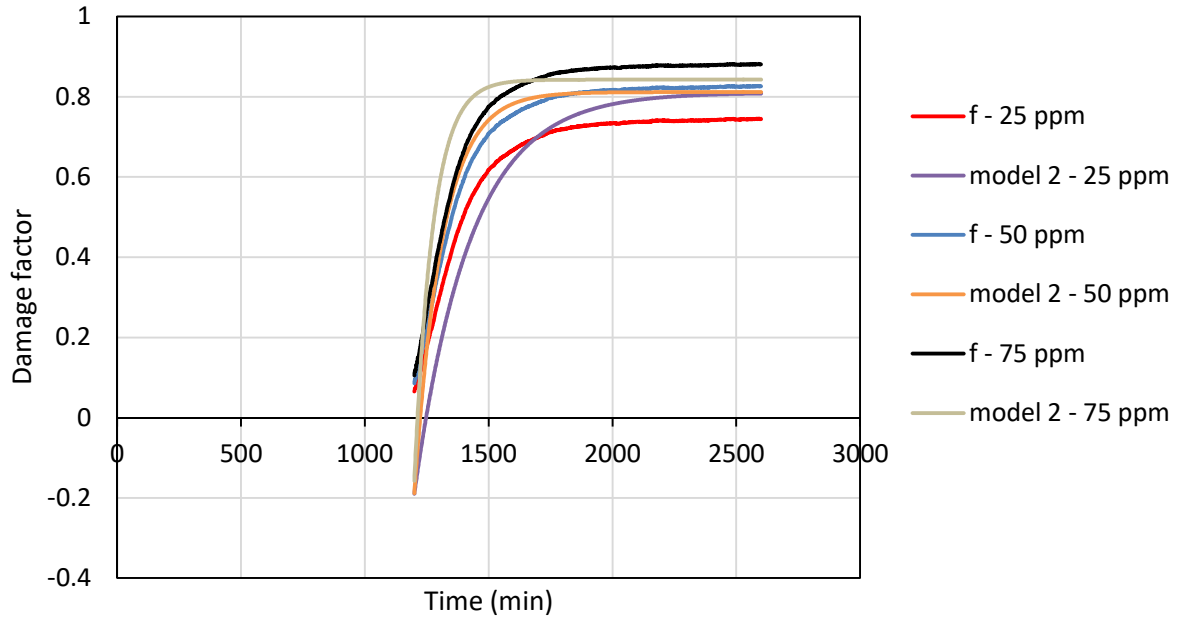


Figure 4.4: Results of model 2 curve fitting – variable  $A$ , constant  $k_2$

In a new approach, it is assumed that both  $A$  and  $k_2$  are functions of  $H_2S$  concentration, thus each series of data are manipulated individually to calculate the corresponding parameters. The calculated parameters are presented in table 4.3.

[H <sub>2</sub> S]	$A$	$k_2$
25	0.74119	0.000312
50	0.82349	0.0001545
75	0.87826	0.0001065

Table 4.3: Model 2 parameters – variable  $A$  and  $k_2$

In comparison to the previous results, this approach yields better results as illustrated in figure 4.5. However, the calculated values of the damage factor are negative at early stage of the plot, which is not expected. According to the model development scheme,  $f$  should be within the range of 0 and 1 ( $0 \leq f < 1$ ).

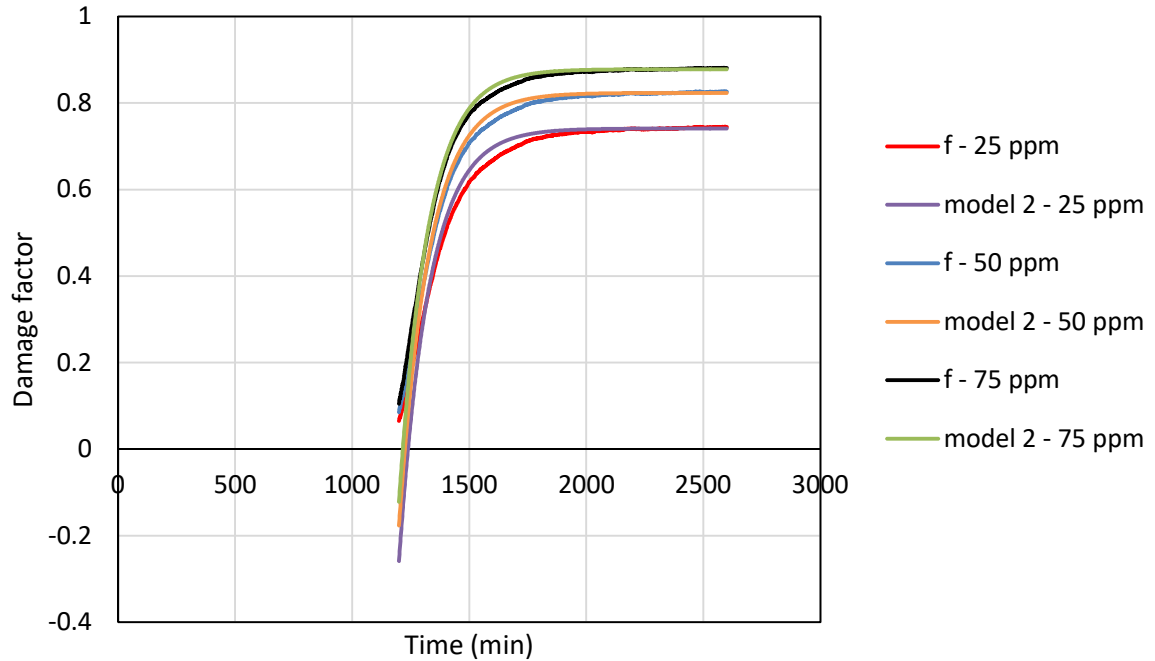


Figure 4.5: Results of model 2 curve fitting – variable  $A$  and  $k_2$

#### 4.4.4 Comparison of the damage models

Figure 4.6 and figure 4.7 compare the voltage drop predicted by model 1 and model 2 with the experimental/synthetic data, respectively. As can be seen in the figures, model 1 yields a better fit than model 2 does, particularly, at the early stage of the voltage drop. This is due to the fact that model 2 resulted in negative values for the damage factor for this period, as illustrated in figure 4.5. A possible reason could be that the initial stage of phase 2 of the voltage profile includes the effects of phase 1 which tends to change the curvature. The model won't be able to cope with that initial curvature, and maybe a case should be made to ignore it and only start the comparison further down. Apart from the initial phase, it can be stated that both models can predict the profile of the voltage drop validly although model 1 is fitted slightly better.

The results of the curve fitting show that all the parameters are independent of the  $H_2S$  concentration for model 1, however, depending on the  $H_2S$  concentration in the case of model 2, as presented in table 4.1 and table 4.3. It should also be noted that the procedure of the curve fitting was carried out using synthetic data which can significantly affect the parameters of the model.

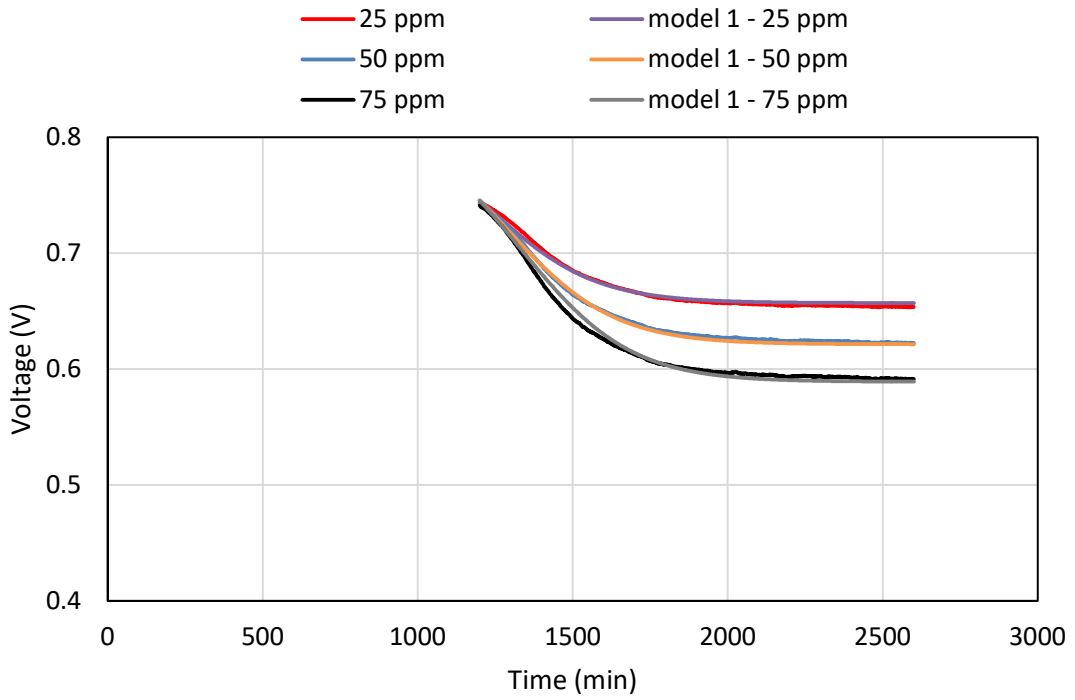


Figure 4.6: Comparison of the data and model 1

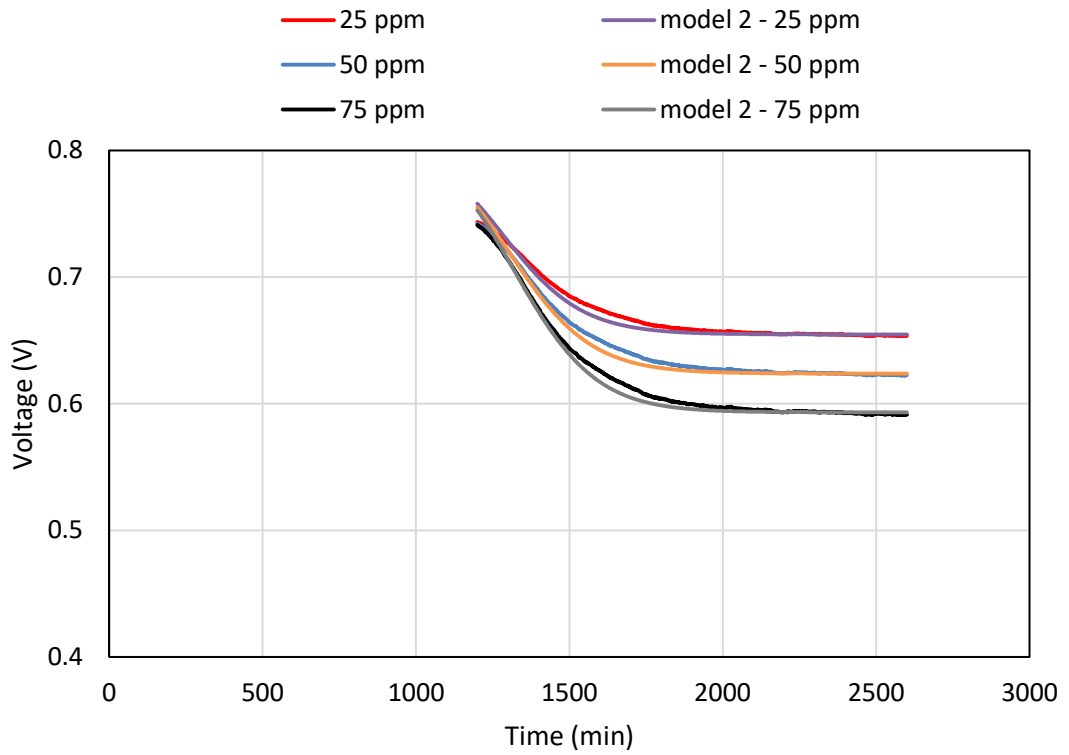


Figure 4.7: Comparison of the data and model 2



# 5 Initial test apparatus

## 5.1 Test set up

In order to investigate the performance of the single cells operating on the simulated biomass-derived syngas (BDS), a test rig has been designed and set up. The test rig consists of different subsystems including gas blender (gas panel), humidifier (water bath), high temperature furnace, manifold (gas delivery housing), individual cells, load bank, water trap and control/data logging system. The design of the test rig has been inspired by the British gas test rig capable of testing single cells and stacks [149]. The schematic of the rig has been illustrated in figure 5.1. Briefly, the fuel composition is set through the gas blender. The fuel mixture, then, is bubbled into the water bath (humidifier). As the result of the gas passing through the humidifier water is added to the fuel stream. Finally, the fuel/water mixture is delivered to the cell to generate electricity. The products of the electrochemical reactions within the cell are directed to vent after passing through the water trap.

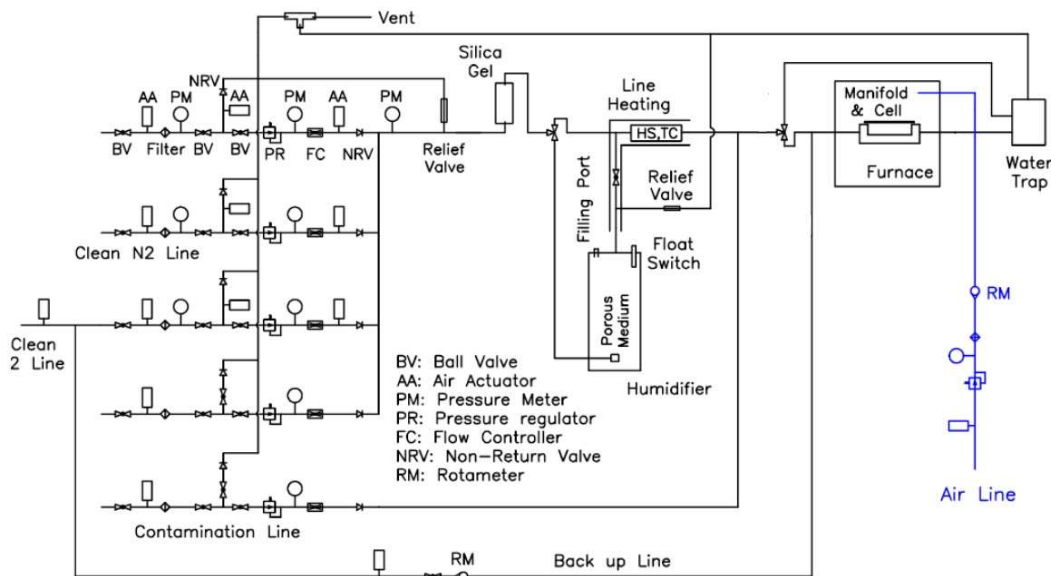


Figure 5.1: Schematic of test rig

### 5.1.1 Gas blender

A gas mixer has been fabricated to prepare the fuel mixture to a set composition, which is capable of mixing up to five gas lines. The schematic of this gas panel has been shown in figure 5.2. On each gas line, a volumetric flow meter/controller has been mounted to control the amount of each gas in the fuel mixture. Since the test

rig has been design to investigate the performance of the single cells operating on biomass-derived syngas the gas blender has been calibrated for N<sub>2</sub>, CO<sub>2</sub>, H<sub>2</sub>, N<sub>2</sub>, and CH<sub>4</sub> which are among the main components of biomass syngas [89, 94-97]. The maximum flow rate of lines is 1, 1, 0.5, 1, and 0.1 L/min respectively. Each of the first three lines consists of a ball valve, an air actuator, a filter, a pressure meter, second ball valve, a vent line (including an air actuator and a non-return valve), third ball valve, pressure regulator, flow controller (Brooks mass flow controller, model 5850TR/DA1B2B1), second air actuator and a non-return valve. Each of last two lines includes a ball valve, an air actuator, a filter, second ball valve, a vent line (including a ball valve and a non-return valve), third ball valve, pressure regulator, flow controller (Brooks mass flow controller, model 5850TR/DA1B2B1) and non-return valve.

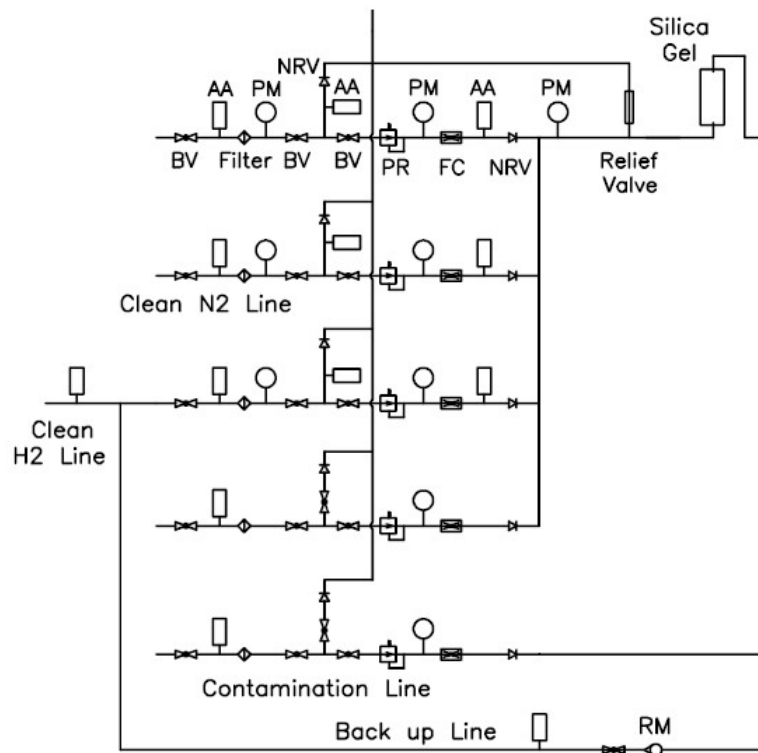


Figure 5.2: Schematic of gas blender

Each line passes a given amount of a particular gas as mentioned above. Lines one to four join together and the mixture then passes through silica gel to make sure that the fuel mixture is vapour free. A relief valve has been mounted on the line to prevent any pressure increase in system. Line number five has been assigned to the contaminant and joins the fuel mixture line before entering the fuel cell to make the final mixture. The gas blender has been illustrated in figure 5.3.



Figure 5.3: SOFC gas blender

### 5.1.2 Humidifier

From the Nernst equation it is clear that the partial pressure of  $H_2O$  appears as the denominator of the partial pressure fraction. Theoretically, the absence of  $H_2O$  may lead to an infinite voltage which can damage the equipment or operators. In order to make sure that the voltage value is limited, water vapour is added to the fuel mixture. In addition, to prevent coking at anode in case of the hydrocarbon fuels it is essential to provide a practical steam to carbon ratio. In order to serve the purpose a humidifier is applied after the gas blender. The humidifier consists of a water bath into which the fuel mixture is bubbled and absorbs water. It is well known that gases can carry a particular amount of water vapour at a given temperature. By controlling the temperature of the water bath through a heating element, the amount of water absorbed by the fuel gas can be adjusted. The humidifier and its schematic are shown in figure 5.4 and figure 5.5, respectively.

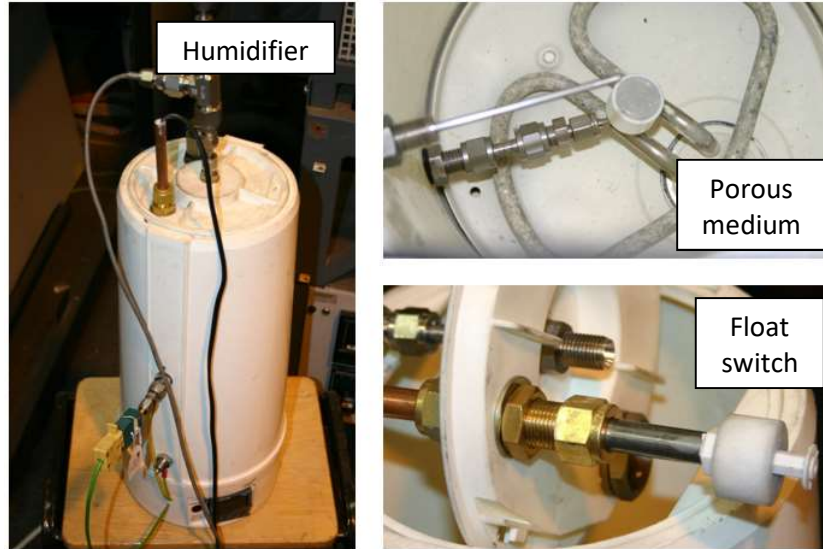


Figure 5.4: Humidifier

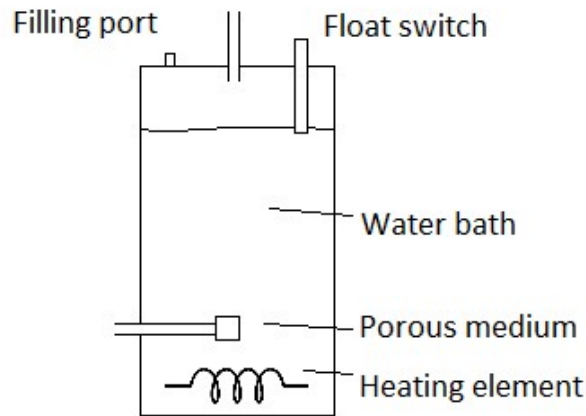


Figure 5.5: Schematic of humidifier

The fuel mixture was bubbled into the water bath through a porous medium to reduce the size of the bubbles and increase the contact surface between gas and water. By definition, the specific and relative humidity ( $\omega$  and  $\phi$ ) are defined as:

$$\omega = \frac{m_v}{m_{gas}} \quad (2.1)$$

$$\phi = \frac{m_v}{m_g} \quad (2.2)$$

Assuming the ideal gas state law for both vapour and gas equations 2.1 and 2.2 can be re-written as:

$$\omega = \frac{R_{gas} p_v}{R_v p_{gas}} = \frac{R_{gas} p_v}{R_v p - p_v} \quad (2.3)$$

$$\phi = p_v/p_g \quad (2.4)$$

where  $m$ ,  $R$  and  $p$  denote the mass, gas constant and pressure and subscripts  $v$ ,  $gas$  and  $g$  refer to vapour, fuel mixture and vapour saturation conditions, respectively.

Combining equations 2.3 and 2.4 specific humidity is written as:

$$\omega = \frac{R_{gas}}{R_v} \frac{\phi p_g}{p - \phi p_g} \quad (2.5)$$

The parameter  $X$  is now defined as the volumetric (molar) fraction of vapour in the humidifier outlet stream (mixture of fuel and vapour):

$$X = \frac{\dot{n}_v}{\dot{n}_v + \dot{n}_{gas}} \quad , \quad \dot{n}: \text{molar flow rate} \quad (2.6)$$

Equation 2.6 can be re-arranged as:

$$\dot{n}_v = \frac{X}{1 + X} \dot{n}_{gas} \quad (2.7)$$

Replacing the molar flow rate with the ratio of mass flow rate ( $\dot{m}$ ) to molar weight ( $M$ ), equation 2.7 can be re-arranged as:

$$\frac{\dot{m}_v}{\dot{m}_{gas}} = \frac{X}{1 + X} \frac{M_v}{M_{gas}} \quad (2.8)$$

The left hand side of equation 2.8 is the specific humidity.

If the water bath is deep enough it can be assumed that the gas will absorb the maximum possible amount of water and thus at the exit of humidifier the relative humidity is 100 %. Replacing this value in equation 2.5 and combining with equation 2.8  $X$  is calculated as:

$$X = p_g / p \quad (2.9)$$

Thus,  $X$  is the ratio of the water saturation pressure to the total (operating) pressure. The saturation pressure of water is a function of temperature (according to the thermodynamic tables for water properties); therefore, by controlling the temperature of the water bath the volumetric fraction of water vapour,  $X$ , can be set at the exit of the humidifier. In order to prevent condensation of water in the tubes before the cell, it is necessary to heat the lines. For this purpose a heating tape is used to cover the tubes from the humidifier exit to the cell inlet as seen in figure 5.1.

### 5.1.3 High temperature furnace

A high temperature furnace with the maximum temperature of 1100 °C is used to provide the operating temperature for cells which can be controlled by a control box. The internal dimension of furnace is 30x30x30 cm<sup>3</sup>. Figure 5.6 illustrates the high temperature furnace. Single cells are placed in the furnace and the controlling thermocouple measures the temperature of the area very close to the surface of the cell.



Figure 5.6: High temperature furnace

#### 5.1.4 Gas delivery manifold

In order to deliver fuel to the anode side of the cell and transport the products out of the cell a manifold has been designed and fabricated. The cell is mounted on the housing with the anode facing the bottom of the manifold. The manifold and its drawing have been presented in figure 5.7 and figure 5.8, respectively.

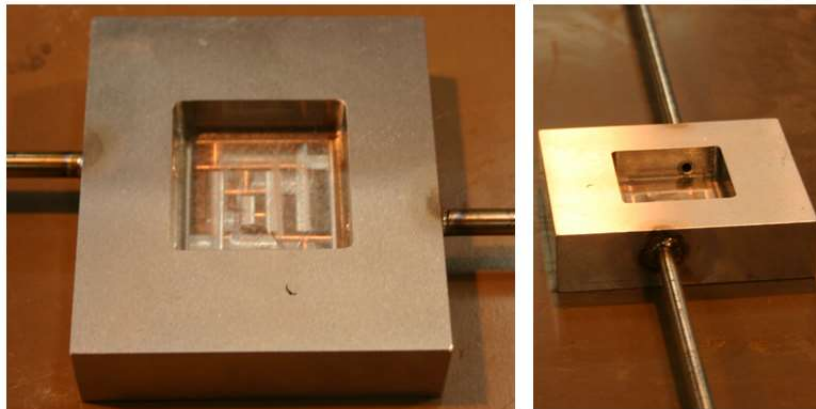


Figure 5.7: Gas delivery manifold

The housing has been made of ferritic stainless steel which in this case is a Fe-Cr-Al alloy. As mentioned in the previous chapter, ferritic stainless steel is widely used as interconnect due to its compatible CTE with those of the cell layers. As reported by the manufacturer, the CTE of Fe-Cr-Al alloy within the same range of temperatures is 15 ppm/K. Also, the composition of the alloy has been reported to be 22 % Cr, 5.3 % Al and 72.7 % Fe [150].

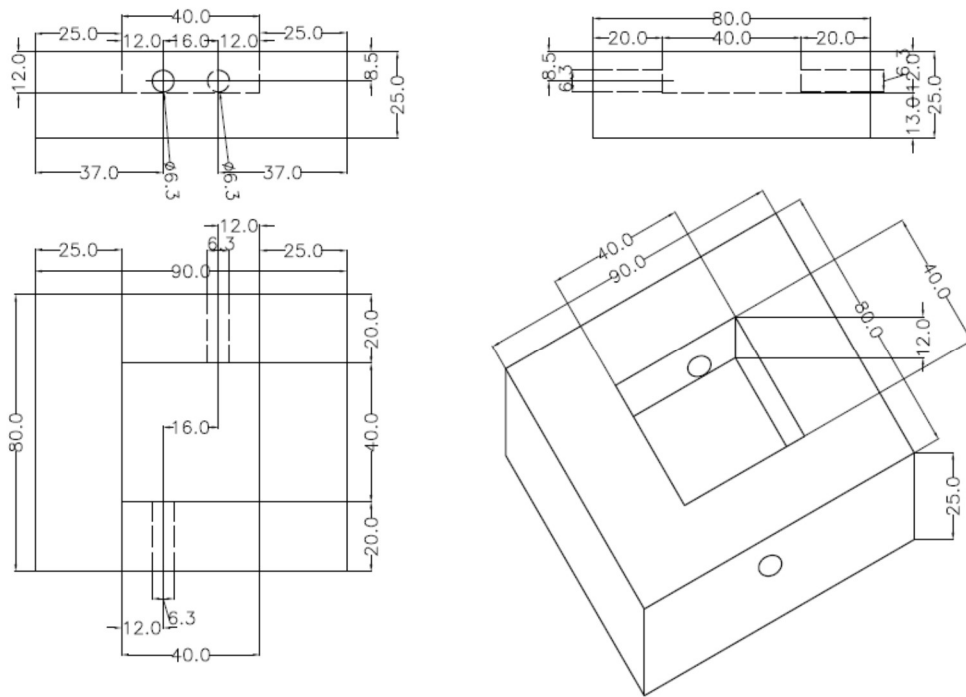


Figure 5.8: Drawing of gas delivery manifold (all dimensions are in mm)

As seen in figure 5.8 the dimensions of the aperture are  $40 \times 40 \text{ mm}^2$  and the depth is 12 mm. Thus, it can accommodate any individual cell larger than  $40 \times 40 \text{ mm}^2$ .

### 5.1.5 Single cell

The cells used in this research are planar anode supported with overall dimension of the cell being  $50 \times 50 \text{ mm}^2$ . The active area of cell (cathode area) is  $40 \times 40 \text{ mm}^2$ . The thickness and material of the cells have been presented in table 5.1 [151].

Contact layer composition	NiO
Contact layer thickness	5 $\mu\text{m}$
Anode support composition	NiO/YSZ
Anode support thickness	500 $\mu\text{m}$
Anode functional composition	NiO/YSZ
Anode functional thickness	12 $\mu\text{m}$
Electrolyte composition	YSZ
Electrolyte thickness	3 $\mu\text{m}$
Barrier composition	GDC
Barrier thickness	2 $\mu\text{m}$
Cathode composition	LSC
Cathode thickness	20-30 $\mu\text{m}$
<b>Total thickness</b>	<b>550 <math>\mu\text{m}</math></b>
Thickness tolerance	+/- 25 $\mu\text{m}$
Suggested operating temperature	600-700 $^{\circ}\text{C}$

Table 5.1: Characteristics of individual cells

The drawing of the different layers of cells has been illustrated in figure 5.9. Each individual cell consists of 6 layers: contact layer, anode support (thickest layer), anode functional layer (AFL), electrolyte, barrier and cathode. The role of the barrier layer is to prevent any reaction between the electrolyte material and cobalt content of the cathode. The reactions can form secondary phases which are detrimental to the performance of the cathode.



Figure 5.9: Drawing of layers of a single cell [151]

A current collecting mesh is attached to each side of the cell in order to provide a path for electrons to travel to/from electrodes. In this test rig silver mesh is used as the current collector and attached to both electrodes using silver ink. In addition, two pieces of silver wire are connected to each side of the cell (current collecting mesh). One set is used to set/measure the current and the other measures the voltage. The reason of using two separate sets of lead wires is to avoid any voltage drop due to the wires electrical resistance. In the case of applying one set a fraction of the cell voltage is lost while drawing current.

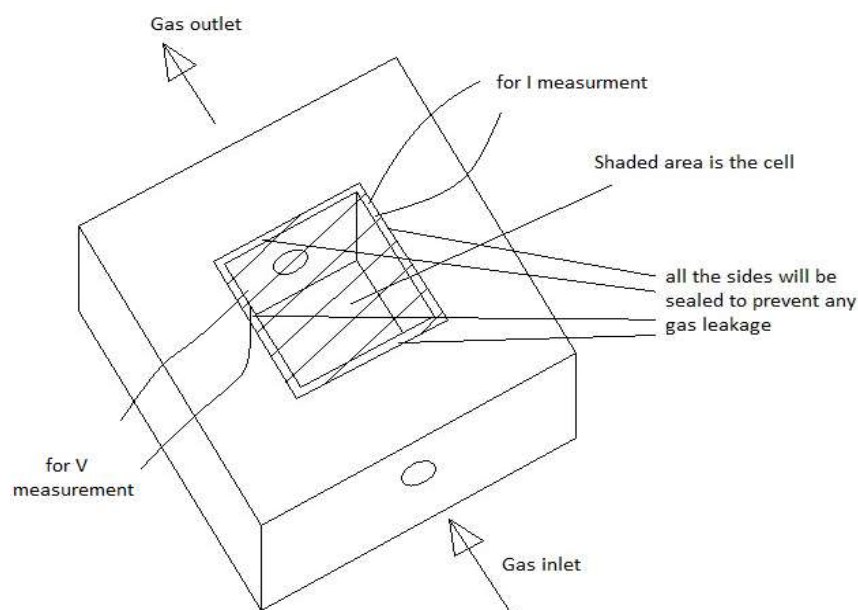


Figure 5.10: Schematic of housing/cell assembly

As seen in figure 5.10 the assembly of single cell/current collecting mesh/lead wires is mounted on the aperture with the cathode side facing outward and sealed to the housing using high temperature sealing material. Through this arrangement the anode would be exposed to the aperture and the fuel entering the manifold.

### 5.1.6 Load bank

The voltage measurement wires are directly connected to the LabVIEW/National Instruments data acquisition system. In order to draw current from the cell a variable resistance should be applied through which the current is imposed. Therefore, the current can be set by altering the resistance of the external load bank. The schematic of the load bank has been shown in figure 5.11.

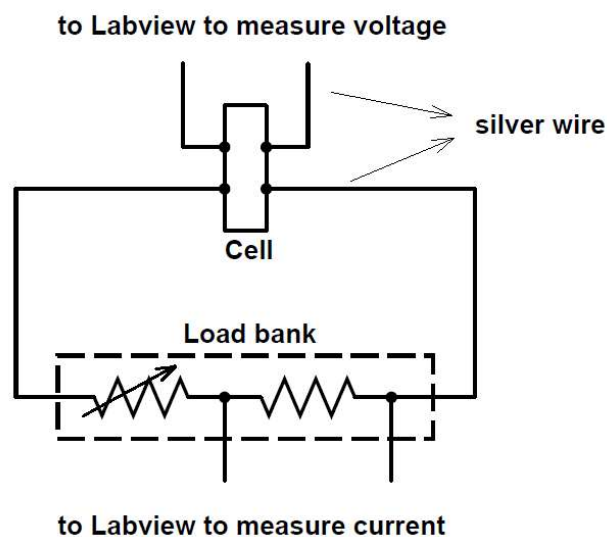


Figure 5.11: Schematic of load bank

The load bank consists of 12 separate resistors. Each resistor can be by-passed by a separate switch. Once a resistor is by-passed the total resistance decreases which results in higher currents drawn from the cell. The front and back views of the load bank have been shown in figure 5.12.

The lower limit of the load bank (minimum resistance) is 0.25 ohm which includes the resistance of the connecting copper wires, contact resistance of switches (all resistors by-passed) and constant resistor. The smallest resistor mounted on load bank is 0.01 ohm, thus the total resistance can be changed in steps of 0.01 ohm.

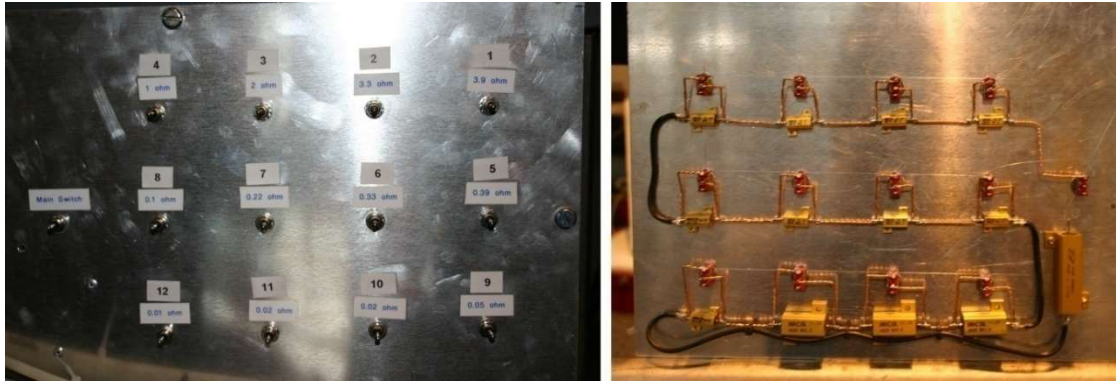


Figure 5.12: Front (left) and back (right) views of load bank

### 5.1.7 Water trap

As a result of the cell reaction (i.e. hydrogen oxidation) the water content of the outlet stream tends to increase. Once coming out of the furnace, the outlet flow including product of the reaction (water), untreated fuel and inert gas (if any) tends to cool down, which can result in vapor condensation. The water condensed in the tubes can be built up over time and block the passage. The blockage of the tubes can in turn lead to the pressure increase in the manifold causing fuel leakage or cell cracking. In order to prevent vapor condensation the outlet flow is passed through a water trap and then directed to the vent through tilted tubes. As a result of this arrangement the condensed water will accumulate in the water trap placed at the lowest level compared to other components of the test rig.

### 5.1.8 Controlling and data logging system

The operating conditions of the test rig are set by a controlling/logging system which controls and monitors the performance of the cell. This system consists of a PC, LabVIEW software, interface and a set of actuators and sensors (e.g. flow controllers and thermocouples). Through LabVIEW software the flow rate of the gases as well as the mode of air actuators are controlled. Furthermore, the voltage and current of the cell along with the temperature of the furnace are monitored and recorded during the tests. The temperature of the furnace and the temperature ramp are set through the furnace control box. The list of control and monitor devices has been summarized in table 5.2.

CONTROL		MONITOR	
Parameter	Device	Parameter	Device
operating mode	LabVIEW	float switch alarm	LabVIEW
fuel flow rate	LabVIEW		
Air actuators	LabVIEW	voltage	LabVIEW
data logging frequency	LabVIEW	current	LabVIEW
furnace temperature	control box	current density	LabVIEW
furnace ramp	control box	furnace temperature	LabVIEW & control box
external resistance	load bank		
ball valves	gas panel	humidifier temperature	humidifier controller
pressure	gas panel		
humidifier temperature	humidifier controller		

**Table 5.2: Summary of control & monitor devices**

The LabVIEW code has two separate functioning modes: operation and manual. Once the operation mode is selected all air actuators are set to the operational mode i.e. the vent line closes and the gas line opens to let the gas enter the humidifier. In this mode the setting of the air actuators cannot be changed while running. However, in the manual mode all the air actuators can be re-set by the operator during the operation of the test rig.

In order to record the temperature, voltage, current, time etc. an array holds the latest values repetitively using the recursive nature of the code. This matrix is built and initialized once the code starts and saves the most recent values during the operation. The front panel of the LabVIEW code has been illustrated in figure 5.13. Figure 5.14 and figure 5.15 show parts of the block diagram.

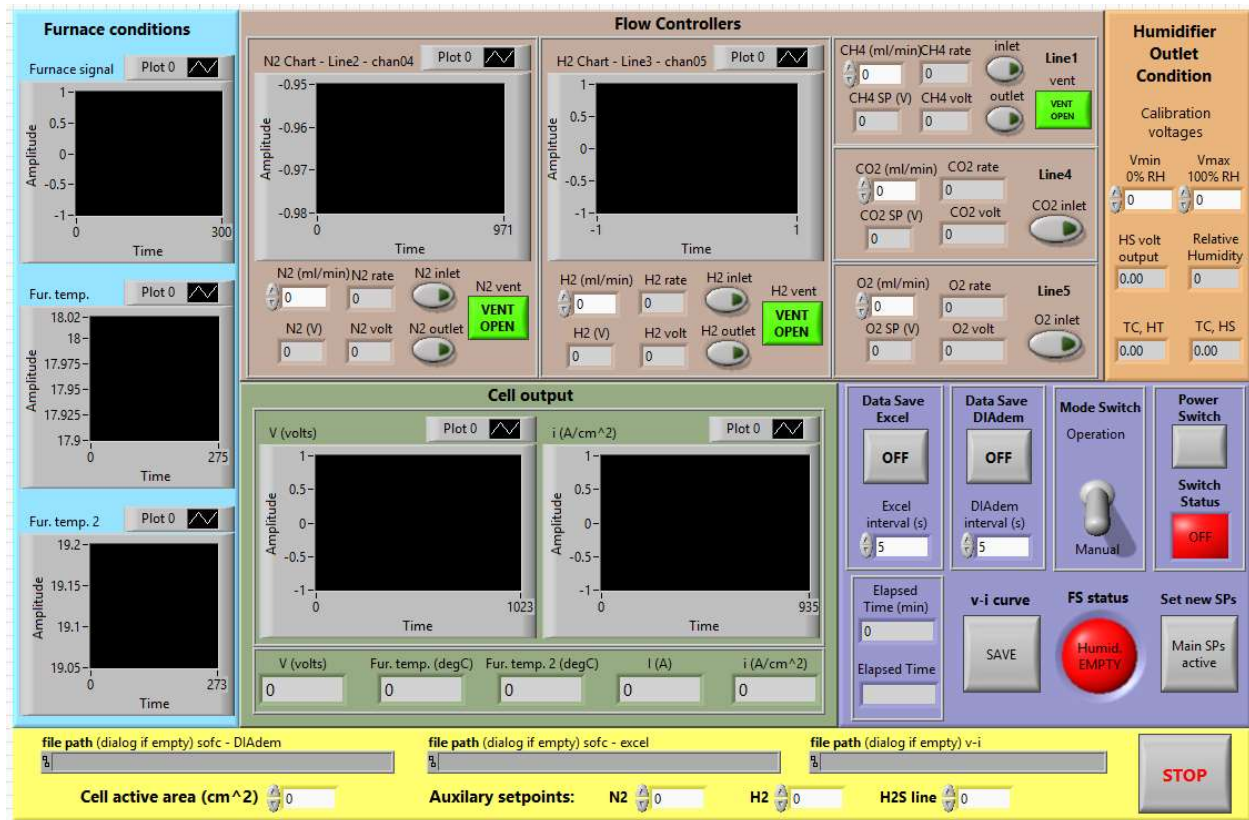


Figure 5.13: LabVIEW code front panel

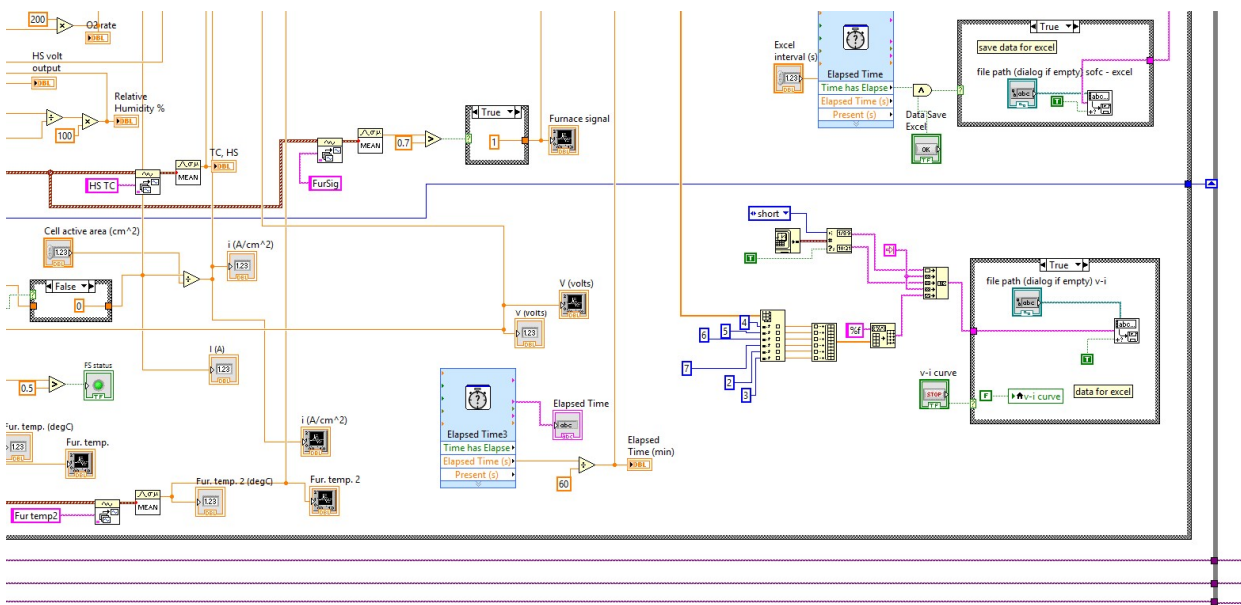


Figure 5.14: LabVIEW code block diagram-part 1

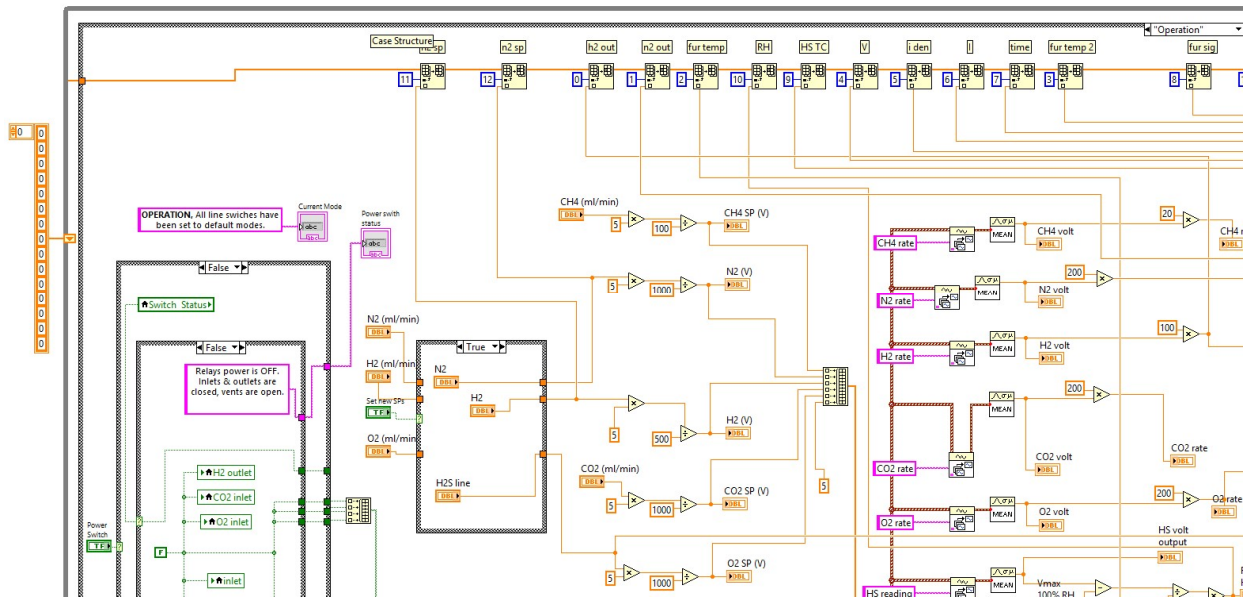


Figure 5.15: LabVIEW code block diagram-part 2

### 5.1.9 Recording the v-i curve

As mentioned previously, the current and voltage of the cell are varied by changing the external resistance of the load bank; therefore there will be a jump in the current and voltage. The value of the jump is imposed by the change in resistance i.e. the larger the change in resistance the larger the jump in current and voltage. The maximum and minimum resistances of the load bank are 11.96 and 0.25  $\Omega$ , respectively.

Once all resistors are by-passed the external resistance drops to its minimum value. However, this value may be still too large which prevents drawing design currents from the cell. Considering Ohm's law ( $I = V/R$ ), in order to draw large current either the resistance should be small or the voltage should be relatively large. For the reason that the external resistance cannot reach very small values due to the resistance of the silver mesh, wires, switches and constant resistor, the current may only be increased by increasing voltage. In order to achieve the purpose a direct current (DC) power supply is connected to the cell in series to increase the total voltage across the circuit. The DC power supply is transparent to the current and added to the circuit to only increase the overall voltage across the load bank. This implies that the current drawn from the cell is not imposed by the power supply, but the external load bank. With this arrangement it will be possible to adjust the current flowing through the cell by changing either the resistance of the load bank or the voltage of the power supply. Figure 5.16 illustrates the schematic of the v-i

measurement circuit. The v-i curve taken at 700 °C using the DC power supply is compared to the v-i curve taken without the power supply later in figure 5.32. This arrangement was used by Rolls-Royce Fuel cell Systems limited and proved to be serving the purpose [152].

It must be noted that the abovementioned set up is only used for the tests presented in this chapter i.e. cells 01 to 08. For the later tests including installation of the commercial set up, base line and contamination tests (cells 9 to 16), the current is imposed by a potentiostat. The results of the latter are presented in the commercial set up, results and discussion chapters (chapter 6, 7 and 8).

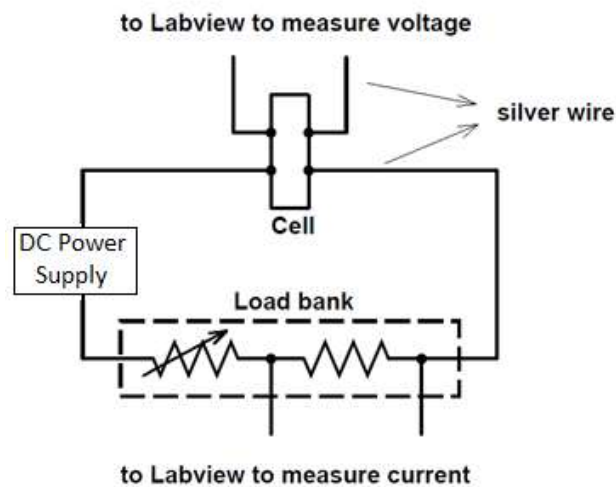


Figure 5.16: Schematic of v-i measurement circuit

## 5.2 Results

As explained in the previous sections all the cells used in the test rig are planar anode supported which are mounted on a stainless steel housing functioning as a gas delivery manifold. The cells are sealed to the manifold using high temperature SOFC sealing paste [153]. In order to prevent the direct connection of the cell (or lead wires) to the manifold which can cause a short circuit, a layer of mica paper is placed between the cell and manifold. First, the mica paper is attached to the manifold, then the cell is mounted and sealed. Figure 5.17 shows the cell/current collectors/manifold assembly. The complete preparation procedure can be found in the appendix.

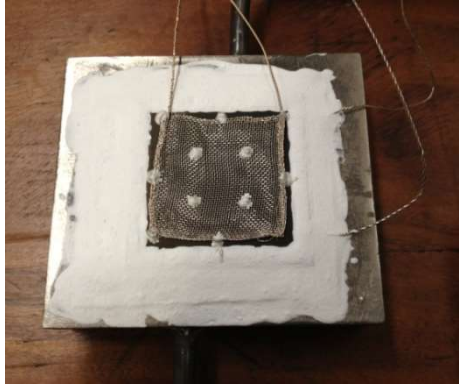


Figure 5.17: Cell/current collector/manifold assembly

A thermocouple positioned about 1 to 2 mm away from the surface of the cell measures the temperature and controls the furnace. The lead wires connected to each electrode are passed through a separate ceramic tube to avoid any connection between the wires and stainless steel tubes. The configuration of the cell inside the furnace has been demonstrated in figure 5.18.



Figure 5.18: Configuration of cell inside furnace

### 5.2.1 Cell 01

The first test was carried out to investigate the performance of the test rig and cell. The data obtained from this test was used as a baseline to which the results of the contaminated fuel tests are compared. The composition of the fuel is 14.5 %  $H_2$ /82.5 %  $N_2$ /3 %  $H_2O$  (volume) which represent the typical composition of biomass-derived syngas. In the early stages of the operation a humidified mixture of  $H_2$  (35 ml/min) and  $N_2$  (100 ml/min) is delivered to the cell to reduce the anode. The anode gas is bubbled through the humidifier being set to room temperature to yield 3 %  $H_2O$  at the exit. Since the focus of the research is on the poisoning effect

of H<sub>2</sub>S on the performance of the cell, other constituents of biomass-derived syngas such as CO and CO<sub>2</sub> have been replaced by N<sub>2</sub>. The characteristics of the baseline test are summarized in table 5.3.

Heating rate	Cooling rate	Set point	N <sub>2</sub> flow rate - Heating & cooling	H <sub>2</sub> flow rate - Heating & cooling	N <sub>2</sub> flow rate – Operation	H <sub>2</sub> flow rate - Operation
4 °C/min	3 °C/min	600 °C	35 ml/min	100 ml/min	100 ml/min	566.67 ml/min

**Table 5.3: Characteristics of the first test**

Figure 5.19 illustrates the profiles of the temperature and corresponding voltage (OCV) during the first test. The voltage fluctuations at the temperatures between 230 and 430 °C (with a local peak at 362 °C), starting after 40 minutes of the test, can be attributed to the reduction of NiO to Ni. As a result of the anode reduction water is generated which tends to decrease the OCV since the partial pressure of H<sub>2</sub>O appears as the denominator of the partial pressure fraction in the Nernst voltage (equation 1.7). After completion of the anode reduction the OCV rises sharply with temperature up to 500 °C. It is known that the change in the Gibbs free energy and thus the Nernst voltage decrease with temperature. However, the electrolyte becomes more active as the temperature rises, therefore there will be a compromise between the activation of the electrolyte and the change in Gibbs free energy. The OCV reaches the maximum value at 500 °C and above that tends to decrease as seen in figure 5.19. Once the temperature reached the set point the fuel composition was set to 100 ml/min of H<sub>2</sub> and 566.67 ml/min of N<sub>2</sub> as can be seen in figure 5.20.

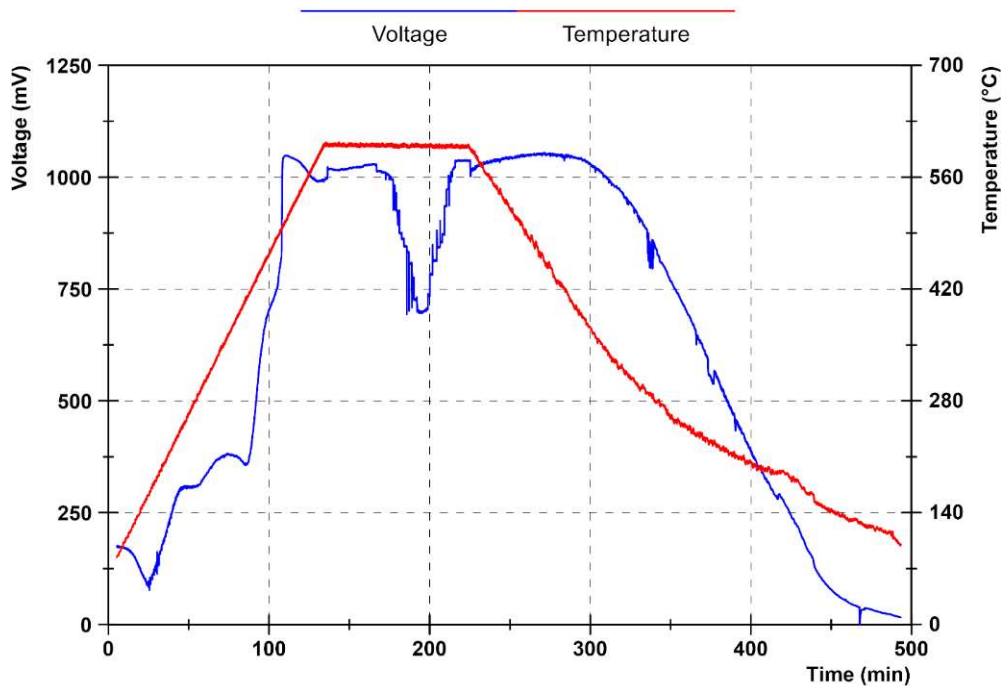


Figure 5.19: Voltage and temperature against time – cell 01

Once the flow rate of the anode gas was increased and set to the operating composition (at  $t=136$  min) a slight rise in voltage (about 20 mV) was observed increasing the OCV from 998 mV to 1018 mV. Upon decreasing the flow rates of  $H_2$  and  $N_2$  to the cooling rates the voltage dropped by 35 mV. These changes in voltage of the cell can be ascribed to the leakage of fuel gas as well as the pressure change. In case of a gas leak, increasing the flow rate of  $H_2$  can compensate for the fuel escaping from the gas delivery manifold. Also, increasing the flow rate of the fuel can lead to a rise in the pressure of manifold, due to the back pressure generated in the pipework to the exhaust which in turn increases the partial pressure of the gas and Nernst voltage.

The change in the cell voltage in the middle of the graphs at around 200 minutes is due to taking  $v-i$  and reverse  $v-i$  curves. Figure 5.21 illustrates  $v-i$ , reverse  $v-i$  and power curves at  $600^\circ C$ . Although both graphs are quite similar the reverse curve shows slightly better performance meaning that the cell had not reached a stabilized operating condition at the current steps. This can also be seen in figure 5.20 as the OCV slightly increased before drawing current from the cell. Once the flow rates are raised to the operating conditions the OCV sharply increased to 1018 mV and then slowly reached 1028 mV. After taking  $v-i$  and reverse  $v-i$  curves (setting current back to 0) the voltage went up to 1036 mV and remained constant afterwards, thus it can be said that the cell has been stabilised.

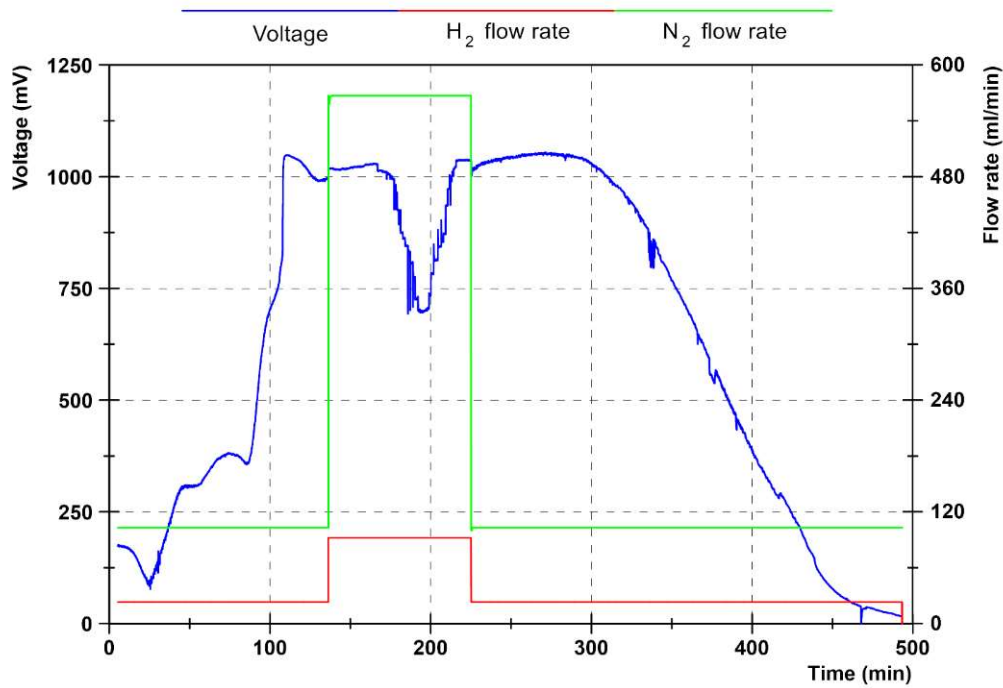
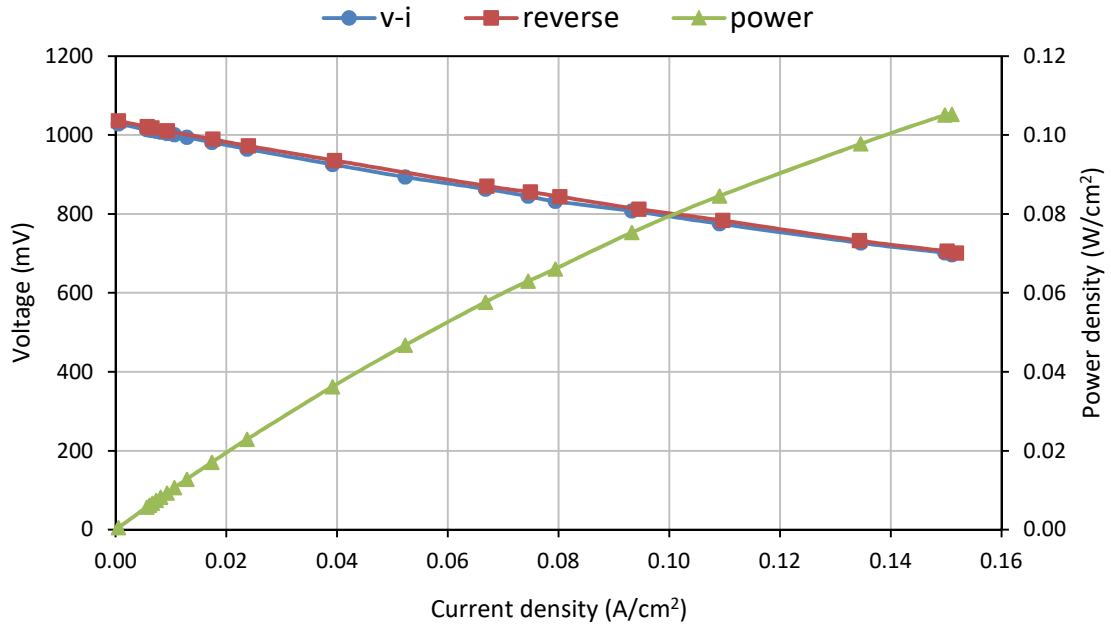


Figure 5.20: Voltage and fuel flow rate – cell 01

The highest current drawn from the cell was  $151.8 \text{ mA/cm}^2$  corresponding to  $2.27 \text{ A}$ . Owing to the large resistance of the circuit including silver meshes, lead wires and switches on the load bank it was not possible to draw higher currents from the cell. Therefore, the test was stopped and the furnace was cooled down to the room temperature at the rate of  $3 \text{ }^\circ\text{C/min}$ . In order to compensate for the large resistance of the circuit, for later experiments a DC power supply was connected to the cell in series to increase the total voltage across the load bank, hence the current passing through the cell.



**Figure 5.21: Characteristic curves - first test**

Once the furnace was cooled down it was seen that a few cracks had been developed in the cell. Also, the sealant had cracked and been detached from the manifold as illustrated in figure 5.22. In case there was a major leak or delamination of the sealant while at the operating temperature it should have been noticed by the unstable performance of the cell. Since the performance was stable and the value of OCV was close to the theoretical value it is believed that the cracks and delamination occurred during the cooling down period.



**Figure 5.22: Cell assembly after cooling – cell 01**

The cell used in the first test was resealed to the manifold and a second test was carried out afterwards. All the operating conditions remained the same as the first

test except for the heating and cooling rates being set to 3 and 2 °C/min, respectively.

Figure 5.23 demonstrates the profiles of the voltage and temperature for the second test of cell 01. The profiles of voltage and flow rates of hydrogen and nitrogen are shown in figure 5.24. It can be seen that the voltage was fluctuating significantly during the test yielding very poor and unstable performance. This can be attributed to the cracks developed in the cell during the cooling down period of the previous test as mentioned above. For this reason the test was stopped and the furnace was cooled down. Similar to the first test the sealant was separated from the manifold and the cell was fully broken.

Cell cracking may be caused due to the oxidation of the anode. Regardless of the amount of H<sub>2</sub> delivered to the cell during the cooling down, if the sealing paste is detached from the manifold, air can pass through the gap created between sealant and manifold and reach the anode. As a result Ni will be oxidized which may be difficult to be reduced again.

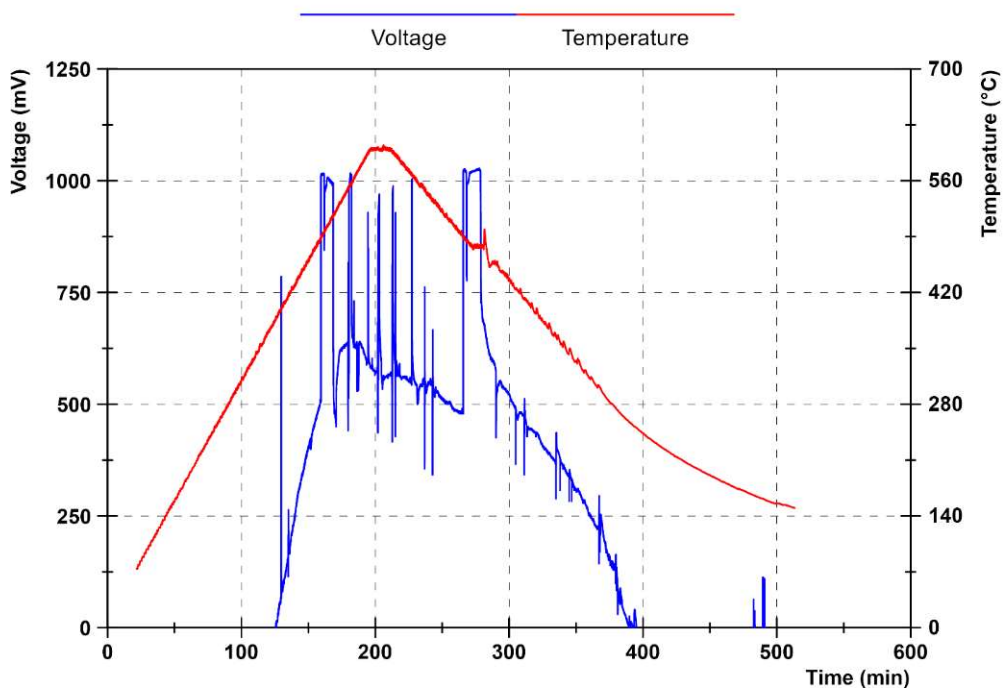


Figure 5.23: Voltage and temperature against time – cell 01 run 2

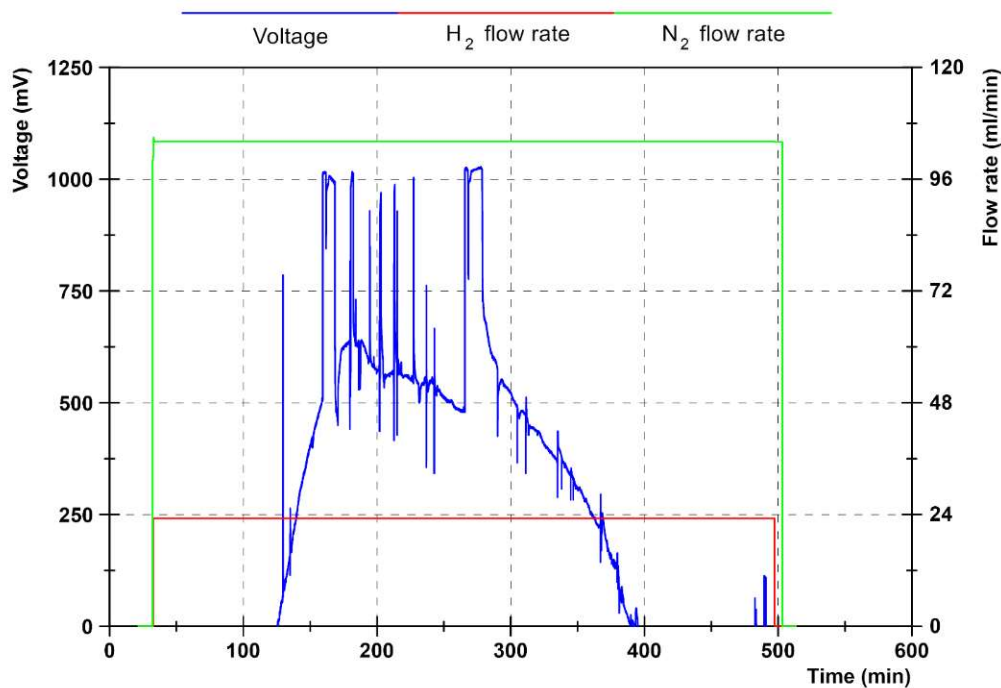


Figure 5.24: Voltage and flow rates against time - cell 01 run 2

The next experiment was performed with a new cell. The cell assembly was prepared in the same way as the previous test. During the preparation, after firing the sealing paste in the furnace, a few cracks were observed in the sealant and cell. This issue was thought to be due to the CTE mismatch between the manifold, sealant and cell, as well as the non-uniform heating owing to the different absorption rates. In order to evaluate this argument a simple experiment was designed and carried out; two identical samples, consisting of a small piece of mica paper sealed to a metal piece and a droplet of the paste spread over the metal piece, were prepared and placed in the furnace. One of the samples was covered with a cap to reduce the impact of radiative heating and the other was left bare. Both samples were heated up to 260 °C which is the advised temperature to fire the sealant for the best performance.

In accordance with figure 5.25 the sample fired without the cap of mica paper has generated more cracks compared with the one with the cap. Based on the results of this experience a ceramic box was built around the cell inside the furnace which buffers out the radiant heat as the furnace elements switch in and out. Figure 5.26 illustrates the ceramic cap under which the cell assembly is mounted. There are two thin holes on the top wall of the cap through which the thermocouples are passed to measure and control the temperature.

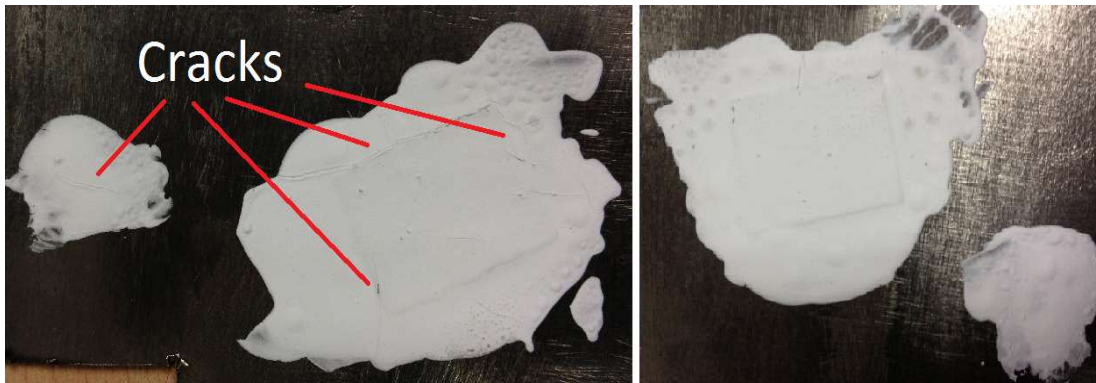


Figure 5.25: Samples: without cap (left), with cap (right)

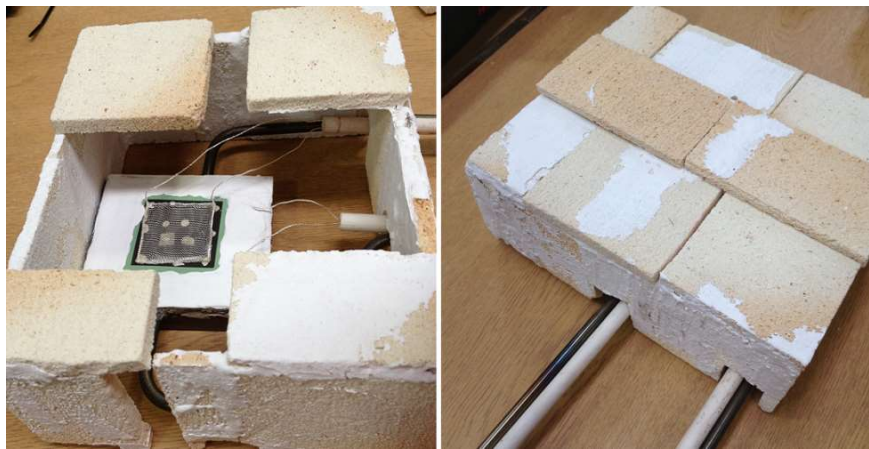


Figure 5.26: Ceramic cap

### 5.2.2 Cell 02

The experiment with the second cell (cell 02) was carried out with the ceramic cap and DC power supply in series to the load bank. The assembly of the cell, mesh and manifold was prepared using the same procedure as the previous test (cell 01). This test consists of several stages summarized in table 5.4.

The composition of the fuel was 35 ml/min of  $H_2$ , 100 ml/min of  $N_2$  and 3 %  $H_2O$  (by volume) during the first heating up and final cooling down stages, and 100 ml/min of  $H_2$  and 566.67 ml/min of  $N_2$  corresponding to 14.5 %  $H_2$ , 82.5 %  $N_2$  and 3 %  $H_2O$  (by volume) during other stages of the test. The latter will hereafter be cited as the normal operating composition within the text.

Step	Action	Condition
1	Heating up to 600 °C	@ 1 °C/min
2	v-i and reverse v-i curves	@ 600 °C & low flow rate
3	v-i and reverse v-i curves	@ 600 °C & normal flow rate
4	Heating up to 700 °C	@ 1 °C/min
5	v-i and reverse v-i curves	@ 700 °C
6	Cooling down to 600 °C	@ 1 °C/min
7	v-i and reverse v-i curves	@ 600 °C
8	Heating up to 700 °C	@ 1 °C/min
9	v-i and reverse v-i curves	@ 700 °C
10	Durability test (taking v-i curve at intervals of 5 hours)	40 hours @ 700 °C and 200 mA/cm <sup>2</sup>
11	Cooling down to room temperature	@ 1 °C/min

**Table 5.4: Test plan of second cell**

The profiles of the voltage/temperature and voltage/flow rates during the test are illustrated in figure 5.27 and figure 5.28, respectively. Similar to the first test the fluctuations in OCV taking place after about 350 minutes can be ascribed to the reduction of NiO. The peak observed at 352 °C suggested that the reduction of the anode commenced slightly prior to that temperature. Incidentally, this result is in agreement with those of the experimental investigation of NiO-YSZ reduction [62]. After completion of the NiO reduction the OCV increased sharply and reached the maximum value (1026 mV) at 520 °C, then slightly decreased due to the further increase in the temperature, as expected.

It should be noted that the reading of the v-i curves is responsible for the spikes in the voltage-time figures, as at 1500 min in figure 5.27 for instance.

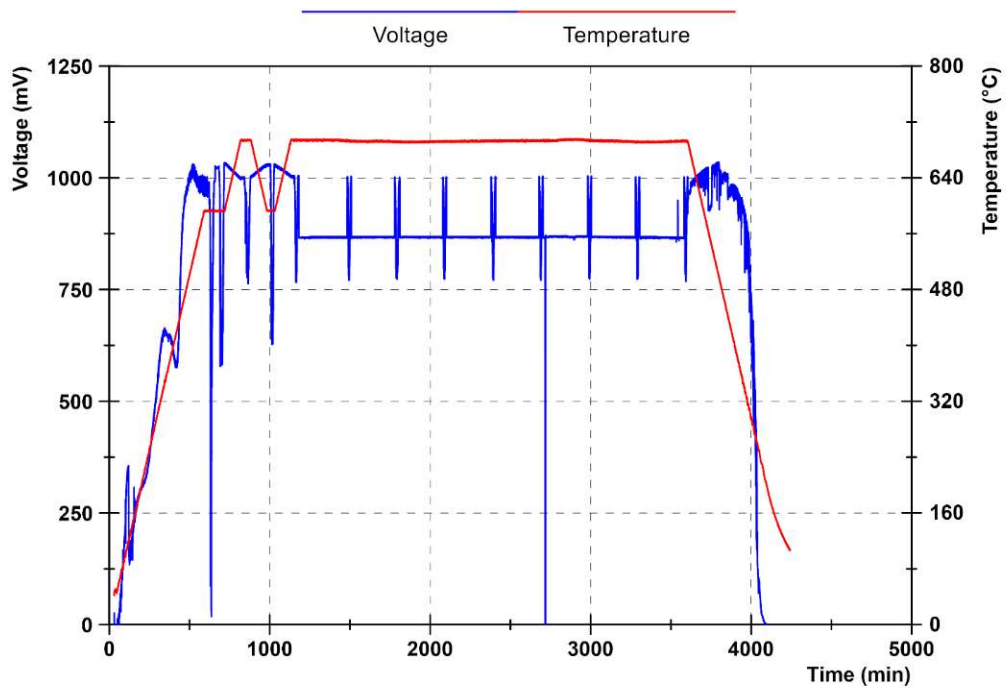


Figure 5.27: Profiles of voltage and temperature against time – cell 02

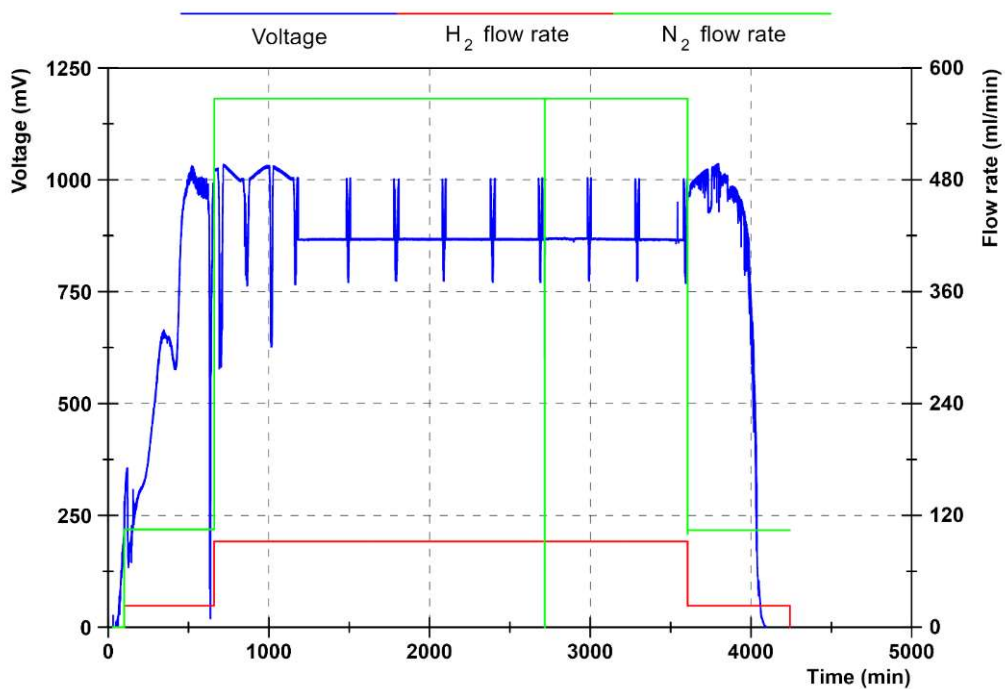


Figure 5.28: Profiles of voltage and fuel flow rate against time – cell 02

Figure 5.29 shows the initial characteristic curves of the cell. The first v-i curve, referred to as low flow rate curve, was taken after 20 minutes of stabilization at the first set point (600 °C) with the same fuel composition as the heating period. Subsequently, the flow rate of the anode gas was adjusted according to the normal

operating composition and the next characteristic curve was taken. The obtained curve has been named 600 °C/1st v-i curve. In order to compare the performance of the cell operating at different temperatures, the next characteristic curve was obtained at 700 °C and named 700 °C/1st v-i curve.

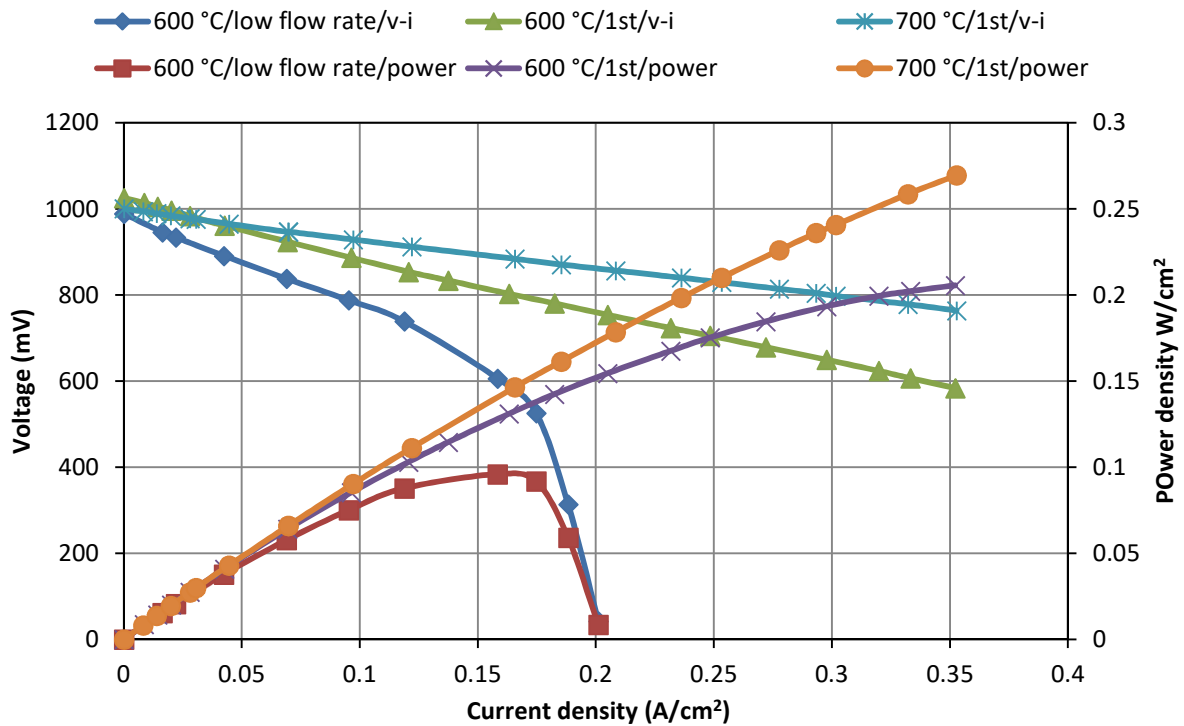


Figure 5.29: Initial characteristic curves – cell 02

As has been demonstrated in the figure, the performance of the cell operating at the low flow rate is poorer than that of the normal operating composition. The drastic decline in the voltage starting at around 150 mA/cm<sup>2</sup> can be attributed to the concentration losses which are dominant at high fuel utilisation. As a result of the small flow rate of H<sub>2</sub> and fairly large current drawn from the cell the fuel utilisation rises which in turn increases the concentration losses yielding lower power.

Moreover, it can be seen that the v-i graph of the cell running on the normal operating composition is linear within the range of the tested current densities. This implies that the only effective overpotential is the ohmic polarization. Theoretically, an increase in the operating temperature should decrease the ohmic resistance of the cell resulting in a higher power density. Figure 5.29 shows that the cell has demonstrated better performance at 700 °C, although the OCV has slightly decreased.

At the following stage of the test the set point was set to 600 °C and another v-i curve was taken. Then, it was increased to 700 °C to take the second characteristic curve at this temperature. All curves have been taken after 20 minutes of stabilisation at the corresponding set point. Figure 5.30 demonstrates the first and second characteristic curves taken at both set points. Comparing the curves confirms that the cell did not stabilize until the time at which the second curve at 700 °C was taken.

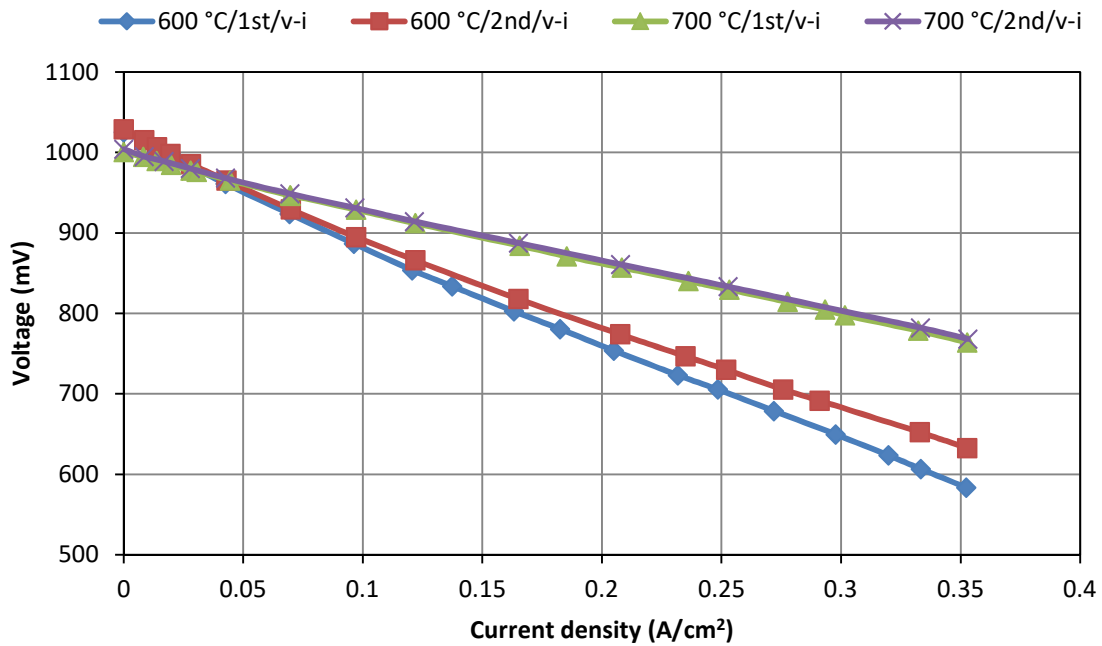


Figure 5.30: First and second characteristic curves – cell 02

Once the second curve at 700 °C was obtained the cell was loaded for a durability test. The durability test was carried out at 200 mA/cm<sup>2</sup> and 700 °C and lasted 40 hours. The initial voltage of the cell at these conditions was 868 mV. The characteristic curves were taken every 5 hours during the durability period. The performance of the cell during the test was stable as seen from figure 5.27. The abrupt drop in the voltage observed at time=2715 min is associated with N<sub>2</sub> bottle change. Due to the cylinder change the flow of N<sub>2</sub> was stopped for a very short period of time which resulted in a temporary decrease in the fuel flow rate. As a consequence, H<sub>2</sub> was not delivered to the cell and the voltage dropped significantly. Also, there is a sharp jump in the voltage at time=33542 min which is attributed to the incorrect setting of the load bank. One of the switches on the load bank was switched off by mistake which led to a decrease in resistance hence an increase in the voltage.

Figure 5.31 shows the v-i curves during the durability test. From this figure it can be stated that the cell has not undergone any significant change in the performance over the test time. Once the cell stabilized under the operating conditions (the time at which the first curve had been taken at 700 °C) the performance remained constant and stable.

The theoretical OCV of a cell operating at the normal operating composition is 1064 and 1039 mV at 600 and 700 °C, respectively. However, this cell had an OCV of 1025 mV at 600°C and 1004 mV at 700 °C remarkably lower than the theoretical values. The lower value of OCV can be attributed to the leakage of the fuel from the manifold in which case the cell is practically operating at lower flow rate of fuel yielding smaller voltage.

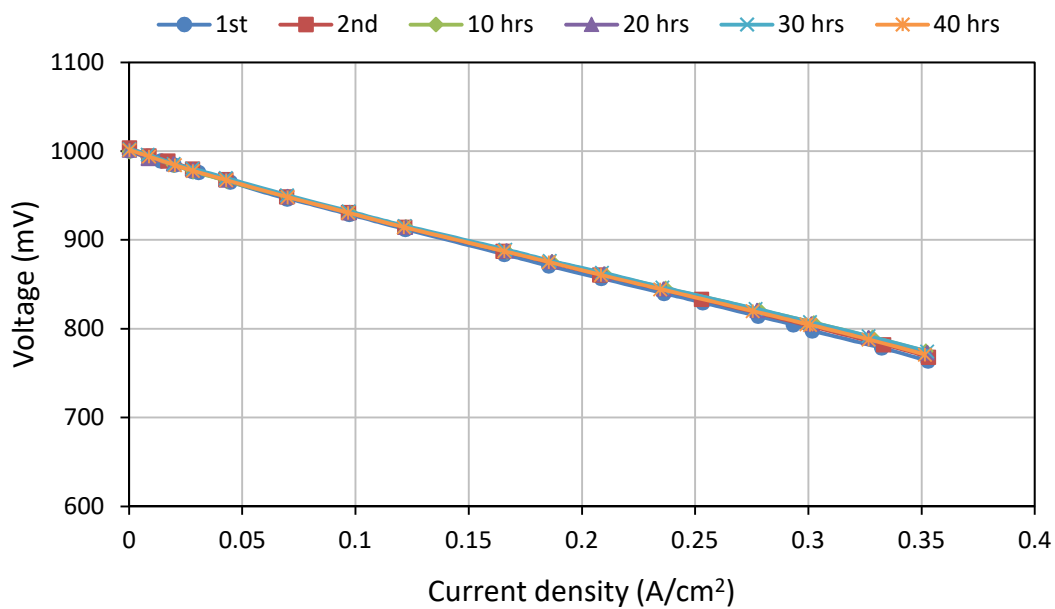


Figure 5.31: Characteristic curves during durability test at 700 °C – cell 02

In order to test the effects of the DC power supply on the performance of the cell, a test was carried out using an old cell. Figure 5.32 demonstrates the v-i curves taken with and without DC power supply at 700 °C (fuel mixture: 100 ml/min of H<sub>2</sub>, 566.67 ml/min of N<sub>2</sub>, no steam). The figure shows that adding the DC power supply in series to the cell does not affect the performance significantly, but allows larger currents to be drawn from the cell, as explained in section 5.1.1. The DC power supply is transparent to the current and tends to increase the overall voltage across the load bank, causing higher current to pass through the cell.

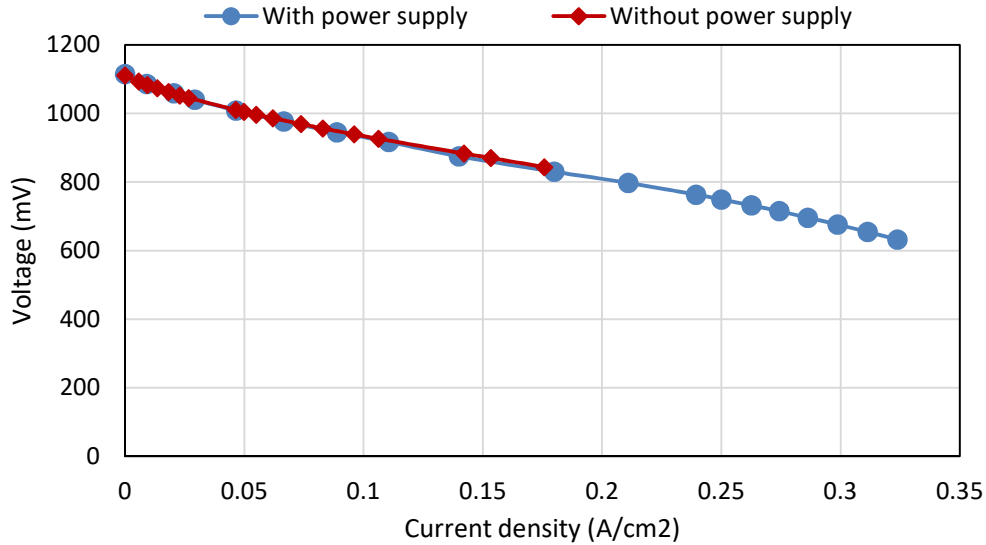


Figure 5.32: Comparison of the v-i curves taken with and without DC power supply

### 5.2.3 Cell 03

In the following test a new cell was mounted on the manifold and sealed using high temperature sealant, as explained in the previous sections. The test was performed under the same conditions as cells 01 and 02. Figure 5.33 and figure 5.34 demonstrate the profiles of voltage/temperature and voltage/flow rates against time, respectively. Looking at the figures it is comprehended that the cell did not generate voltage as the temperature increased. Once the cell was cooled down to room temperature and taken out of the furnace it was fully broken.

The unexpected behavior of the cell is ascribed to the long time between the set up preparation and start of the test. As explained before, high temperature sealing material is used to seal the cells on the manifold. Over the long period of time the seal tends to harden and becomes extremely solid. Therefore, it does not allow the cell to expand as the temperature increases resulting in cell cracking over the heating up period. The assembly of the cell 03, manifold and current collectors rested a few days before the start of the test causing the cell to break, thus resulting in test failure.

### 5.2.1 50 ppm test (cell 04)

Upon completion of the baseline test (cell 02), a contamination test was planned for 50 ppm of hydrogen sulfide. A new set of cell/current collectors/manifold was built up for this purpose and placed in the furnace. The characteristics and stages of the test are summarized in table 5.5 and table 5.6, respectively.

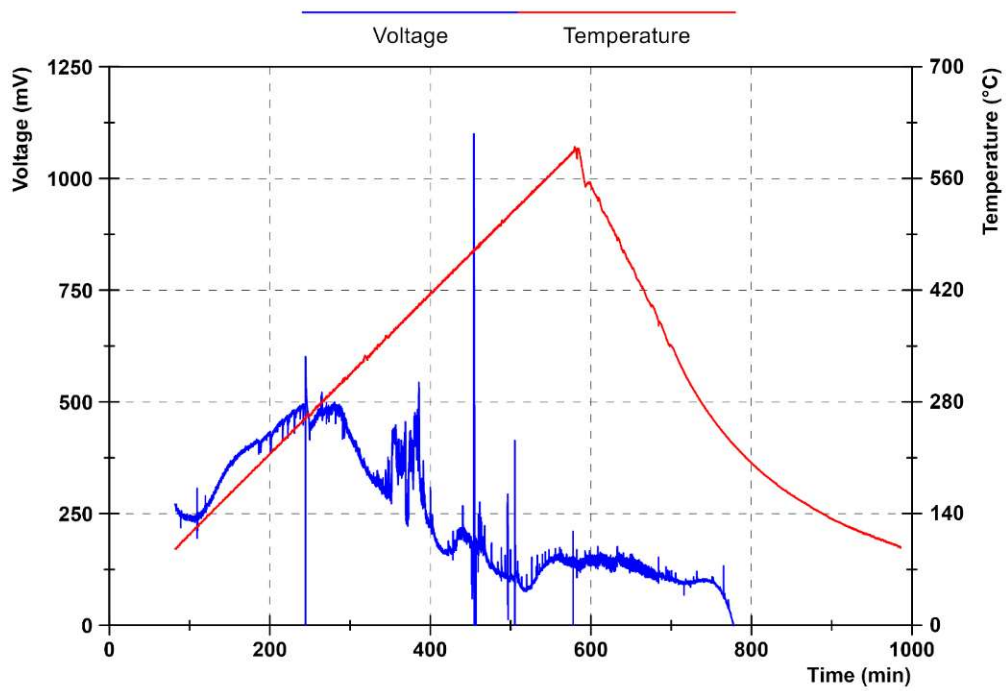


Figure 5.33: Profiles of voltage and temperature - cell 03

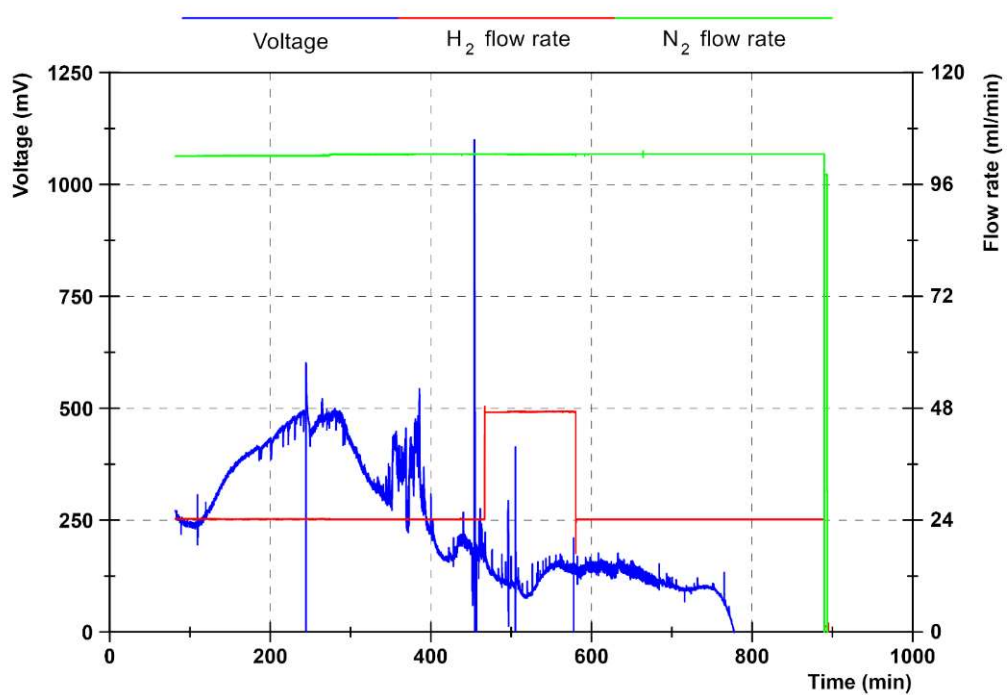


Figure 5.34: Profiles of voltage and flow rates - cell 03

Heating rate	Cooling rate	Set point	N <sub>2</sub> flow rate - Heating & cooling	H <sub>2</sub> flow rate - Heating & cooling	N <sub>2</sub> flow rate - Operation	H <sub>2</sub> flow rate - Operation
1 °C/min	3 °C/min	700 °C	35 ml/min	100 ml/min	100 ml/min	566.67 ml/min

Table 5.5: Characteristics of 50 ppm test (cell 04)

Step	Action	Condition
1	Heating up to 700 °C	@ 1 °C/min
2	v-i curve	@ 700 °C & normal flow rate
3	Running at OCV	@ 700 °C for 2:30 (hr:mm)
4	v-i curve	@ 700 °C & normal flow rate
5	Running at 0.2 A/cm <sup>2</sup>	@ 700 °C for 2:45 (hr:mm)
6	v-i curve	@ 700 °C & normal flow rate
7	Running at 0.2 A/cm <sup>2</sup>	@ 700 °C for 00:20 (hr:mm)
8	Exposure to 50 ppm of H <sub>2</sub> S	for 25:00 (hr:mm)
9	Recovery	for 25:00 (hr:mm)
10	v-i curve	@ 700 °C & normal flow rate
11	Cooling down	@ 1 °C/min

**Table 5.6: Test plan of 50 ppm test**

The composition of the fuel mixture during the contamination test was the same as that of the baseline test (normal operating composition). The H<sub>2</sub>S-contaminated fuel was prepared by blending a mixture of clean H<sub>2</sub> and N<sub>2</sub> with a pre-determined mixture of N<sub>2</sub>-H<sub>2</sub>S, referred to as carrier gas. The concentration of H<sub>2</sub>S in the carrier gas was 500 ppm. The desired composition was 100 ml/min of H<sub>2</sub>, 566.67 ml/min of N<sub>2</sub> and 50 ppm of H<sub>2</sub>S. Prior to blending with the carrier gas, the mixture of clean hydrogen and nitrogen is bubbled through the humidifier to add the desired amount of steam to the fuel.

The profiles of the voltage and temperature against time are presented in figure 5.35. The initial fluctuations of the voltage occurred at early stages of the test (between the start of the test and t=150 min) are due to the data logging system which tends to read unrepresentative values when there is no signal (voltage) from the cell. The secondary fluctuation is attributed to the reduction of NiO to Ni as described in the previous sections.

As a general trend the voltage increased with the temperature and reached a maximum at 462 °C. Beyond this temperature the OCV started to decrease slightly and fairly large fluctuations were observed.

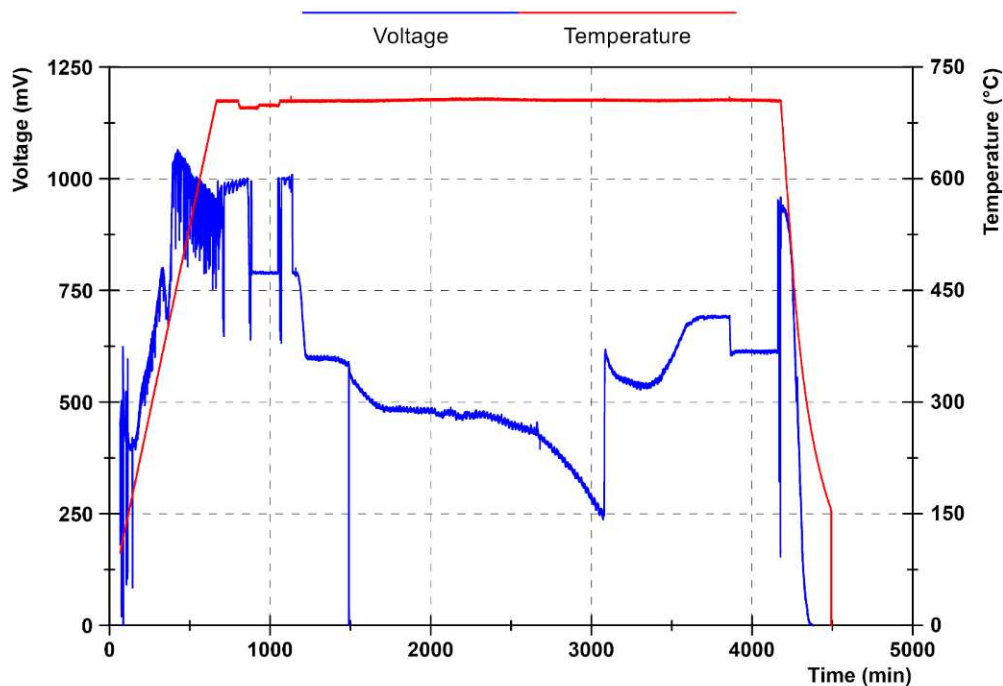


Figure 5.35: Profiles of voltage and temperature - 50 ppm test cell 04

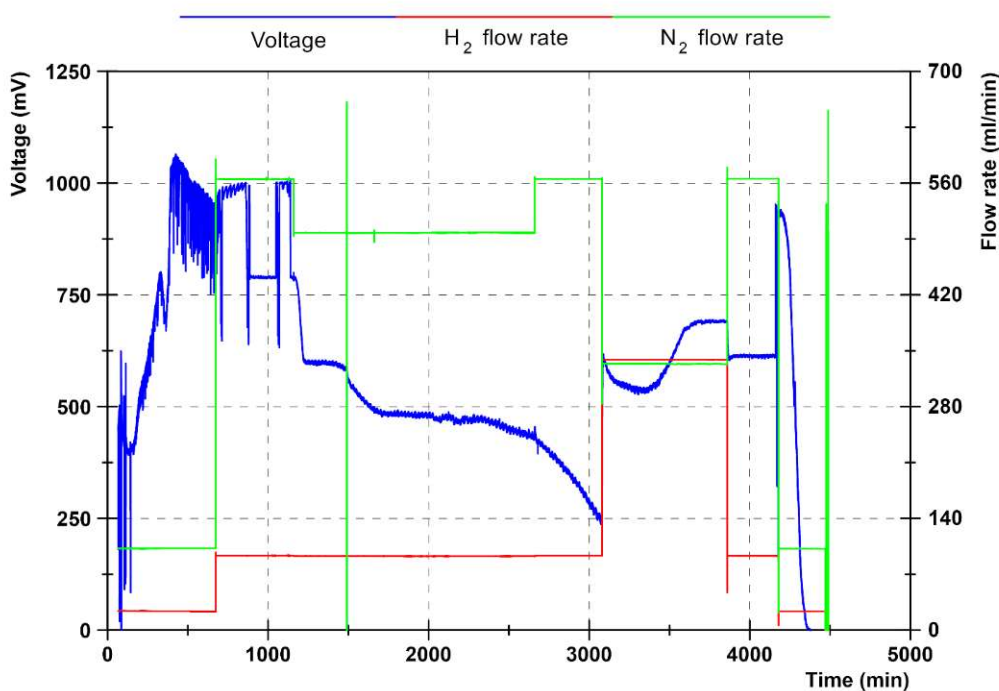
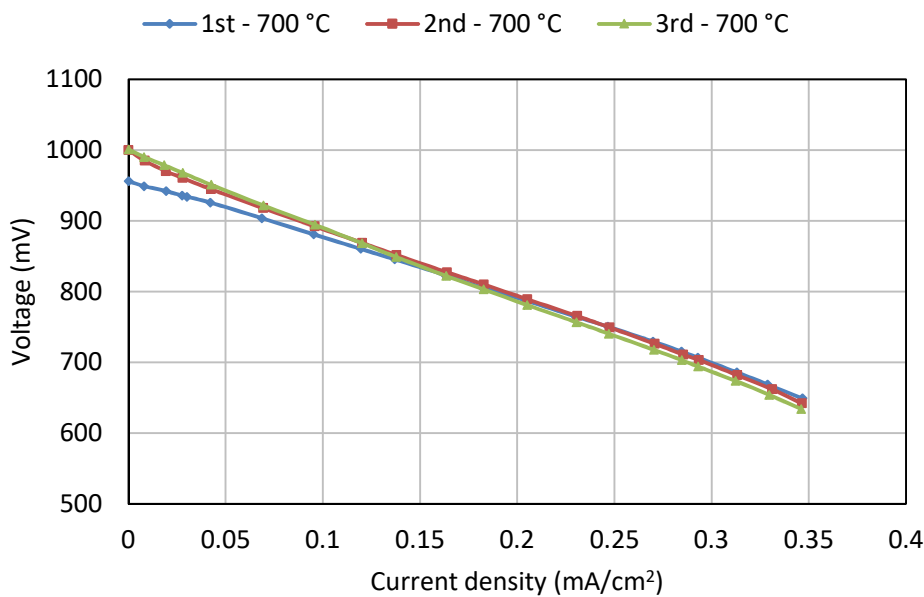


Figure 5.36: Profiles of voltage and flow rates - 50 ppm test cell 04

Figure 5.36 illustrates the profiles of voltage and flow rates against time during the 50 ppm test. As seen in the figure once the flow rates were set to the operating composition (at  $t=700$  min) the OCV slightly increased. It also decreased the amplitude of the fluctuations. These fluctuations are thought to be due to the lack

of hydrogen i.e. the cell did not receive enough fuel, leading to instabilities. In general, the OCV should be stable, however, if locally the anode is starved of hydrogen in any point of the cell, it starts to oxidize which leads to fluctuations in voltage. Based on the graphs, it can be stated that the system seems to be at borderline in sense of the fuel availability.

The OCV of the cell was about 1000 mV, 39 mV lower than the theoretical value. Similar to the test with cell 02, this difference can be due to the leakage of fuel from the manifold. This can also support the idea of the cell starvation discussed above.



**Figure 5.37: Initial characteristic curve - 50 ppm test cell 04**

Figure 5.37 shows the initial v-i curves taken at intervals of 2.5 hours, before running H<sub>2</sub>S. The first polarization curve is slightly lower than 2<sup>nd</sup> and 3<sup>rd</sup> curves at low current densities suggesting that it took a while for the cell to stabilize and reach a steady state. Also, it can be seen that 2<sup>nd</sup> and 3<sup>rd</sup> curves are fairly overlapping showing a stable performance over the test duration.

Similar to the baseline test, the cell was loaded at 0.2 A/cm<sup>2</sup> for the durability test. The corresponding voltage was 790 mV which is about 9 % lower than that of the baseline best (868 mV). Several reasons can be associated with the observed drop of performance such as any leakage in piping and sub-systems of the test rig, any cracks in the cell or sealant (which can lead to fuel leakage), poor connection of the current collecting mesh and cell and different microstructure of the cell.

H<sub>2</sub>S started running at time=1159 min and the voltage drop was initiated after 13 minutes. As can be seen in figure 5.36, the observed drop in the cell voltage can be

divided into two steps: an initial sharp drop and a secondary sluggish loss which are reasonably compatible with the mechanisms of H<sub>2</sub>S contamination stated in the literature. The initial drop lasted for about 49 minutes and was followed by a secondary drop. However, the test was interrupted due to a change in the pressure of clean N<sub>2</sub>. Once the pressure of N<sub>2</sub> dropped the flow rate and composition of the fuel started to change. As a result the cell was subjected to a new operating condition which highly affected the performance. The last voltage of the cell before interruption was 590 mV.

Considering the flow rate of the different gases and pipework design, the test interruption can be divided into 4 stages:

- Stage 0: before interruption - The cell is exposed to the normal operating composition and flow rates.
- Stage 1: due to the gas trapped in the pipework from the point that the contamination line joins the clean mixture to the manifold - The composition of the fuel is the same as stage 0 (normal operating condition before interruption), however, the flow rate is smaller since the driving force is 100 ml/min of H<sub>2</sub> and 66 ml/min of N<sub>2</sub>/H<sub>2</sub>S mixture. This is a short period due to the short length of this part of the pipework.
- Stage 2: due to the gas trapped in the humidifier - The composition of the clean mixture trapped in the humidifier will be the same as the stage 0 but the flow rate is lower; the driving force is 100 ml/min of H<sub>2</sub>. The flow rate of the contamination line is constant so the fuel mixture is composed of 100 ml/min (1/6 H<sub>2</sub> and 5/6 N<sub>2</sub>) and 66 ml/min of N<sub>2</sub>/H<sub>2</sub>S. This results in a higher concentration of H<sub>2</sub>S which will cause the test to deviate from desired conditions.
- Stage 3: Once all the gas trapped in the pipework is consumed the composition will be 100 ml/min of H<sub>2</sub> and 66 ml/min of N<sub>2</sub>/H<sub>2</sub>S. At this stage the concentration of H<sub>2</sub>S remains higher than the desired value.

As the N<sub>2</sub> pressure is restored the composition of the fuel will be the same as stage 0 and cell is exposed to the normal operating condition again. A summary of the stages of interruption has been presented in table 5.7.

Stage	Total N <sub>2</sub>	Clean N <sub>2</sub>	H <sub>2</sub>	H <sub>2</sub> S/N <sub>2</sub>	H <sub>2</sub> S ppm	Total rate	
0	566.66 (85 %)	500	100 ml/min (15 % in final mixture)	66.66	50	666.66	Normal operation composition
1	166.66x0.85 =141.66 ml/min (85 %)	-	166.66x0.15 =25 ml/min (15 % in final mixture)	66.66	50	166.66	Trapped gas in pipes just before the manifold
2	83.33+66.66 =150 ml/min	100x5/6= 83.33 %, 83.33 ml/min in clean line	100x1/6= 16.67 %, 16.67 ml/min in clean line	66.66	$\frac{500 \times 66.66}{166.66} = 199$	166.66	Trapped gas in humidifier
3	66.66	0	100 ml/min	66.66	$\frac{500 \times 66.66}{166.66} = 199$	166.66	Only H <sub>2</sub>

**Table 5.7: Summary of stages of test interruption**

The time between the start of H<sub>2</sub>S running and test interruption (N<sub>2</sub> pressure drop) was 5 hours and 31 minutes. For this period the cell operated at the desired operating conditions and the results were notable, however, owing to the deviation from the favourite settings, the results were no longer remarkable immediately after the onset of the interruption.

### 5.2.2 Tests failure (cells 05, 06 and 07)

Once the first contamination test was finished, a new cell (cell 05) was used to prepare the set up for another test. The test conditions were kept the same as the previous test (table 5.5). However, the initial v-i curves taken at 600 and 700 °C showed that the performance was very low compared with that of the previous tests. The same scenario happened for two more cells (cells 06 and 07) i.e. the v-i curves were much lower than expected. The profiles of voltage and temperature for cells 05, 06 and 07 are shown in figure 5.38, figure 5.39 and figure 5.40, respectively.

The results of these three tests were not comparable with those of the baseline (cell 02) and 50 ppm (cell 04) tests raising the problem of irreproducibility of tests. Figure 5.41 and figure 5.42 compare the v-i curves of different cells at 600 and 700 °C, respectively.

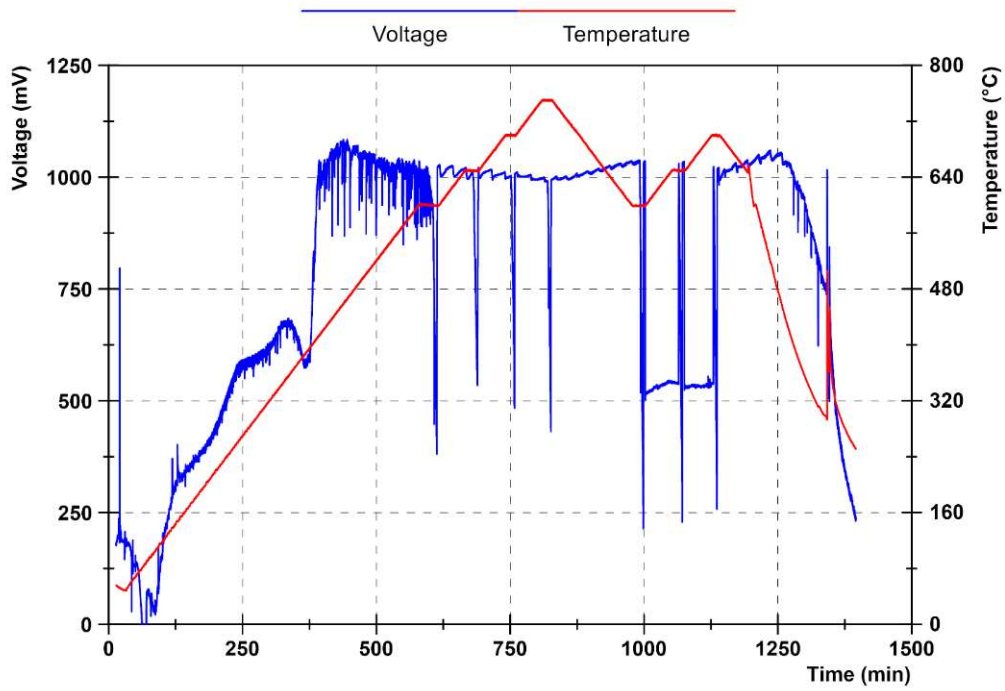


Figure 5.38: Profiles of voltage and temperature – cell 05

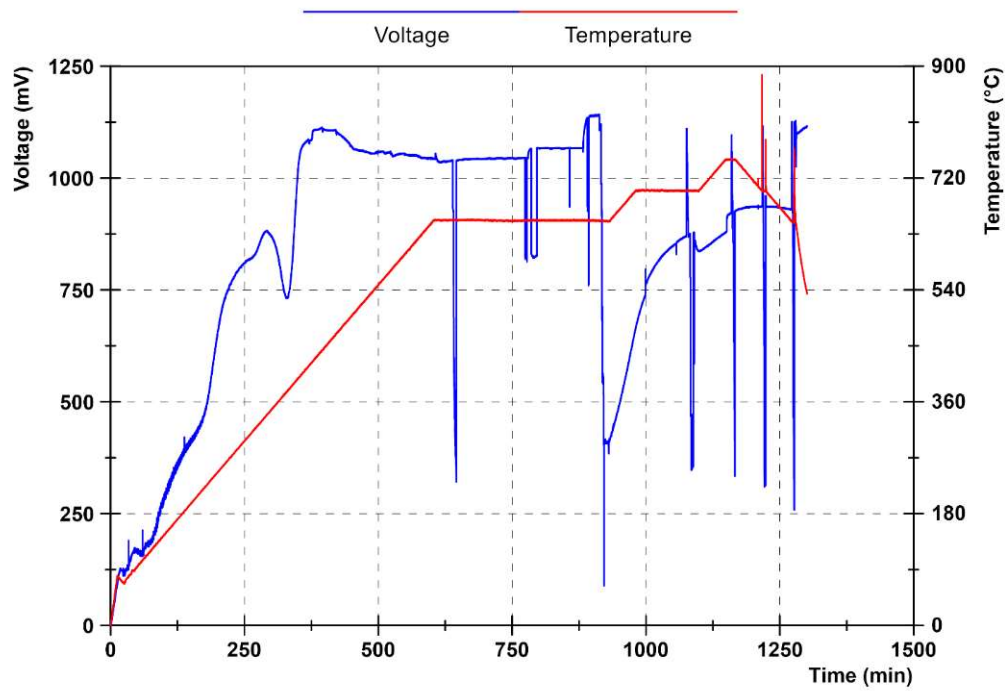


Figure 5.39: Profiles of voltage and temperature – cell 06

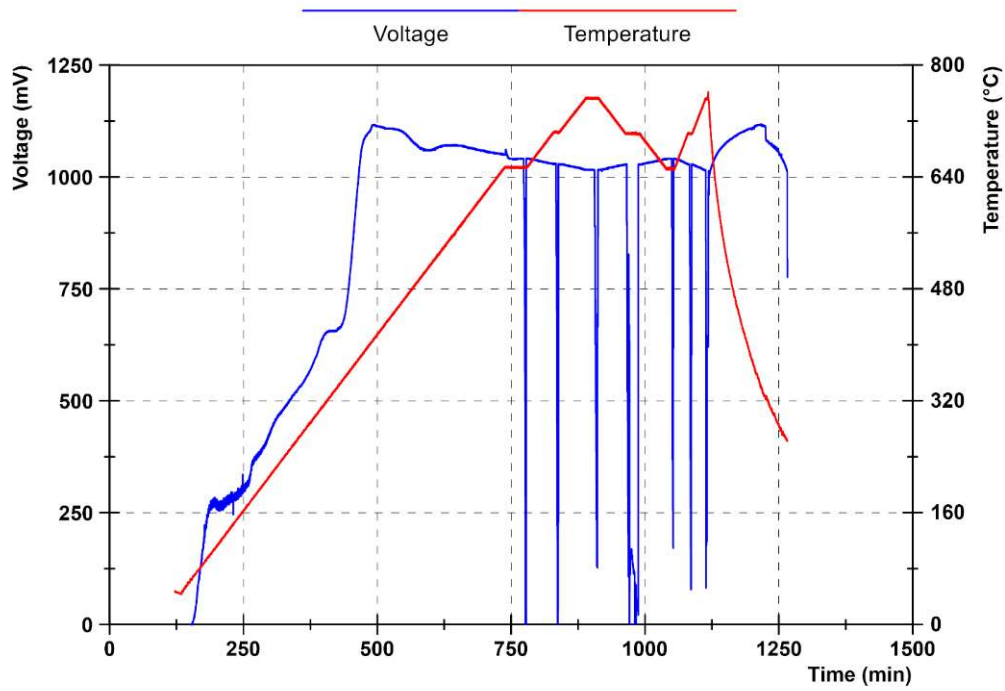


Figure 5.40: Profiles of voltage and temperature – cell 07

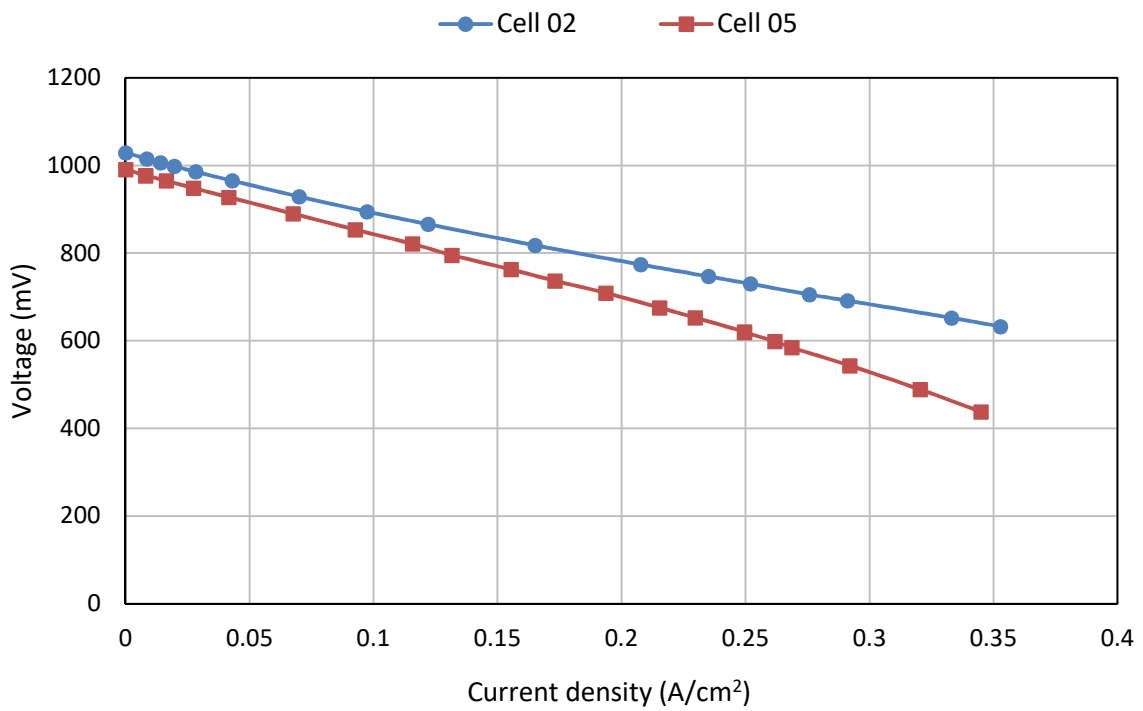


Figure 5.41: Comparison of v-i curves at 600 °C

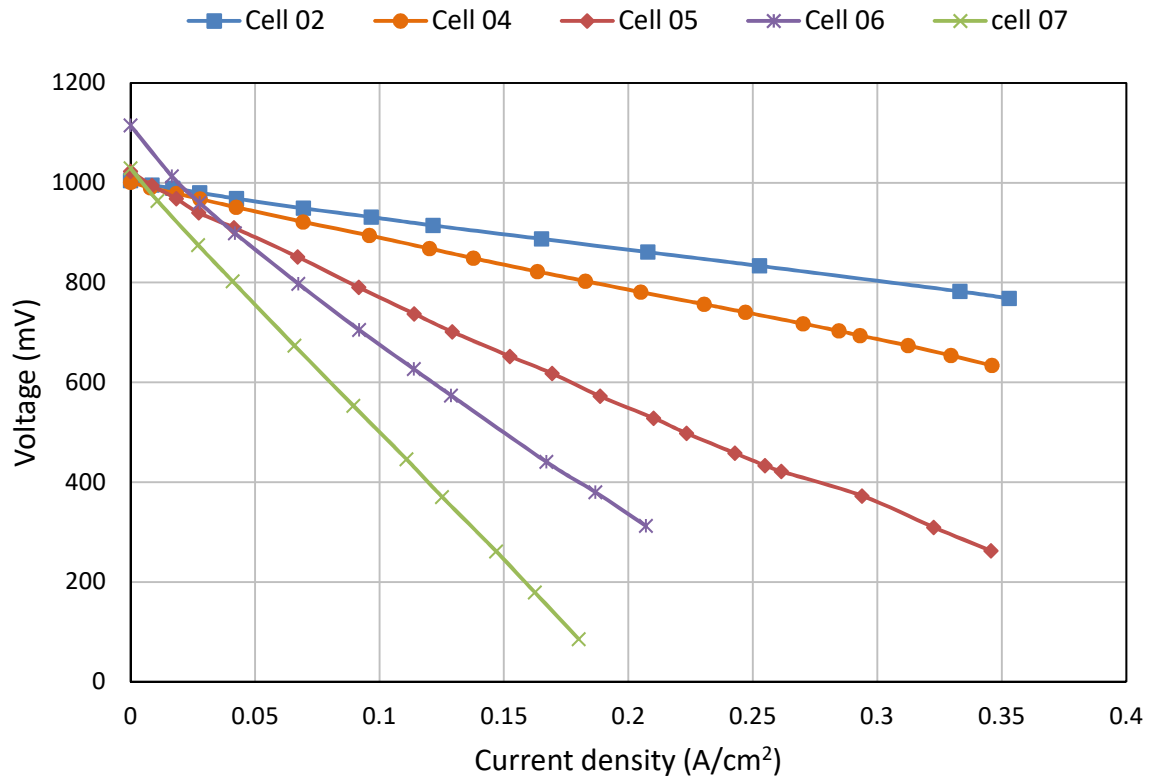


Figure 5.42: Comparison of v-i curves at 700 °C

### 5.3 Problem investigation (cell 08)

The problem, as explained above, was that the results obtained from the different tests were erratic and incomparable, i.e. the identical cells yielded different performance. Several scenarios can be considered for this issue such as cells being structurally different, dissimilar operating conditions and different assemblies of the cell/current collectors/manifold.

In order to identify the main cause of the inconsistent results, a number of meeting and discussion with the supervisory team, manufacturer of the cells and academics from other departments and universities were arranged. The outcome of the meetings was that the first and second possibilities - different cells and operating conditions - can be ruled out. All the cells were received in one batch and according to the manufacturer's statements, they were made of the same materials through the same fabrication method and procedure.

It was also stated that the operating conditions of cells were the same for all the tests as they were controlled through the same flow controllers, thermocouples and furnace. It should be noted that all the control and logging instruments were tested after the failure of the experiments and no fault was revealed.

Considering the argument above, the erratic performance of the cells was attributed to the poor assembly of cell/current collectors/manifold. This was also confirmed by the local community of researchers involved in the meetings. In the implemented assembly the current collector meshes are attached to the electrodes using silver ink. Thus, there will be a few locations at which the mesh is fully connected to the electrode and the rest of the mesh may be not in contact with the surface of the cell. As a result, the electrons involved in the electrochemical reactions will be collected only from the points with full contact. This will increase the length of the electron path (the path through which the electrons travel between the mesh and triple phase boundaries) resulting in large overpotential and low performance. As the number and size of the silver ink drops are uncontrolled variables test to test, it should perhaps be expected in hindsight that the performance test to test is dissimilar.

The outer layer of the cell at anode side is made of NiO and once exposed to hydrogen will be reduced to pure nickel which is highly conductive. This supporting layer collects the electrons all over the anode functioning layer and passes them to the mesh through the silver drops. As the electrical conductivity of pure nickel is significantly high, the electrons will easily travel to the ink drops and then to the mesh. Therefore, the poor performance can be ascribed to the cathode side.

In order to verify this argument a test was designed and carried out. The cathode current collector mesh was divided into two pieces: one covering one quarter of the cathode surface and the other covering three quarters. The larger piece was attached to the cell with a larger number of ink drops as seen in figure 5.43. The performance of the cell was measured with the one of the pieces connected at a time and also with both pieces connected simultaneously to compare the effects of the mesh size and number of the silver ink drops.

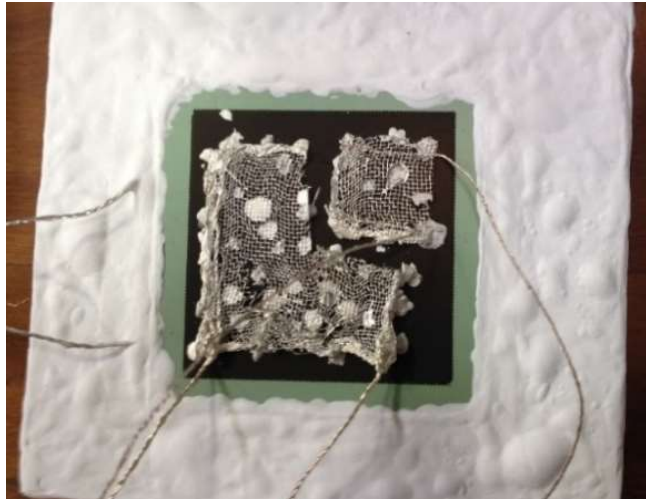


Figure 5.43: Cathode current collector

Figure 5.44 and figure 5.45 illustrate the performance of the cell at 600 and 700 °C, respectively. The graphs show that the performance of the cell is a strong function of the current collection method. The performance taken from the small mesh is much lower than that of the large mesh implying that a surprising portion of the cell voltage is lost due to the longer path for the electrons to travel.

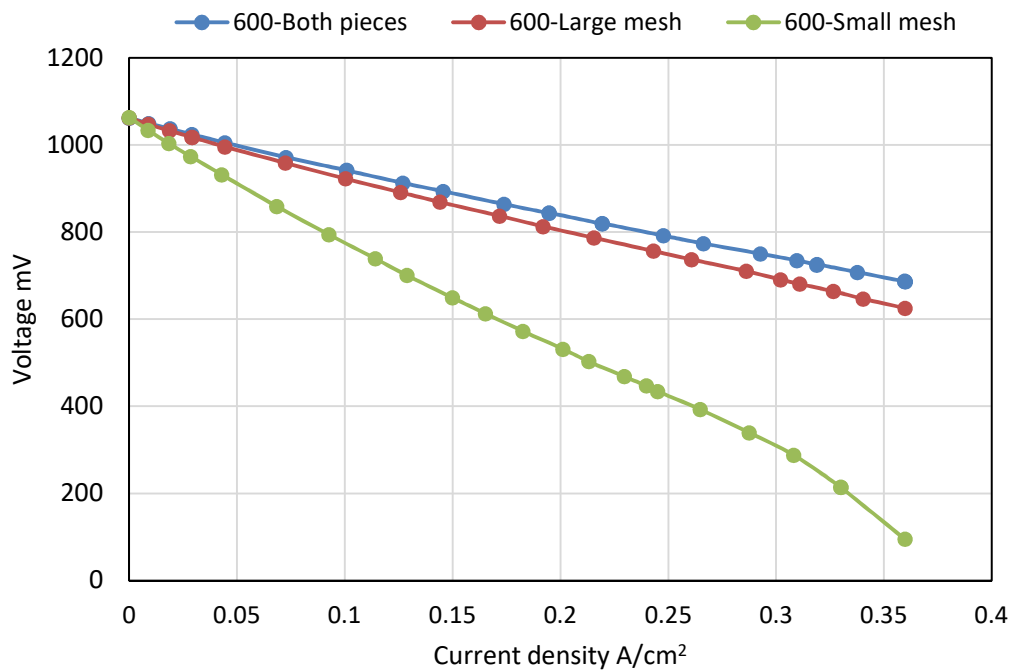


Figure 5.44: v-i curve at 600 °C – problem investigation test

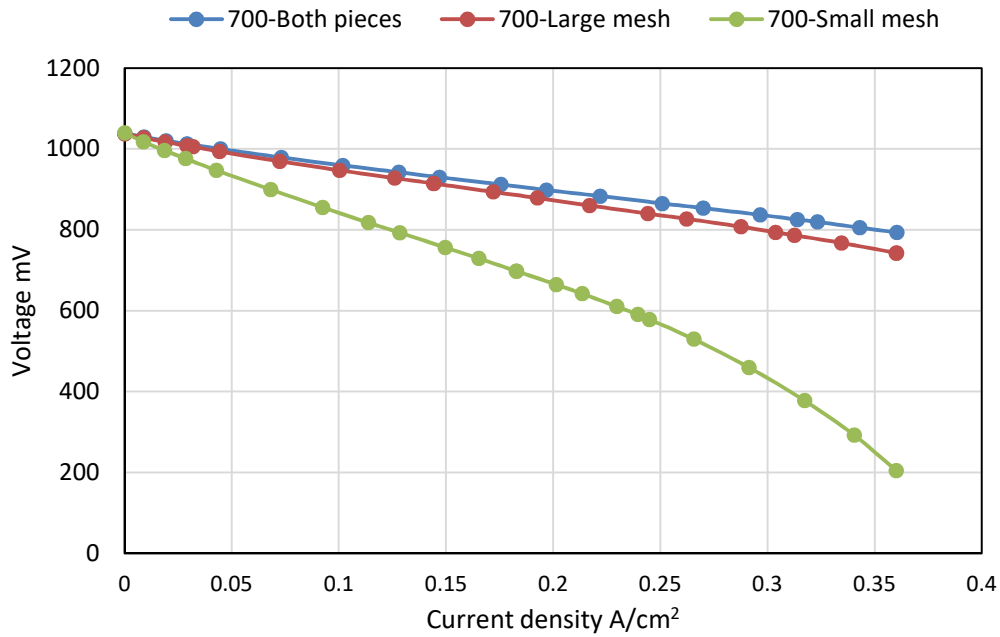


Figure 5.45: v-i curve at 700 °C – problem investigation test

The results of this test showed that the cathode current collection method plays an important role on the performance and thus should be efficient to minimize the losses. Therefore, a commercial SOFC test set up was purchased which provides a full contact between the cell and current collecting meshes using a clamping mechanism.

## 5.4 Conclusions

The results of the experiments carried out in this chapter can be summarised as:

- Time between preparation and testing has a large impact on the cells cracking.
- Covering the set up with a cap can reduce the temperature distribution in the set-up, which helps to reduce the potential for cracking of the cell.
- A power supply can be added to the measurement circuit to increase the current drawn from the cell.
- The assembly of silver mesh and cell using silver ink is not efficient (lack of compression force).
- Full contact between the current collector and cell is an important factor to assemble the set up and deliver sufficient currents.

## 6 Commercial test apparatus

### 6.1 Commercial set up

In the previous chapter it was discussed that the results were not reproducible due to the inefficient current collecting method, particularly at the cathode side of the cell. Thus, the gas delivery manifold was replaced with a commercial set up to maximise the contact between the cell and current collecting meshes.

As shown in figure 6.1, the commercial set up [154] consists of two open flanges made of Inconel, sandwiching the cell and current collectors. A diffuser, made of pure nickel, is used to deliver the fuel to the anode and transport the products of the electrochemical reaction out of the set up. The diffuser is a flat piece of nickel to which three tubes have been welded. The middle one is six mm thick and used to deliver the fuel mixture to the cell. Two side tubes are four mm thick and used to pass the exhausted gas from cell to the vent. In order to seal the anode side a layer of mica paper is placed on the diffuser which encircles the anode current collector, as can be seen in figure 6.2. Finally, the cell is mounted on the mica paper and current collector. Nickel foam and gold grid are used as the current collector at the anode and cathode, respectively.

A three mm thick nickel wire has been welded to the diffuser in order to measure the voltage. The current is measured through the fuel inlet tube. There are three wires connected to the gold grid, two of which to measure the current and the third one for the voltage. Electrical insulation of the cell is assured using two layers of alumina-silica felt. These layers are placed in the set-up to insulate the gold wires against other parts as seen in figure 6.3. The alumina –silica felt is highly porous to allow air to diffuse and reach the cathode. A clamping mechanism consisting of four springs is used to apply uniform pressure on the set up.

Along with the commercial set up a different high temperature furnace was used to raise the temperature to the desired operating value. The furnace model, load and maximum operating temperature are Rohde TE 10 Q, 1.8 kW and 1320 °C, respectively. It is supplied with a Thermocomputer TC504 controller to set the temperature, heating/cooling ramp and dwell time. This furnace is shown in figure 6.4.

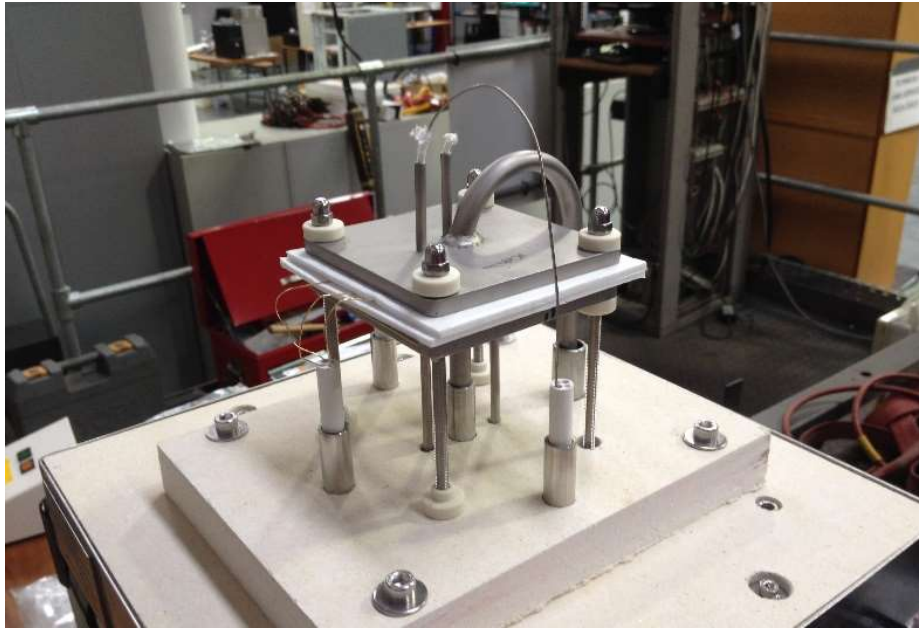


Figure 6.1: Open flange set up

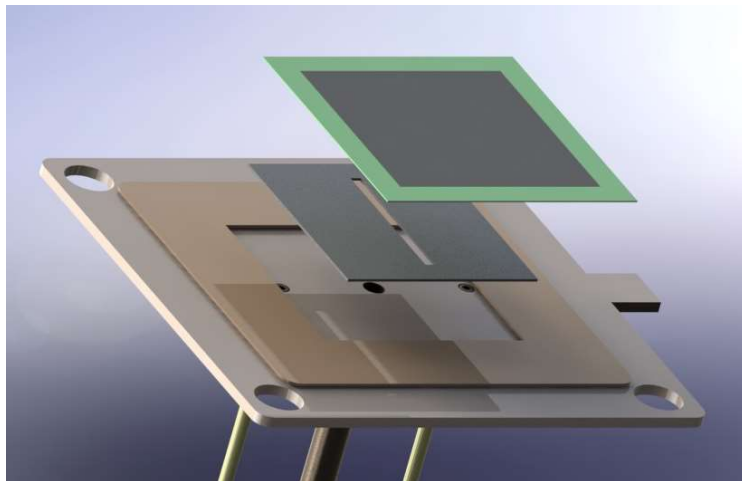


Figure 6.2: Commercial set up diffuser [154]

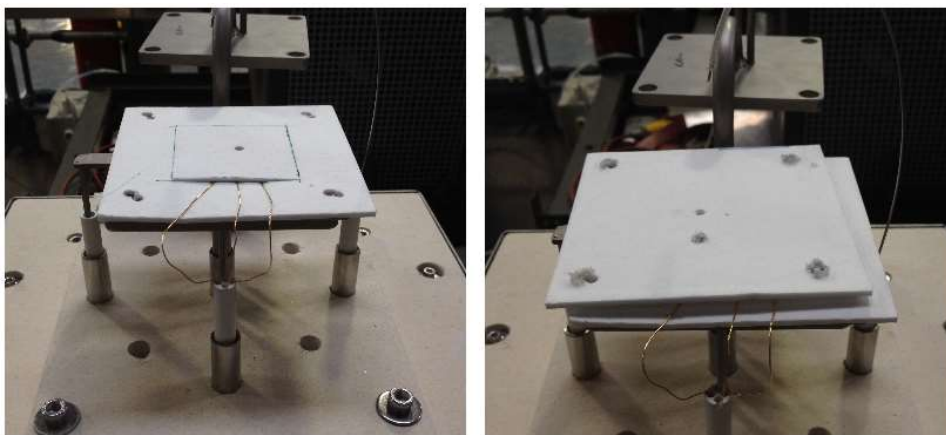


Figure 6.3: Electrical insulation of set up



Figure 6.4: High temperature furnace for commercial set up

## 6.2 Installation tests

In order to investigate the performance of the cells mounted in the new set up a few installation tests were carried out before the main baseline and contamination tests.

### 6.2.1 Cell 09

As explained before, the commercial set up consists of two open flanges which sandwich the cell, current collectors, mica paper and alumina-silica felt. Nickel foam and gold grid are used as current collector at anode and cathode, respectively. The flow rate and composition of the fuel were set according to table 5.5, however, the heating and cooling ramps were set to 2 °C/min. The steps of the test are summarised in table 6.1. The profiles of the voltage and temperature are demonstrated in figure 6.5. The results of the test can be summarised as follows:

- Maximum OCV: 1101 mV at 415 °C (low flow rate – observed while heating)
- OCV at 600 °C and normal flow rate: 1060 mV (during step 4)
- Voltage at @ 200 mA/cm<sup>2</sup> and 600 °C: 875 mV (during step 6)
- OCV at 700 °C and normal flow rate: 1040 mV (during step 9)
- Voltage at @ 200 mA/cm<sup>2</sup> and 700 °C: 937 mV (at the beginning of the durability period)

- Voltage at @ 200 mA/cm<sup>2</sup> and 700 °C: 914 mV (at the end of the durability period)
- 23 mV drop over 30 hours of durability

Step	Action	Condition
1	Heating up to 600 °C	@ 2 °C/min - low flow rate
2	Stabilisation	1 hour - normal flow rate
3	v-i curve	@ 600 °C
4	Running at OCV	3 hours
5	v-i curve	@ 600 °C
6	Loaded	@ 200 mA/cm <sup>2</sup> - 3 hours
7	v-i curve	@ 600 °C
8	Heating up to 700 °C	@ 2 °C/min
9	Stabilisation	1 hour
10	v-i curve	@ 700 °C
11	Durability test (taking v-i curve at intervals of 5 hours)	30 hours @ 700 °C and 200 mA/cm <sup>2</sup>
12	Cooling down	@ 2 °C/min - normal flow rate

Table 6.1: Steps of commercial set up initial test - cell 09

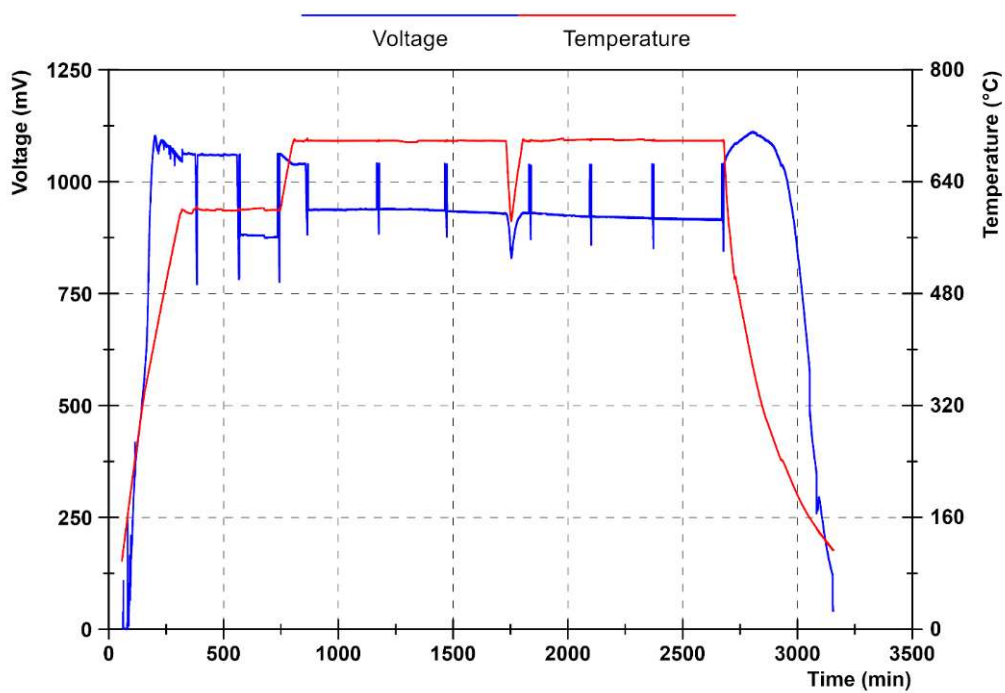


Figure 6.5: Profiles of voltage and temperature - cell 09

As can be seen in figure 6.5, a slight drop in the cell voltage was observed during the durability test. The drop in voltage can be attributed to evaporation of chromium from the set up during the first run. The flanges are made of Inconel which contains chromium. Once the set up is heated up to elevated temperatures chromium tends to evaporate and contaminate the cell which results in a drop during the test. It is expected that the set up stabilises after a few runs, i.e. a protective oxide layer is formed and no further evaporation of chromium occurs. The other possible cause can be the evaporation of particles from mica paper or alumina-silica felt diffusing into the cell and decreasing the performance.

Considering the composition of the fuel the theoretical OCV is 1064 and 1039 mV at 600 and 700 °C, respectively. The obtained OCV of the cell was 1060 and 1040 mV at 600 and 700 °C, respectively, which is close to the theoretical values.

Figure 6.6 illustrates the profile of the voltage and flow rates of hydrogen and nitrogen during the test. Once the temperature reached 600 °C the flow rates were increased to the normal operating composition. As a result, the OCV increased slightly which may be due to the increase of pressure as the flow rate rose.

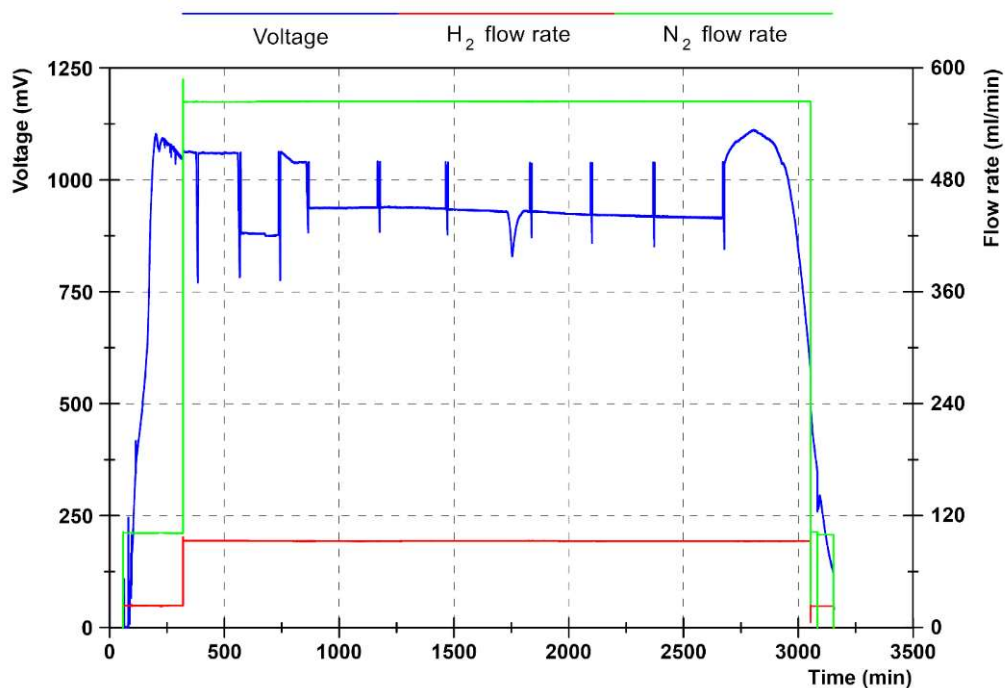


Figure 6.6: Profiles of voltage and flow rates - cell 09

The v-i curves taken at the end of each step are plotted in figure 6.7 and figure 6.8 for 600 and 700 °C, respectively. They have been also compared to those of the

previous tests. The results show better performance as the set up provides better connection between the cell and current collectors.

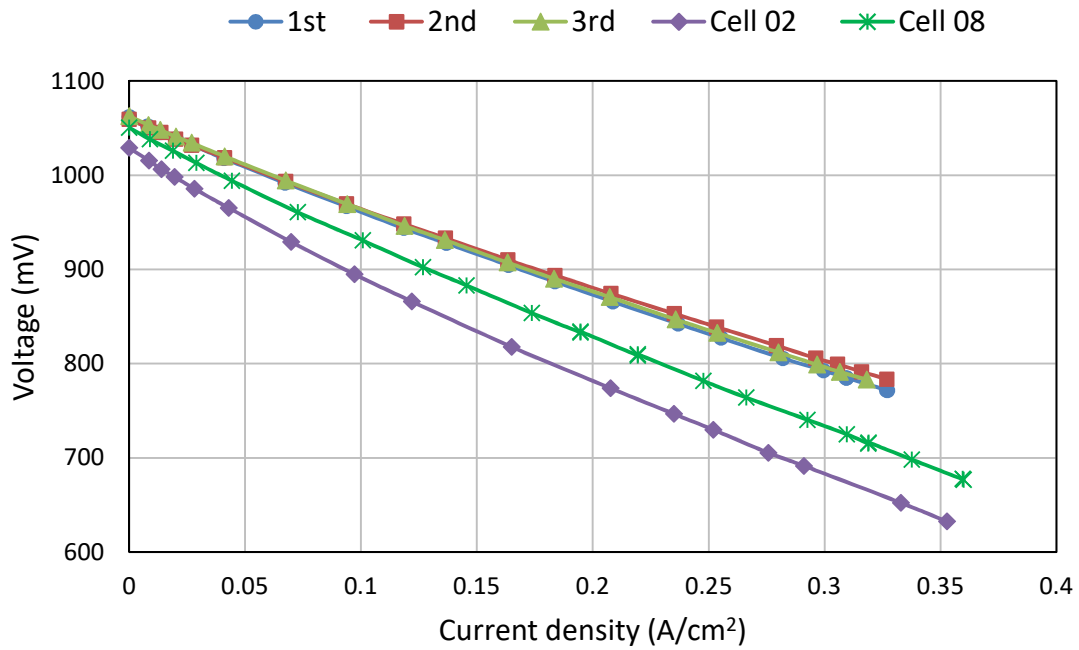


Figure 6.7: v-i curves at 600 °C - cell 09

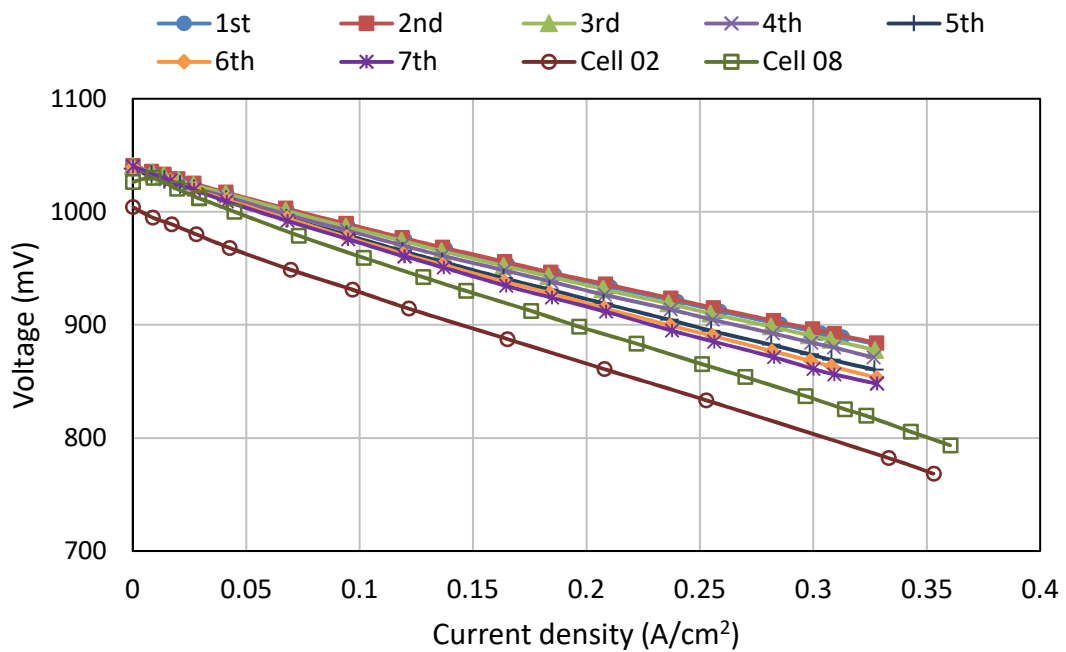


Figure 6.8: v-i curves at 700 °C - cell 09

The drop in the performance, discussed above, can be also observed in figure 6.7 and figure 6.8. As has been shown in the figures, the characteristic curves of the cell tend to drop slightly during the durability period.

## 6.2.2 Cell 10

The next test was carried out with a new cell under the same conditions as table 5.5. The only difference compared to the previous test was the heating ramp which was set to 2.5 °C/min. The profiles the voltage, temperature and flow rates against time are illustrated in figure 6.9 and figure 6.10, respectively.

The results of the test can be summarized as follows:

- Maximum OCV: 1110 mV at 444 °C (low flow rate – observed while heating)
- OCV at 600 °C and normal flow rate: 1065 mV
- Voltage at @ 200 mA/cm<sup>2</sup> and 600 °C: 827mV
- OCV at 700 °C and normal flow rate: 1029 mV
- Voltage at @ 200 mA/cm<sup>2</sup> and 700 °C: 913 mV (at the beginning of the durability period)
- Voltage at @ 200 mA/cm<sup>2</sup> and 700 °C: 891 mV (at the end of the durability period)
- 22 mV drop over 15 hours of durability

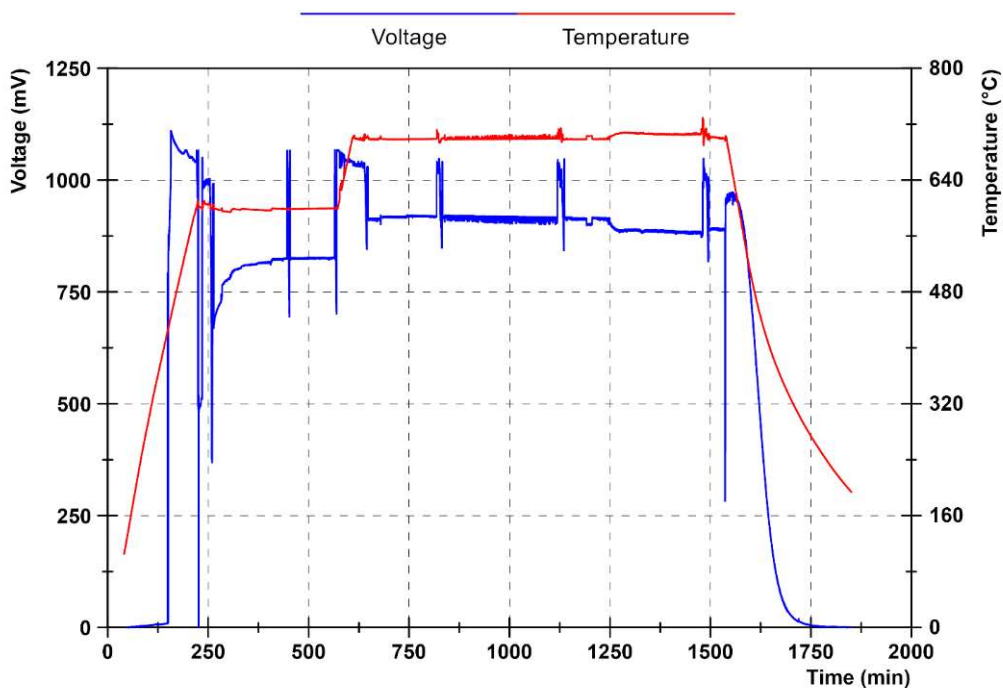


Figure 6.9: Profiles of voltage and temperature - cell 10

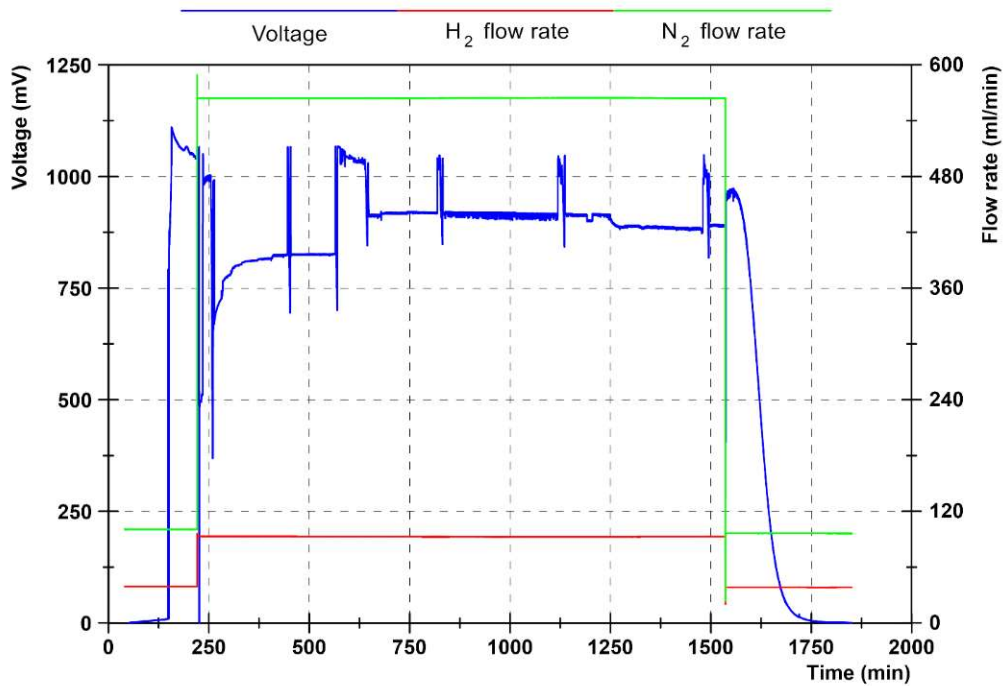


Figure 6.10: Profiles of voltage and flow rates - cell 10

Similar to the previous test a decrease was observed in the voltage profile. As seen in figure 6.9, both voltage and temperature were fluctuating over the durability period.

Theoretically, it is known that the voltage of cell increases as the temperature is elevated. As demonstrated in figure 6.9, the temperature slightly rose at  $t=1250$  min, however, the voltage decreased which is not expected.

Another test was carried out with the same cell the results of which have been illustrated in figure 6.11 and figure 6.12.

The results of this run can be summarized as follows:

- Maximum OCV: 1070 mV at 485 °C (low flow rate – observed while heating)
- OCV at 600 °C and normal flow rate: 1069 mV
- Voltage at @ 200 mA/cm<sup>2</sup> and 600 °C: 780 mV
- OCV at 700 °C and normal flow rate: 1045 mV
- Voltage at @ 200 mA/cm<sup>2</sup> and 700 °C: 895 mV (at the beginning of the durability period)
- Voltage at @ 200 mA/cm<sup>2</sup> and 700 °C: 878 mV (at the end of the durability period)
- 17 mV drop over 40 hours of durability

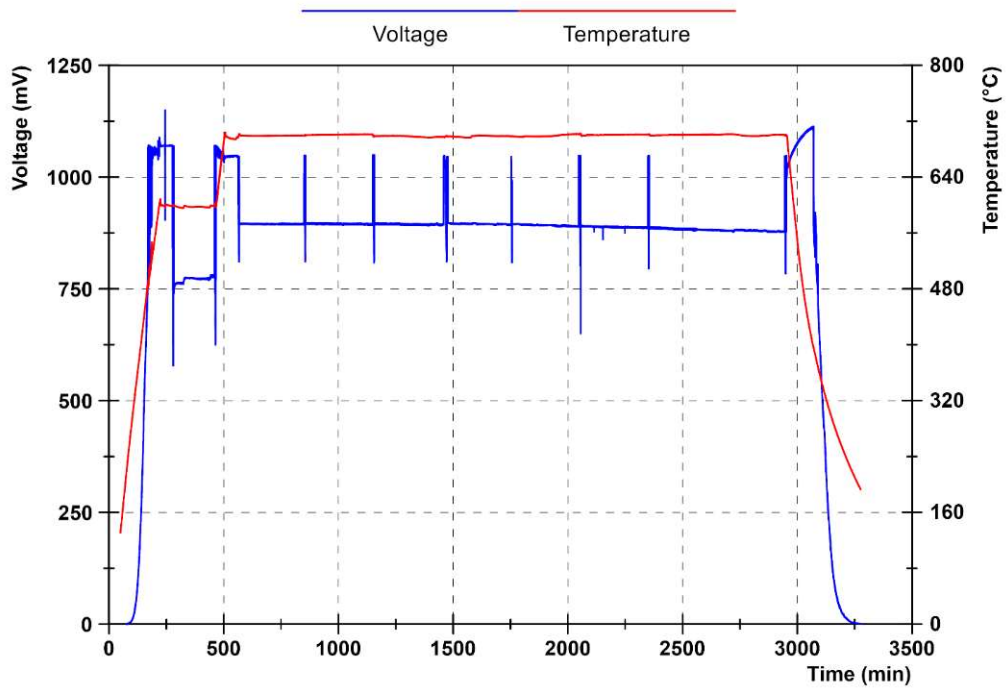


Figure 6.11: Profiles of voltage and temperature - cell 10 run 2

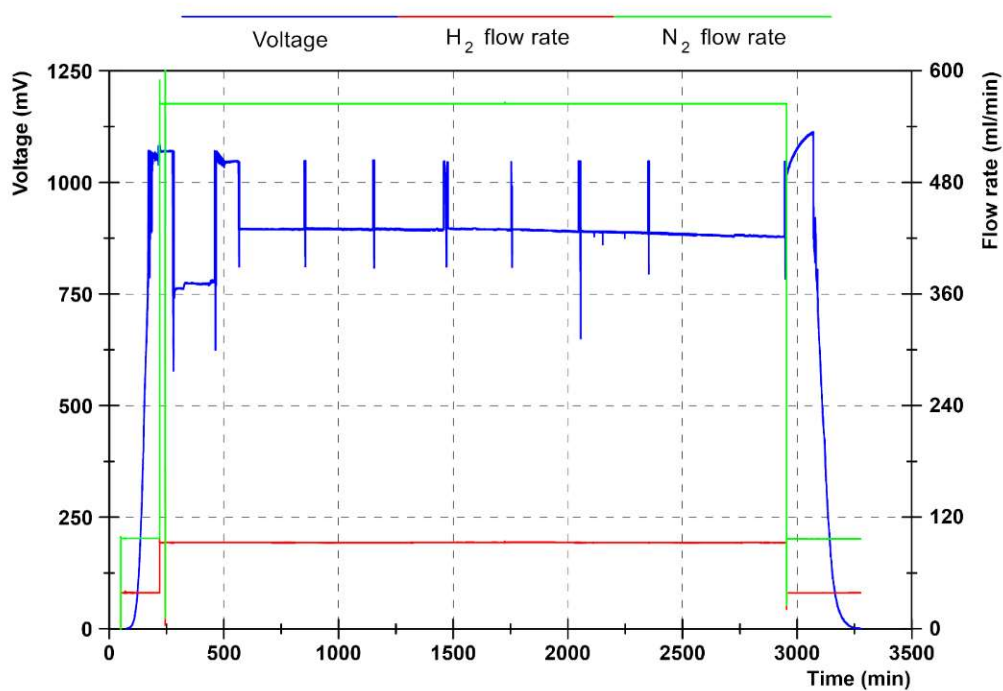


Figure 6.12: Profiles of voltage and flow rates - cell 10 run 2

Unlike the first run, the temperature was stable during the second run. However, a slight drop in the voltage was observed over 40 hours of the durability test. Comparing the results of two runs it can be said that the erratic performance of the first run may be related to a fault during set up preparation. Wrong/inaccurate

position of the thermocouple, lack of sufficient compression force or misalignment of the cell, mica paper or silica felt can affect the performance during the test resulting in unstable or lower voltage.

The OCV of the cell in this test was slightly higher than the theoretical values. This could be due to the actual operating conditions at which the cell was operating, i.e. the cell was working at slightly different pressure, temperature or flow rates than measured. One possibility could be that the operating temperature was below the desired set point causing the voltage to be larger. The temperature of the cell is measured by a thermocouple which touches the alumina-silica felt covering the cathode of the cell. In the preparation procedure of different tests the position of the thermocouple can be different; although the thermocouple reading is the same for all tests, the actual surface temperature of the cells could be different. In order to minimise this effect, the thermocouples should always be mounted according to the set up manual, i.e. a particular length of the thermocouples should be placed in the set up to make sure that the temperature of the same place is measured in all tests.

### **6.2.3 Cell 11**

Another experiment was carried out with a new cell under the same operating conditions as the previous test. The profiles of voltage, temperature and flow rates over the test period are illustrated in figure 6.13 and figure 6.14, respectively.

Similar to the test with cell 09, a very slight increase in the voltage at the early stages of the durability period is observed. This increase is followed by a gradual drop making the voltage level out after about 50 hours.

The results of the test are as follows:

- Maximum OCV: 1084 mV at 470 °C (low flow rate – observed while heating)
- OCV at 600 °C and normal flow rate: 1069 mV
- Voltage at @ 200 mA/cm<sup>2</sup> and 600 °C: 796 mV
- OCV at 700 °C and normal flow rate: 1045 mV
- Voltage at @ 200 mA/cm<sup>2</sup> and 700 °C: 926 mV (at the beginning of the durability period)
- Voltage at @ 200 mA/cm<sup>2</sup> and 700 °C: 899 mV (at the end of the durability period)

- 27 mV drop over 60 hours of durability

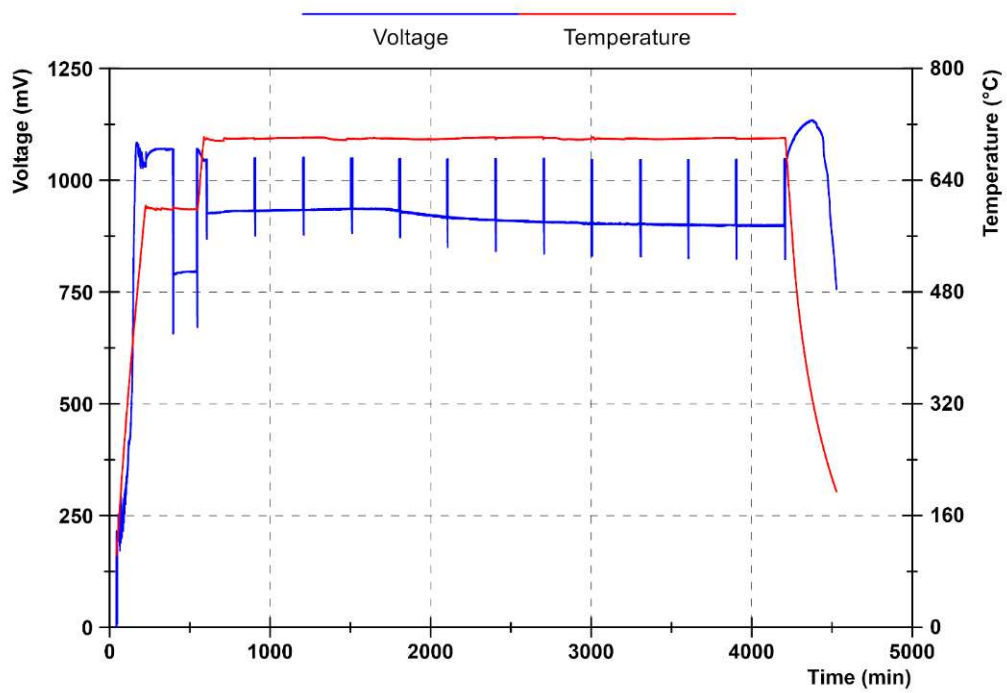


Figure 6.13: Profiles of voltage and temperature - cell 11

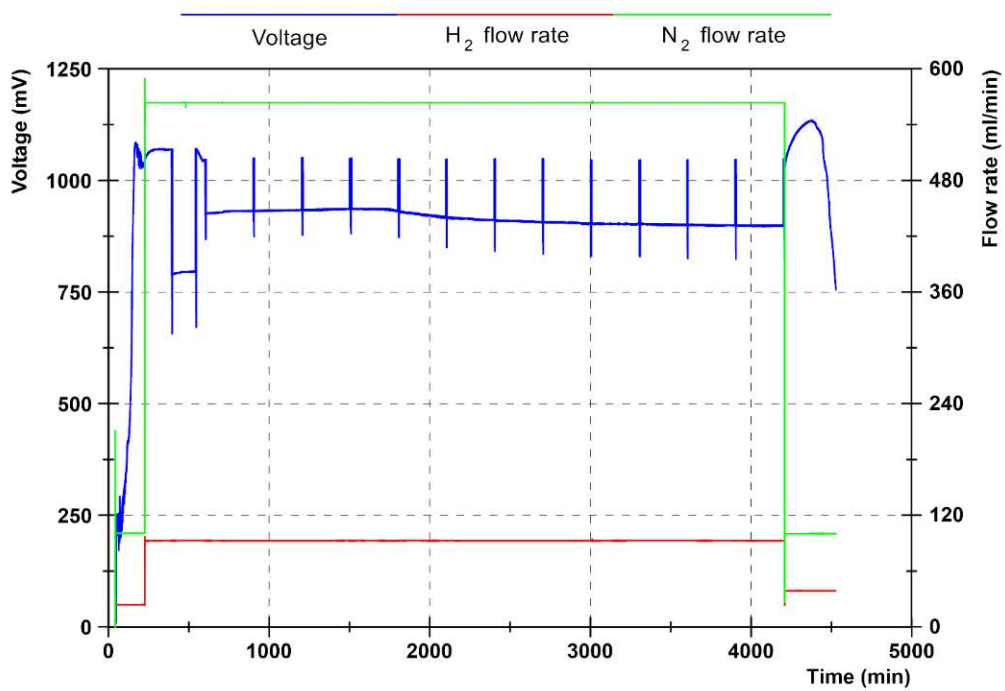


Figure 6.14: Profiles of voltage and flow rates - cell 11

From the previous tests, it can be said that there is a general trend which the cell voltage tends to follow during the durability period. This trend starts with a small

increase over the early stages of test followed by a decrease and finally reaching a constant value.

In order to find out if the same trend happens in every run or just the first run cell 10 was mounted in the set up for another test. Figure 6.15 and figure 6.16 illustrate the results of the test for 40 hours of durability.

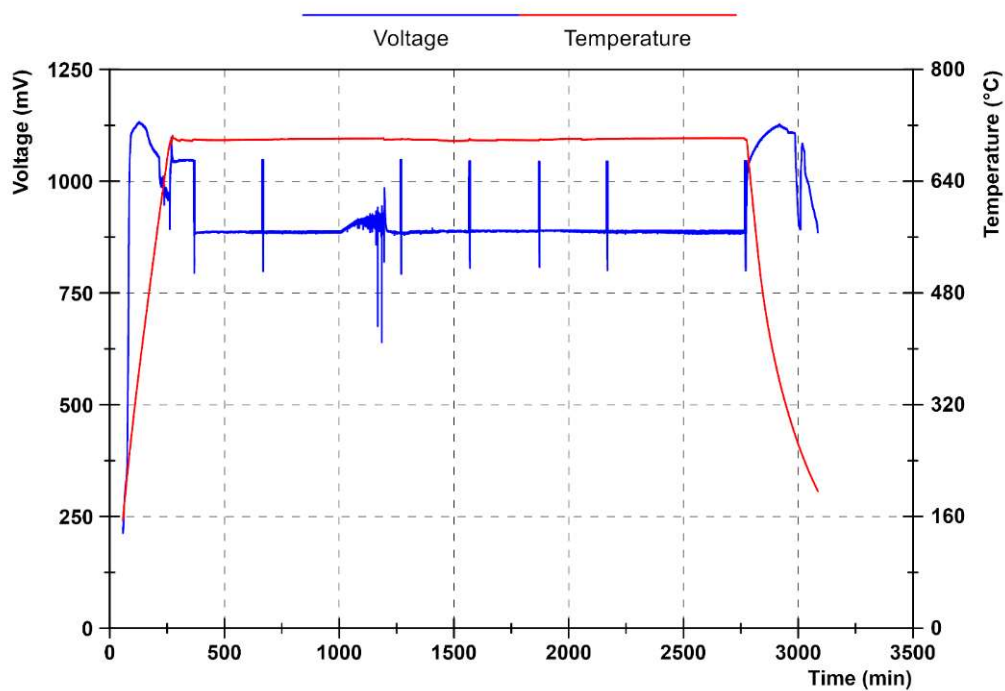


Figure 6.15: Profiles of voltage and temperature - cell 11 run 2

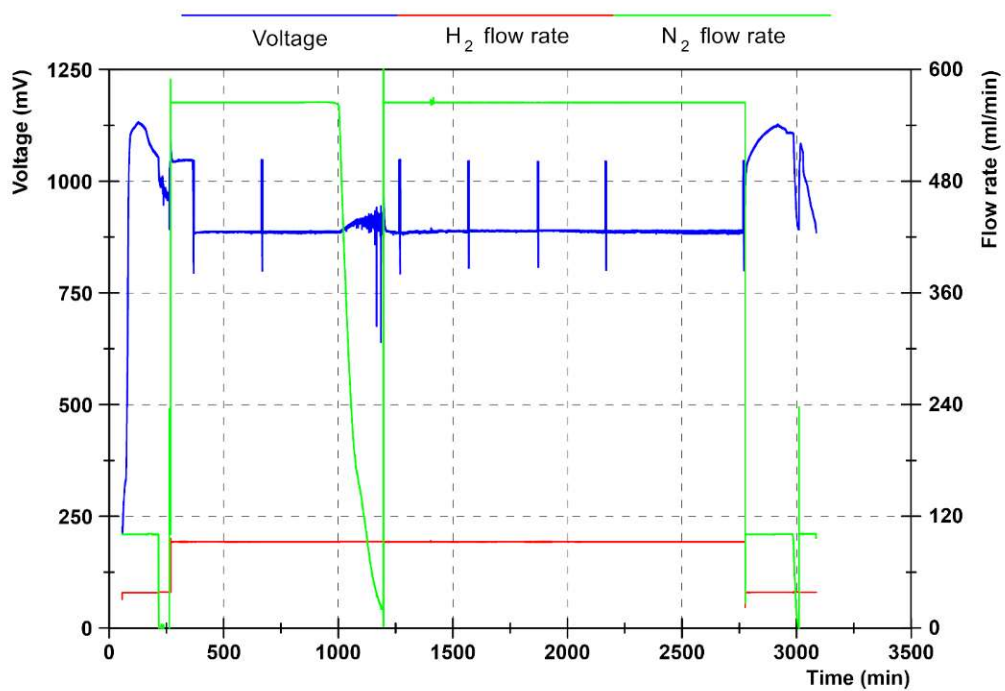


Figure 6.16: Profiles of voltage and flow rates - cell 11 run 2

As can be seen in figure 6.15 the voltage is almost constant (889 mV) over the durability period. However, large instabilities are observed from  $t=1005$  min to  $t=1200$  min which are related to the change in the flow rate of the fuel. As shown in Figure 6.16 there is a major drop in the flow rate of nitrogen causing the voltage to fluctuate significantly. Once the flow rate was re-set to the desired value the voltage went back to its previous value.

In this run the voltage of the cell at  $0.2 \text{ A/cm}^2$  was 889 mV, 10 mV lower than the first run. This difference can be attributed to the thermal cycle through which the cell has gone during two tests. From the results of the first and second runs it can be said that the change in the voltage during the early stages of durability test can be due to the interaction of the new cell and set up or the change in the cell properties at the early stages of the first run. Once this period is past the voltage tends to stabilize and remain constant.

#### **6.2.4 Cell 12**

A new cell was mounted in the set up in order to test the performance with contaminated fuel containing 50 ppm of  $\text{H}_2\text{S}$ . The test was carried out under the same conditions as the previous tests. The results of the test for 55 hours of durability, 14 hours of  $\text{H}_2\text{S}$  exposure and 14 hours of recovery (removal of  $\text{H}_2\text{S}$  from the fuel mixture) are shown in figure 6.17 and figure 6.18.

Based on the results of the previous tests, the cell was loaded for 55 hours to stabilize. Then, 50 ppm of  $\text{H}_2\text{S}$  was added to the fuel mixture at  $t=3930$  min.

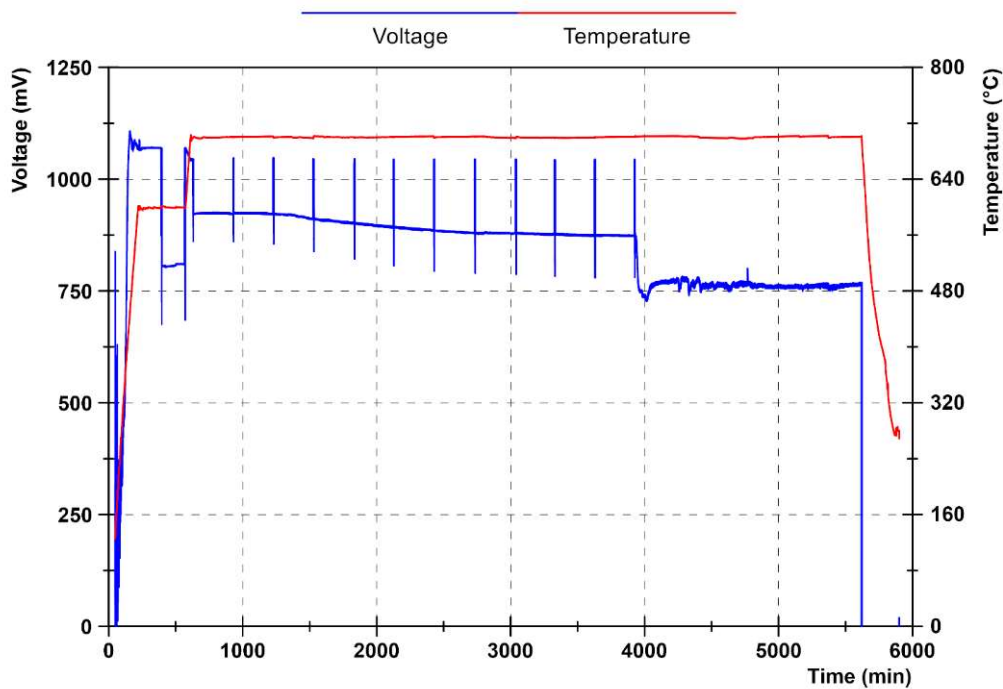


Figure 6.17: Profiles of voltage and temperature - cell 12 50 ppm

The results of the durability period can be presented as follows:

- Maximum OCV: 1107 mV at 451 °C (low flow rate – observed while heating)
- OCV at 600 °C and normal flow rate: 1069 mV
- Voltage at @ 200 mA/cm<sup>2</sup> and 600 °C: 810 mV
- OCV at 700 °C and normal flow rate: 1044 mV
- Voltage at @ 200 mA/cm<sup>2</sup> and 700 °C: 922 mV (at the beginning of the durability period)
- Voltage at @ 200 mA/cm<sup>2</sup> and 700 °C: 874 mV (at the end of the durability period)
- 46 mV drop over 55 hours of durability

According to the literature an initial sharp drop followed by a secondary sluggish fall in the voltage was expected as a result of the exposure to H<sub>2</sub>S. As can be seen in figure 6.17, 7 minutes after addition of H<sub>2</sub>S to the fuel mixture, the voltage started to drop sharply. However, it recovered partially and then, started to fluctuate around a constant value.

Figure 6.18 shows the profiles of H<sub>2</sub>, N<sub>2</sub> and N<sub>2</sub>/H<sub>2</sub>S flow rates against time. During the heating up, durability (stabilisation) and cooling down periods the flow rate of N<sub>2</sub>/H<sub>2</sub>S mixture was zero, although the graph shows value of 19 ml/min due to the

flow meter reading error. It can be also seen that there is an overshoot in the  $N_2/H_2S$  flow rate. The observed spike, occurred due to the flow controller fluctuations at the beginning of the operation, led to an extra amount of  $H_2S$  added to the fuel mixture. This caused the cell to run on undesired conditions for a short period and the voltage dropped further, then recovered slowly after the concentration is set to 50 ppm. Although this can be a possibility for the recovery, further studies are required to ensure whether it is due to the flow rate overshoot or a characteristic behavior of the cell.

Figure 6.19 compares the v-i curves taken at the end of the durability test at 700 °C for cells 09, 10, 11 and 12. As can be seen in the figure, the results of the tests with the new set up are close and much more reproducible than the previous set up. It is quite important to prepare the set up (assembly of cell, current collectors, mica paper and silica felt) correctly since any fault in the preparation process can affect the performance and yield inaccurate and erratic results.

Another key point is to apply sufficient compression force on the flanges, the lack of which can lead to large leakage of the fuel mixture from the set up and inefficient current collection. The clamping mechanism includes four springs to apply the force on the set up; it is important to adjust the length of the springs according to the set up manual to ensure uniform and sufficient pressure.

A comparison of the durability tests carried out up to this point, including all the tests and runs, has been demonstrated in figure 6.20. Looking at the figure it is appreciated that there is a general trend for all cells in which the voltage increases slightly at the early stages of the tests, then decreases gradually and finally tends to stabilise. This trend is approximately similar for cells 09, 11 and 12, but different for cell 10 as discussed in the corresponding section.

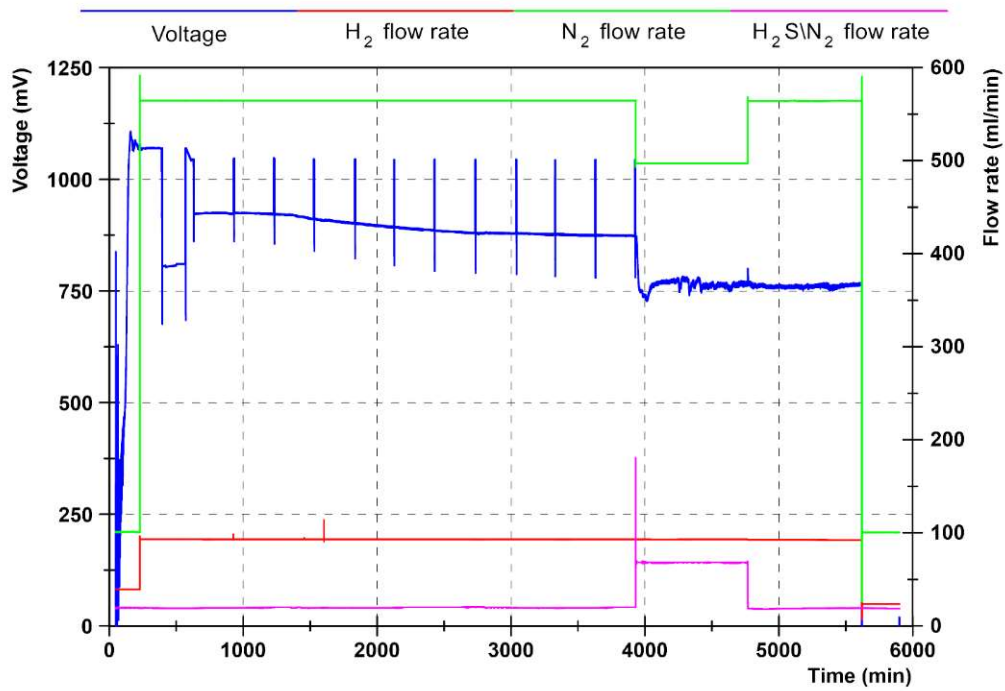


Figure 6.18: Profiles of voltage and flow rates - cell 12 50 ppm

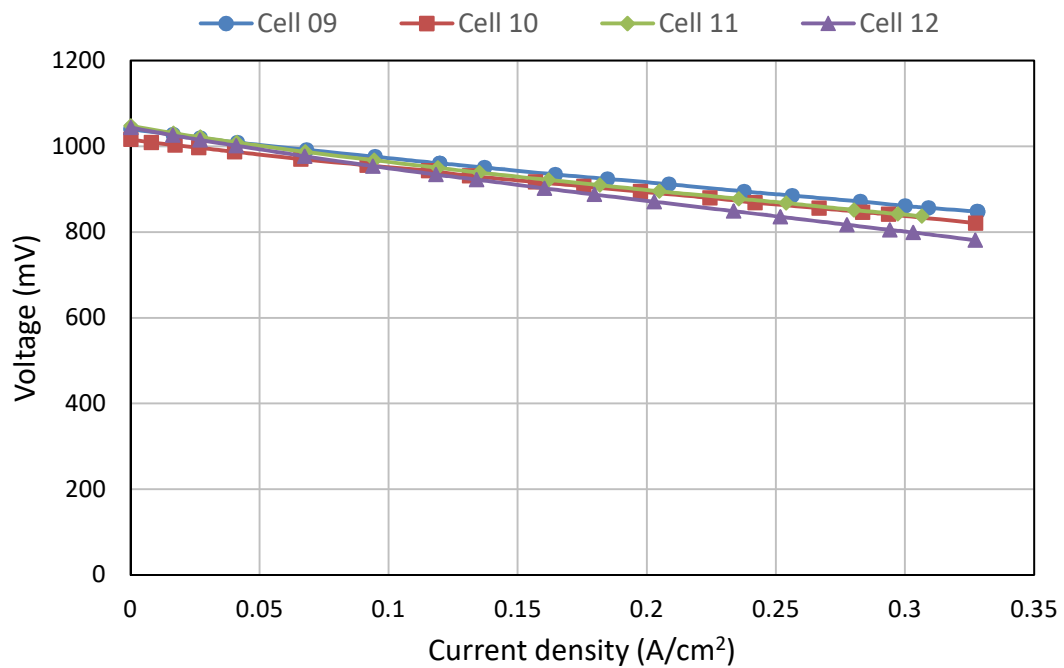


Figure 6.19: Comparison of last V-i curves at 700 °C - cells 09, 10, 11 & 12

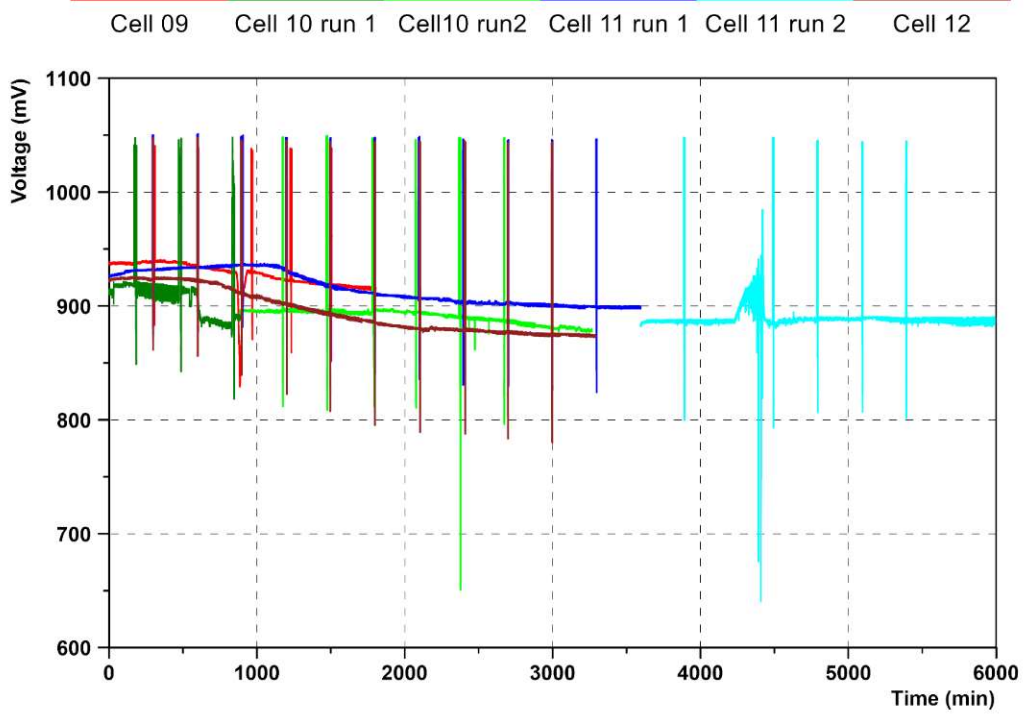


Figure 6.20: Comparison of durability tests at 700 °C - cells 09, 10, 11 & 12



# 7 Results

## 7.1 Baseline tests (Cell 13)

A series of tests with a new cell were carried out in order to run a baseline test and investigate the effects of different operating conditions on the cell performance. In these tests the effects of time, hydrogen partial pressure and temperature were investigated using electrochemical impedance spectroscopy (EIS) analysis. EIS and v-i curves were taken every 5 hours during the tests.

### 7.1.1 Effect of time (run 1)

In the first run of the cell the effect of time was investigated at 700 °C. The profiles of voltage/temperature and voltage/flow rates have been shown in figure 7.1 and figure 7.2, respectively. The results can be summarized as follows:

- Maximum OCV: 1104 mV at 449 °C (low flow rate – observed while heating)
- OCV at 700 °C and normal flow rate: 1043 mV
- Voltage at @ 200 mA/cm<sup>2</sup> and 700 °C: 904 mV (at the beginning of the durability period)
- Voltage at @ 200 mA/cm<sup>2</sup> and 700 °C: 843 mV (at the end of the durability period)
- 61 mV drop over 85 hours of durability

The voltage was did not change for the first 20 hours of the durability period and then, started to decrease slowly. As shown in figure 7.1, voltage stabilized after 65 hours at about 846 mV and remained almost constant for the rest of the durability period showing no major degradation. This trend is used for the contamination tests in which H<sub>2</sub>S is introduced to the cell once the voltage stabilizes, thus it can be assumed that the degradation is only due to the presence of the contaminant.

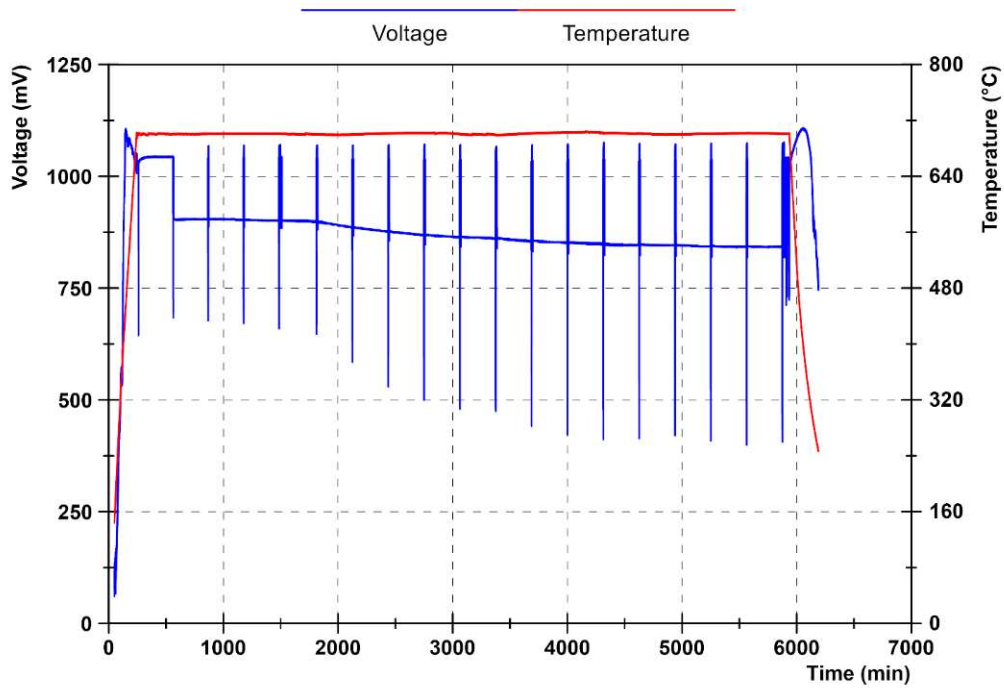


Figure 7.1: Profiles of voltage and temperature - cell 13 run 1

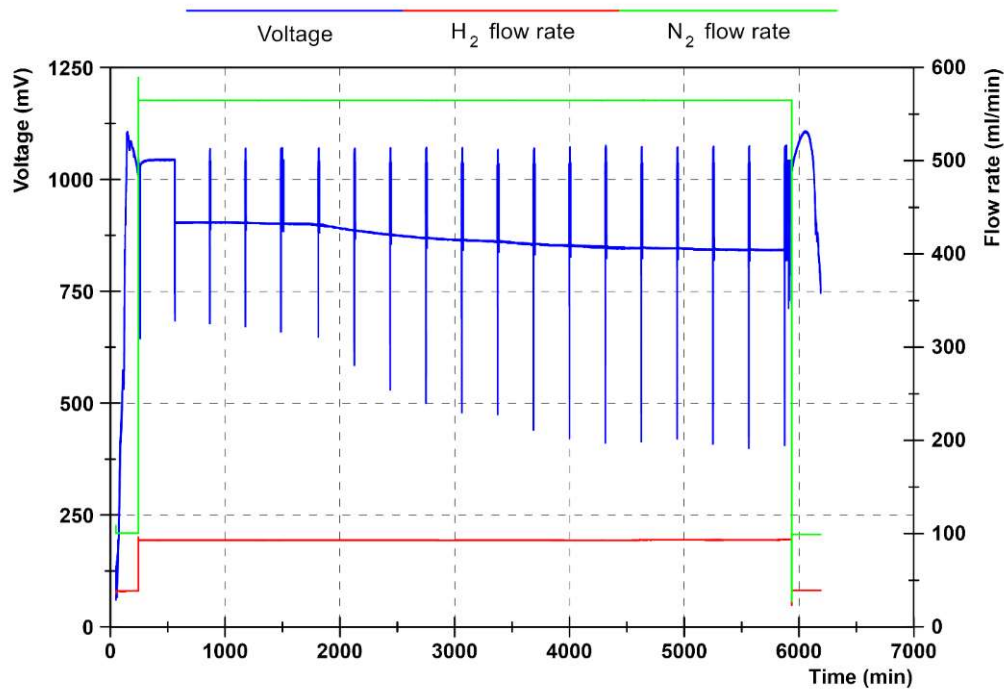


Figure 7.2: Profiles of voltage and flow rates - cell 13 run 1

The profiles of v-i curves has been illustrated in figure 7.3. Similar to the previous tests, it can be seen that the performance slightly improved at the early stages of the test (from first v-i curve to the second one) and then, tended to decrease with time. The stabilization of voltage can be also seen in this figure in which the v-i curves taken after 65, 75 and 85 hours are almost overlapping.

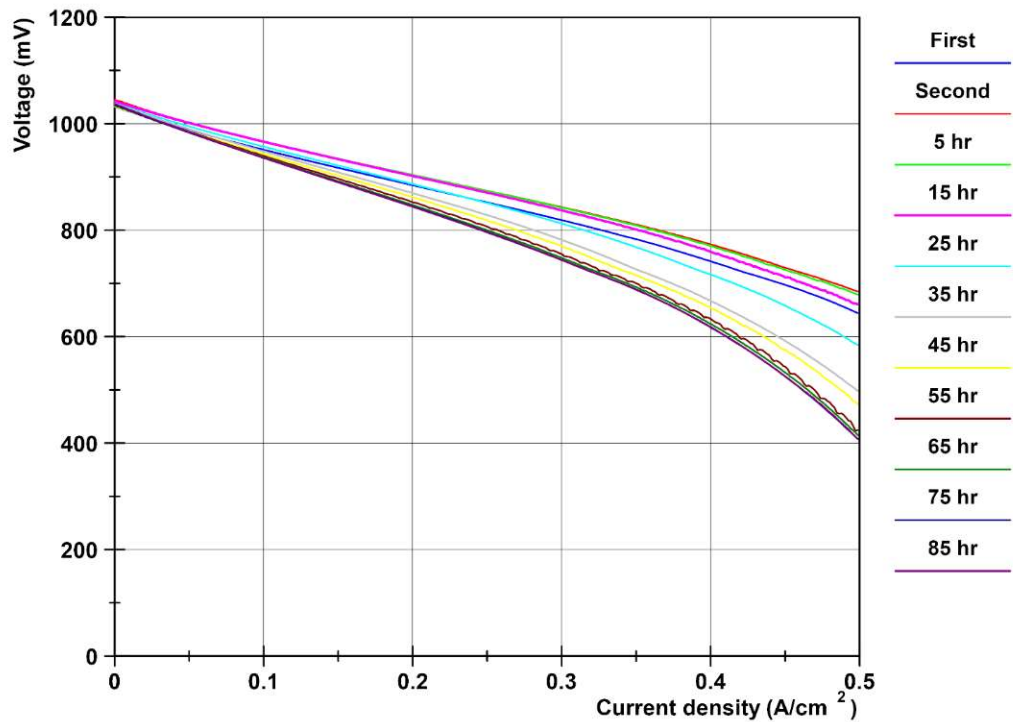


Figure 7.3: Profiles of v-i curves – cell 13 run 1

It can be also seen that the onset of the concentration losses area occurred at lower current densities as time elapsed, suggesting that the diffusion of the reactants and products was affected with time. This can be due to the changes in the electrodes microstructure such as size or blockage of the pores.

EIS curves taken at OCV and 200 mA/cm<sup>2</sup> have been shown in Figure 7.4 and figure 7.5, respectively.

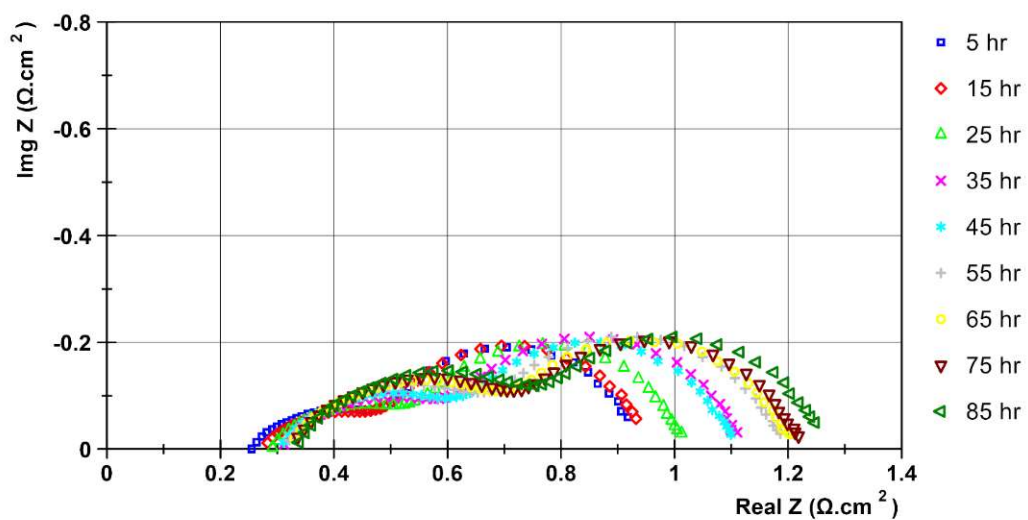


Figure 7.4: EIS curves at OCV over durability period - cell 13 run 1

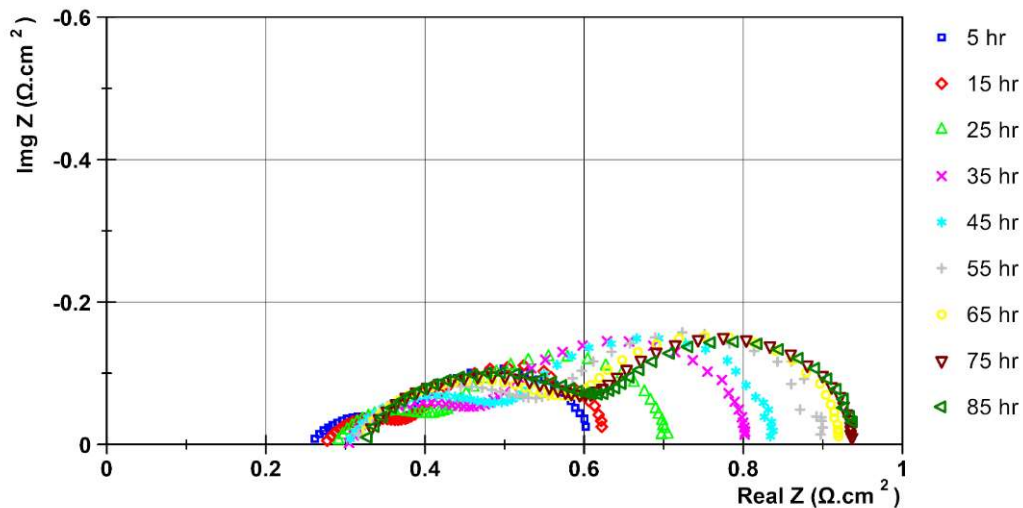


Figure 7.5: EIS curves at 200 mA/cm<sup>2</sup> over durability period - cell 13 run 1

Both figures it show that the resistance of the cell increased over time and almost stabilized after 65 hours. It can be also seen that both ohmic and activation/concentration (electrodes) polarisations tend to increase with elapsed time, however, the increase in the ohmic resistance is much lower than that of activation/concentration resistance suggesting that the active sites of the electrodes (electrochemical characteristics of the cell) are affected more than the electrolyte over time.

### 7.1.2 Effect of hydrogen partial pressure (run 2)

The effect of hydrogen partial pressure on the internal resistance of the cell was investigated in another run with the same cell. The EIS and v-i curves were taken at three different values of hydrogen partial pressure: 0.145, 0.291 and 0.436 bar. The total pressure of the fuel gas remained at atmospheric pressure and the partial pressure changes were simply due to the change in concentration. The total flow rate of fuel was 666.67 ml/min containing 3 % water, thus, the composition of fuel was 100 ml/min H<sub>2</sub> – 566.67 ml/min N<sub>2</sub>, 200 ml/min H<sub>2</sub> – 466.67 ml/min N<sub>2</sub> and 300.15 ml/min H<sub>2</sub> – 366.52 ml/min N<sub>2</sub> corresponding to H<sub>2</sub> partial pressures of 0.145, 0.291 and 0.436 bar, respectively. The operating temperature of the cell was 700 °C for all curves.

Figure 7.6 illustrates the profiles of voltage and temperature. Before taking curves, the cell was loaded at 200 mA/cm<sup>2</sup> for 17.5 hours to make sure that the voltage has reached a constant value and cell has stabilized.

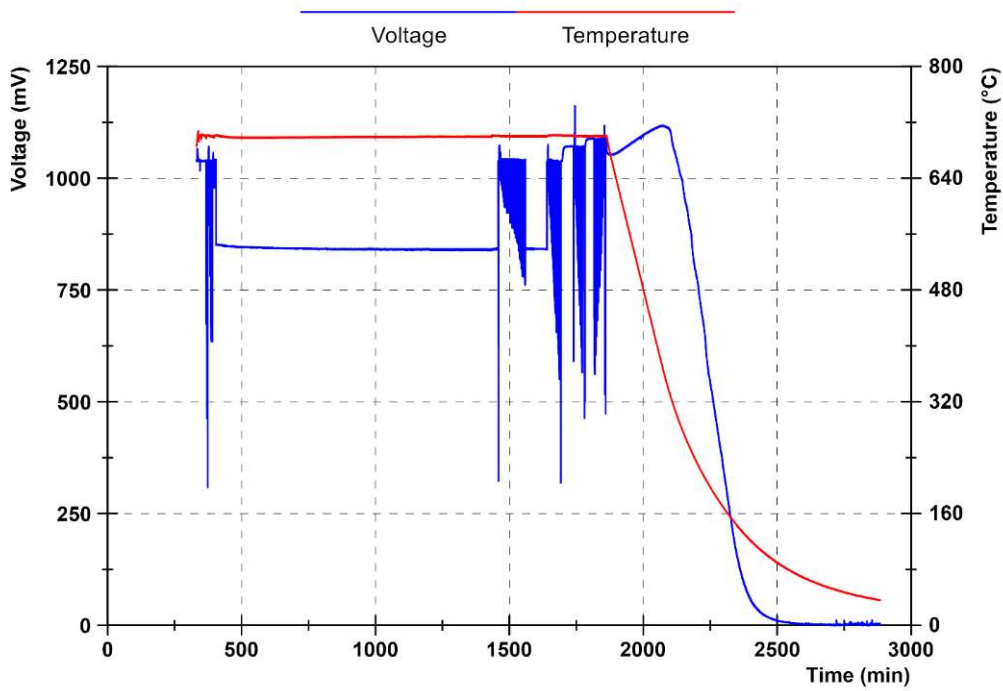


Figure 7.6: Profiles of voltage and temperature - cell 13 run 2

The profiles of voltage and flow rates are illustrated in figure 7.7. As can be seen, in order to have the same total flow rate and desired  $H_2$  partial pressure the flow rates of  $H_2$  and  $N_2$  were changed accordingly. Figure 7.8 shows the v-i curves taken at different partial pressures of  $H_2$ .

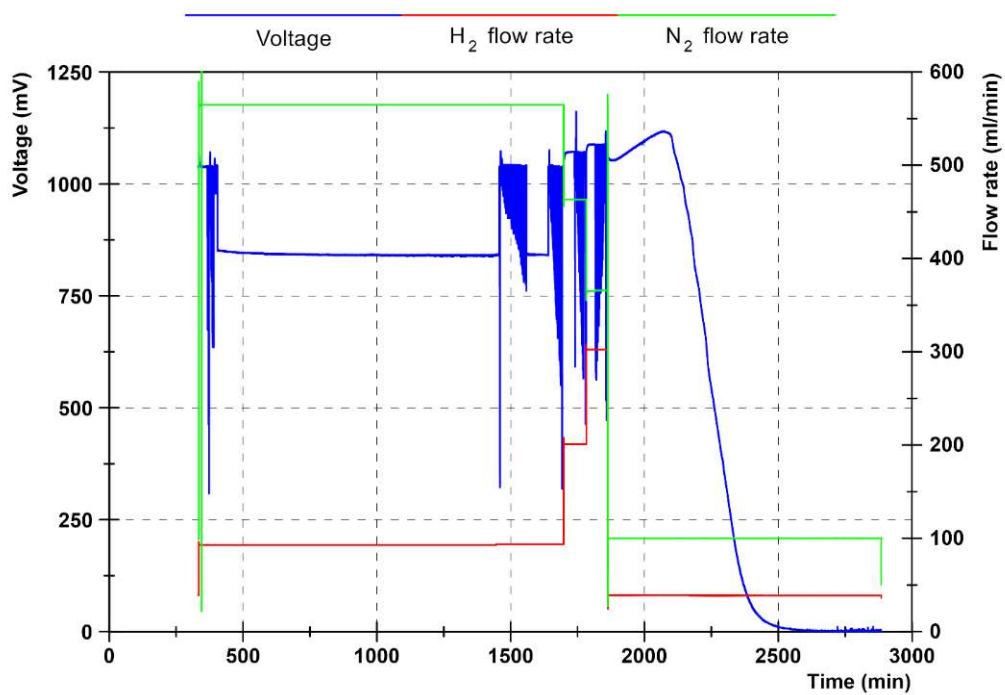


Figure 7.7: Profiles of voltage and flow rates - cell 13 run 2

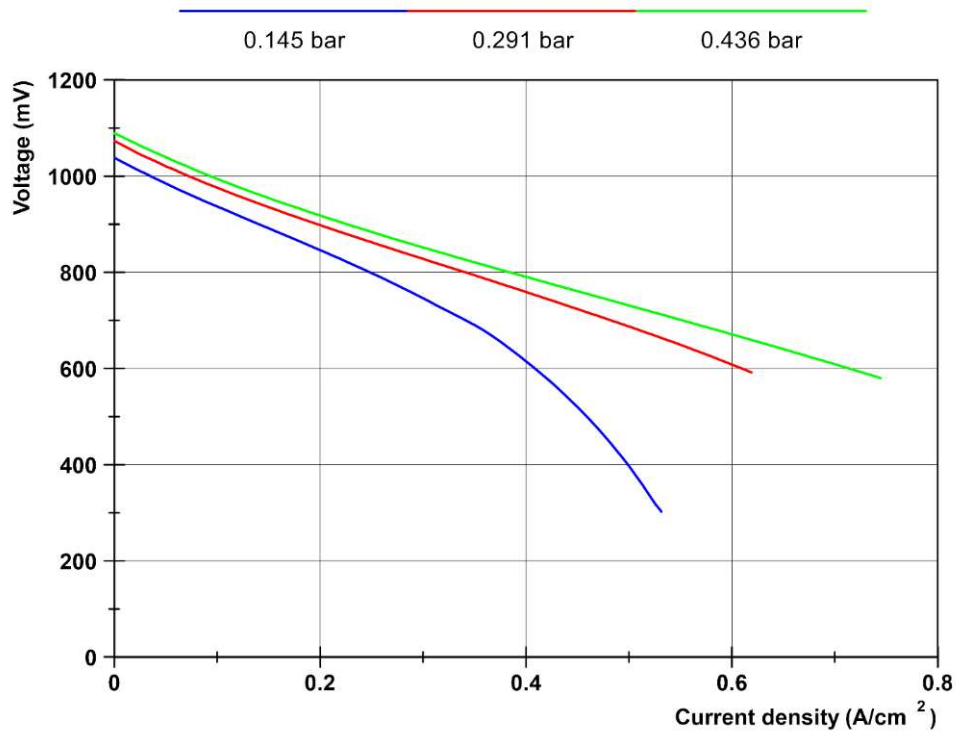


Figure 7.8: Profiles of v-i curves – cell 13 run 2

As expected the performance of the cell increased with the flow rate of hydrogen. For H<sub>2</sub> partial pressure of 0.145 bar (100 ml/min) the v-i curve started to fall into the concentration losses region at around 0.35 A/cm<sup>2</sup>, whereas, for higher partial pressures, it remained within the Ohmic losses area even at higher current densities. Since the amount of available hydrogen was less for the case of 0.145 bar, drawing higher current increased the consumption of hydrogen and left the cell with less fresh fuel. The remaining amount of hydrogen, which was small, could not reach the active sites efficiently causing the performance to drop into the concentration losses region. The larger amount of available hydrogen for the cases of 0.291 and 0.436 bar allowed drawing of higher currents without major concentration overpotentials. Figure 7.8 also shows a rise in OCV as the partial pressure of H<sub>2</sub> increases. Theoretically, this is an expected trend in which the Nernst voltage tends to increase with H<sub>2</sub> partial pressure.

Figure 7.9 shows the EIS curves taken at 0 to 0.375 A/cm<sup>2</sup> for H<sub>2</sub> partial pressure of 0.145 bar. As illustrated in the figure, the ohmic resistance of the cell remained almost constant for the current densities between 0 and 0.3125 A/cm<sup>2</sup>. It can be also seen that there was a rise in the ohmic resistance for i=0.375 A/cm<sup>2</sup> which is the starting point of the concentration losses region. For the operating conditions

before this area the value of the ohmic resistance tended to remain constant, however, it started to increase in the concentration losses area.

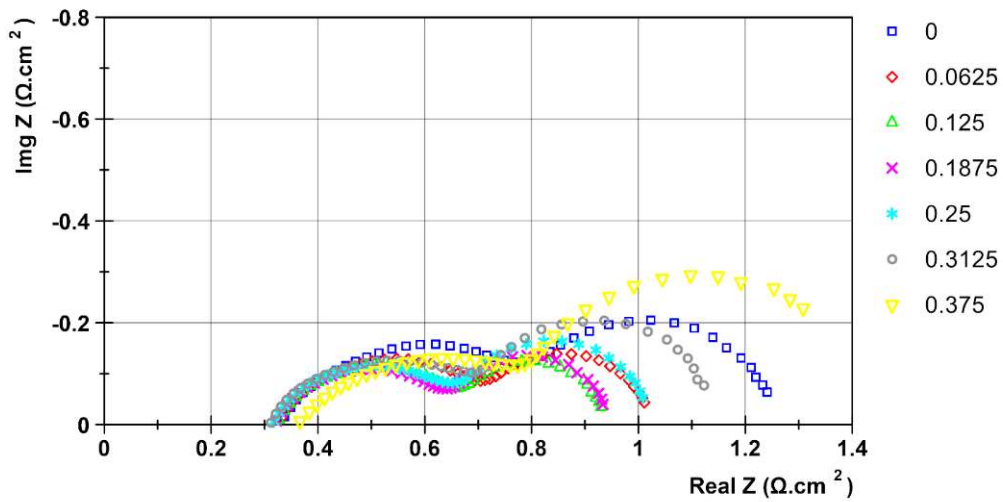


Figure 7.9: EIS curves at different current densities (A/cm<sup>2</sup>) for  $P_{H_2} = 0.145$  bar

EIS curves for  $H_2$  partial pressure of 0.291 bar are illustrated in figure 7.10. For the current densities between 0 and 0.625 A/cm<sup>2</sup> the ohmic resistance was almost constant and then increased at 0.6875 A/cm<sup>2</sup>. This trend is similar to what observed for  $H_2$  partial pressure of 0.145 bar as mentioned above, however, the corresponding v-i curve did not cover the concentration losses region, making it difficult to attribute the increase to the concentration losses.

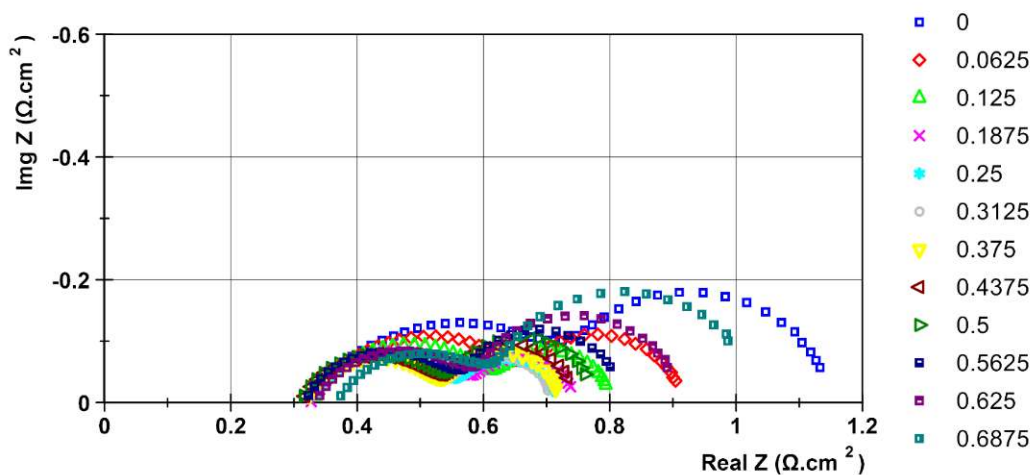


Figure 7.10: EIS curves at different current densities (A/cm<sup>2</sup>) for  $P_{H_2} = 0.291$  bar

Figure 7.11 shows the EIS curves for  $H_2$  partial pressure of 0.436 bar at different current densities. Similar to the previous case, the ohmic resistance was approximately constant within the range of 0 to 0.8125 A/cm<sup>2</sup>. As the corresponding v-i curve did not show that the operating point had fallen in the

concentration losses area, it is not possible to assign the values of current density to the operation regions.

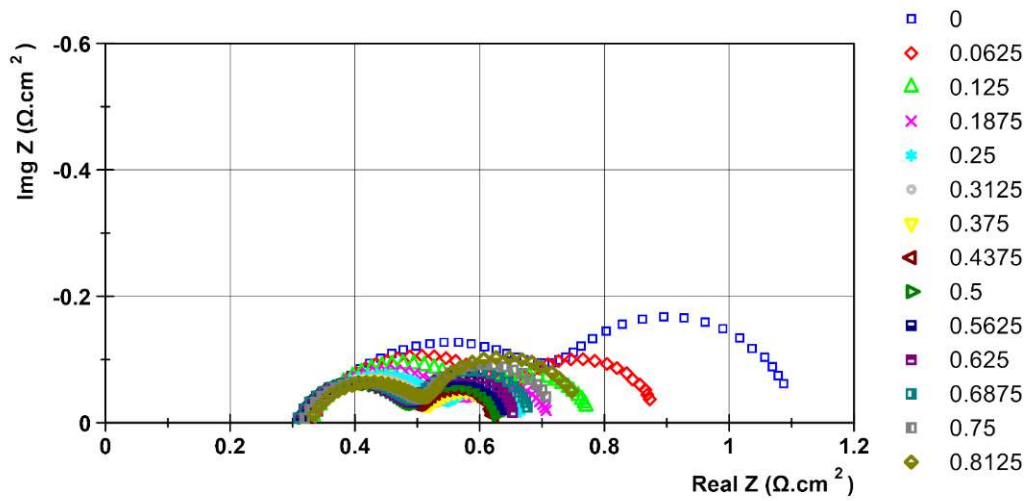


Figure 7.11: EIS curves at different current densities (A/cm<sup>2</sup>) for P<sub>H<sub>2</sub></sub> = 0.436 bar

All sets of the EIS curves for three H<sub>2</sub> partial pressures show a similar trend in which the resistance of the cell tends to decrease at low current densities and then rises once larger currents are drawn from the cell. This trend which is similar to the results reported in the literature [143], has been illustrated in figure 7.12.

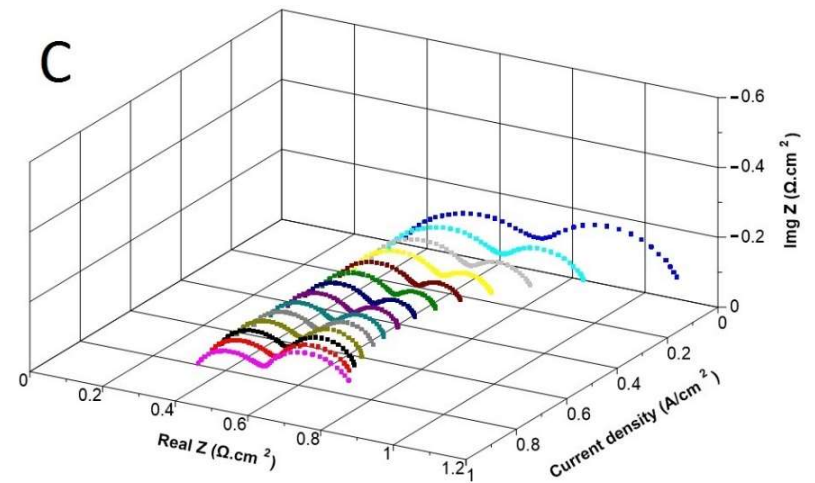
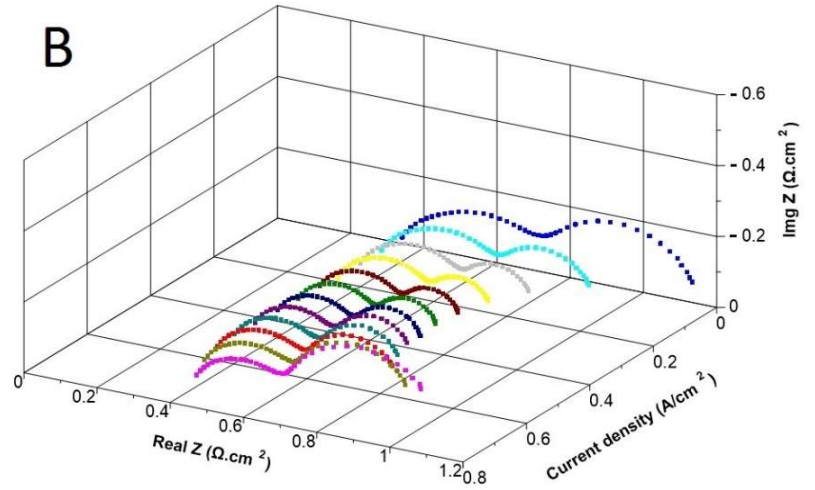
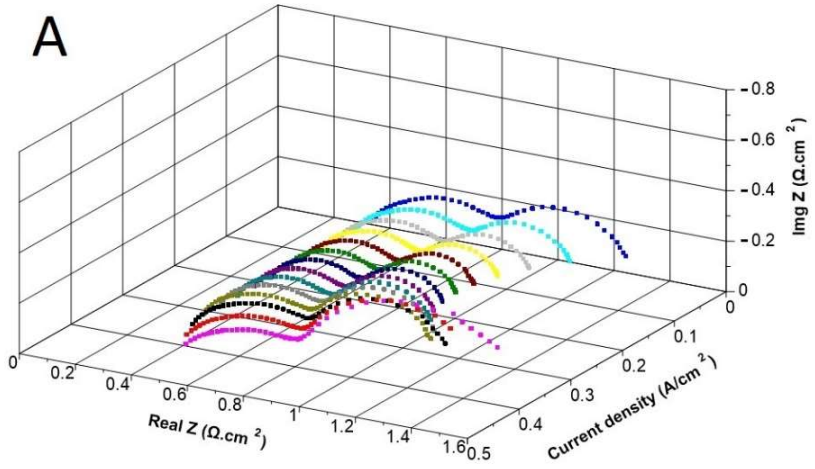


Figure 7.12: 3D plot of EIS curves – A: 0.145 bar, B: 0.291 bar, C: 0.436 bar

This is an expected behaviour as it is compatible with the v-i curve. EIS analysis measures the internal resistance of the cell which is the gradient of the v-i curve. As can be seen in figure 7.8, the gradient of the curves tends to decrease at low current densities, followed by an increase at higher current densities.

The current of lowest resistance for H<sub>2</sub> partial pressures of 0.145, 0.291 and 0.436 bar was 0.156, 0.312 and 0.437 A/cm<sup>2</sup>, respectively. Thus, the current of lowest resistance increases as the partial pressure of hydrogen rises. Generally, the cell resistance is due to the activation, ohmic and concentration components. As the activation and concentration losses are smaller at higher partial pressures of hydrogen, it is expected for the current of lowest resistance to increase with P<sub>H<sub>2</sub></sub>.

As a general trend it can be stated that the ohmic losses, except for high current densities, remain approximately constant as the current increases, however, the sum of activation and concentration losses is larger at low and high currents, and have smaller values for middle currents yielding an optimum operating point.

Figure 7.13 compares the EIS curves taken at 0.0625 A/cm<sup>2</sup> for three partial pressures of hydrogen. As illustrated, the ohmic resistance did not change with P<sub>H<sub>2</sub></sub>, however, the activation/concentration component dropped for higher P<sub>H<sub>2</sub></sub>.

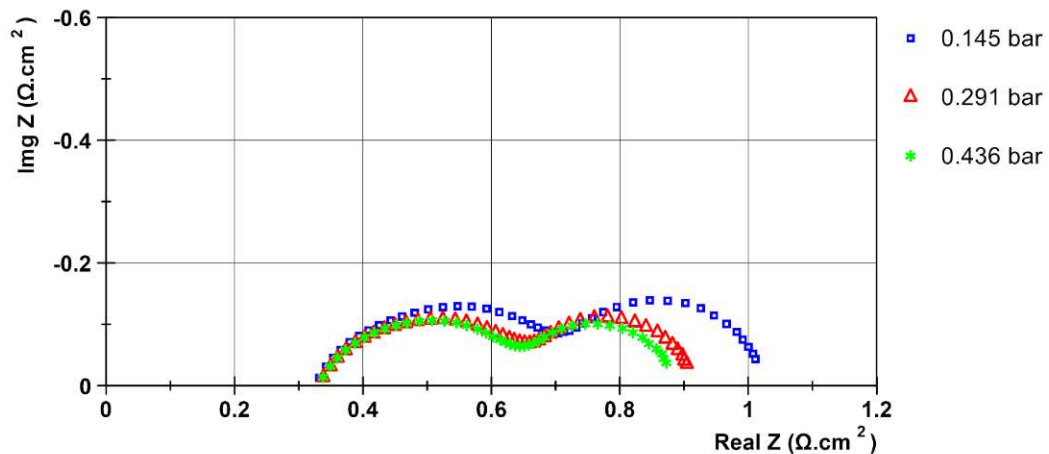


Figure 7.13: EIS curves at 1 A (0.0625 A/cm<sup>2</sup>) for P<sub>H<sub>2</sub></sub> of 0.145, 0.291 and 0.436 bar

The same trend was observed for the EIS curves taken at 0.1875 and 0.375 A/cm<sup>2</sup> as demonstrated in figure 7.14 and figure 7.15, respectively. However, for the case of 0.375 A/cm<sup>2</sup> the EIS curve yielded a larger value for the ohmic resistance at 0.145 bar as the corresponding operating point fell within the concentration losses region.

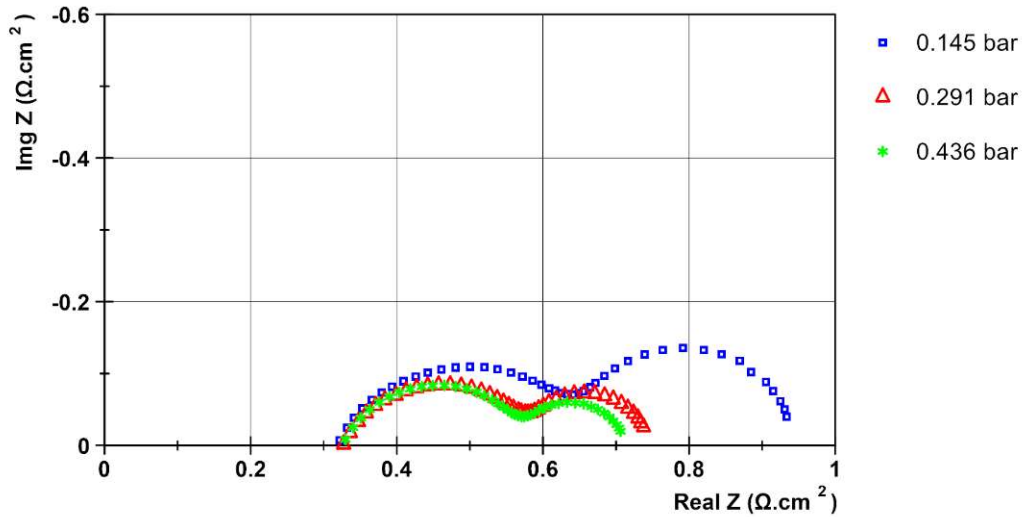


Figure 7.14: EIS curves at 3 A ( $0.1875 \text{ A/cm}^2$ ) for  $P_{\text{H}_2}$  of 0.145, 0.291 and 0.436 bar

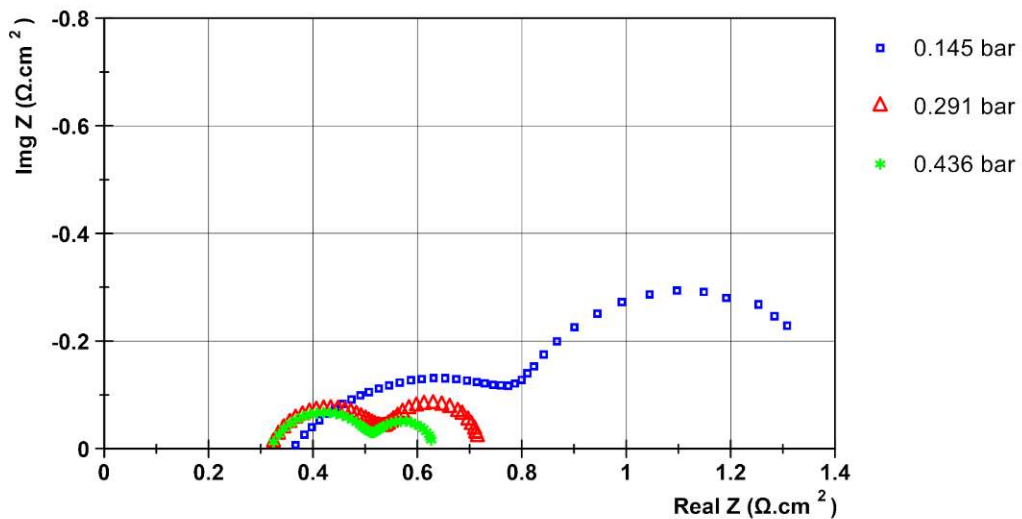


Figure 7.15: EIS curves at 6 A ( $0.375 \text{ A/cm}^2$ ) for  $P_{\text{H}_2}$  of 0.145, 0.291 and 0.436 bar

In accordance with the results, it can be stated that the decrease in the  $\text{H}_2$  partial pressure causes an increase in the electrode resistance, however, the ohmic resistance remains constant. Once the concentration of  $\text{H}_2$  is raised at the anode, the right-hand-side semi-circle of the EIS curves tends to create a smaller arch, while the left-hand-side semi-circle does not change significantly. The former arch corresponds to the lower frequencies and represents the diffusion effects at the electrodes, thus subject to change as the  $P_{\text{H}_2}$  is altered. This behaviour is the same as that reported in reference [142].

### 7.1.3 Effect of temperature (run 3)

The effect of temperature on the internal resistance of cell was studied in another run with the same cell. Theoretically, it is known that at higher operating temperatures the performance is improved, which results from the smaller resistance of cell.

The fuel composition in this run was 100 ml/min of H<sub>2</sub>, 566.67 ml/min of N<sub>2</sub> and 3 % of H<sub>2</sub>O. The profiles of voltage/temperature and voltage/flow rates are demonstrated in figure 7.16 and figure 7.17, respectively. As the first step of the test, the cell was loaded at 600 °C and 0.131 A/cm<sup>2</sup> (2.1 A), corresponding to 792 mV, for 18 hours to make sure it has stabilised.

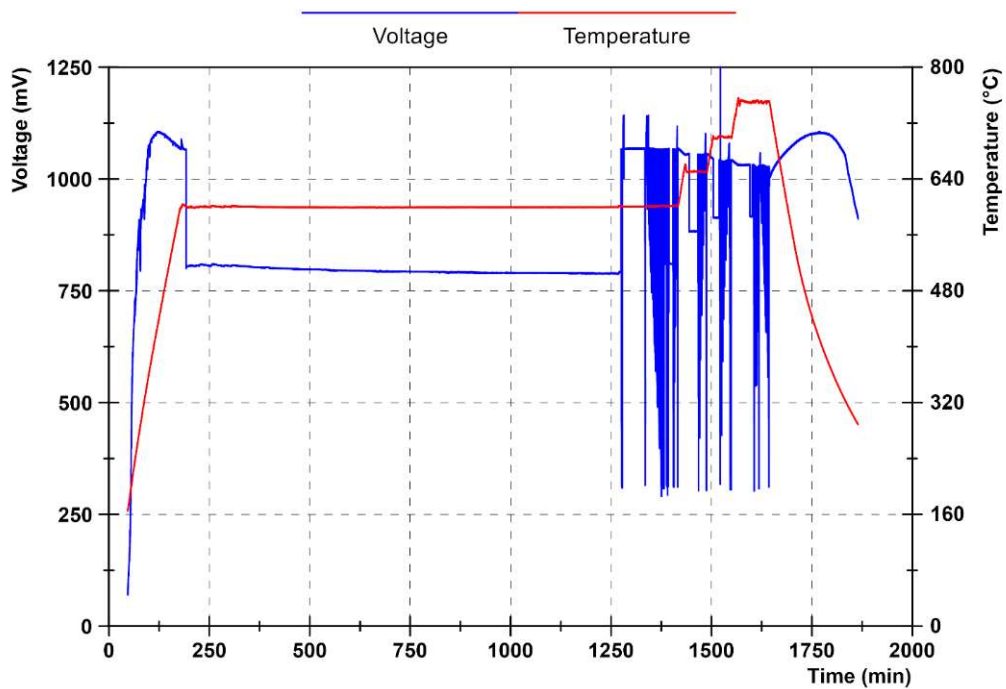


Figure 7.16: Profiles of voltage and temperature - cell 13 run 3

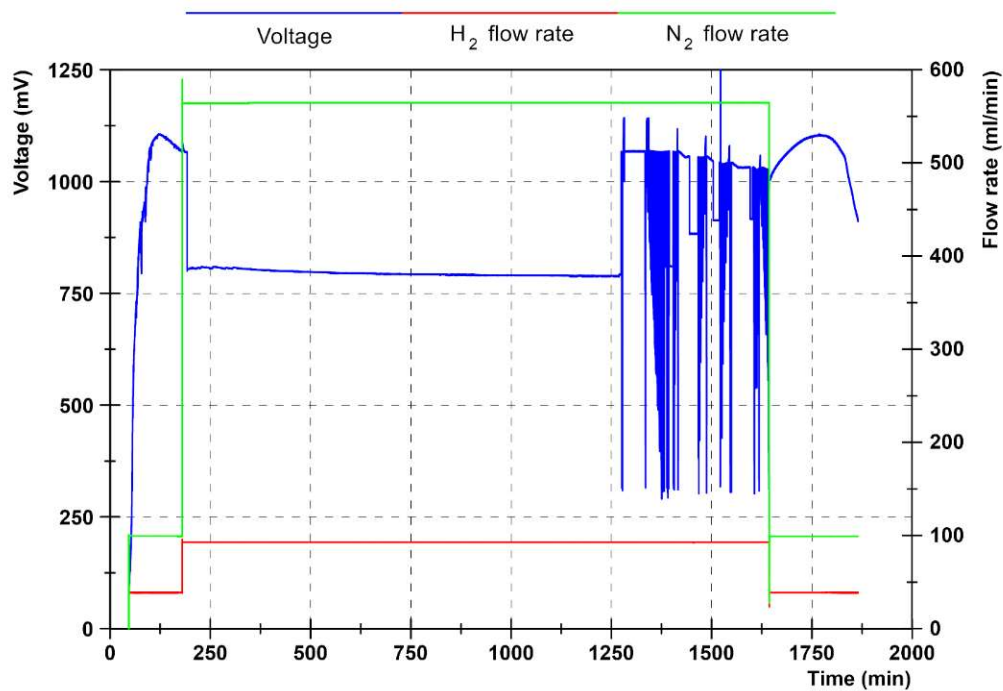


Figure 7.17: Profiles of voltage and flow rates - cell 13 run 3

The v-i and EIS curves were taken at four different values of operating temperature: 600, 650, 700 and 750 °C. The v-i curves, illustrated in figure 7.18, cover a wide range of current densities to show the cell performance in all regions including concentration losses area. As expected, the OCV decreased with temperature since the change in the Gibbs free energy of H<sub>2</sub> and O<sub>2</sub> reaction is larger at lower temperatures.

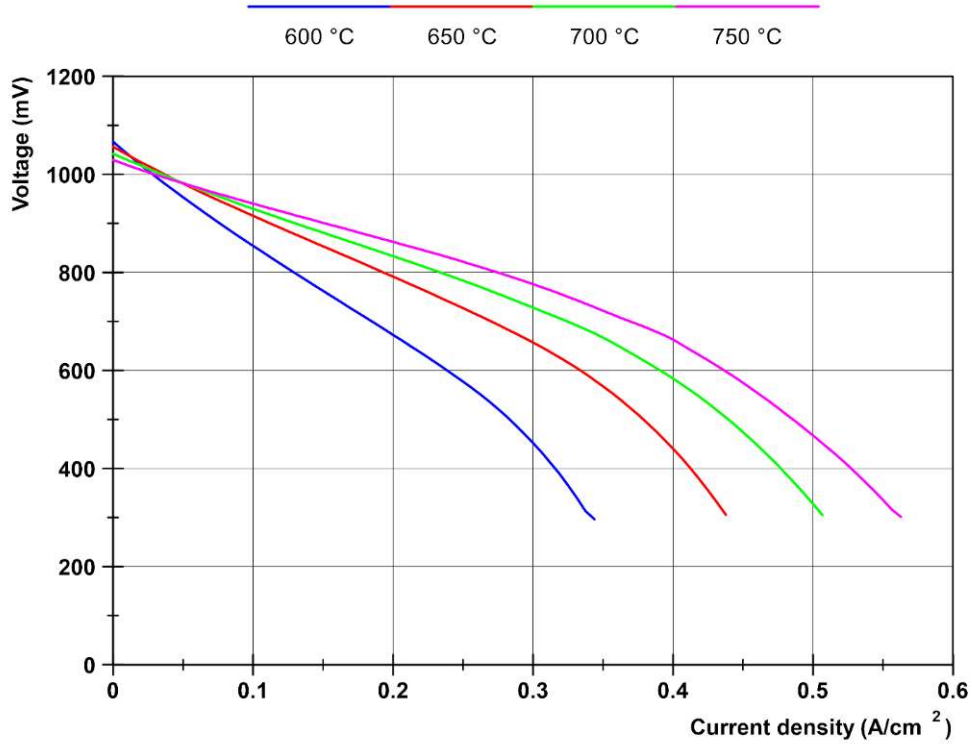


Figure 7.18: Profiles of v-i curves – cell 13 run 3

The profiles of the EIS curves at different current densities for each temperature have been shown in figure 7.19 to figure 7.22.

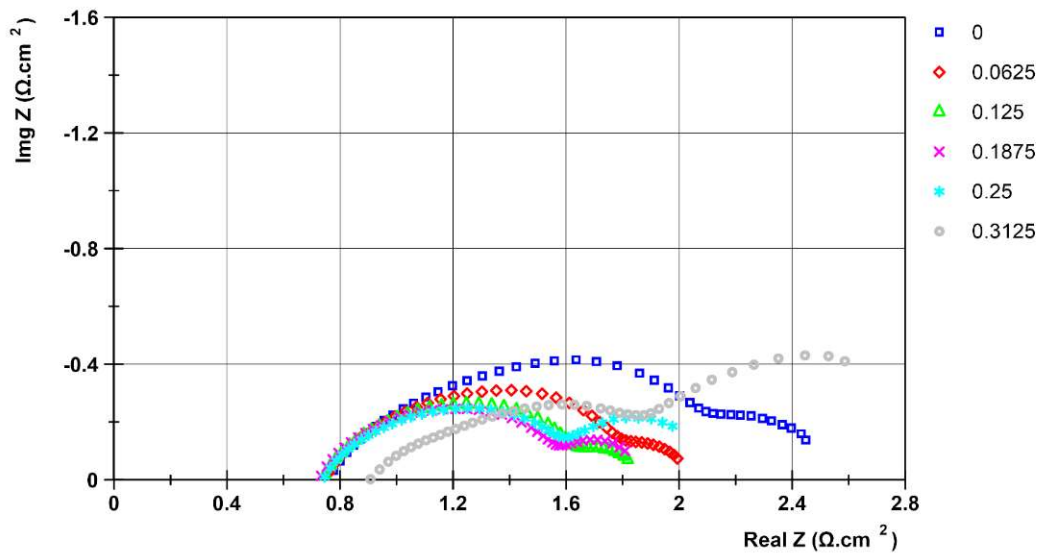


Figure 7.19: EIS curves at different current densities (A/cm<sup>2</sup>) for 600 °C

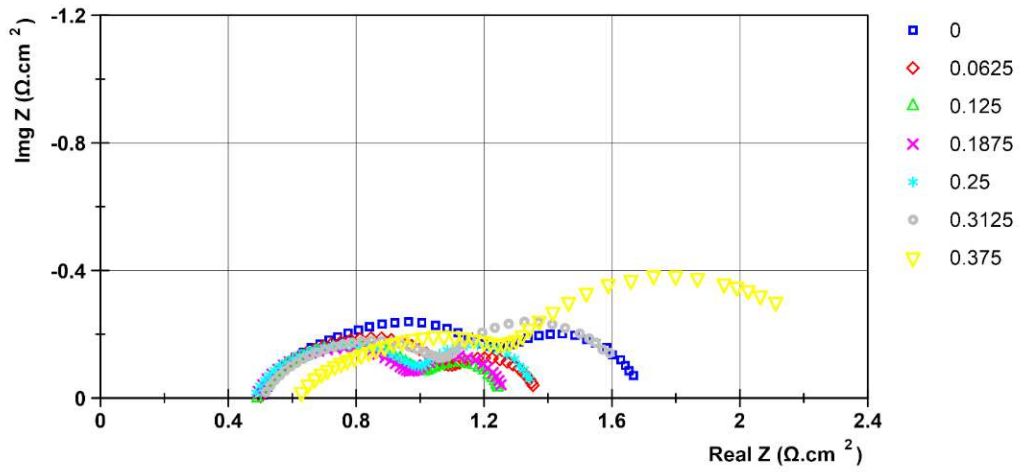


Figure 7.20: EIS curves at different current densities (A/cm<sup>2</sup>) for 650 °C

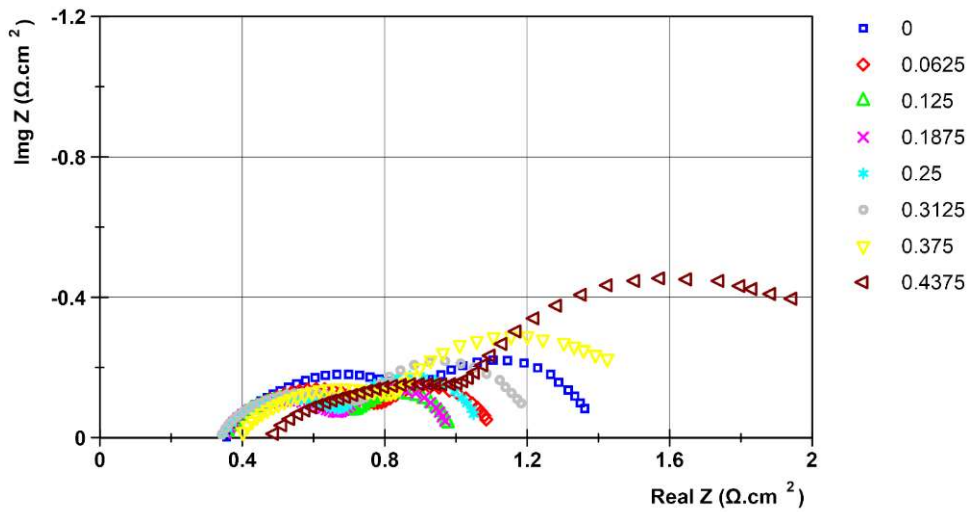


Figure 7.21: EIS curves at different current densities (A/cm<sup>2</sup>) for 700 °C

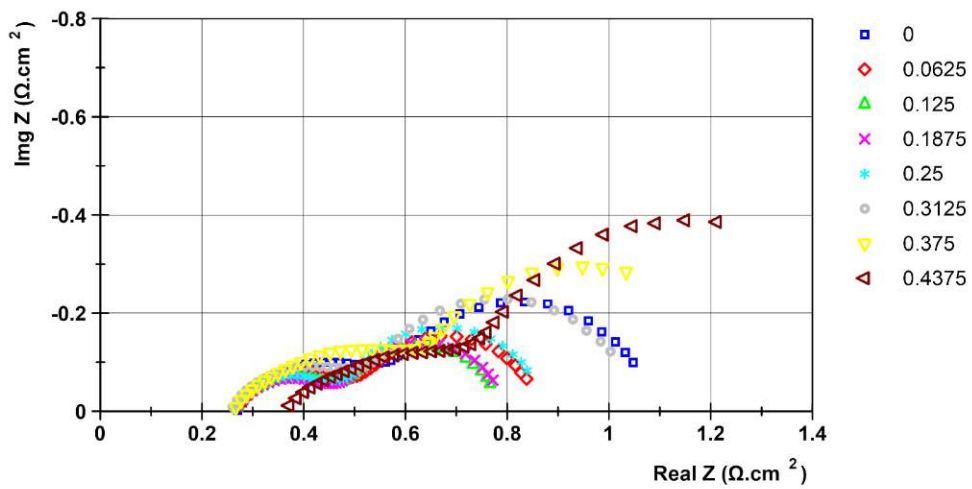


Figure 7.22: EIS curves at different current densities (A/cm<sup>2</sup>) for 750 °C

As can be seen in the above figures, the ohmic resistance is almost constant over a large range of current densities for each temperature, however, it grows at high current densities. As illustrated in figure 7.18, the start of the concentration losses region is 0.24, 0.31, 0.36 A/cm<sup>2</sup> and 0.4 for 600, 650, 700 and 750 °C, respectively. Thus, higher temperature retards the onset of the concentration losses region. At 600 °C the largest ohmic resistance occurred at 0.3125 A/cm<sup>2</sup> which is within the concentration losses area. At 650, 700 and 750 °C the jump in the ohmic resistance was observed at 0.375, 0.375 and 0.4375 A/cm<sup>2</sup>, respectively; all these current densities are within the corresponding concentration losses region suggesting that the rise is associated with this region.

A comparison of the EIS curves taken at 1A (0.0625 A/cm<sup>2</sup>) for different temperatures has been illustrated in figure 7.23. Similar graphs have been plotted in figure 7.24 and figure 7.25 for 3A (0.1875 A/cm<sup>2</sup>) and 5A (0.3125 A/cm<sup>2</sup>). It can be seen in all these figures that the ohmic resistance tends to decrease with temperature; this results from the fact that the ionic conductivity of electrolyte (as the major component of the ohmic resistance) improves as the operating temperature is elevated, as discussed in the first chapter.

In figure 7.23 to figure 7.25 it can be also seen that the increase in the temperature tends to decrease the activation/concentration resistance of the cell. In accordance with the definitions, the activation overpotential is a portion of energy which is consumed by reactants to overcome the reaction barrier. Thus, at higher temperatures a part of the required activation energy comes from the high temperature of the environment which results in smaller percentages of the cell power consumed by reacting species to take part in reactions. It is also known from theory that at higher temperatures the diffusion of gases in electrodes is improved, giving a decrease to the concentration losses.

Once the temperature is varied the left-hand-side arch on the EIS curve changes, while the other does not change significantly. The left-hand-side semi-circle is obtained at high frequencies and associated with the kinetics of the electrodes. Due to the fact that the kinetics of the cell strongly depends on the temperature and is favoured at higher temperature, the EIS curve yields a smaller vault for the corresponding semi-circle at higher values of temperature. The latter is in accordance with the trends stated in the literature [142].

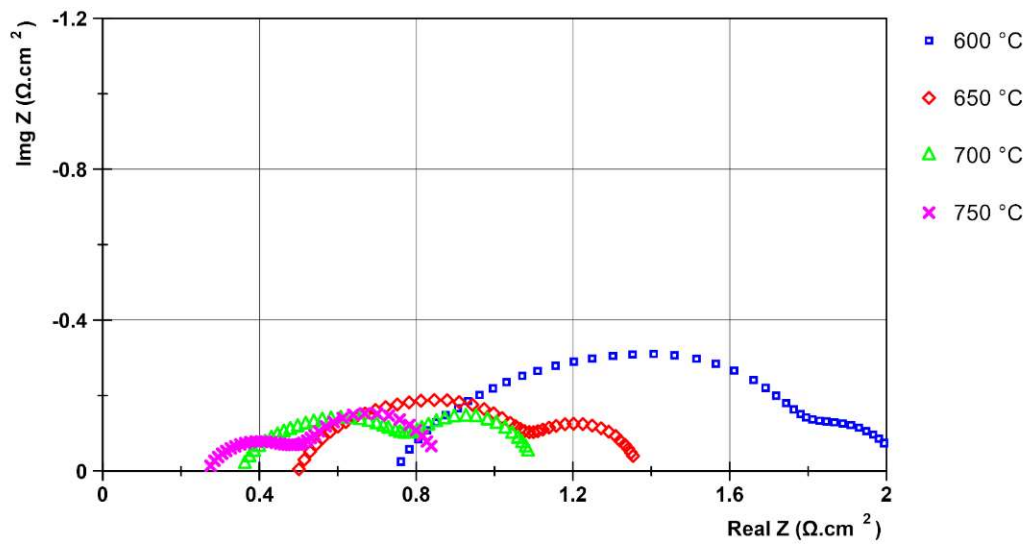


Figure 7.23: EIS curves at 1 A (0.0625 A/cm<sup>2</sup>) for 600, 650, 700 and 750 °C

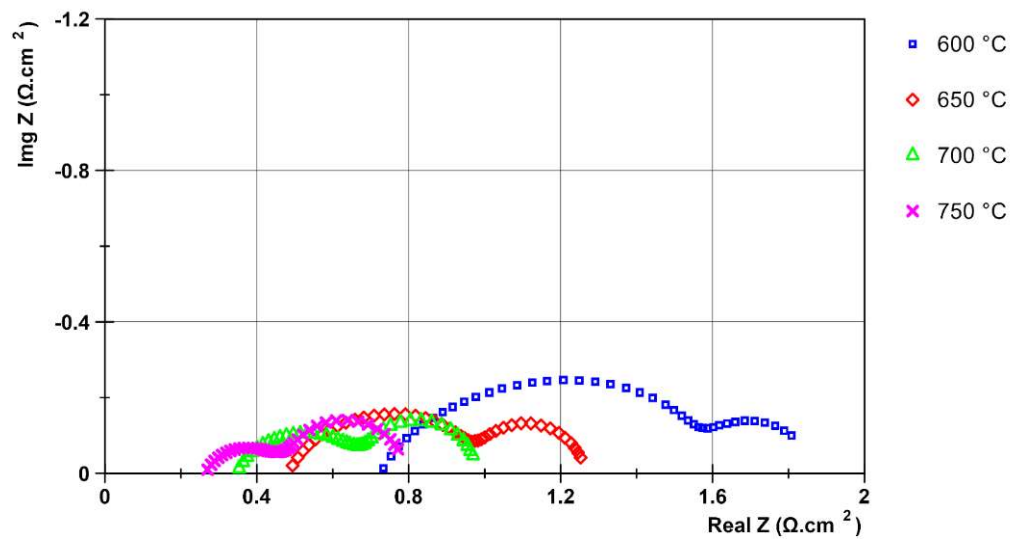


Figure 7.24: EIS curves at 3 A (0.1875 A/cm<sup>2</sup>) for 600, 650, 700 and 750 °C

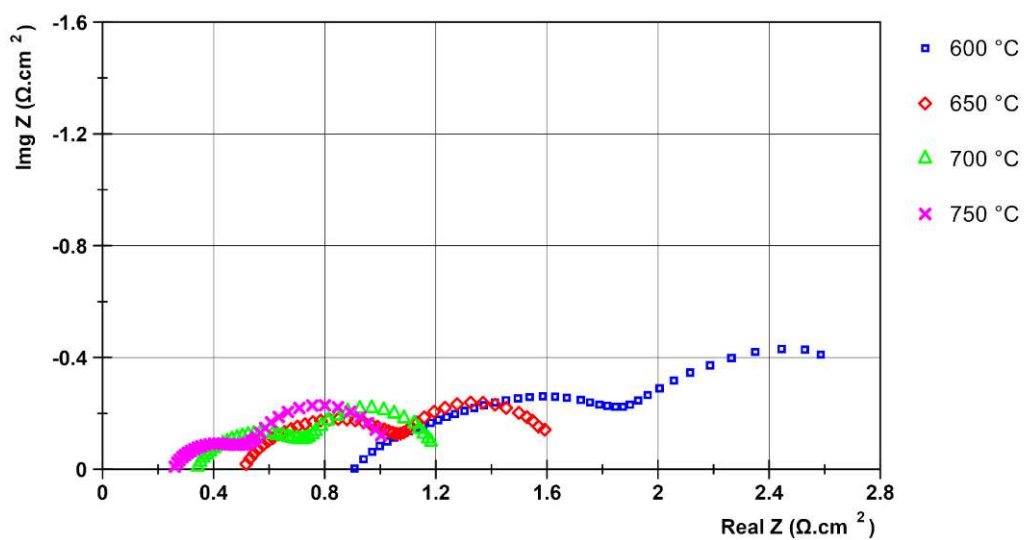


Figure 7.25: EIS curves at 5 A (0.3125 A/cm<sup>2</sup>) for 600, 650, 700 and 750 °C

Figure 7.26 demonstrates 3D plots of the EIS curve at four tested temperatures.

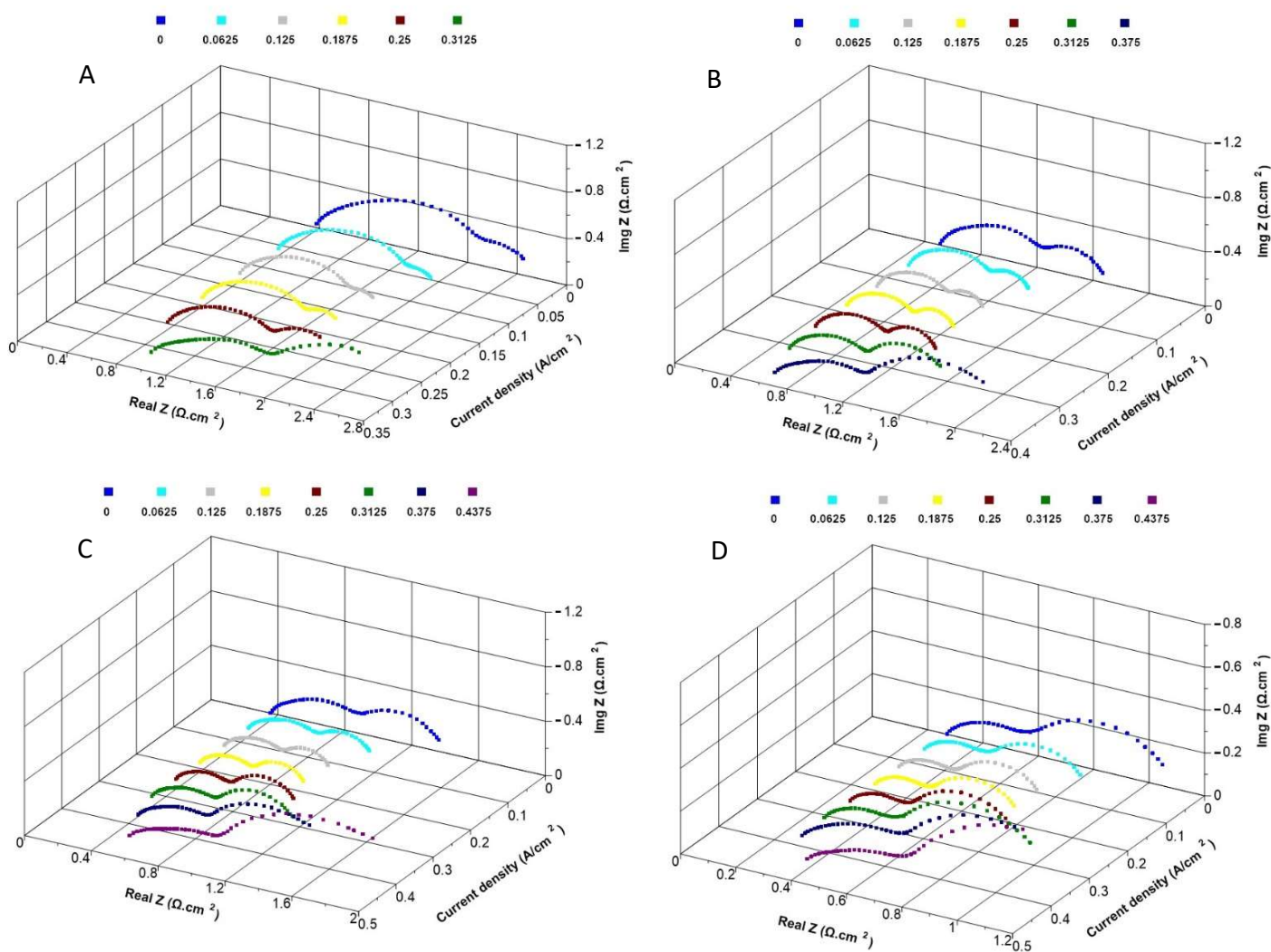


Figure 7.26: 3D plot of EIS curves – A: 600 °C, B: 650 °C, C: 700 °C, D: 750 °C

Looking at figure 7.26, it is observed that the current of lowest resistance is around  $0.15 \text{ A}/\text{cm}^2$  ( $2.4 \text{ A}$ ) for all four temperatures, although the lowest resistance of the cell drops at lower temperatures. Thus, it can be stated that the current of lowest resistance is independent of temperature, whereas the value of the corresponding resistance depends on the operating temperature.

## 7.2 Contamination tests

In this section the results of the tests with contaminated fuel are presented. Four levels of  $\text{H}_2\text{S}$  contamination has been considered in this research: 50, 100, 150 and 200 ppm. All tests were carried out at  $700 \text{ }^\circ\text{C}$ .

### 7.2.1 50 ppm (cell 14)

In this experiment a new cell was mounted in the set up in order to test the performance in the presence of 50 ppm of H<sub>2</sub>S at 700 °C. The profiles of voltage/temperature and voltage/flow rates are illustrated in figure 7.27 and figure 7.28, respectively. The fuel composition was 100 ml/min of H<sub>2</sub>, 566.67 ml/min of N<sub>2</sub> and 3 % of H<sub>2</sub>O. The results of the durability period can be summarized as:

- Maximum OCV: 1078 mV at 478 °C (low flow rate – observed while heating)
- OCV at 700 °C and normal flow rate: 1050 mV
- Voltage at @ 200 mA/cm<sup>2</sup> and 700 °C: 899 mV (at the beginning of the durability period)
- Voltage at @ 200 mA/cm<sup>2</sup> and 700 °C: 748 mV (at the end of the durability period)
- 151 mV drop over 95 hours of durability

As can be seen in the above figures, the voltage started to drop at the beginning of the durability test (cell was loaded at 0.2 A/cm<sup>2</sup>) and stabilised after about 85 hours. The whole durability period was 95 hours, thus, the voltage remained almost constant for the last 10 hours. At this point, 50 ppm of H<sub>2</sub>S was introduced to the fuel mixture for 12 hours under the same operating conditions. As a result, the voltage started to decrease sharply after 9 minutes followed by a secondary drop slower than the initial one. After 12 hours of exposure to the contaminated fuel, a recovery period was started in which H<sub>2</sub>S was removed and cell was exposed to clean fuel mixture for 24 hours.

The EIS and v-i curves were taken every 5 hours during the stabilisation period, and also after H<sub>2</sub>S exposure and recovery periods. Figure 7.29 shows the v-i curves in steps of 20 hours. As demonstrated, the v-i curves after 85 and 95 hours did overlap stating that the voltage was stable within the last 10 hours of the durability period.

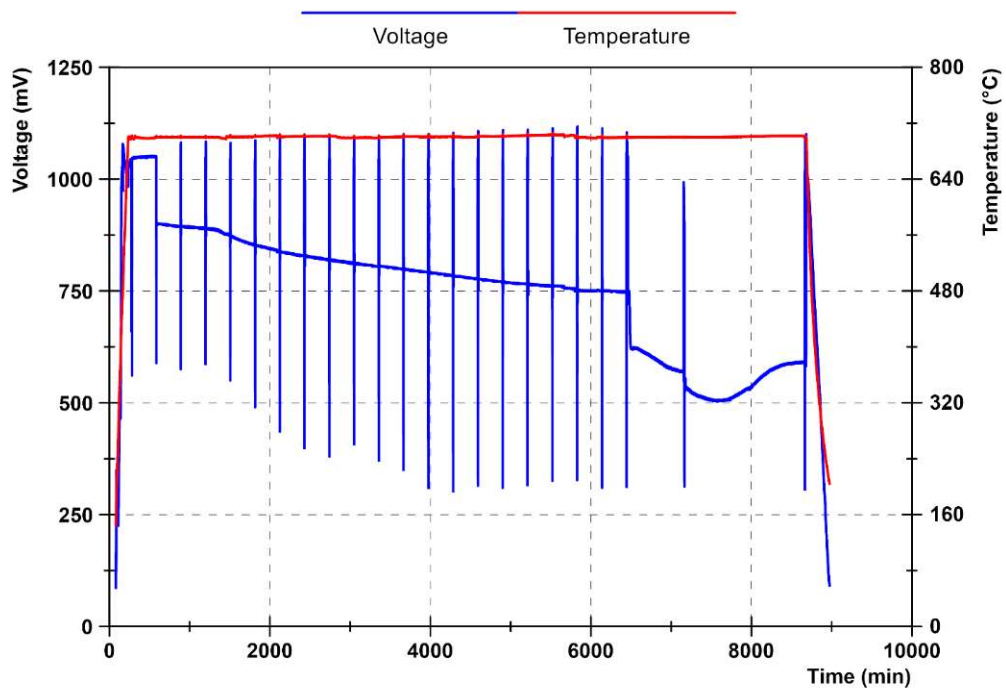


Figure 7.27: Profiles of voltage and temperature - cell 14

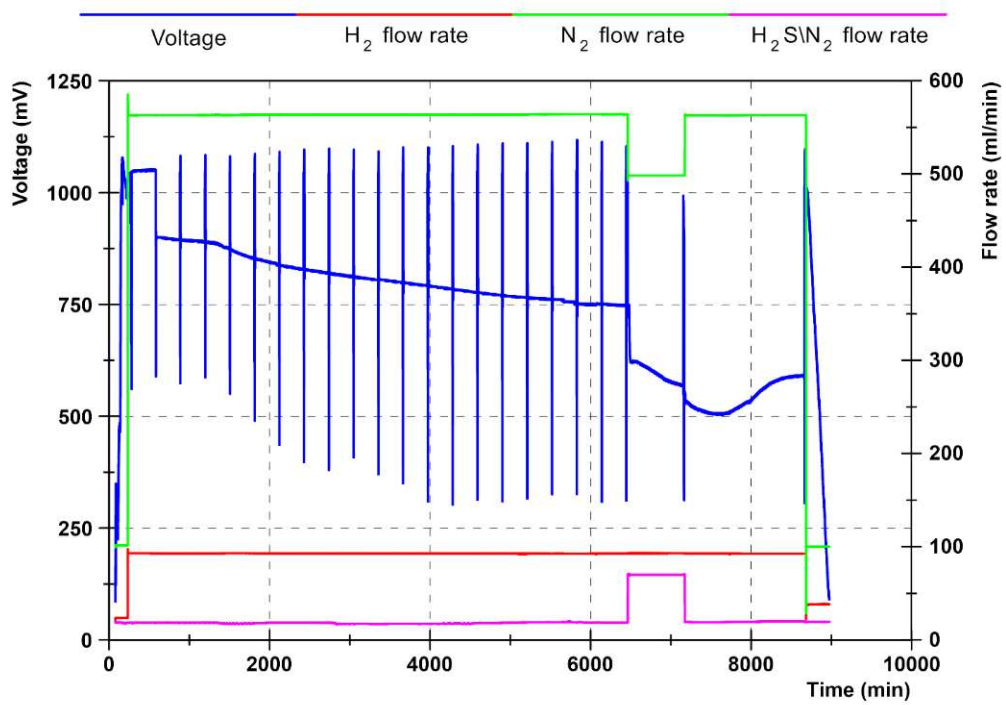


Figure 7.28: Profiles of voltage and flow rates - cell 14

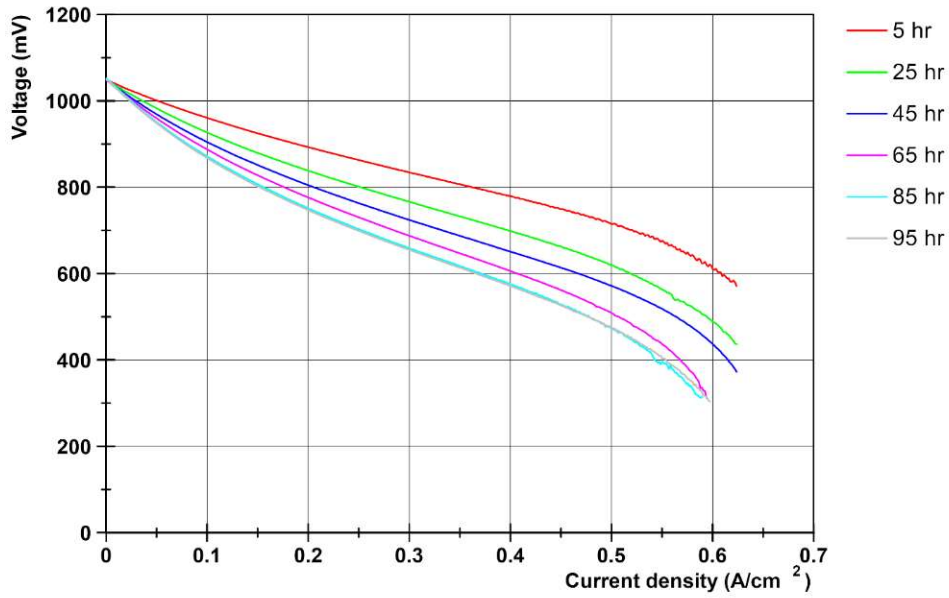


Figure 7.29: Profiles of v-i curves during stabilisation period – cell 14

The EIS curves at OCV and  $0.2 \text{ A/cm}^2$  are illustrated in figure 7.30 and figure 7.31, respectively. These figures also show that the performance was constant for the last 10 hours of durability period as the corresponding curves were overlapping. The results of  $\text{H}_2\text{S}$  exposure and recovery periods will be presented and discussed in the next chapter.

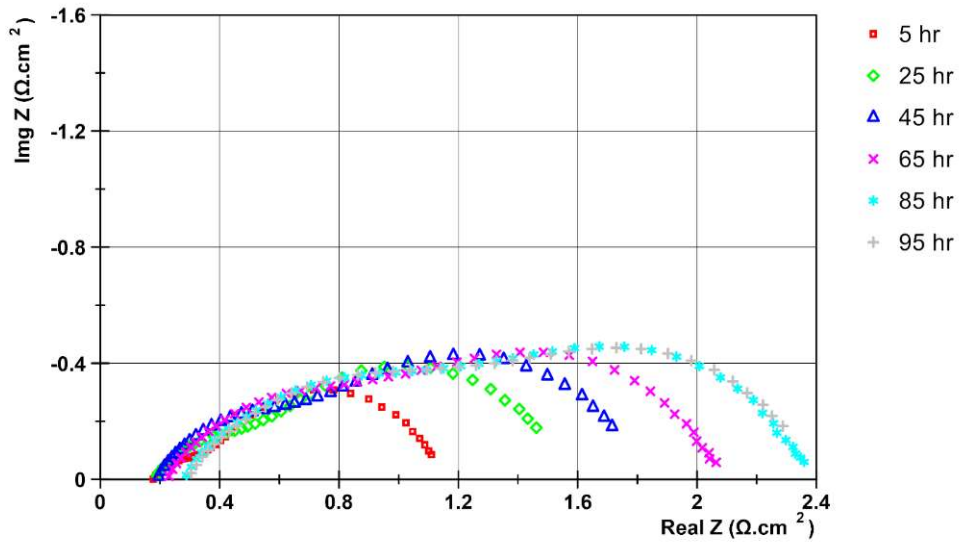


Figure 7.30: Profiles of EIS curves at OCV during durability period - cell 14

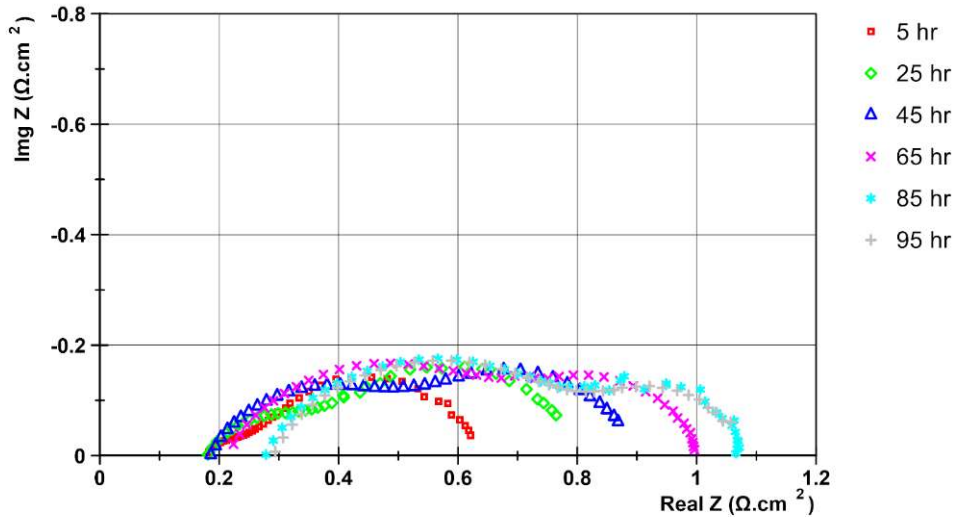


Figure 7.31: Profiles of EIS curves at 0.2 A/cm<sup>2</sup> during durability period - cell 14

### 7.2.2 100 ppm (cell 15)

For the test with 100 ppm of H<sub>2</sub>S another cell was mounted in the set up and was heated up to 700 °C under the same operating conditions as the previous test. The results of the durability period can be summarized as:

- Maximum OCV: 1069 mV at 548 °C (low flow rate – observed while heating)
- OCV at 700 °C and normal flow rate: 1049 mV
- Voltage at @ 200 mA/cm<sup>2</sup> and 700 °C: 814 mV (at the beginning of the durability period)
- Voltage at @ 200 mA/cm<sup>2</sup> and 700 °C: 467 mV (at the end of the durability period)
- 347 mV drop over 85 hours of durability

Figure 7.32 and figure 7.33 show the profiles of voltage/temperature and voltage/flow rates during the whole test. In this test the voltage significantly dropped over the stabilization period and finally stabilized at a much lower value compared to the previous tests. Once stabilized, 100 ppm of H<sub>2</sub>S was introduced in the fuel mixture for 5 hours causing the voltage to start dropping after 5 minutes. At the end of the exposure time the voltage of the cell was 140 mV. At this point H<sub>2</sub>S was removed in order to start the recovery period with clean fuel for 19.5 hours. However, the voltage dropped to 10 mV after about 45 minutes and the rest of the recovery period was carried out at OCV. Before this point the cell had been

loaded at 0.2 A/cm<sup>2</sup> throughout stabilization, H<sub>2</sub>S exposure period and early stages of the recovery duration.

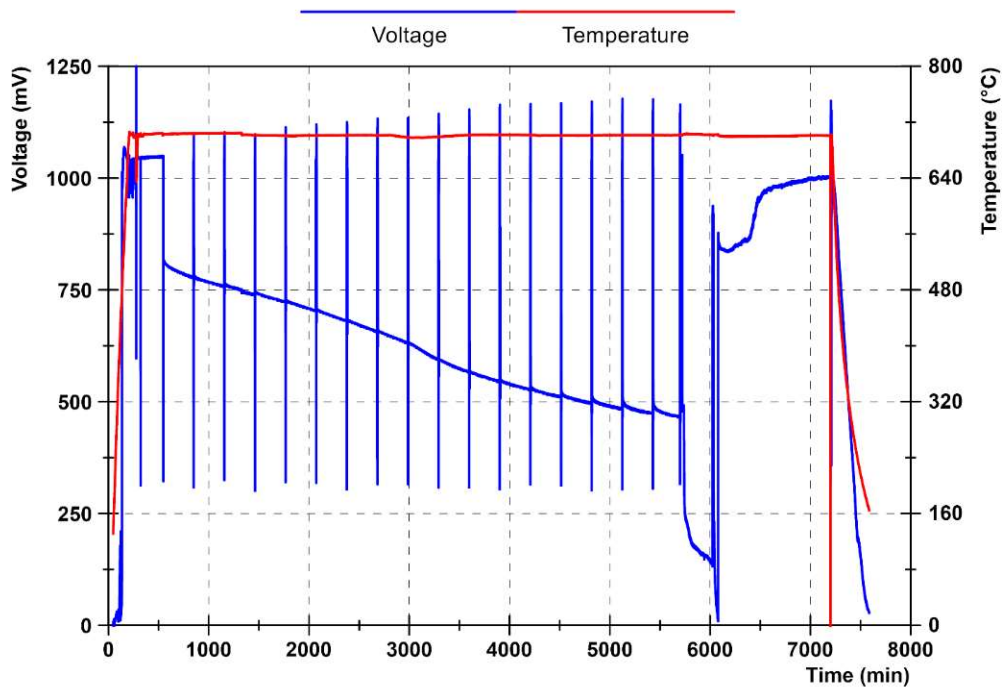


Figure 7.32: Profiles of voltage and temperature - cell 15

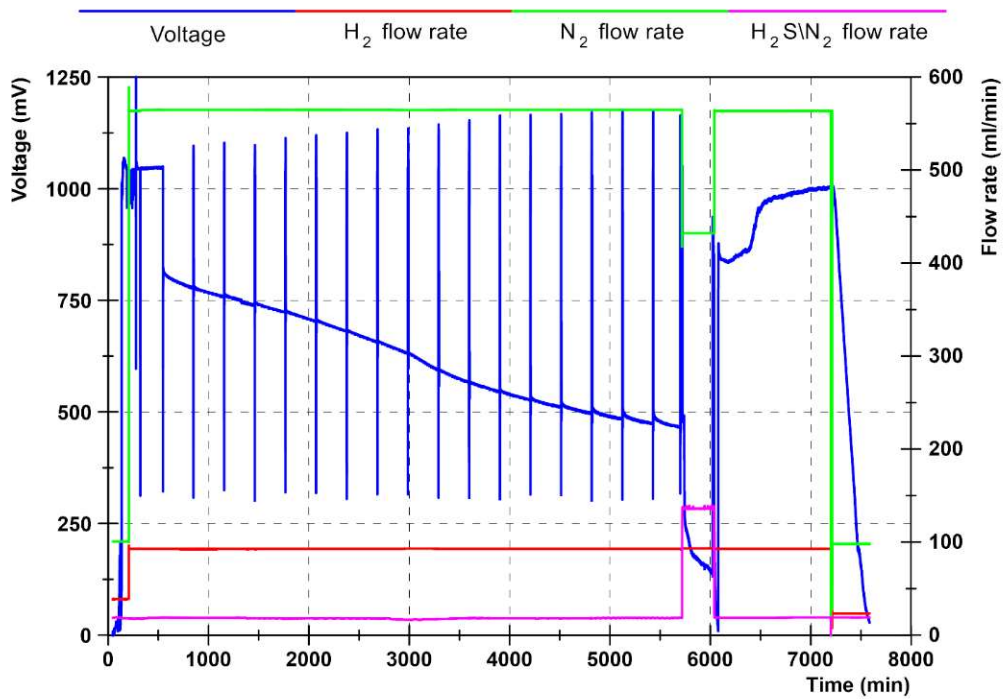


Figure 7.33: Profiles of voltage and flow rates - cell 15

The curves of v-i, EIS at OCV and EIS at 0.2 A/cm<sup>2</sup> over the stabilization period are shown in figure 7.34, figure 7.35 and figure 7.36, respectively. As illustrated, the performance of the cell almost stabilizes after 85 hours of durability. This was the point at which 100 ppm of H<sub>2</sub>S was added to the fuel mixture.

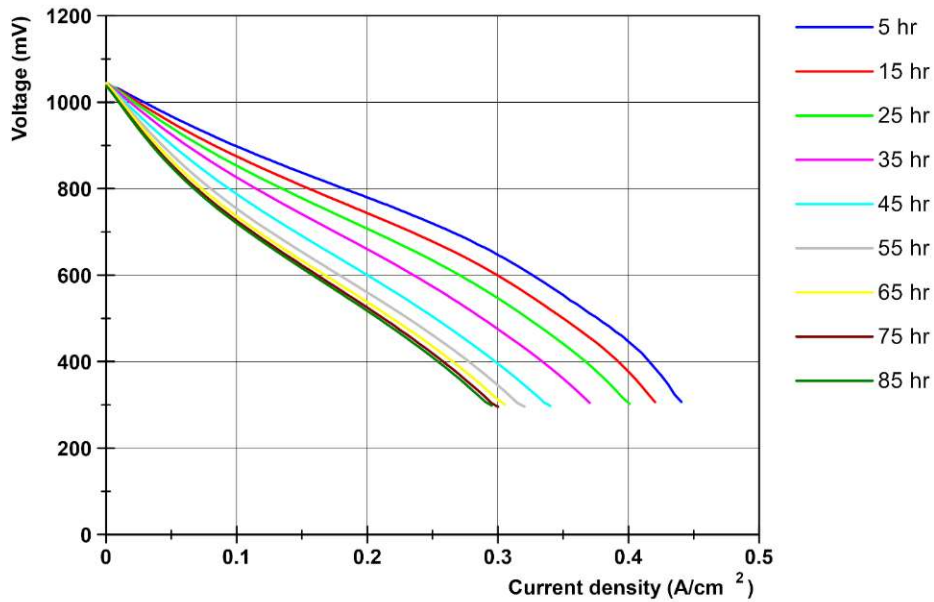


Figure 7.34: Profiles of v-i curves during stabilisation period – cell 15

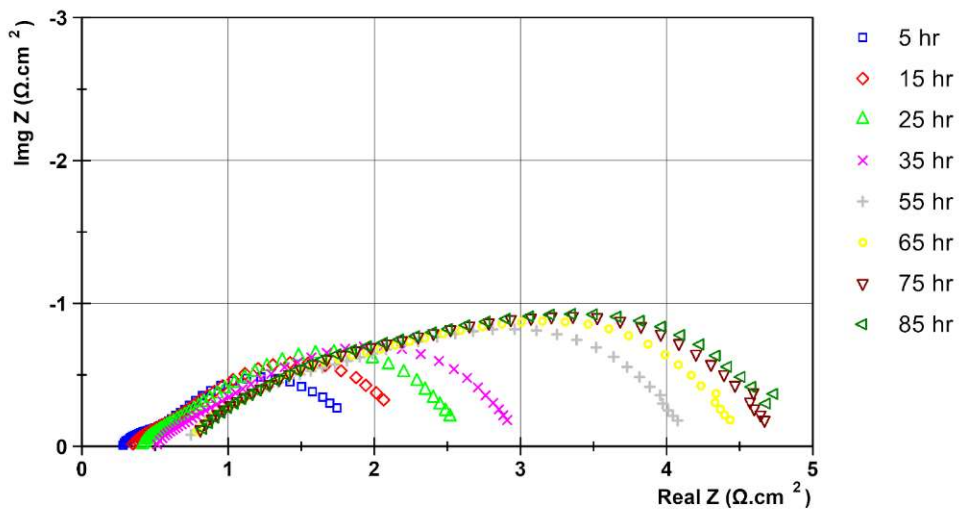


Figure 7.35: Profiles of EIS curves at OCV during durability period - cell 15

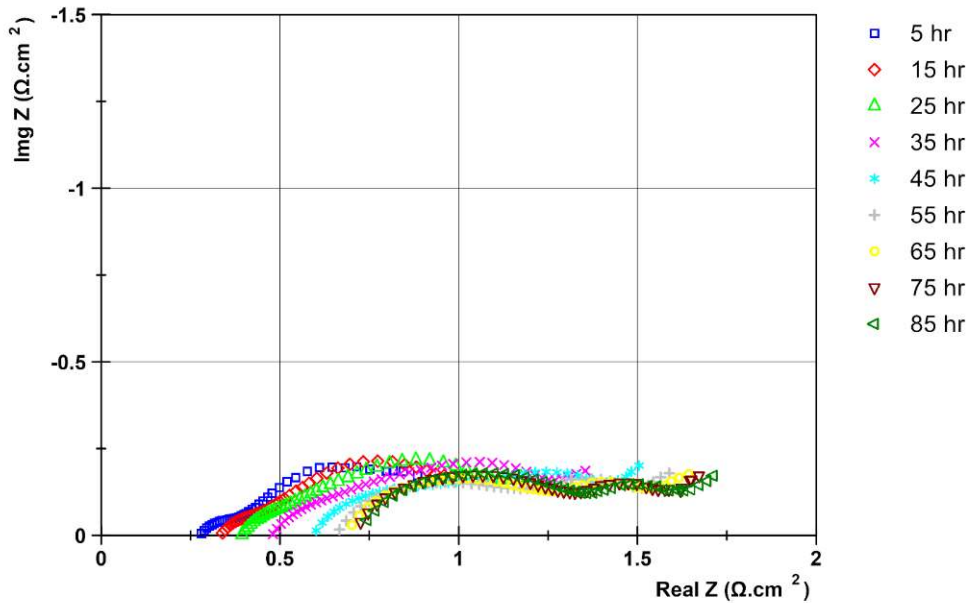


Figure 7.36: Profiles of EIS curves at 0.2 A/cm<sup>2</sup> during durability period - cell 15

In the next chapter the results of the H<sub>2</sub>S exposure and recovery periods will be demonstrated and discussed.

### 7.2.3 150 ppm (cell 13 run 4)

In order to investigate whether the low performance observed in the last test was due to cell or set up preparation, a used cell, previously proved to be functional, was mounted in the set up. The heating procedure and operating conditions were the same as the earlier tests. The profiles of voltage/temperature and voltage/flow rates against time are illustrated in figure 7.37 and figure 7.38, respectively.

As can be seen in the figures, the voltage stabilized at 756 mV after about 15 hours of running at 0.2 A/cm<sup>2</sup>. After 20 hours of stabilization 150 ppm of hydrogen sulfide was added to the fuel mixture for a duration of 11 hours. After 3 minutes of H<sub>2</sub>S addition to the fuel, the cell voltage started to drop sharply as expected, however, it recovered slightly and then slowly decreased during the exposure period. A 24-hour long recovery period, then, followed the exposure time to monitor the performance of the poisoned cell operating on clean fuel. After about 6.4 hours the voltage dropped to 10 mV, thus, the cell was unloaded and continued recovering at OCV.

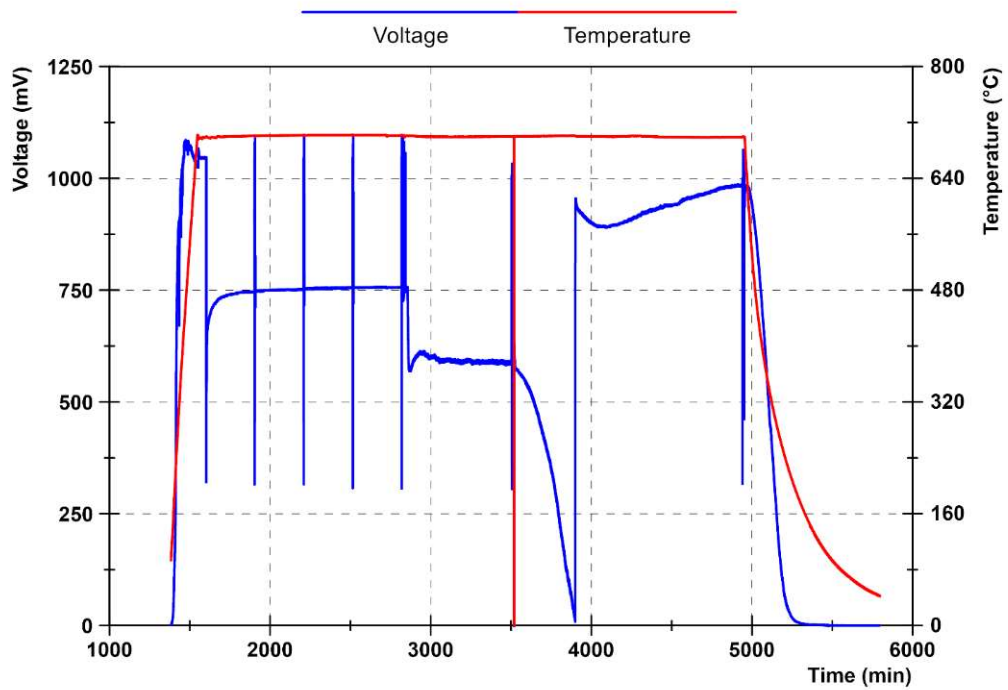


Figure 7.37: Profiles of voltage and temperature – cell 13 run 4

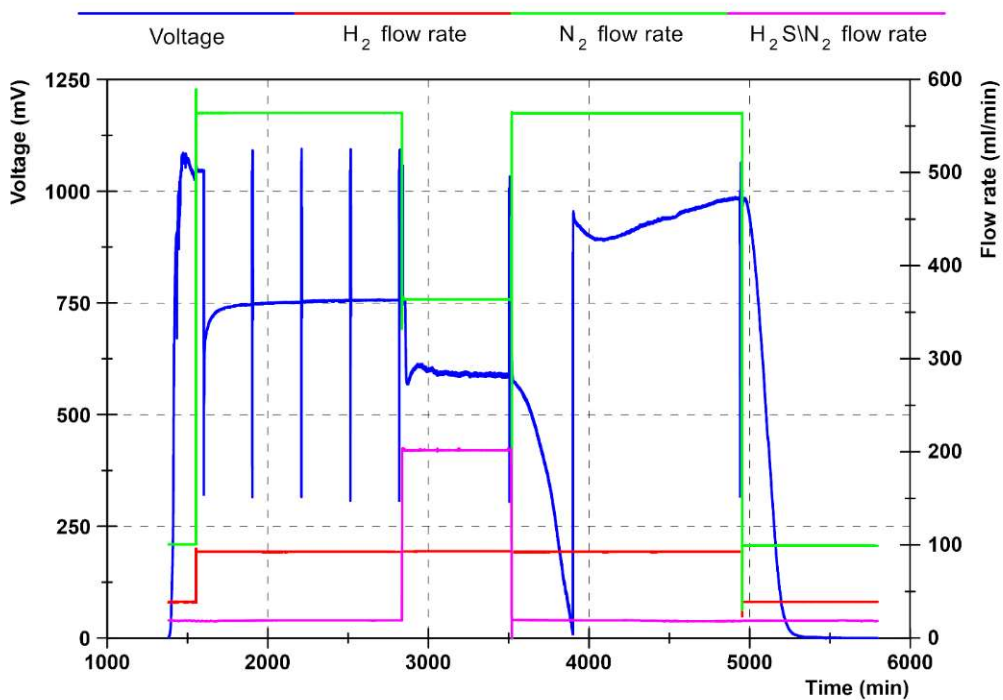


Figure 7.38: Profiles of voltage and flow rates - cell 13 run 4

The profiles of v-i curves, EIS curves at OCV and EIS curves at  $0.2 \text{ A/cm}^2$  are demonstrated in figure 7.39, figure 7.40 and figure 7.41, respectively. As can be seen, the curves taken after 15 and 20 hours have overlapped in all three figures

indicating that the cell has reached a stable operating point. At this point H<sub>2</sub>S was added to the fuel mixture to start the contamination test.

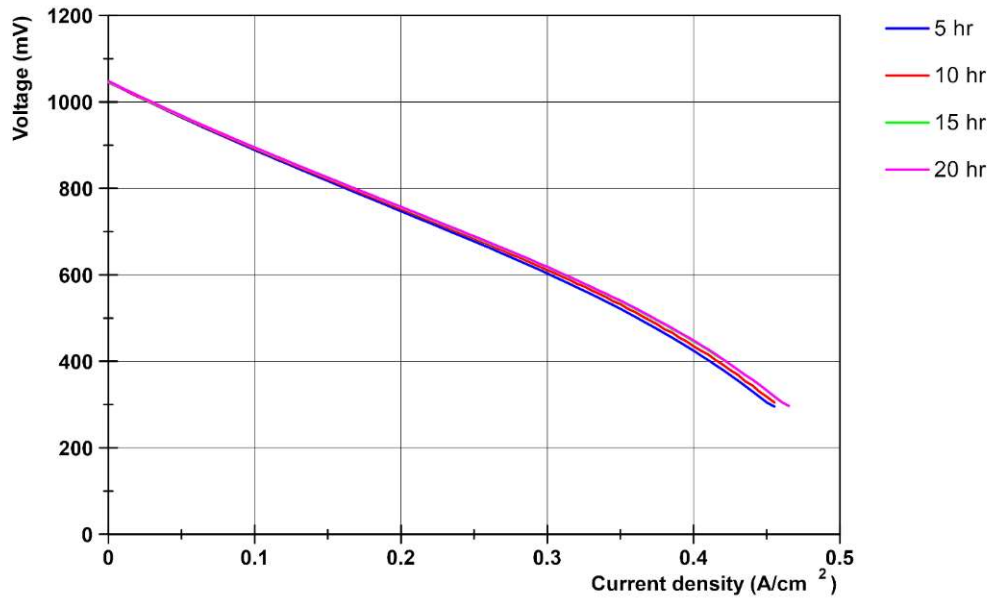


Figure 7.39: Profiles of v-i curves during stabilisation period – cell 13 run 4

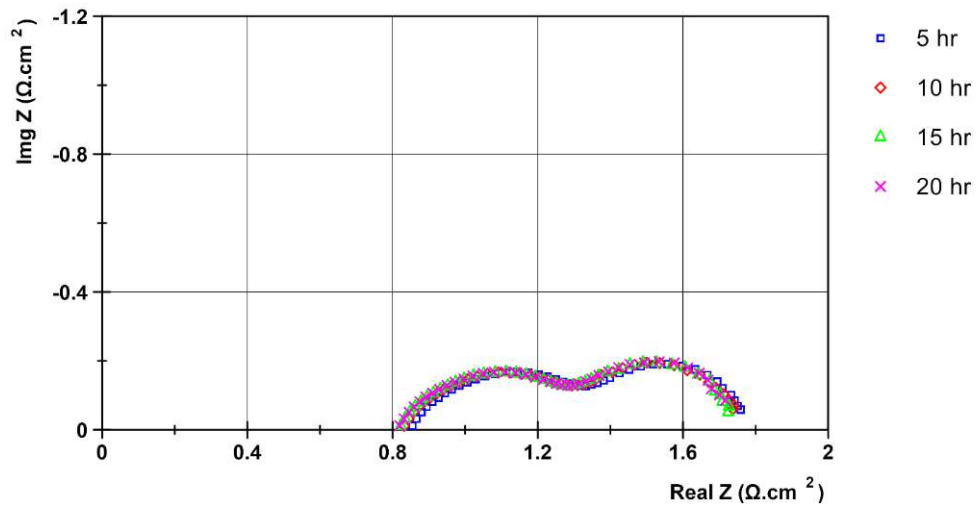


Figure 7.40: Profiles of EIS curves at OCV during durability period - cell 13 run 4

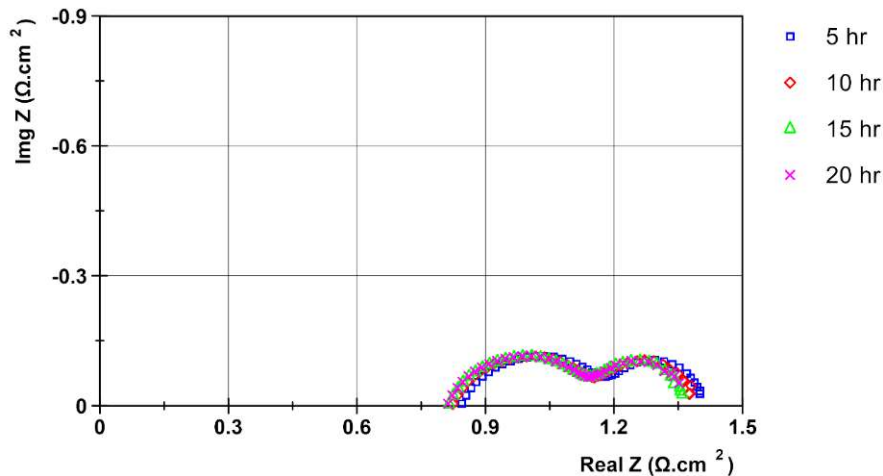


Figure 7.41: Profiles of EIS curves at 0.2 A/cm<sup>2</sup> during durability period – cell 13 run 4

Similar to the previous tests, the results of the exposure and recovery periods will be discussed in the next chapter.

#### 7.2.4 200 ppm (cell 16)

Another experiment was carried out with a new cell in order to investigate the cell performance with 200 ppm of H<sub>2</sub>S. The same procedure and operating conditions as the previous tests were applied in this test. The profiles of voltage/temperature and voltage/flow rates versus time are shown in and figure 7.42 and figure 7.43, respectively. The results of the initial stage and durability section of the test can be summarised as:

- Maximum OCV: 1096 mV at 449 °C (low flow rate – observed while heating)
- OCV at 700 °C and normal flow rate: 1049 mV
- Voltage at @ 200 mA/cm<sup>2</sup> and 700 °C: 906 mV (at the beginning of the durability period)
- Voltage at @ 200 mA/cm<sup>2</sup> and 700 °C: 881 mV (at the end of the durability period)
- 25 mV drop over 60 hours of durability

In order for the cell to stabilise it was loaded at 0.2 A/cm<sup>2</sup> at 700 °C for 60 hours. Once it stabilised 200 ppm of H<sub>2</sub>S was introduced in the fuel mixture for about 12 hours causing the voltage to drop sharply after 2 minutes of H<sub>2</sub>S addition. Then, the voltage recovered partially and for the rest of the exposure period a very slow voltage decrease was observed. The exposure period was followed by a recovery

duration in which the cell was exposed to clean fuel for 24 hours. After 19 hours of recovery the voltage dropped to 10 mV; at this point the cell was unloaded and continued recovering at OCV.

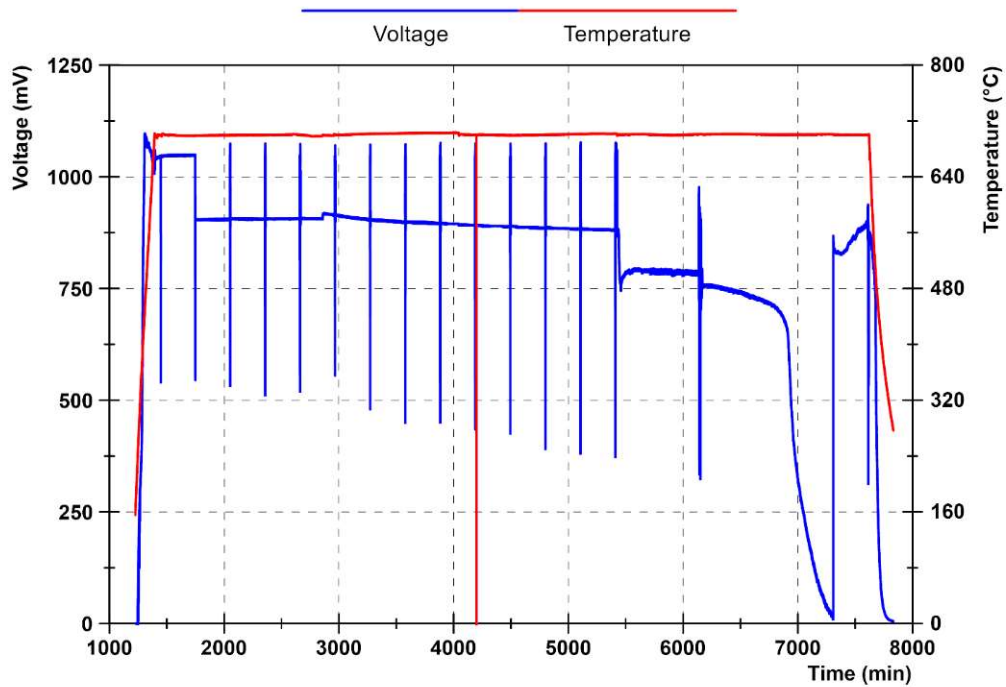


Figure 7.42: Profiles of voltage and temperature - cell 16

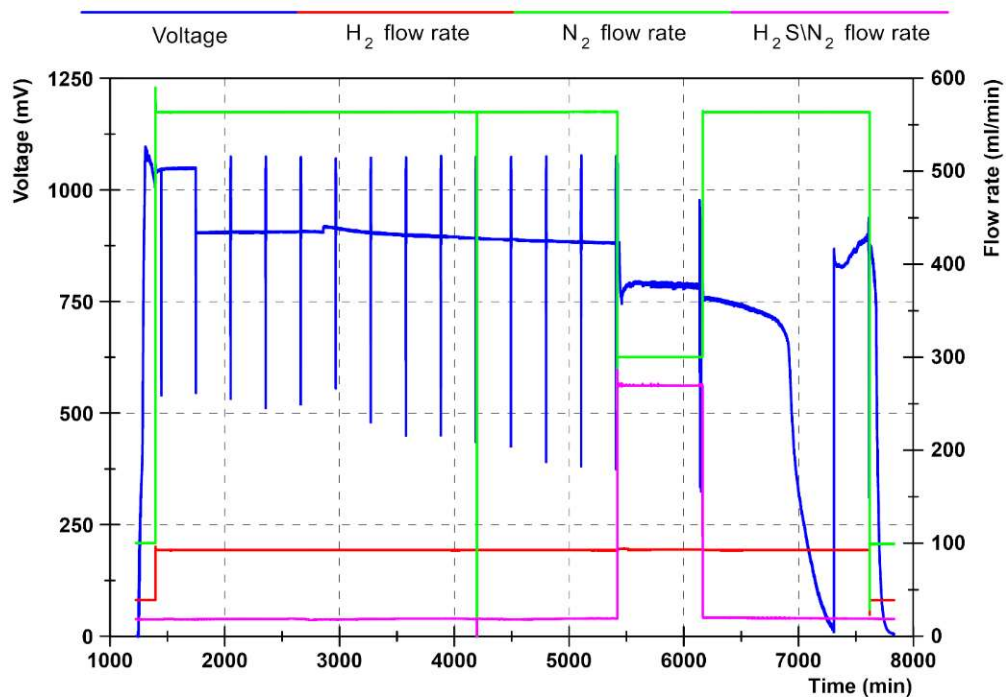


Figure 7.43: Profiles of voltage and flow rates - cell 16

The profiles of v-i curves, EIS curves at OCV and EIS curves at 0.2 A/cm<sup>2</sup> are demonstrated in figure 7.44, figure 7.45 and figure 7.46, respectively.

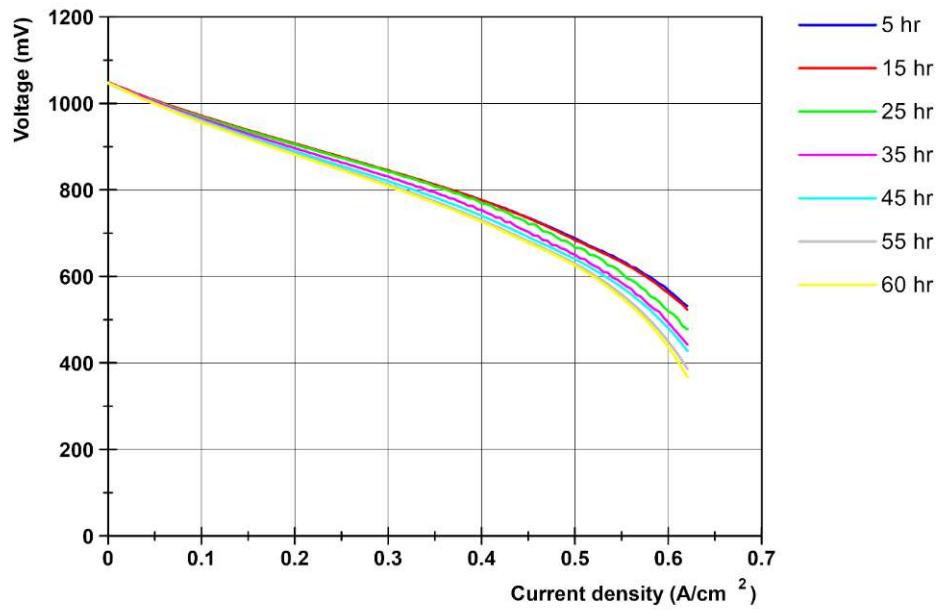


Figure 7.44: Profiles of v-i curves during stabilisation period – cell 16

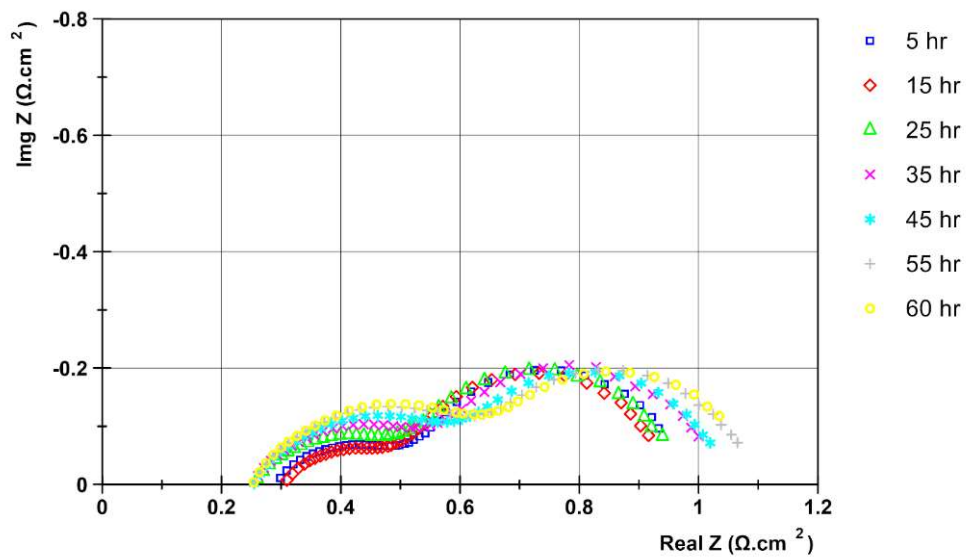


Figure 7.45: Profiles of EIS curves at OCV during durability period – cell 16

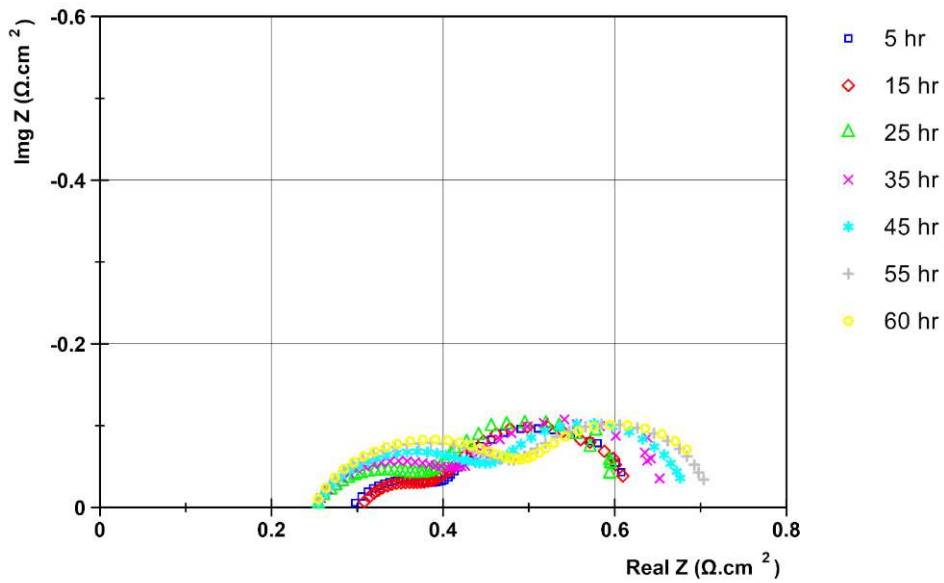


Figure 7.46: Profiles of EIS curves at 0.2 A/cm<sup>2</sup> during durability period – cell 16

As shown in the above figures the cell stabilised after 55 hours of durability since the graphs of 55 and 60 hours are overlapping in all three figures. The results of the H<sub>2</sub>S exposure and recovery sections will be explained and discussed in the next chapter.

### 7.2.5 Comparison of v-i and EIS curves before H<sub>2</sub>S exposure

Figure 7.47 illustrates the v-i curves for the contamination tests before exposure of H<sub>2</sub>S. As it can be seen in the figure, the performance of the cells in the 50 and 150 ppm test is almost similar at 0.2 A/cm<sup>2</sup>. However, the performance of the cell at the end of the stabilisation period of the 100 ppm test is lower compared to that of the other tests. On contrary, the cell tested in the 200 ppm test yielded the best performance.

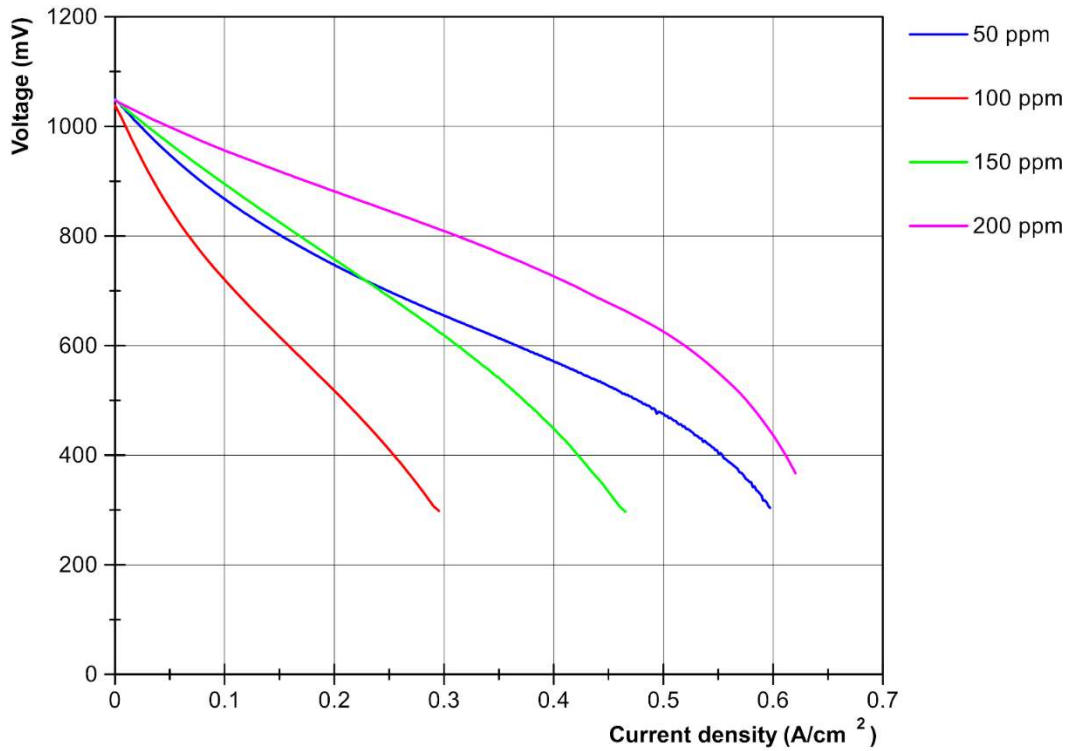


Figure 7.47: Comparison of the v-i curves before exposure to H<sub>2</sub>S

Figure 7.48 and figure 7.49 demonstrate the EIS response of the cells at OCV and 0.2 A/cm<sup>2</sup> before running H<sub>2</sub>S. Looking at the figures it is comprehended that the 100 ppm cell have the largest resistance among all the tested cells. It can also be seen that the profile of the EIS curve for this test differs from that of the other tests. This will be analysed and discussed in the next chapter of the thesis.

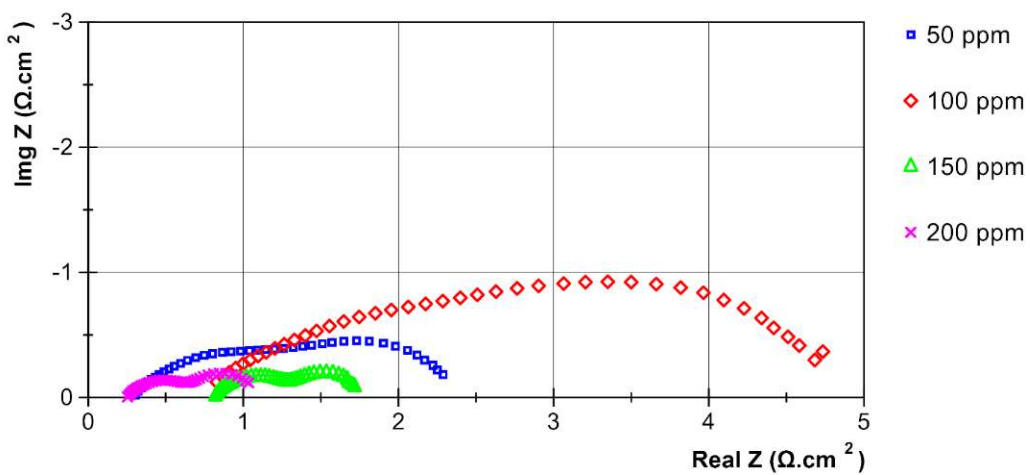


Figure 7.48: Comparison of the EIS curves at OCV before exposure to H<sub>2</sub>S

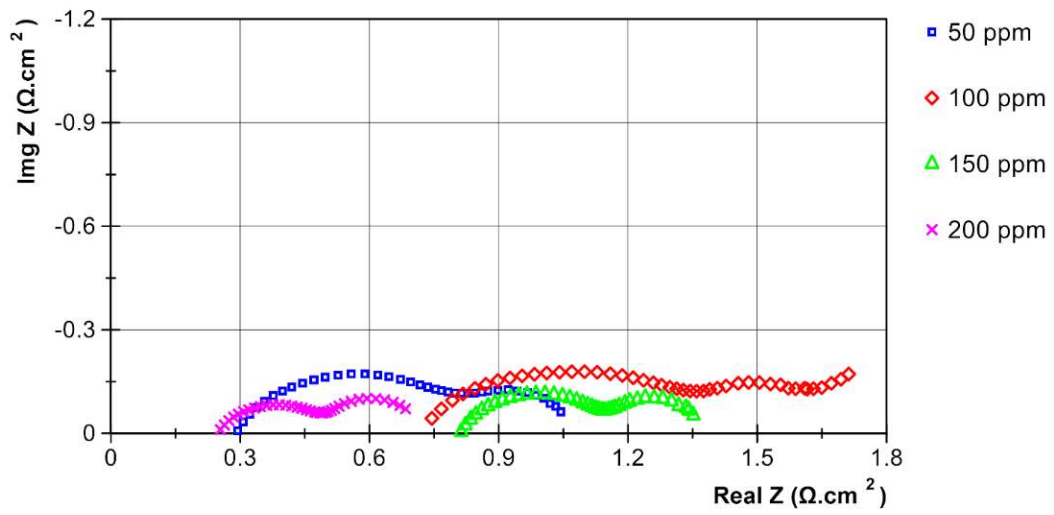


Figure 7.49: Comparison of the EIS curves at 0.2 A/cm<sup>2</sup> before exposure to H<sub>2</sub>S



## 8 Analysis and discussion

### 8.1 Baseline tests

In this section the results of cell 13 (baseline tests) are used to fit an electrical model and calculate the parameters of the equivalent circuit. As seen in figure 8.1, the equivalent circuit consists of an inductor, a resistor and two sets of parallel resistor and constant phase element (CPE). An inductor has been introduced to the circuit due to the presence of metal in fuel cell and wires. The resistor in series with the inductor takes into account the ohmic resistance of anode, cathode and electrolyte. The effect of each electrode is simulated with a set of parallel resistance and CPE.

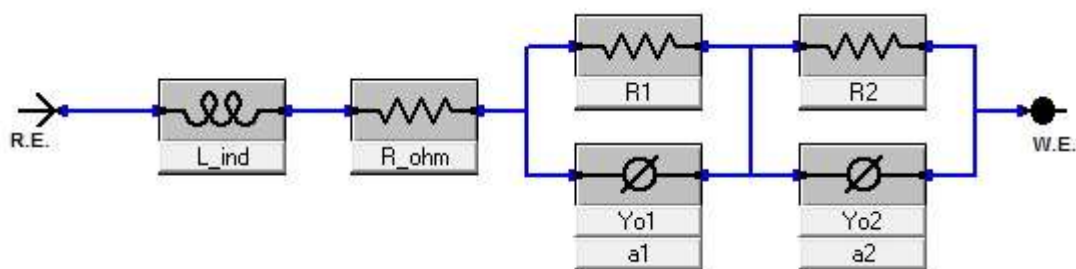


Figure 8.1: The equivalent electrical circuit used for curve fitting

#### 8.1.1 Effect of time (cell 13 run 1)

The results of the EIS curve fitting at several stages of the durability test (cell 13 – run 1) are summarised in table 8.1. As can be seen, at both OCV and 200 mA/cm<sup>2</sup> the value of all resistors tended to increase with time. As an example, at OCV the ohmic resistance increased from 0.0113 (after 5 hours) to 0.0176 Ω (after 85 hours). At 200 mA/cm<sup>2</sup> it increased from 0.0128 to 0.0172 Ω over the same period of time. This suggests that the microstructural and electrochemical properties of the cell were subject to change as time elapsed.

The assumed model resulted in a good fit for a number of the EIS curves, whereas, the fitting results were comparatively poor for a few cases. This has been shown in the “Goodness of Fit” column in the above table. Goodness of fit is defined as the summation of the weighted residuals. The weighting parameter for each point is the inverse measured impedance of the point. Smaller values of “Goodness of Fit” show better fit and larger values correspond to poorer curve fitting.

	OCV				200 mA/cm <sup>2</sup>			
	R <sub>ohm</sub> (Ω)	R1 (Ω)	R2 (Ω)	Goodness of Fit	R <sub>ohm</sub> (Ω)	R1 (Ω)	R2 (Ω)	Goodness of Fit
5 hr	1.13E-02	2.53E-02	2.15E-02	8.09E-05	1.28E-02	1.22E-02	1.30E-02	1.57E-05
25 hr	1.46E-02	2.43E-02	2.43E-02	4.95E-05	1.58E-02	1.22E-02	1.62E-02	6.97E-06
45 hr	1.56E-02	2.79E-02	2.50E-02	4.39E-05	1.61E-02	1.74E-02	1.90E-02	8.20E-06
65 hr	1.70E-02	3.16E-02	2.59E-02	6.78E-05	2.02E-02	1.66E-02	2.12E-02	2.24E-04
85 hr	1.76E-02	3.53E-02	2.52E-02	5.32E-05	1.72E-02	2.38E-02	1.80E-02	8.44E-06

**Table 8.1: Values of model parameters – cell 13 run 1 – effect of time**

As shown in figure 8.1. an inductor has been included in the circuit which is expected due to the metal content in fuel cell and wires, however, its value is very small (order of magnitude of 10<sup>-9</sup>). Thus, the values of inductance are not presented in the tables of the cell parameters.

Figure 8.2 illustrated the comparison between experimental data and curve fitting at 65 and 85 hours for 200 mA/cm<sup>2</sup>. As illustrated in the figure, the results after 85 hours are better fitted onto the model yielding 8.44E-06 as the value of Goodness of fit, whereas it has the value of 2.24E-04 for the results after 65 hours. The reason of the relatively poorer fitting can be the change in the electrochemical properties of cell or presence of noise in the operating voltage which deviate the performance from the ideal behaviour.

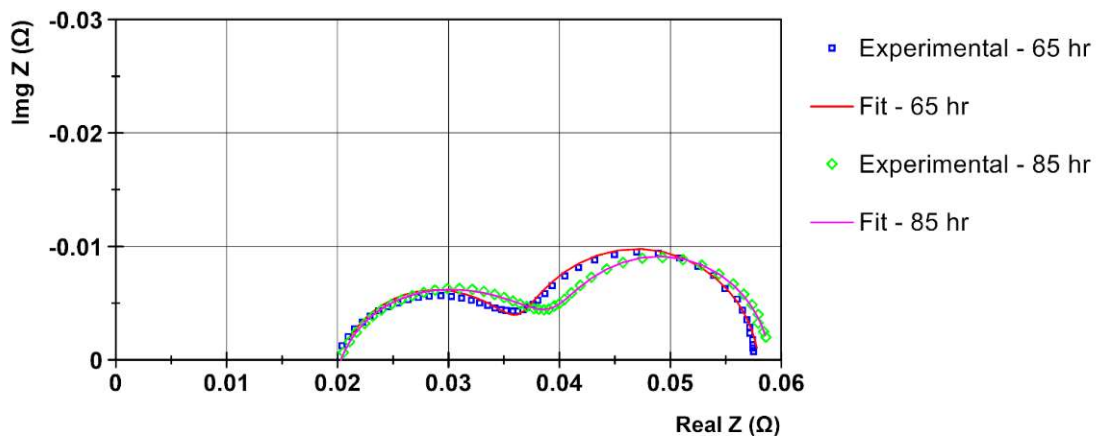


**Figure 8.2: Comparison of curve fit and experiment at 0.2 A/cm<sup>2</sup> – cell 13 run 1**

### 8.1.1.1 Calculation of exchange current density

As mentioned above, the resistance of both electrodes increased over durability period at OCV and 200 mA/cm<sup>2</sup> meaning that the performance dropped with time until it stabilised after about 70 hours. The values of the electrode resistance can be used to calculate the exchange current density of the electrodes at each time step.

Looking at the corresponding v-i curves (figure 7.3) it is appreciated that 200 mA/cm<sup>2</sup> (3.2 A) falls within the ohmic losses region implying that the concentration losses are small and negligible. This is an important and valid assumption which simplifies the  $i_0$  calculation. It is worth to emphasise that the EIS curve must be taken at low current densities, thus, the operating point is well before the concentration losses area. With this assumption, the total resistance of cell can be attributed to the ohmic and activation components. Considering the curve fit results after 85 hours of durability the ohmic resistance is 1.72E-02  $\Omega$  and the resistance of electrodes, which is due to the activation overpotential, is 2.38E-02 and 1.80E-02. Equations 2.26 and 2.27 can now be used to calculate the value of  $i_0$  assuming that the charge transfer coefficient is equal to 0.5 [71, 73, 74].

Re-witting equations 2.26 or 2.27, the expression for  $i_0$  is:

$$i_0 = \frac{i}{2 \sinh\left(\frac{\alpha z F \eta_{act}}{RT}\right)} \quad (8.1)$$

The activation loss is the product of the current at which the cell was running and the electrode resistance calculated from EIS curve fitting:

$$\eta_{act} = I \cdot R_{electrode} \quad (8.2)$$

Combining equations 8.1 and 8.2 the value of  $i_0$  is 0.13436 and 0.09644 A/cm<sup>2</sup> for electrodes. However, it is difficult to distinguish which value corresponds to the anode or cathode. Since the equivalent electrical circuit used for curve fitting is symmetric to the anode and cathode, with the available data it is not possible to assign the calculated values to the electrodes. In order to do separate anode and cathode features, experiments with reference electrode were carried out in which a silver wire was connected to the electrolyte using silver ink. However, due to the complexity of the implementation, the obtained results were inaccurate. In a number of the tests short out between electrolyte and anode was observed and in some others the voltage between the reference electrode and electrode of interest was severely noisy, which prevented the study of individual electrodes.

#### 8.1.1.2 SOFC semi-empirical model

In the previous sections the values of ohmic resistance and  $i_0$  were determined using the results of the EIS curves analysis. These parameters are now used to model the performance of the cell. The 0D semi-empirical model takes into account the ohmic and activation losses, therefore it is valid for small and moderate current densities.

The first step is to calculate the Nernst voltage using equation 2.7. The values of species partial pressure depends on the fuel composition. The value of standard Gibbs free energy is calculated using the data provided in [17] for hydrogen and oxygen reaction. Once the current drawn from the cell increases, a portion of hydrogen is consumed and water is generated. Thus, at each current there will be a new amount of available hydrogen and water which is different from that of the inlet. This change is considered to calculate the value of the Nernst voltage at different current densities. In other words, there is a maximum value of voltage which depends on the local partial pressure of the reactants and products at any current. This is the value used as  $E$  in equation 2.25. The activation losses are calculated using equations 2.26 and 2.27, and ohmic losses are given by equation 2.30.

The operating conditions, fuel composition and cell parameters used in the OD model are summarised in table 8.2.

Operating conditions		Fuel composition			Cell parameters		
P	T	H <sub>2</sub>	N <sub>2</sub>	H <sub>2</sub> O	R <sub>ohm</sub>	i <sub>0,1</sub>	i <sub>0,2</sub>
1 bar	700 °C	100 ml/min	566.67 ml/min	3 %	0.0172 Ω	0.13436 A/cm <sup>2</sup>	0.09644 A/cm <sup>2</sup>

**Table 8.2: Operating condition and cell parameters for SOFC OD model**

Figure 8.3 compares the experimental data of cell 13 run1 after 85 hours of durability test and results of the OD model based on the EIS results. As illustrated, the results of the semi-empirical model are close to those of the experiment for low and moderate current densities. However, at higher currents the model tends to deviate from the experimental data. This is due to the presence of concentration overpotential at high currents which are not considered in the OD model. Thus, it should be noted that the model is valid for low and moderate current densities only, as explained earlier in this section.

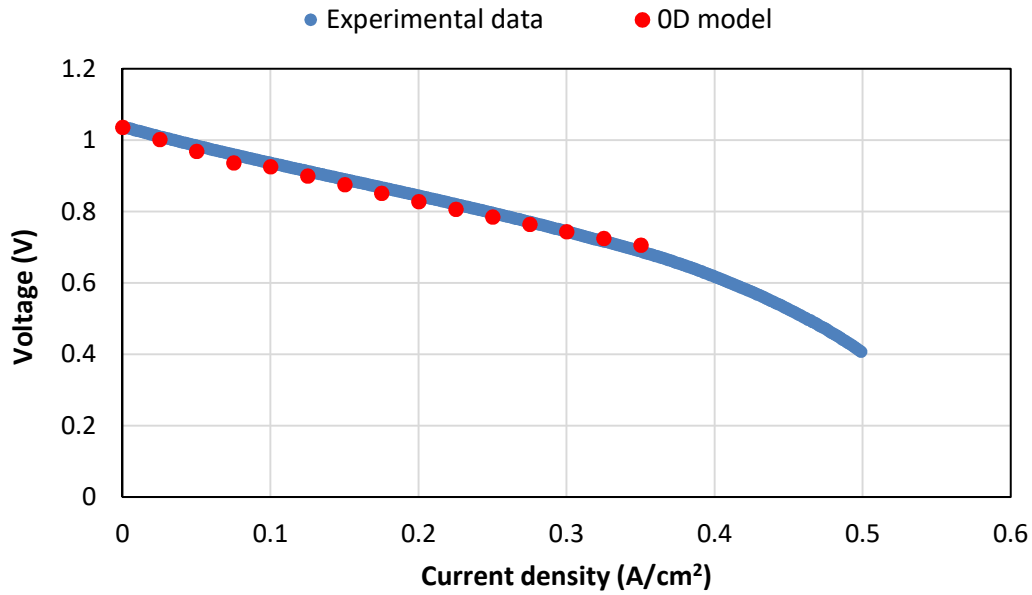


Figure 8.3: Comparison of experimental data and OD model - cell 13 run 1 - 85 hrs

### 8.1.2 Effect of H<sub>2</sub> partial pressure (cell 13 run 2)

The electrical model illustrated in figure 8.1 has been used to determine the resistance of the cell 13 operating under different partial pressures of hydrogen. The EIS curves were taken at three values of P<sub>H<sub>2</sub></sub>: 0.145, 0.291 and 0.436 bar. Table 8.3 summarizes the results of the EIS curve fitting for a wide range of the current densities for each case.

	P <sub>H<sub>2</sub></sub> = 0.145 bar				P <sub>H<sub>2</sub></sub> = 0.291 bar				P <sub>H<sub>2</sub></sub> = 0.436 bar			
	R <sub>ohm</sub> (Ω)	R1 (Ω)	R2 (Ω)	Goodness of Fit	R <sub>ohm</sub> (Ω)	R1 (Ω)	R2 (Ω)	Goodness of Fit	R <sub>ohm</sub> (Ω)	R1 (Ω)	R2 (Ω)	Goodness of Fit
0A	1.75E-02	3.71E-02	2.35E-02	5.77E-05	1.71E-02	3.21E-02	2.24E-02	3.03E-05	1.74E-02	3.04E-02	2.12E-02	2.34E-05
1A	1.74E-02	2.99E-02	1.65E-02	3.36E-05	1.73E-02	2.60E-02	1.38E-02	1.98E-05	1.75E-02	2.47E-02	1.31E-02	1.58E-05
2A	1.72E-02	2.66E-02	1.48E-02	2.08E-05	1.72E-02	2.26E-02	1.04E-02	1.28E-05	1.74E-02	2.15E-02	9.67E-03	1.13E-05
3A	1.70E-02	2.53E-02	1.67E-02	1.38E-05	1.70E-02	2.04E-02	9.10E-03	1.04E-05	1.73E-02	1.93E-02	7.85E-03	8.08E-06
4A	1.67E-02	2.69E-02	2.02E-02	1.22E-05	1.70E-02	1.88E-02	8.90E-03	5.99E-06	1.70E-02	1.80E-02	6.89E-03	6.62E-06
5A	1.60E-02	3.17E-02	2.38E-02	3.28E-05	1.68E-02	1.79E-02	9.54E-03	4.91E-06	1.69E-02	1.68E-02	6.57E-03	6.77E-06
6A	1.65E-02	3.89E-02	3.57E-02	2.11E-04	1.67E-02	1.77E-02	1.07E-02	4.64E-06	1.68E-02	1.60E-02	6.68E-03	5.03E-06
7A					1.63E-02	1.82E-02	1.21E-02	3.36E-06	1.65E-02	1.54E-02	7.19E-03	5.03E-06
8A					1.58E-02	2.00E-02	1.24E-02	9.46E-06	1.63E-02	1.52E-02	8.00E-03	4.51E-06
9A					1.65E-02	2.00E-02	1.47E-02	1.02E-05	1.62E-02	1.53E-02	8.93E-03	3.79E-06
10A					1.77E-02	2.03E-02	1.89E-02	1.73E-05	1.59E-02	1.55E-02	9.70E-03	5.33E-06
11A					1.95E-02	2.04E-02	2.44E-02	3.07E-05	1.60E-02	1.57E-02	1.10E-02	4.45E-06
12A									1.67E-02	1.56E-02	1.28E-02	8.60E-06
13A									1.77E-02	1.49E-02	1.52E-02	1.26E-05

Table 8.3: Values of model parameters – cell 13 run 2 – effect of hydrogen partial pressure

As seen in the table, at a constant current density, once the partial pressure of H<sub>2</sub> increases the electrodes resistance tends to decrease, however, the ohmic resistance remains almost constant. As discussed before, at low currents the resistance of electrodes can be attributed to the activation losses only. Considering the change of the electrode resistance with P<sub>H<sub>2</sub></sub> at low currents, it can be stated that it is the activation overpotential which is affected by hydrogen partial pressure the most. This suggests that the exchange current density strongly depends on the fuel composition (partial pressure of hydrogen) and operating conditions, which agrees well with the trends reported in the literature [73].

It can be also seen in the table that the goodness of fit varies once the current drawn from the cell is altered. For low and high current densities the value of goodness of fit is larger than that of the moderate currents. Thus, it can be stated that the electrical model fits onto the curves the best for the moderate currents and the performance of the cell tends to deviate from that at low and high values of current.

Table 8.3 also shows that the value of both electrode resistances change once the conditions at the anode are altered. This suggests that fuel cells are working as a system i.e. the performance of the anode and cathode is interlinked and any variation in the operating conditions of one will affect the performance of the other internally.

Table 8.4 shows the values of the fuel utilization for different partial pressures of hydrogen. From figure 7.12 (3D plots of EIS curve at different P<sub>H<sub>2</sub></sub>) it can be seen that the current of lowest resistance is 0.154 (2.5), 0.312 (5) and 0.437 A/cm<sup>2</sup> (7.5 A) for 0.145, 0.291 and 0.436 bar, respectively. These currents correspond to fuel utilization of 17.4, 17.4 and 16.3 %, respectively. The corresponding lowest resistance was 5.82E-2, 4.42E-2 and 3.91E-2 Ω. Thus, it can be concluded that the lowest resistance of cell occurs at almost constant fuel utilization (around 17 %). However, the value of the lowest resistance depends on the partial pressure of hydrogen, i.e. it decreases as P<sub>H<sub>2</sub></sub> rises.

Current (A)	Fuel utilization		
	0.145 bar	0.291 bar	0.436 bar
0	0	0	0
1	6.96	3.48	2.32
2	13.93	6.96	4.64
3	20.89	10.45	6.96
4	27.86	13.93	9.28
5	34.82	17.41	11.60
6	41.79	20.89	13.92
7		24.38	16.25
8		27.86	18.57
9		31.34	20.89
10		34.82	23.21
11		38.31	25.53
12			27.85
13			30.17

Table 8.4: Fuel utilization for different  $P_{H_2}$

### 8.1.3 Effect of temperature (cell 13 run 3)

The same electrical model for SOFC (figure 8.1) has been used to fit the EIS results of the 3<sup>rd</sup> test with cell 13 in which the effect of temperature was investigated. As explained in the previous chapter, EIS curves were taken at four operating temperature: 600, 650, 700 and 750 °C. The results of the curve fitting and value of the electrical circuit components are summarized in table 8.5.

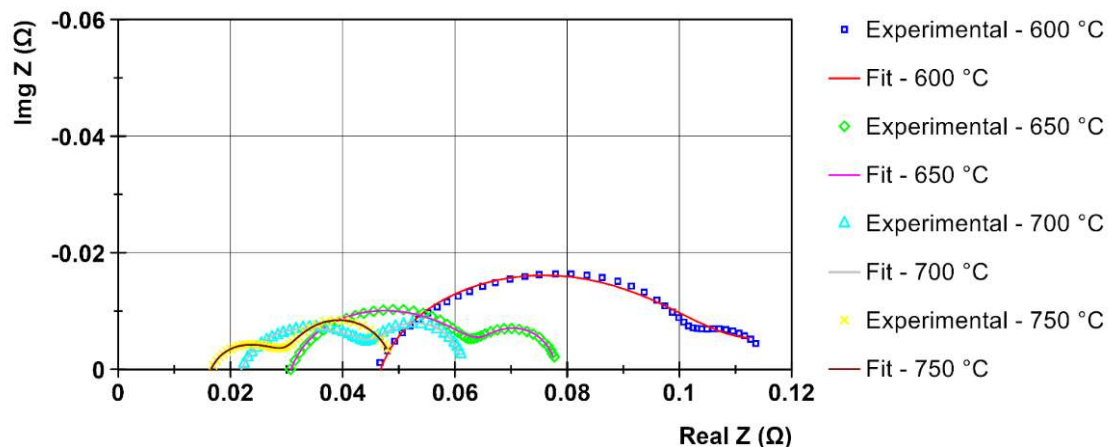
Similar to the results of the previous test, it can be seen in table 8.5 that the goodness of fit is larger at low and high currents, and smaller at moderate values. Therefore, the cell follows the electrical circuit at moderate current densities better than it does at high or low currents.

Table 8.5 excludes the results for 600 °C as the model did not fit on the EIS curves, resulting in large values of goodness of fit. At the other temperatures the fitting yielded better results, thus, shown in the table.

	T=650 °C				T=700 °C				T=750 °C			
	R_ohm (Ω)	R1 (Ω)	R2 (Ω)	Goodness of Fit	R_ohm (Ω)	R1 (Ω)	R2 (Ω)	Goodness of Fit	R_ohm (Ω)	R1 (Ω)	R2 (Ω)	Goodness of Fit
0A	2.65E-02	6.06E-02	1.83E-02	8.73E-05	1.80E-02	4.63E-02	2.20E-02	1.04E-04	1.24E-02	2.76E-02	2.74E-02	2.15E-05
1A	2.64E-02	4.73E-02	1.16E-02	5.62E-05	1.76E-02	3.67E-02	1.43E-02	5.46E-05	1.22E-02	2.21E-02	1.95E-02	9.41E-06
2A	2.60E-02	4.08E-02	1.12E-02	4.63E-05	1.75E-02	3.07E-02	1.34E-02	3.16E-05	1.20E-02	1.97E-02	1.74E-02	5.22E-06
3A	2.59E-02	3.87E-02	1.41E-02	4.10E-05	1.73E-02	2.76E-02	1.62E-02	1.91E-05	1.22E-02	1.90E-02	1.84E-02	4.17E-06
4A	2.56E-02	4.10E-02	1.80E-02	4.87E-05	1.73E-02	2.84E-02	2.08E-02	2.12E-05	1.22E-02	1.99E-02	2.22E-02	6.56E-06
5A	2.69E-02	4.62E-02	2.92E-02	1.19E-04	1.69E-02	3.37E-02	2.49E-02	7.01E-05	1.24E-02	2.41E-02	2.87E-02	2.14E-05
6A					1.89E-02	3.73E-02	4.30E-02	2.77E-04	1.18E-02	3.52E-02	3.56E-02	3.42E-04

**Table 8.5: Values of model parameters – cell 13 run 3 – effect of temperature**

Figure 8.4 compares the experimental data and results of the curve fitting at 2 A for 600, 650, 700 and 750 °C. As can be seen in the figure, the model does not fit well on the experimental data points at 600 °C, whereas, yields better fits at 650, 700 and 750 °C.



**Figure 8.4: Comparison of curve fit and experiment at 2 A – cell 13 run 2**

Looking at figure 8.4 it can be stated that the behavior of the cell deviates from the equivalent circuit at low temperatures, whereas, it is in accordance with the circuit at higher operating temperatures.

Based on the calculated values a strong dependency is observed between the ohmic resistance of cell and operating temperature, which is in agreement with the mathematical models suggested in the literature [73, 77]. In EIS analysis the resistance obtained at the low values of frequency represents the ohmic resistance, as the capacitors in the circuit tend to bypass the resistors under this condition. At

low frequencies the fitted curves, even at low temperatures, match the experimental data points well, thus, the calculated value of ohmic resistance can be valid.

Figure 8.5 illustrates the ohmic resistance of the cell as a function of inverse temperature. The values of ohmic resistance have been identified by curve fitting of the EIS results at 2 A. Considering the electrolyte as the major component of the ohmic losses, the conductivity of the electrolyte is calculated as  $62.5\exp(-6298.5/T)$   $\Omega^{-1}\text{m}^{-1}$ .

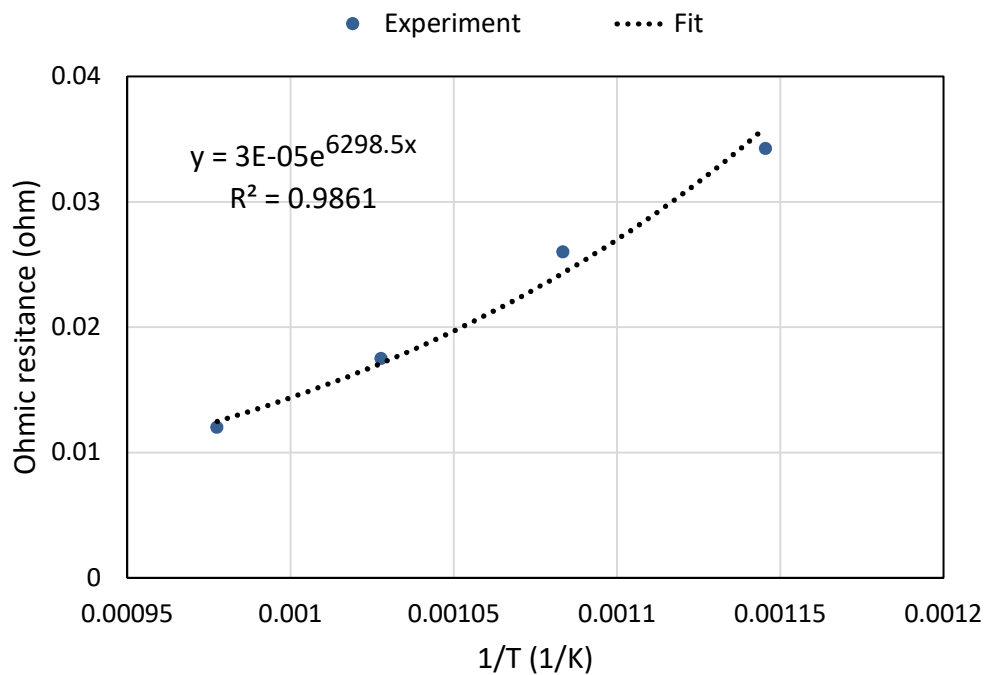


Figure 8.5: Plot of ohmic resistance vs temperature

## 8.2 Contamination tests

In this section the results of the contamination tests, including 50, 100, 150 and 200 ppm of  $\text{H}_2\text{S}$ , are presented and discussed.

### 8.2.1 50 ppm test

Figure 8.6 compares the v-i curves taken before introduction of  $\text{H}_2\text{S}$  (after cell stabilisation), after the exposure period and after the recovery duration.

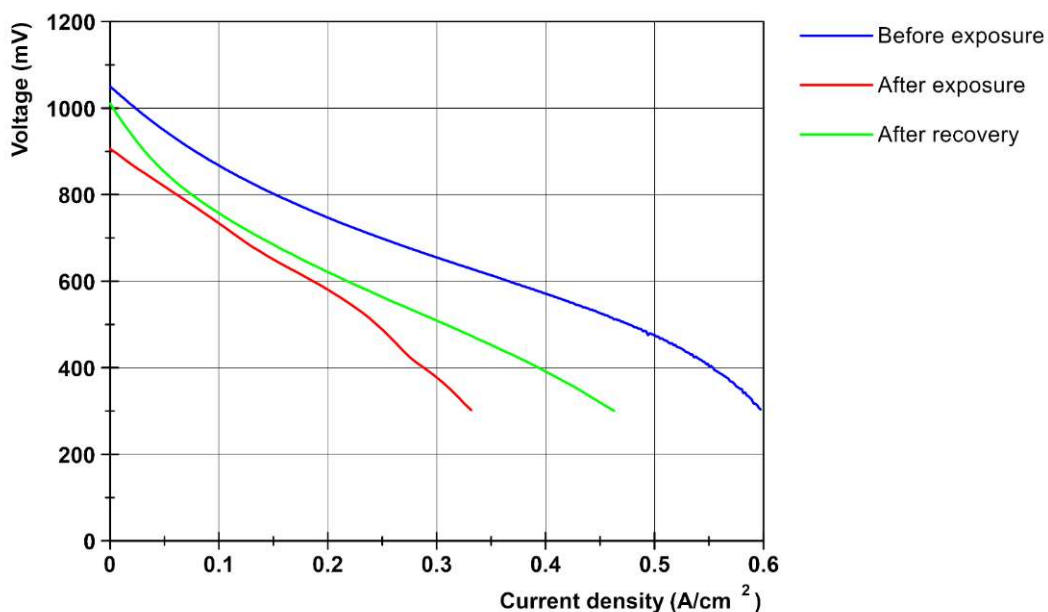


Figure 8.6: Profiles of v-i curves during H<sub>2</sub>S exposure and recovery periods - 50 ppm

As can be seen, the performance of the cell dropped after the exposure period. The voltage at 0.2 A/cm<sup>2</sup> was 747 mV at the end of the durability test and then, decreased to 580 mV at the end of the H<sub>2</sub>S exposure duration. This yields a drop of around 22 % in the operating voltage of the cell. Once H<sub>2</sub>S was removed from the fuel mixture and cell was re-operated on clean fuel, the voltage increased to 621 mV at the end of the recovery period.

The voltage and ASR of the cell at the different stages of the test at 0.2 A/cm<sup>2</sup> has been calculated using the voltage values from the v-i curves and shown in table 8.6.

Test stage	Before exposure	After exposure	After recovery
Voltage (V)	0.747	0.58	0.621
ASR (Ω.cm <sup>2</sup> )	1.515	2.35	2.145

Table 8.6: ARS of cell - 50 ppm test

As it can be seen in the above table, the ASR of the cell was 1.515 Ω.cm<sup>2</sup> before introducing H<sub>2</sub>S. After running H<sub>2</sub>S it increased to 2.35 Ω.cm<sup>2</sup> (an increase of 55 % in ASR), and finally decreased to 2.145 Ω.cm<sup>2</sup> after the recovery period. This trends states that the cell has partially recovered after removal of 50 ppm of H<sub>2</sub>S.

The profiles of the EIS curves, taken before/after H<sub>2</sub>S exposure and after recovery at 0.2 A/cm<sup>2</sup>, are illustrated in figure 8.7. The EIS curves show that both ohmic and electrode polarisations have increased after introducing 50 ppm of H<sub>2</sub>S into the fuel

mixture. The EIS curve taken after the recovery period shows that the ohmic losses increased further during the recovery time, however, the electrode resistance tended to decrease.

The results of the equivalent circuit curve fitting before exposure and after recovery are summarised in table 8.7. This table does not include the values of the equivalent parameters after the exposure period as the accuracy of the curve fitting was relatively poor implying that the equivalent circuit cannot be well fitted onto the experimental results. Before H<sub>2</sub>S exposure the ohmic and total electrode resistance were 1.36E-02 and 5.37E-02 Ω, respectively, which increased to 2.08E-02 and 5.79E-02 Ω after recovery.

Comparing the EIS curves and results of the curve fitting, it can be stated that H<sub>2</sub>S caused both ohmic and electrode polarisations to increase during the exposure period. Upon removal of H<sub>2</sub>S the electrode polarisation tended to decrease and almost reached its initial value (the value before exposure). However, the ohmic resistance became larger during the recovery, implying that H<sub>2</sub>S has left behind a continuous poisoning effect on the cell.

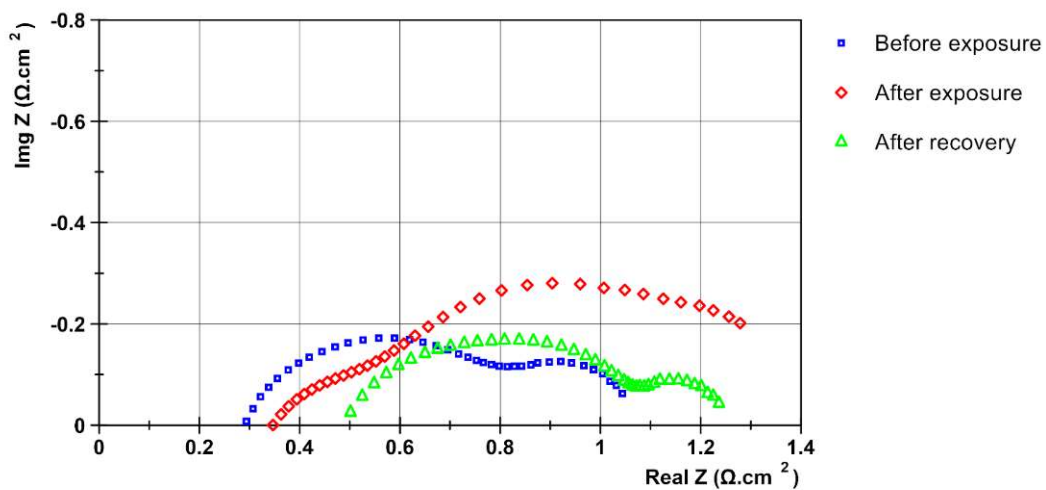


Figure 8.7: Profiles of EIS curves at 0.2 A/cm<sup>2</sup> during H<sub>2</sub>S exposure and recovery periods - 50 ppm

	R <sub>ohm</sub> (Ω)	R1 (Ω)	R2 (Ω)	R1+R2 (Ω)	Goodness of Fit
Before exposure	1.36E-02	1.30E-02	4.07E-02	5.37E-02	1.50E-05
After recovery	2.08E-02	5.07E-02	7.18E-03	5.79E-02	5.90E-05

Table 8.7: Equivalent circuit parameters - 50 ppm test

### 8.2.2 100 ppm test

The profiles of the v-i curves before/after the exposure duration and after the recovery period are illustrated in figure 8.8. The cell voltage after stabilization (before exposure) was 0.518 V at 0.2 A/cm<sup>2</sup>; during the exposure period the voltage dropped and reached 0.346 V at the end of the exposure time, corresponding to 33 % drop in the cell output. At the end of the recovery period the voltage increased slightly and reached 0.401 V.

Table 8.8 summarises the values of the operating voltage and ASR at 0.2 A/cm<sup>2</sup>. Before introducing H<sub>2</sub>S the ARS was 2.6 Ω which increased by 33 % and reached 3.46 Ω.cm<sup>2</sup> at the end of the exposure time. During the recovery period the ASR of the cell tended to decrease slightly and reached 3.185 Ω.cm<sup>2</sup> at the end. This states that the cell has recovered after removal of H<sub>2</sub>S from the fuel mixture, however, it has recovered less than the case with 50 ppm of H<sub>2</sub>S.

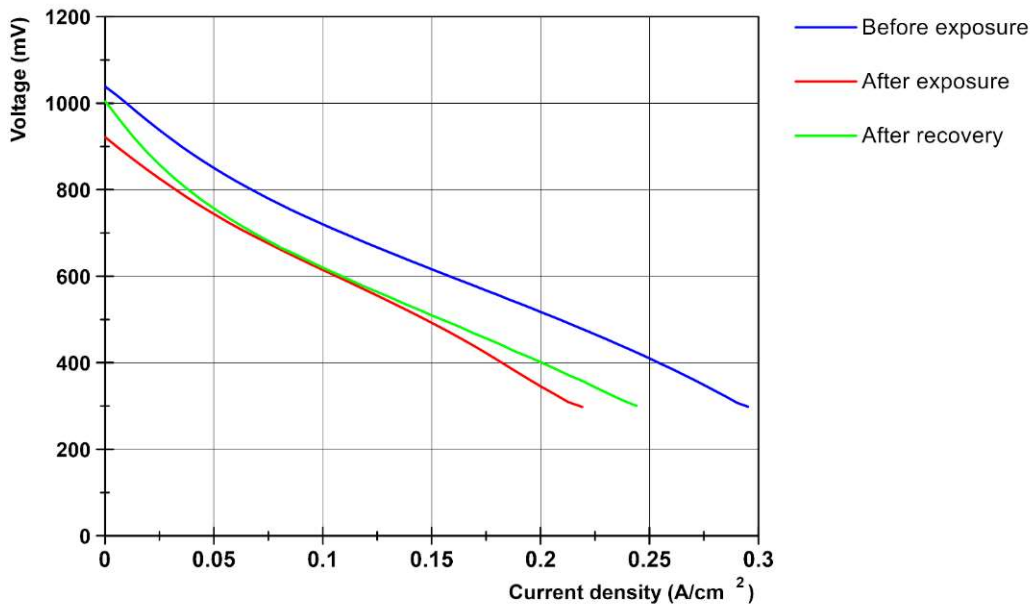


Figure 8.8: Profiles of v-i curves during H<sub>2</sub>S exposure and recovery periods - 100 ppm

Test stage	Before exposure	After exposure	After recovery
Voltage (V)	0.518	0.346	0.401
ASR (Ω.cm <sup>2</sup> )	2.6	3.46	3.185

Table 8.8: ARS of cell - 100 ppm test

Figure 8.9 shows the EIS curves taken at 0.2 A/cm<sup>2</sup> at different stages of the contamination test. The EIS curve taken at the end of the exposure time shows that the electrode polarizations have increased significantly during this period, however,

the ohmic resistance increased slightly. This trend can be also seen from the v-i curve taken at the end of the exposure as the slope of the curve is approximately the same as that of the curve taken before introducing H<sub>2</sub>S, whereas, the overall performance is lower than the initial one, suggesting that the electrode resistance has increased due to the presence of H<sub>2</sub>S. Based on the EIS curve taken at the end of the recovery period it can be stated that the ohmic losses increased further during this time, however, the electrode resistance tended to decrease. A similar trend of ohmic and electrode resistances change during the recovery was also observed in the previous test with 50 ppm of H<sub>2</sub>S test.

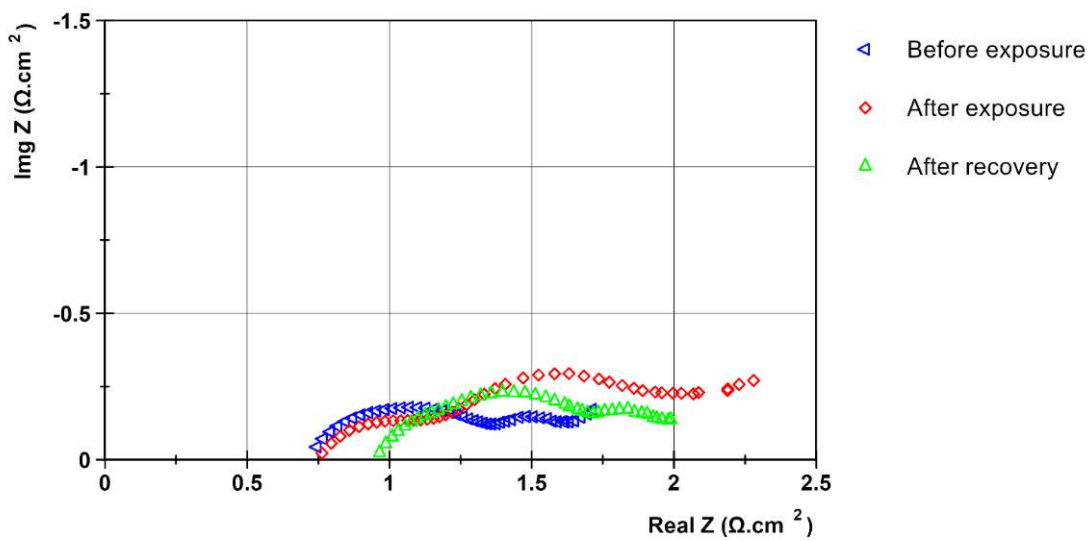


Figure 8.9: Profiles of EIS curves at 0.2 A/cm<sup>2</sup> during H<sub>2</sub>S exposure and recovery periods - 100 ppm

The results of the equivalent circuit curve fitting before exposure are summarised in table 8.9. The values of the equivalent parameters after the exposure and recovery periods are not included in this table as the accuracy of the curve fitting was poor for these two cases. This implies that the equivalent electrical circuit did not fit well onto the experimental data points.

	R <sub>ohm</sub> (Ω)	R1 (Ω)	R2 (Ω)	R1+R2 (Ω)	Goodness of Fit
Before exposure	4.53E-02	2.83E-02	3.77E-02	6.60E-02	2.43E-04

Table 8.9: Equivalent circuit parameters - 100 ppm test

Looking at the v-i and EIS curves it can be stated that H<sub>2</sub>S has caused the electrode polarizations to increase during the exposure time, whereas the ohmic resistance

remained almost the same. However, the ohmic resistance tended to increase over the recovery period implying that H<sub>2</sub>S had a long term impact on the cell after being removed from the fuel mixture.

The profile of the EIS curves in this test was different from that of the previous tests. As it can be seen in figure 8.9, at high frequencies the imaginary impedance tended to increase which can be attributed to other physical phenomena degrading the overall performance of the cell. Figure 8.10 illustrates an equivalent electrical circuit including 3 sets of parallel resistor and CPE used for curve fitting. The third set of the parallel R and CPE can represent another type of loss which caused the performance to be poorer rather than the previous tests.

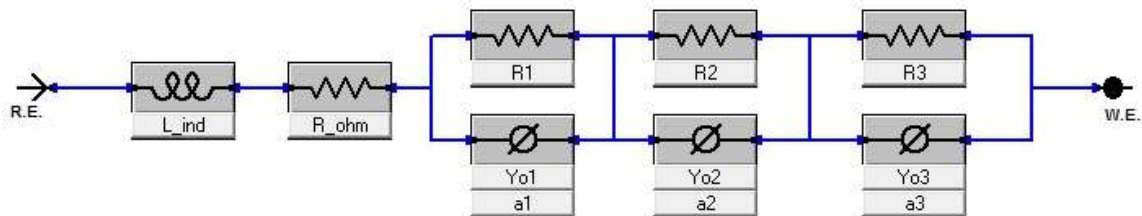


Figure 8.10: Equivalent electrical circuit for 100 ppm test

The equivalent circuit has been fitted on the experimental results of the EIS curve taken before exposure at 0.2 A/cm<sup>2</sup> to calculate the circuit parameters. Figure 8.11 demonstrates the experimental data points and fitted curve. The corresponding goodness of fit was 9.85E-05 in this case. In accordance with the curve fitting and equivalent circuit, it can be stated that there is another type of resistance which tended to decrease the voltage of cell during the durability period. This resistance was not observed in the previous cells as the EIS results were well fitted on the equivalent circuit with 2 sets of parallel R and CPE.

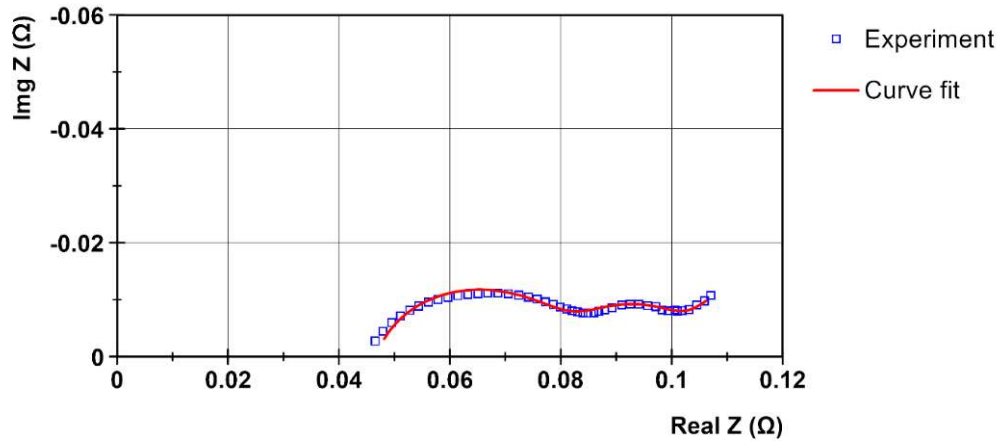


Figure 8.11: Comparison of EIS experimental data and curve fit at  $0.2 \text{ A/cm}^2$  – before exposure to 100 ppm of  $\text{H}_2\text{S}$

### 8.2.3 150 ppm test

The profiles of the v-i curves before exposure, after exposure and after recovery periods are illustrated in figure 8.12. The cell voltage before introducing  $\text{H}_2\text{S}$  was  $0.757 \text{ V}$  at  $0.2 \text{ A/cm}^2$ . Once 150 ppm of  $\text{H}_2\text{S}$  was added to the fuel mixture the voltage started to drop and finally reached  $0.595 \text{ V}$  at the end of the exposure time which yields a drop of 21 % in the cell voltage. After the recovery period the voltage was  $0.530 \text{ V}$  which is below the value at the end of the exposure. This implies that not only the cell failed to recover but also deteriorated further.

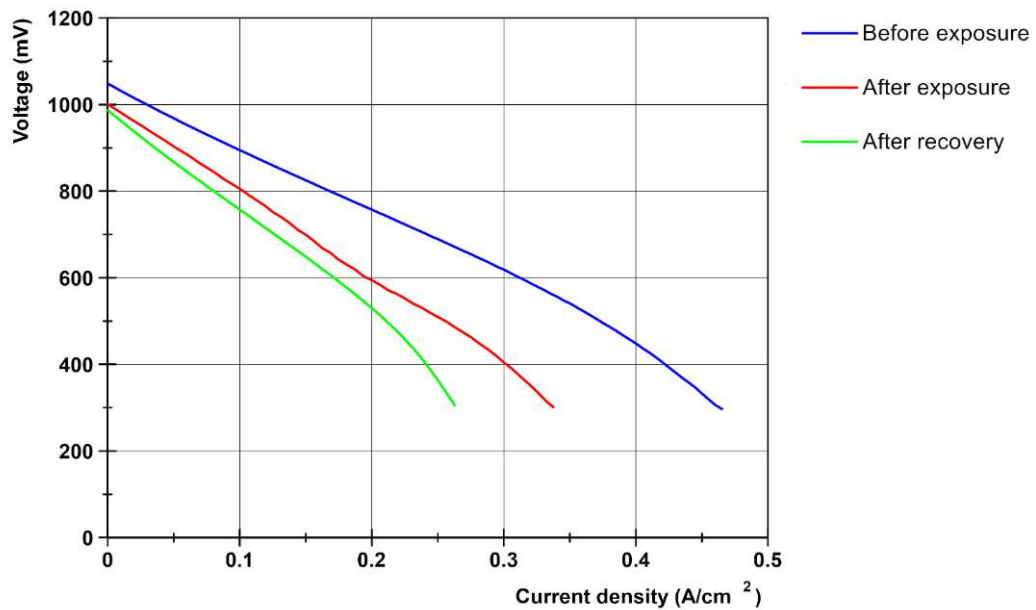


Figure 8.12: Profiles of v-i curves during  $\text{H}_2\text{S}$  exposure and recovery periods - 150 ppm

The values of the ASR of the cell at different stages of test has been summarised in table 8.10. The initial ASR (before exposure) was  $1.445 \Omega \cdot \text{cm}^2$  at  $0.2 \text{ A/cm}^2$  using the values of the v-i curve. After the exposure time the ASR increased by about 55 % and reached  $2.265 \Omega \cdot \text{cm}^2$ . Dissimilar to the tests with 50 and 100 ppm of  $\text{H}_2\text{S}$ , the ASR tended to increase further during the recovery period and reached  $2.59 \Omega \cdot \text{cm}^2$  at the end.

Test stage	Before exposure	After exposure	After recovery
Voltage (V)	0.757	0.595	0.530
ASR ( $\Omega \cdot \text{cm}^2$ )	1.455	2.265	2.59

Table 8.10: ARS of cell - 150 ppm test

Figure 8.13 demonstrates the profiles of the EIS curves taken at  $0.2 \text{ A/cm}^2$  before/after exposure and after recovery periods. Looking at the figure, it is appreciated that both ohmic and electrode resistances of the cell has increased during the exposure time, as expected. The increase in the ohmic and electrode resistances can be also seen in the v-i curves as the slope of the curve (representing the ohmic resistance) has become larger at the end of the exposure time. During the recovery period both types of resistance tended to increase further yielding lower performance at the end this stage.

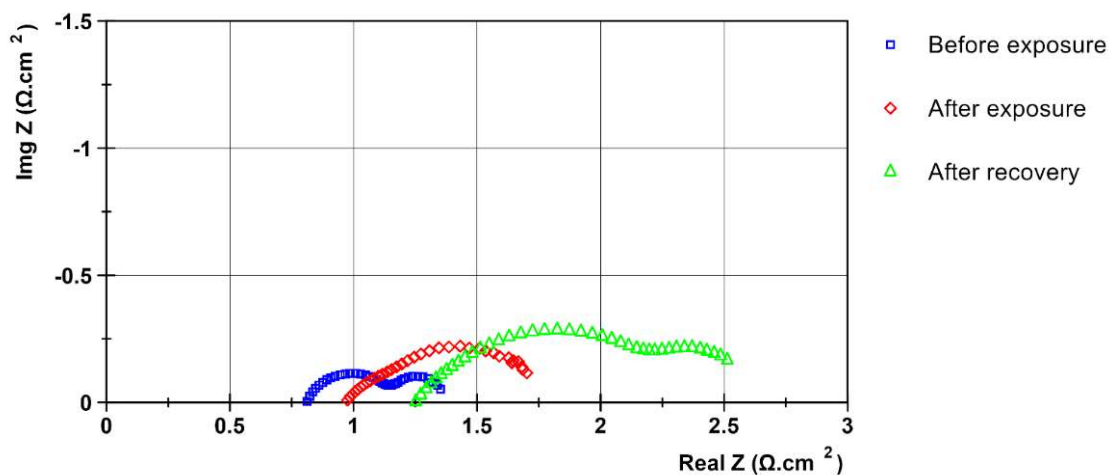


Figure 8.13: Profiles of EIS curves at  $0.2 \text{ A/cm}^2$  during  $\text{H}_2\text{S}$  exposure and recovery periods - 150 ppm

Table 8.11 summarises the results of the equivalent circuit curve fitting for different stages of the contamination test.

	R <sub>ohm</sub> ( $\Omega$ )	R1 ( $\Omega$ )	R2 ( $\Omega$ )	R1+R2 ( $\Omega$ )	Goodness of Fit
Before exposure	4.73E-02	2.64E-02	1.19E-02	3.83E-02	4.74E-06
After exposure	5.18E-02	2.43E-02	7.23E-01	5.78E-02	5.07E-05
After recovery	7.46E-02	7.36E-02	1.84E-02	9.19E-02	4.78E-05

**Table 8.11: Equivalent circuit parameters - 150 ppm test**

Considering the v-i and EIS curves it can be stated that both ohmic and electrode resistances increased in presence of 150 ppm of hydrogen sulfide. At the end of the recovery time the performance was poorer as none of the resistances decreased during the recovery time. The continuous increase of the ohmic resistance during the exposure and recovery periods was also observed in the 50 ppm test, however, the further rise in the electrodes resistance during the recovery time was not seen in the previous tests.

#### **8.2.4 200 ppm test**

Figure 8.14 illustrates the profiles of the v-i curves taken at different steps of the test i.e. before exposure, after exposure and after the recovery period. The initial voltage of the cell (before exposure) was 0.881 V at 0.2 A/cm<sup>2</sup> and 700 °C, and once 200 ppm of H<sub>2</sub>S was introduced to the fuel mixture the voltage started to decrease. At the end of the exposure time, the cell was unloaded to take v-i and EIS curves (1<sup>st</sup> set of data points), however, the voltage was changing quickly at this point of the test. Due to the fluctuations and changes associated with the experimental results, the data logging for v-i and EIS curves were repeated after five minutes (2<sup>nd</sup> set of data points). The first and second voltages at 0.2 A/cm<sup>2</sup> were 0.763 and 0.722 V, respectively, corresponding to 15 and 18 % of voltage drop at the end of the exposure time. The voltage of the cell tended to drop further during the recovery period and reached 0.616 V at the end of this stage, showing that the cell did not recover upon removal of H<sub>2</sub>S from the fuel mixture.

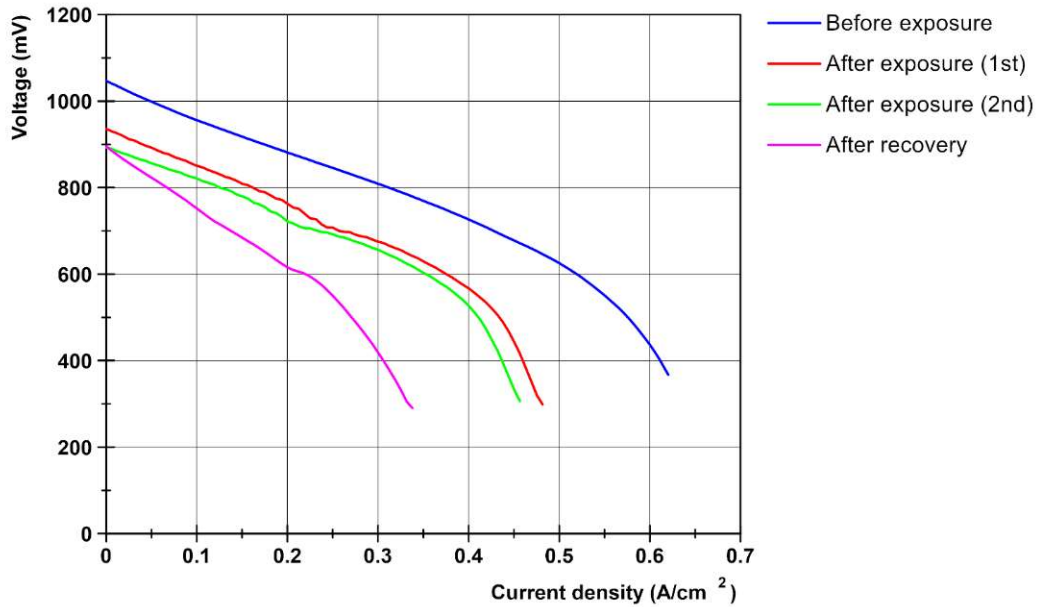


Figure 8.14: Profiles of v-i curves during H<sub>2</sub>S exposure and recovery periods - 200 ppm

It can be also seen that after the exposure period the cell fell into the concentration losses zone at lower current densities, which can be associated with the changes in microstructure of the cell. The latter has limited the diffusion of the reactants and products through the porous anode. This trend tended to deteriorate over the recovery period causing the cell to fall into concentration losses zone at smaller current densities compared to the results after the exposure time. This trend was also observed in the test with 150 ppm H<sub>2</sub>S, as shown in figure 8.12.

The voltage and ASR of the cell at different stages of the contamination test are summarised in table 8.12. Using the data points of the v-i curves, the ASR at 0.2 A/cm<sup>2</sup> was initially 0.83 Ω.cm<sup>2</sup> which increased to 1.42 and 1.625 Ω.cm<sup>2</sup> after exposure in the first and second curves, respectively. These values correspond to 71 and 95 % of increase in ASR of the cell at the end of the exposure period. Similar to the 150 ppm test the ASR increased during the recovery period and reached 2.155 Ω.cm<sup>2</sup> at the end, stating that the cell did not recover but yielded lower performance.

Test stage	Before exposure	After exposure 1 <sup>st</sup>	After exposure 2 <sup>nd</sup>	After recovery
Voltage (V)	0.881	0.763	0.722	0.616
ASR (Ω.cm <sup>2</sup> )	0.83	1.42	1.625	2.155

Table 8.12: ARS of cell - 200 ppm test

The profiles of the EIS curves at 0.2 A/cm<sup>2</sup> taken at different steps of the test are plotted in figure 8.15. The curves at the end of the exposure time show that the ohmic resistance did not change significantly at this stage, however, the electrode resistance tended to rise. Based on the curve taken at the end of the recovery period, it is comprehended that both ohmic and electrode resistances of the cell continued to increase during the recovery period causing the overall resistance to become larger at the end this period compared to the resistance at the end of the exposure.

Table 8.13 summarises the results of the equivalent circuit curve fitting. It only includes the results before the exposure time, as the equivalent circuit did not fit well onto the experimental data points logged at the other stages of the test.

Considering the v-i and EIS curves at different steps of the test, it can be stated that the electrode resistance of the cell increased during the exposure period. Over the recovery time, both ohmic and electrode resistances tended to rise which dropped the overall performance of the cell further down. Similar to the test with 150 ppm of H<sub>2</sub>S, the cell performance did not improved once the contaminant was removed and cell re-operated on clean fuel. A comparison between the tests with 150 and 200 ppm of H<sub>2</sub>S shows that the drop of the voltage (or rise in ASR) during the recovery period was more severe in the case of 200 ppm.

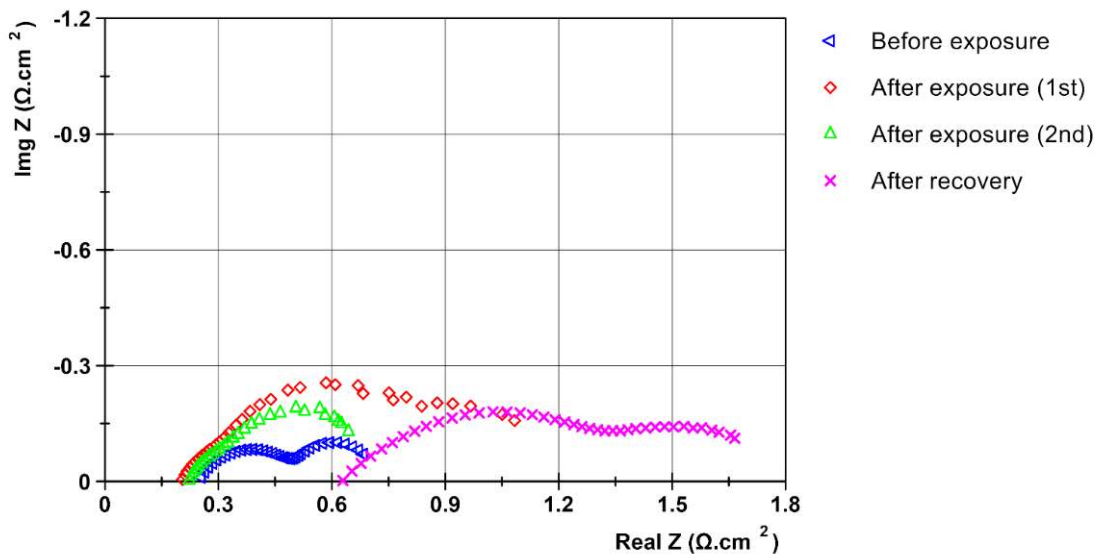


Figure 8.15: Profiles of EIS curves at 0.2 A/cm<sup>2</sup> during H<sub>2</sub>S exposure and recovery periods - 200 ppm

	R_ohm ( $\Omega$ )	R1 ( $\Omega$ )	R2 ( $\Omega$ )	R1+R2 ( $\Omega$ )	Goodness of Fit
Before exposure	1.16E-02	2.17E-02	1.15E-02	3.32E-02	1.80E-05

**Table 8.13: Equivalent circuit parameters - 200 ppm test**

### 8.2.5 Comparison of contamination tests

In order to compare the results of the contamination tests the ASR of the cells is normalised using the initial value i.e. the ASR before exposure. For each test the ASR at different stages (before exposure, after exposure and after recovery) is divided by the corresponding initial value. Figure 8.16 illustrates the normalised ARS of the cells exposed to different levels of H<sub>2</sub>S. For all cases the ASR of the cells increased after the exposure period, nevertheless, it changed in different ways after the recovery time. The maximum uncertainty in the normalised ASR data was about  $\pm 0.091$ , which corresponds to the normalised ASR after recovery for the 200 ppm test. The uncertainty in the measurement originates from the accuracy of the potentiostat used for voltage and current monitoring. This uncertainty propagates in the calculation of ASR. Thus, the normalised ASR for the maximum uncertainty case can be expressed as:  $2.596 \pm 0.091$  in non-dimensional units.

For the test with 50 ppm of H<sub>2</sub>S the ASR decreased after removal of H<sub>2</sub>S and the voltage partially recovered. The same trend was observed in the test with 100 ppm, however, the cell recovered less compared to the 50 ppm test. On the contrary, for the test with 150 ppm the ASR increased during the recovery period causing a further drop in the voltage. A similar pattern was characterised for the 200 ppm test in which the secondary rise in the voltage (the voltage increase during recovery) was larger than that of the test with 150 ppm.

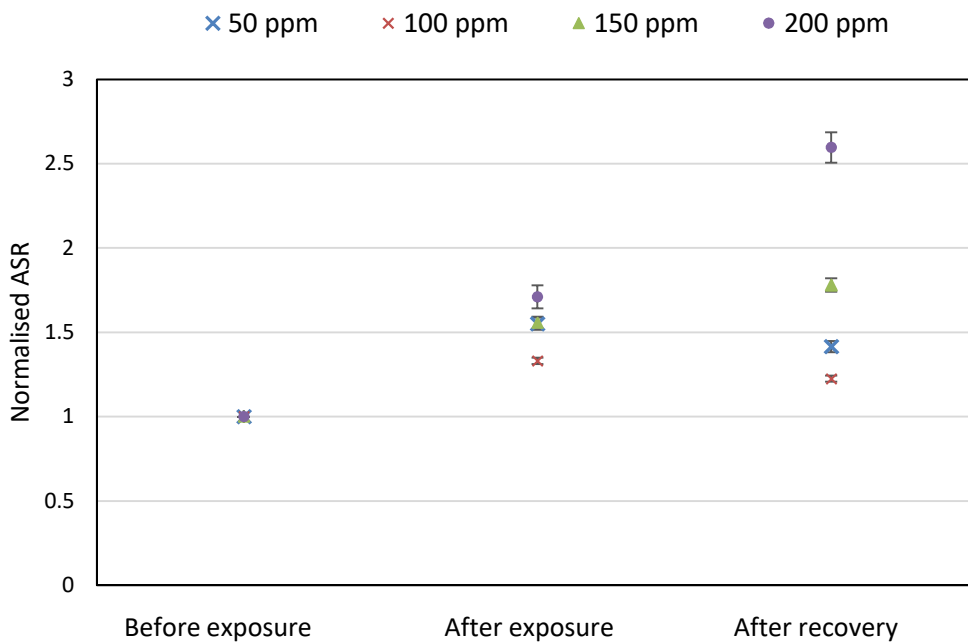


**Figure 8.16: Normalised ASR at different stages of contamination tests**

Based on the results of the tests it is perceived that at lower concentration of  $H_2S$  the voltage recovers partially after the recovery period. However, as the concentration of  $H_2S$  increases the cell voltage tends to drop further once the contaminant is removed.

For all levels of  $H_2S$  the ohmic resistance increased over the recovery period suggesting that  $H_2S$  has a long term effect on the ohmic resistance of the anode which continues during the recovery time. The electrode resistance also increased during the exposure time for all levels, however, the trend during the recovery was different; at lower concentrations it partially recovered causing the voltage to rise, whereas, it continued to increase for higher levels of  $H_2S$ .

The normalised voltage of the cells at different stages of the contamination test is plotted in figure 8.17. The maximum measurement uncertainty was about 0.003 for the normalised voltage of the cells. This uncertainty is a result of the propagation of the measurement uncertainty in the normalisation process.

This plot shows that the normalised voltage after the exposure period is similar for all cases, thus independent of the  $H_2S$  concentration. As a results, it can be stated that for the tested range of the  $H_2S$  concentration (50, 100, 150 and 200 ppm) the output of the cell is approximately the same. Comparing these results to the previous studies (lower  $H_2S$  concentrations) it can be stated that there should be a

concentration level above which the voltage of the cell does not remarkably change, but remains more or less constant once exposed to H<sub>2</sub>S.

Figure 8.18 illustrates the profiles of the normalised voltage during the exposure period for all cells. According to the figure, the degradation mechanism consists of two steps: an initial sharp drop and a secondary sluggish drop. The observed mechanism which is similar for all cases, agrees well with the trends reported in the literature [119-122].

Due to the fact that no trend was observed in the normalised voltage, the results cannot be fitted on the damage models developed in chapter 4. The damage factor takes into account the effect of H<sub>2</sub>S concentration, time and temperature. As the results are similar the models will return a similar damage factor for all tested levels of H<sub>2</sub>S.

The performance drop of the cells exposed to 0.18 to 10 ppm of H<sub>2</sub>S have been reported in reference [135]. These experimental results were obtained under potentiostatic mode i.e. the voltage is kept constant and the current is monitored during the test. The reported performance loss corresponded to the power of the cell at the end of the exposure time which was 5 minutes. However, the profile of current during the exposure period is not provided in this reference. The damage model proposed in chapter four was developed under galvanostatic mode i.e. the current is kept constant over the test time and the voltage is recorded. It also includes the effect of time on the voltage drop. As the profile of the voltage during the contamination period is not found in the literature, it is not possible to evaluate the damage model with real data. However, the models were tested and compared using synthetic data as explained in chapter 4.

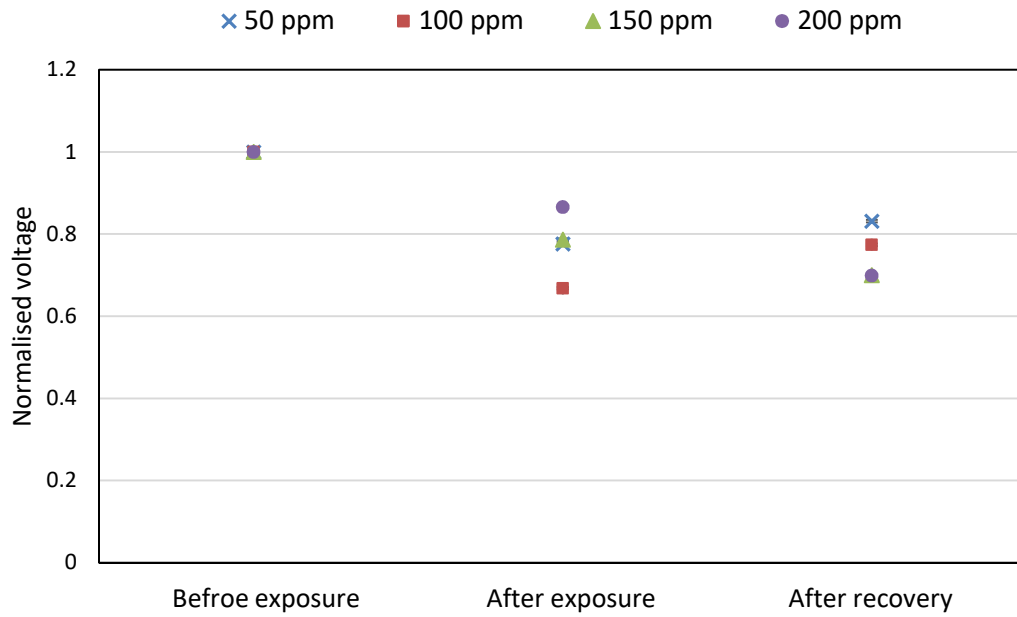


Figure 8.17: Normalised voltage at different stages of contamination tests

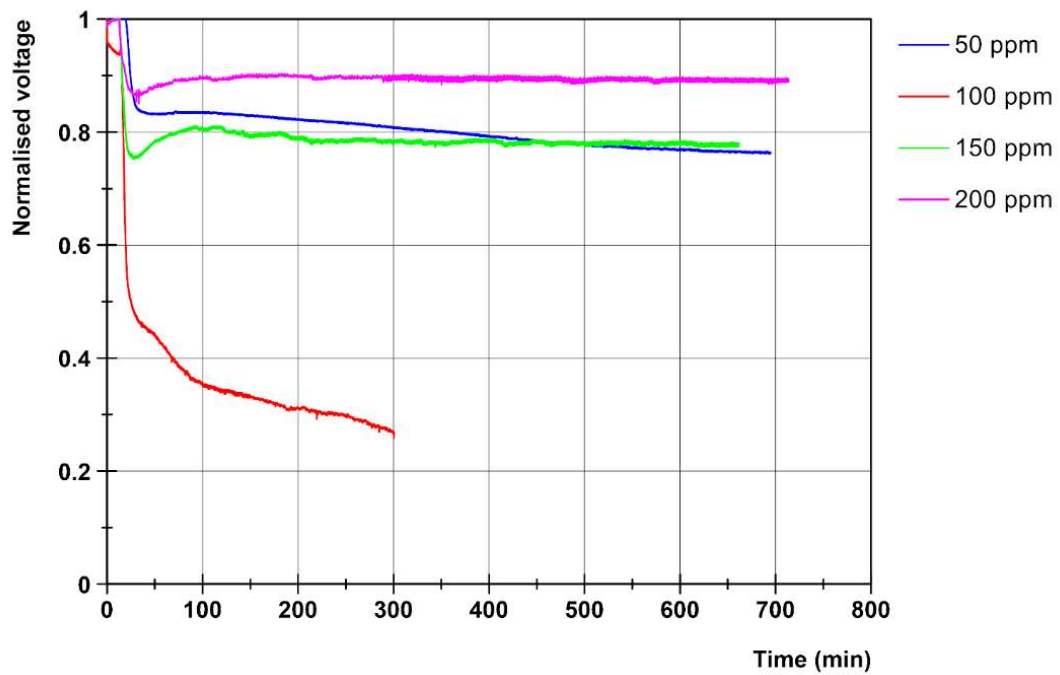
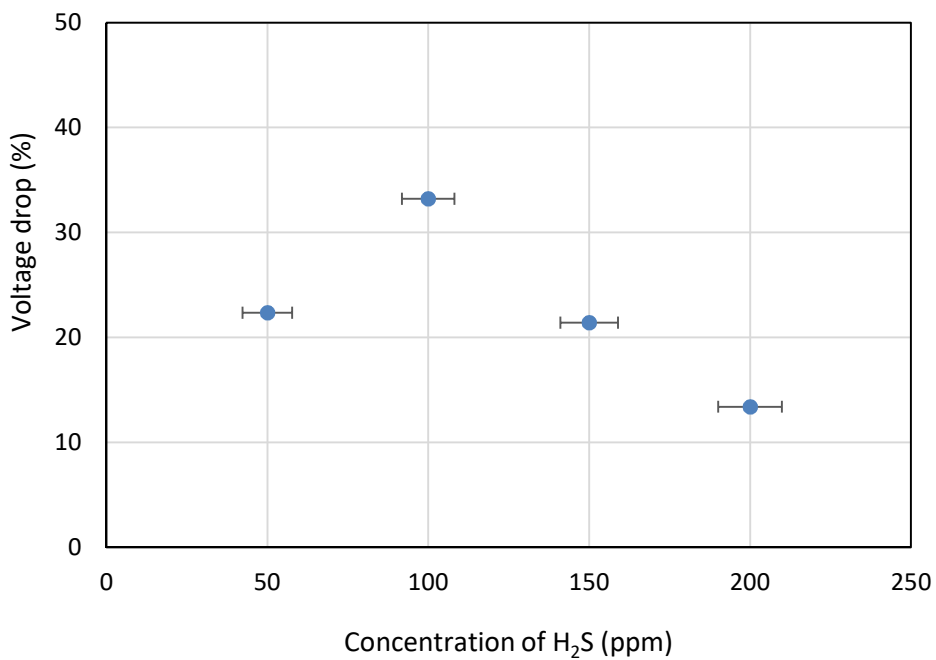


Figure 8.18: Normalised voltage during exposure period

As mentioned in the literature review chapter, the poisoning effect of  $H_2S$  has been investigated for 0.18 ppm to 10 ppm, as shown in figure 2.16 [135]. This figure illustrates a sharp performance drop at  $H_2S$  concentrations between 0.18 and 2 ppm. In addition, the gradient of the performance drop with respect to  $H_2S$  concentration decreased for higher values of concentration. Taking into account

the results of the current work, it can be stated that the plot of the performance drop against  $H_2S$  concentration reaches a plateau for high concentrations between 50 and 200 ppm. This is in agreement with figure 2.16 in which the gradient of the performance drop curve tends to zero as the concentration increases. The obtained results also accord with the study by Zhang et al. in which the voltage drop was reported to remain almost the same for high levels of  $H_2S$  concentrations [136].

Figure 8.19 shows the performance drop of the cells exposed to different levels of  $H_2S$  poisoning. Looking at the figure, it is observed that the results for the 50 and 150 ppm tests are similar, although the cells were exposed to very different  $H_2S$  concentrations. It can also be seen that the performance drop was larger for 100 ppm case and smaller for 200 ppm test. The initial voltage - the voltage of cell before  $H_2S$  exposure - was 747, 518, 757 and 881 mV for the 50, 100, 150 and 200 ppm tests, respectively. Thus, it is observed that the percentage of the voltage drop will be lower for higher initial voltage and vice versa.



**Figure 8.19: Voltage drop of contaminated cells**

### **8.3 SEM/EDX analysis**

In this section the results of the SEM/EDX analysis for both clean and contaminated cells are presented. The clean cell section includes the pictures of cells 07 and 08 which were tested by the initial test set up. The pictures of cell 11 are also presented in this section. In the contaminated cells section the SEM results of the cells exposed to 50, 100, 150 and 200 ppm of H<sub>2</sub>S are shown and discussed.

#### **8.3.1 Clean cells**

Figure 8.20 illustrates the cross sectional view of the anode supported cells used in this research. Five different layers can be distinguished in this picture: cathode (at the top), barrier, electrolyte, anode functioning layer and anode support layer (at the bottom).

Figure 8.21 shows the SEM pictures of cells 07 and 08. Both cells were used in the initial test set up i.e. the fuel delivery manifold. As described in chapter 5, in this set up, the cells were sealed to the manifold using high temperature sealing paste. Also, silver ink was used to attach the current collecting mesh to the electrodes.

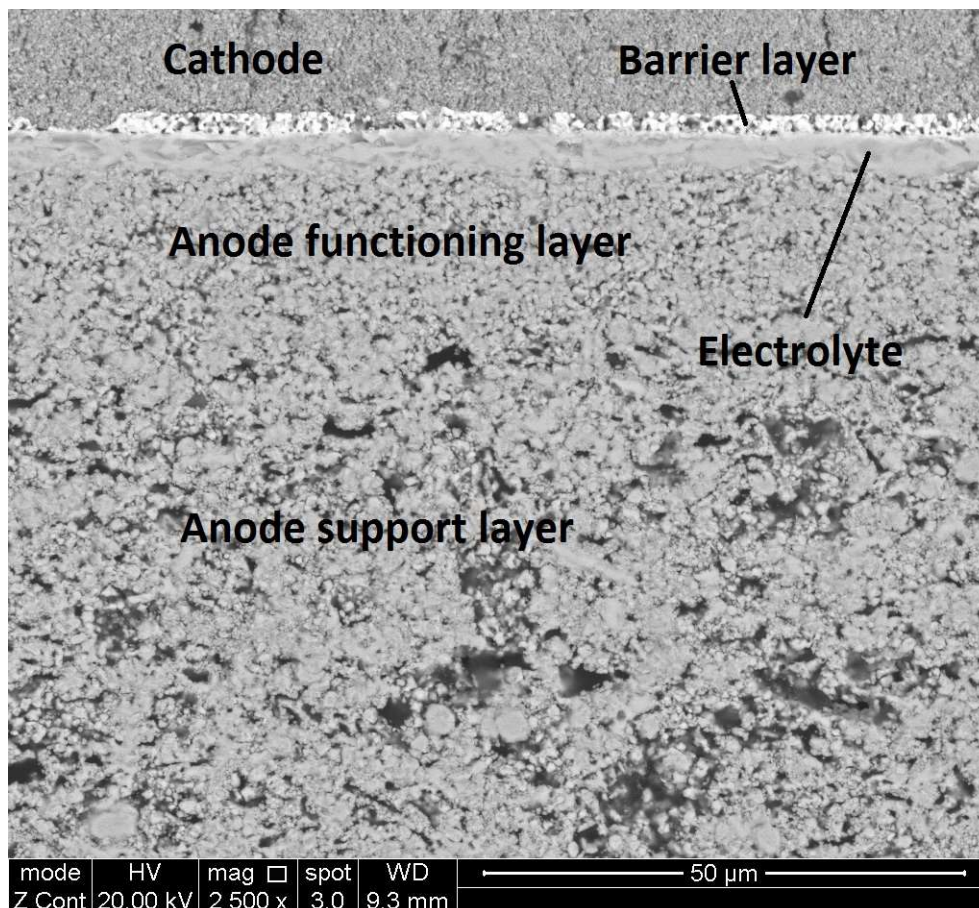


Figure 8.20: Layers of anode supported cells

As can be seen in figure 8.21, the cathode of both cells (top layer in the pictures) has been damaged during the test. This can be attributed to the cell/manifold assembly and sealing paste. The sealing paste tends to become hard once heated in the furnace. As a result, it will not allow the cell to compress during the cool down stage causing the cell to crack.

In addition to the sealing paste issues, the thermal mismatches between cathode and electrolyte materials can lead to cathode cracking. Similarly, the CTE mismatch between the cathode and silver ink drops used to attach the current collector, can contribute to this issue.

The SEM picture of cell 11, tested in the commercial set up, is shown in figure 8.22. As is clear in the figure, there are several cracks in the cathode, which can be ascribed to the thermal cycles. As mentioned in chapter 6, cell 11 was used in two test runs, each of which included heating up, loading and cooling down to the room temperature.

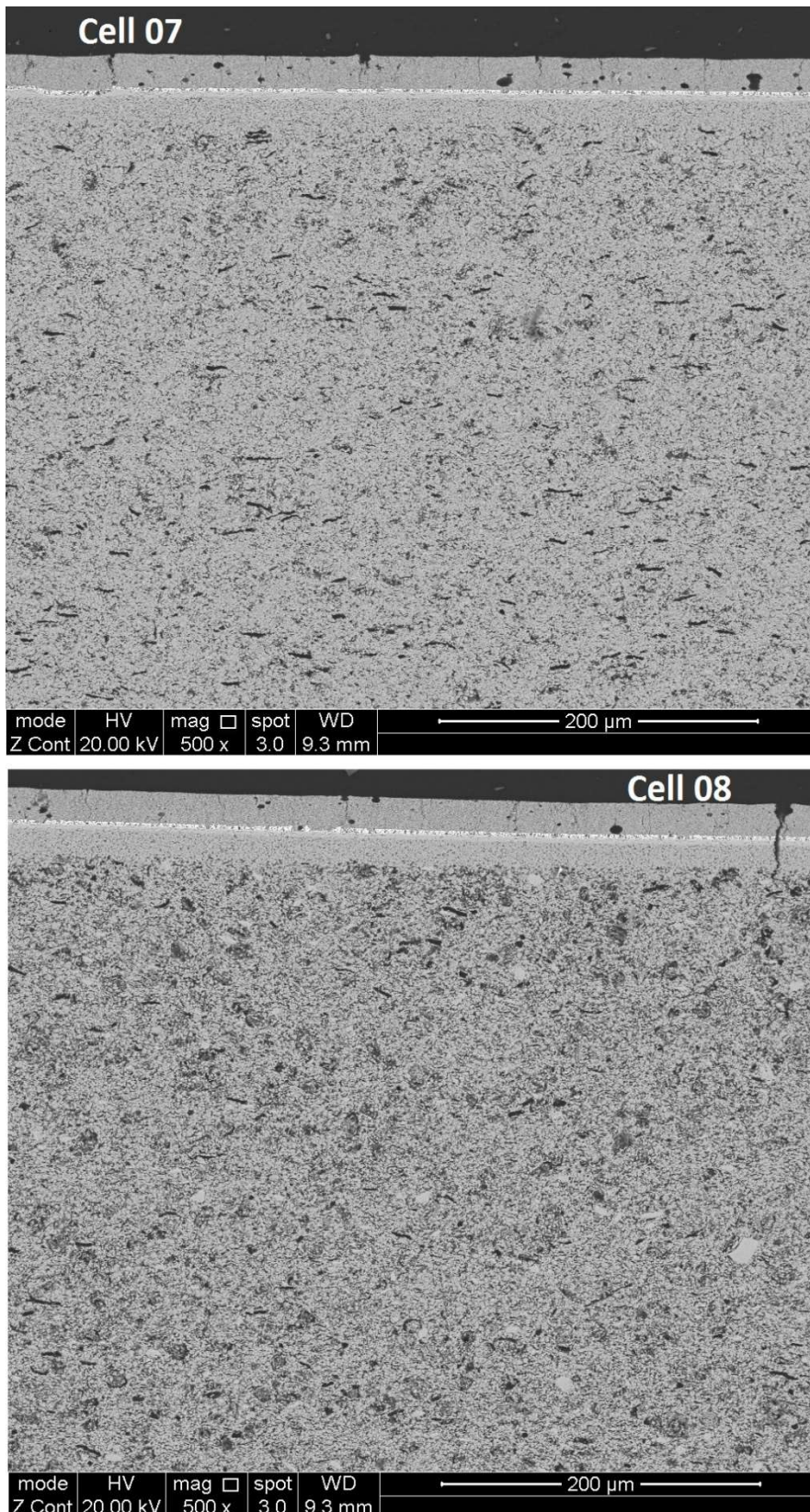


Figure 8.21: SEM pictures of cell 07 (top) and cell 08 (bottom)

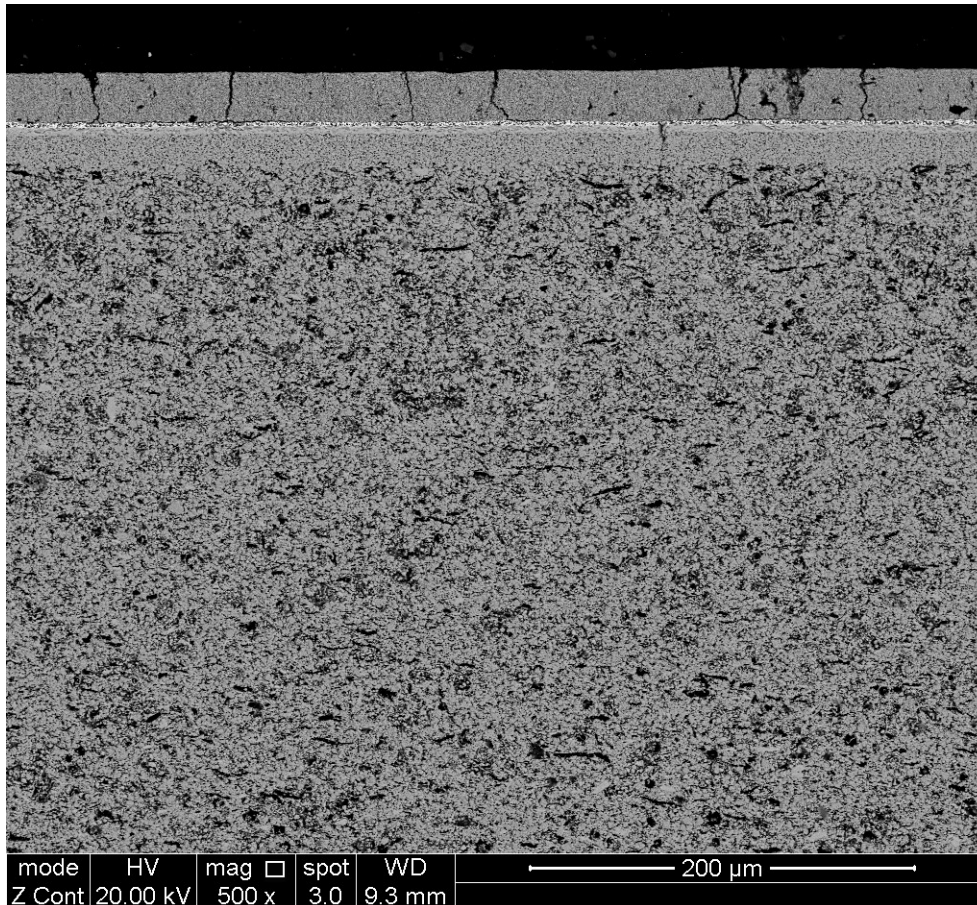


Figure 8.22: SEM picture of cell 11

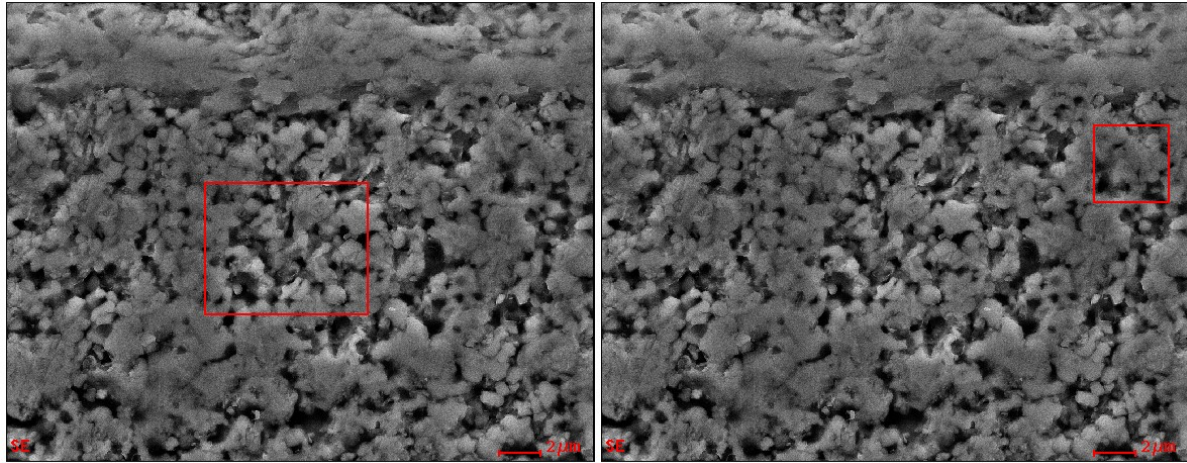
As seen in the previous chapters, a drop in voltage was observed during the durability (stabilisation) period. This trend was more or less similar for all the cells tested in the commercial set up. One possibility is the diffusion of silicon and aluminium for the felt into the cathode, as mentioned before. However, the EDX analysis did not reveal the presence of Si or Al in the cathode.

### 8.3.2 Contaminated cells

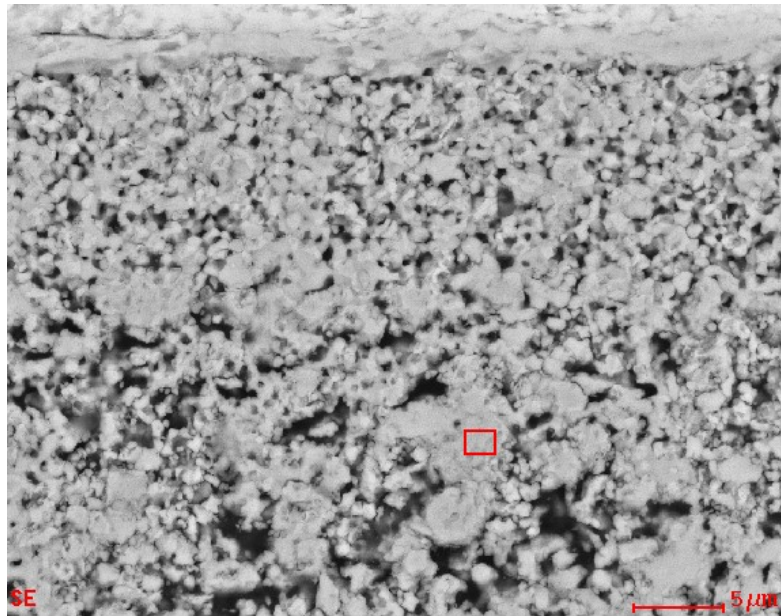
- 50 ppm test

Figure 8.23 and figure 8.24 demonstrate the SEM pictures of the cell at the end of the test with 50 ppm of H<sub>2</sub>S. The red rectangles in the figures show the areas over which the EXD analysis has been done. The results of EDX analysis show that Ni and YSZ are more or less evenly distributed across the anode.

Also, it should be stated that No sulfur was detected in anode functioning and support layers. Similar to cell 11, Si or Al were not detected across the cathode.



**Figure 8.23: Anode functioning layer – 50 ppm test**



**Figure 8.24: Anode functioning and supports layer – 50 ppm test**

- 100 ppm test

It was mentioned in chapter 7, that the overall performance of this cell was lower than the others, before introducing  $H_2S$  to the fuel mixture. This can be attributed to the structure of the cell, as illustrated in figure 8.25. It can be seen that the porosity of the anode at the areas between the functioning and support layers, has significantly decreased. In other words, the anode was partially blocked. This prevented the fuel to reach the active sites (anode functioning layer) and consequently, caused the cell to yield lower voltage. Since the voltage of the cell was as expected at the beginning of the durability test, it can be stated that the change in the structure occurred during this period.

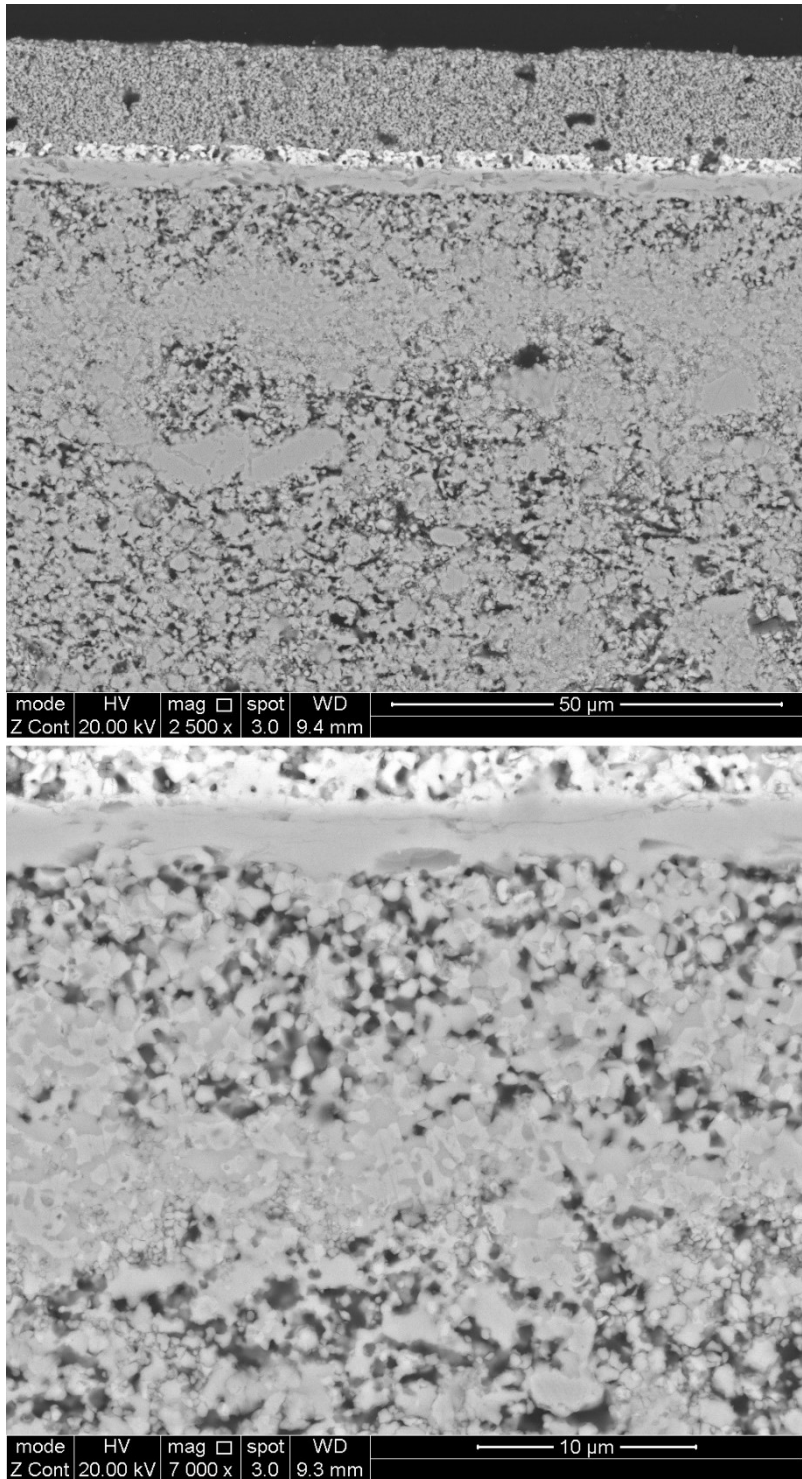


Figure 8.25: SEM picture of cell – 100 ppm test

Similar to the 50 ppm test, the EDX results show an almost uniform distribution of Ni and YSZ across the anode. In accordance with the EDX results, no sulfur was found at the anode. It should also be mentioned that EDX did not detect any Si or Al in the cathode.

- 150 ppm test

The structure of the cell after exposure to 150 ppm of H<sub>2</sub>S and recovery is illustrated in figure 8.26. As can be seen, cracks have developed in the cathode. This damage can be ascribed to the thermal cycles, similar to cell 11. This cell was used in several test runs, thus, undergoing thermal cycling.

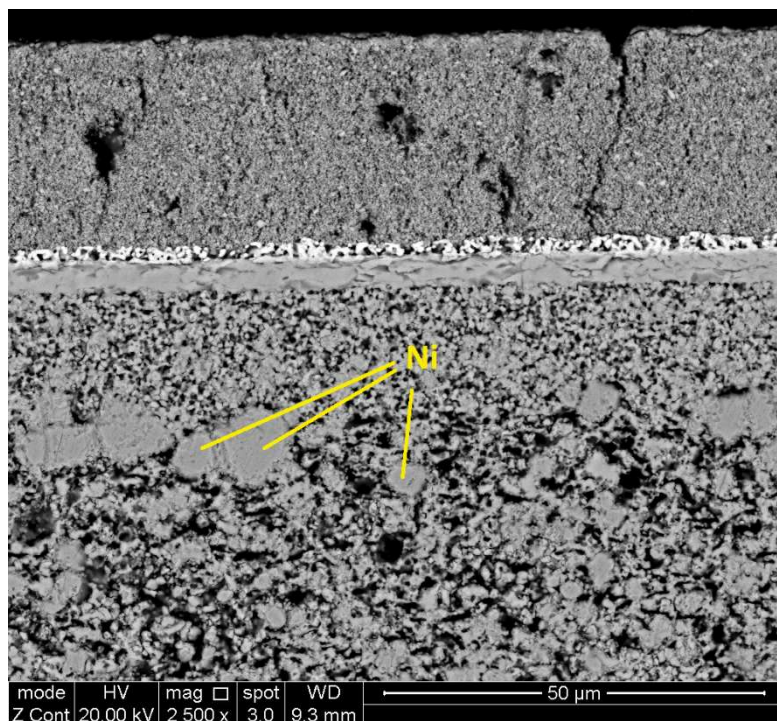


Figure 8.26: SEM picture and EDX analysis of cell – 150 ppm test

The SEM and EDX results indicate that, although no sulfur was detected in the anode layers, the structure of the anode has changed significantly. It can be seen in figure 8.26 that the size of the Ni particles has increased, specifically, at the interface of the functioning and support layers. This suggests that the anode has been re-structured as a result of the exposure to H<sub>2</sub>S.

- 200 ppm test

The structure of the cell at the end of the 200 ppm test is shown in figure 8.27. Similar to the 150 ppm test, the structure of the anode has changed, i.e. the size of the Ni and YSZ particles has increased. In accordance with the figure, it can be stated that Ni and YSZ have coarsened, due to the exposure to sulfur. The EDX analysis in this case did not reveal any sulfur in the anode layer, similar to the previous contaminated cells.

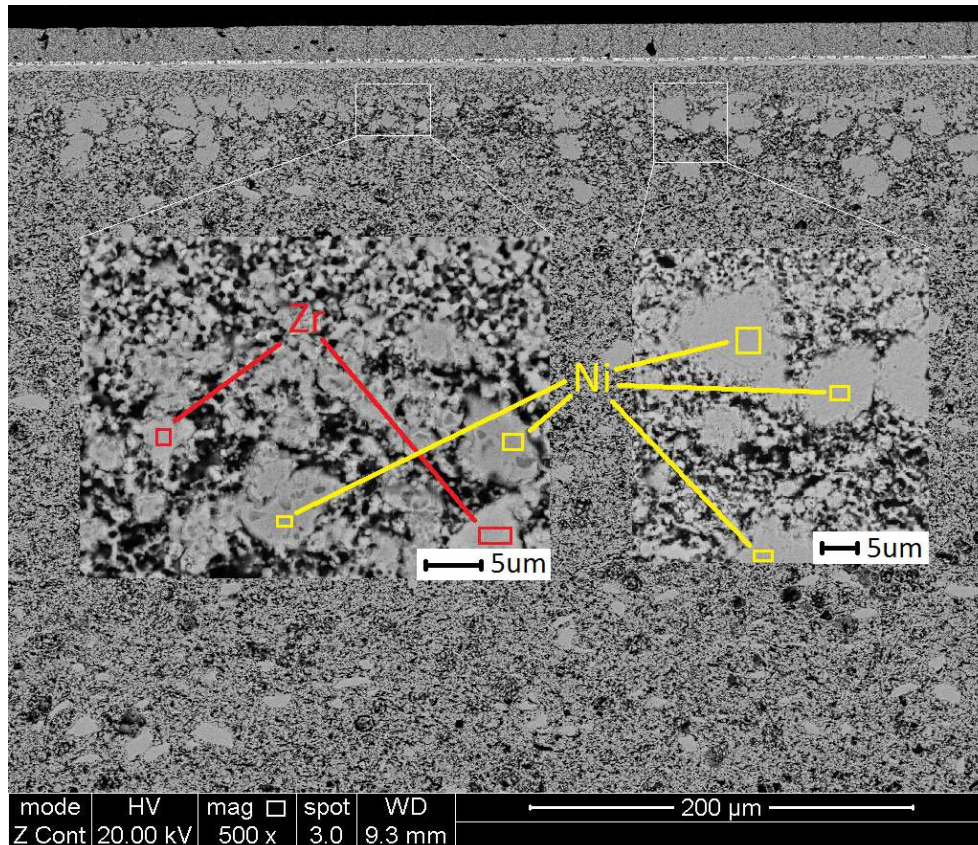


Figure 8.27: SEM picture and EDX analysis of cell – 200 ppm test

### 8.3.3 Comparison of cells

Figure 8.28 illustrates the SEM pictures of the contaminated cells. In accordance with the SEM and EDX results, it can be stated that in none of the cells sulfur was found at the anode. This suggests that the deposited sulfur should have been removed from the anode during the recovery period. It can also be deduced that Ni did not react with S under the tested operating conditions, which is in agreement with the results of the experimental and thermodynamic studies reported in the literature [128, 134]. It should also be stated that the EDX did not detect any Si or Al at the cathode in all cases.

In accordance with the results, it is deduced that, the degree of the particles coarsening has increased with the H<sub>2</sub>S concentration. In the case of 50 ppm, coarsening of the anode materials was not observed, however, it was detected for the 150 and 200 ppm cases. The highest degree of the coarsening corresponds to the cell exposed to 200 ppm of H<sub>2</sub>S.

It can also be seen that the coarsening has occurred at the interface of the anode functioning and support layers. Although the materials of both layers is the same, their corresponding structure is different. As is clear in figure 8.20, the size and distribution of the particles are different for anode functioning and support layers. As a result, the change in the structure has occurred at the interface.

As shown in figure 8.28, the anode of the cell tested with 100 ppm of H<sub>2</sub>S, was partially blocked at the interface of anode functioning and support layers. The change in the structure may be caused due to the issues associated with the cell manufacturing process, as it was not observed in any other cases.

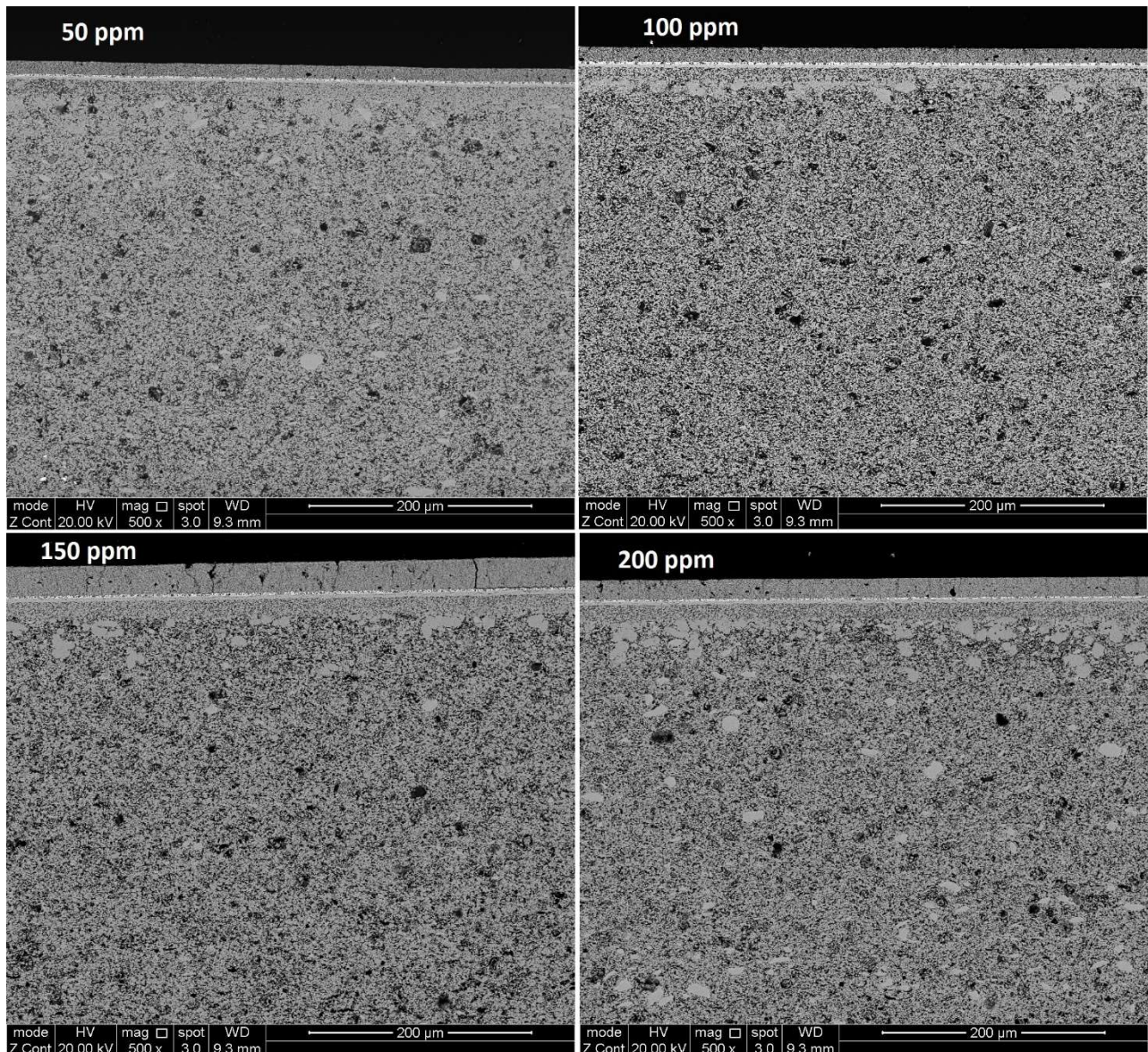


Figure 8.28: Comparison of SEM pictures of contaminated cells

As explained before, the voltage drop of the cells, measured at the end of the exposure period, was more or less similar for all the contamination levels. However, the performance at the end of the recovery was different. Considering the performance of the cells and SEM results, the observed behaviour can be attributed to the change in the structure of anode. In the 50 and 100 ppm tests, the cells partially recovered after removal of  $H_2S$ , whereas, in the cases of 150 and 200 ppm the performance tended to deteriorate further during the recovery. It can be seen in figure 8.28 that the change in the structure was more severe in the 200 ppm test, therefore, the performance at the end of the recovery period was the lowest. On

contrary, the cell exposed to 50 ppm of H<sub>2</sub>S underwent less level of change, thus, partially recovered.

According to the results, it can be stated that, at the higher concentrations, H<sub>2</sub>S affects the performance during the recovery period, through the change in the anode structure. The anode re-structure is not recoverable and tends to deteriorate as the H<sub>2</sub>S concentration increases. However, the performance can partially recover for lower concentrations of H<sub>2</sub>S.



## 9 Conclusion and future work

In this research a test rig was set up to study the performance of single solid oxide fuel cells. A series of experiments were conducted to investigate the performance of cells operating on clean and H<sub>2</sub>S-contaminated fuels. The clean fuel tests include the effect of time, fuel composition and temperature on the performance. Contamination tests were carried out for four levels of poisoning: 50, 100, 150 and 200 ppm of H<sub>2</sub>S.

### 9.1 Conclusions

The findings of this study are divided in three categories: test rig commissioning, clean fuel tests and contamination tests and are summarised as follows:

#### 9.1.1 Test rig commissioning

- Current collecting method plays a key role in the performance. The current collectors should be attached to the electrodes all across the surface. In case the number of the connection points between the electrode and current collection mesh is small, the electrons need to travel across the surface to reach the points. Therefore, a significant part of the cell voltage is lost due to the long electron paths. A clamping mechanism can be used to place uniform pressure on the cell/collectors assembly and provide efficient connection all across the electrode surface.
- The amount of the compression force is an important parameter which can affect the performance of cell. Applying large pressure can lead to blockage of the Si/Al felt pores. This will prevent the fuel to reach to the active site and cause the performance to drop. In addition to blockage, extremely large pressure can result in cell breaking. Conversely, small pressure can lead to poor connection between the electrode and current collector. Therefore, there will be a compromise between the performance and clamping force.
- The position of the control thermocouple is also of great importance while preparing the set up. In the preparation procedure, the position of the thermocouple can be different from test to test. Although the thermocouple may read the same value for all tests, the actual surface

temperature of the cells can be different. In order to minimise this effect, the thermocouples should always be mounted according to the set up manual, i.e. a particular length of the thermocouples is placed in the set up to make sure that the temperature of the same place is measured in all tests.

### 9.1.2 Clean fuel tests

The results of the tests with clean fuel under different operating conditions (baseline tests) can be summarised as follows:

- In order to stabilise the cells, they were loaded at  $0.2 \text{ A/cm}^2$  at the beginning of the tests. The results showed that both ohmic and electrode resistance tended to increase during this period. The change in the electrode resistance (activation and concentration) was much larger than that of the ohmic resistance. It can also be seen from the EIS curves that both semi-circles become larger over time, suggesting that both kinetics and diffusion effects are subject to change during the stabilisation period.
- With the intention of investigating the effect of  $\text{H}_2$  partial pressure on the cell performance, three values of  $P_{\text{H}_2}$  were selected and tested in this study. The results showed that the decrease in the  $\text{H}_2$  partial pressure caused an increase in the electrode resistance, however, the ohmic resistance remained constant. Once the concentration of  $\text{H}_2$  is raised at the anode, the right-hand-side semi-circle of the EIS curves tends to create a smaller arch, while the left-hand-side semi-circle does not change significantly. The former arch corresponds to the lower frequencies and represents the diffusion effects at the electrodes, thus subject to change as  $P_{\text{H}_2}$  is altered.
- To study the effect of temperature on the performance of the cells, the operating temperature was set to a range of values i.e. 600, 650, 700 and 750 °C. The results indicated that the both electrode and ohmic resistances are considerably influenced by the temperature and tend to decrease as the temperature is increased. Once the temperature is varied the left-hand-side arch on the EIS curve is subject to change, while the other does not change significantly. The left-hand-side semi-circle, obtained at high frequencies, is associated with the kinetics of the electrodes. Due to the fact that the kinetics of the cell strongly depends on the temperature and

is favoured at higher temperature, the EIS curve yields a smaller vault for the corresponding semi-circle at higher values of temperature.

- The current of lowest resistance is independent of the operating temperature and remains the same as the temperature changes. However, it depends on the H<sub>2</sub> flow rate (concentration) and increases as the H<sub>2</sub> partial pressure rises.
- The lowest resistance of the tested cells occurs at almost constant fuel utilization which was equal to 17 % in this research. Besides, it tends to decrease as the temperature or H<sub>2</sub> partial pressure increase.
- The results of the EIS curve fitting showed that the resistance of both electrodes will change if the H<sub>2</sub> partial pressure changes. This suggests that the electrode performances are interlinked.

### 9.1.3 Contamination tests

The results of the performance of the cells exposed to 50, 100, 150 and 200 ppm of H<sub>2</sub>S can be summarised as follows:

- In the 50 ppm test, H<sub>2</sub>S caused both ohmic and electrode polarisations to increase over the exposure time. Once H<sub>2</sub>S was removed from the fuel mixture, the electrode polarisation tended to decrease and almost reached its initial value (the value before the exposure period). However, the ohmic resistance became larger during the recovery period, suggesting that H<sub>2</sub>S has left behind a continuous poisoning effect on the cell. The v-i curves showed that the overall performance of the cell was considerably degraded over the exposure time and partially recovered during the recovery.
- The results of the test with 100 ppm of H<sub>2</sub>S showed that both ohmic and electrode resistances increased during the exposure period. However, the rise in the ohmic resistance was much smaller than that of the electrode resistance. Upon removal of H<sub>2</sub>S, the electrode polarisation tended to decrease. On the contrary, the ohmic resistance increased further over the recovery time. This trend was similar to the results of the 50 ppm of H<sub>2</sub>S test. According to the v-i curves, the overall performance of the cell exposed to 100 ppm of H<sub>2</sub>S, magnificently dropped and slightly recovered once the contaminant was removed.

- In the 150 ppm of H<sub>2</sub>S test, both ohmic and electrode resistances of the cell increased during the exposure time, similar to the previous tests. During the recovery period both types of the cell resistance tended to increase further, causing the cell to yield a lower voltage at the end of this stage. In other words, the cell did not recover once H<sub>2</sub>S was removed from the fuel mixture and the polarisations kept increasing over the recovery period.
- The EIS curves taken at different stages of the test with 200 ppm of H<sub>2</sub>S, showed that the ohmic resistance increased inconsiderably over the exposure period, however, the electrode resistance tended to rise significantly. During the recovery period, both ohmic and electrode resistances of the cell continued to increase, causing the overall resistance to become larger at the end this period compared to the resistance at the end of the exposure. The v-i curves showed that the degree of the cell degradation over the recovery period of the 200 ppm test, was larger than that of the 150 ppm test. The curves also indicated that after the exposure period the cell fell into the concentration losses zone at lower current densities which can be associated with the changes in microstructure of the cell. The latter tends to limit the diffusion of the reactants and products through the porous anode. This trend deteriorated over the recovery period, causing the cell to fall into concentration losses zone at smaller current densities compared to the results after the exposure time. This trend was also observed in the test with 150 ppm H<sub>2</sub>S.
- The voltage drop at the end of the exposure period was similar for all degrees of poisoning. However, the performance at the end of the recovery was different.
- During the recovery period, the cell partially recovered for lower H<sub>2</sub>S concentration, whereas, the performance dropped further in the case of higher concentrations. The degree of recovery decreased as the concentration of H<sub>2</sub>S increased.
- Different behaviour during the recovery time suggests that H<sub>2</sub>S has a long term effect on the cells, after being removed from the fuel mixture.
- The SEM picture of the contaminated cells showed that the change in the anode structure is more severe for higher concentrations. At low

concentrations the particles were almost uniformly distributed, whereas, they tended to coarsen at higher concentrations.

- The change in the anode structure occurred at the interface of anode functioning and support layers and tended to expand in the support layer as the H<sub>2</sub>S concentration increased.

## 9.2 Recommendations and future work

In this section a list of recommendations for future work is presented. This list includes the suggestions to improve and optimise the performance of the test rig, increase the capability of the set up and widen the area of the research on the cell behavior operating on both clean and H<sub>2</sub>S contaminated fuels.

Test rig development:

- Replacement of the humidifier with a steamer to achieve larger steam to carbon ratios
- Modification of the test rig to test the performance of SOFC stacks

Clean fuel tests:

- Investigation of H<sub>2</sub>O partial pressure on the performance of SOFCs
- Investigation of the performance of the cells running on hydrocarbons, e.g. internal reforming and coking
- Study of the cell voltage drop during the stabilisation period
- Modification of the test rig to increase the pressure of system
- Investigation of thermal and redox cycle on the performance and structure

Contamination tests:

- Applying more sensitive microscopy techniques to detect the elements and phases within the cell layers. In order to find out whether sulfur is fully removed from the anode or very small amount of S tends to remain in the cell, other microscopy techniques can be applied. Elements like Si originating from the silica felt, may affect the cell during the stabilisation period, which may be detected by other methods.
- Conducting a series of tests with a wider range of the H<sub>2</sub>S concentration. A series of tests can be carried out to cover smaller concentrations of H<sub>2</sub>S (0 to 50 ppm). As all tests are conducted with identical cells and under the

same operating conditions, the results can be effectively compared to investigate the poisoning effect of H<sub>2</sub>S.

- Studying the effect of the operating conditions (temperature, pressure, fuel composition and current density) on cell poisoning
- Analysing the structure of cells before and after recovery. As the performance of the cells at the end of the exposure period was similar, the structure of the cells before and after the recovery period can be compared to identify the effect of H<sub>2</sub>S during the recovery.

## **Appendix 1 Operating Faults**

System	Fault		Cause	Effect	Solution
<b>Gas blender</b>	<b>Flow</b>	No flow	<ul style="list-style-type: none"> <li>• Cylinder empty/closed</li> <li>• Ball valves closed</li> <li>• Pressure regulator fault/closed &amp; incorrect setting</li> <li>• Air actuator fault/closed               <ul style="list-style-type: none"> <li>- Compressor off</li> <li>- Solenoid valves relay off</li> <li>- Solenoid valves power supply off</li> <li>- Solenoid valves air supply valve closed</li> <li>- LabVIEW fault/power switch off</li> </ul> </li> <li>• Flow controllers fault/closed &amp; incorrect setting</li> <li>• Vent open/Leakage</li> <li>• Filters blocked</li> </ul>	<ul style="list-style-type: none"> <li>• Oxidation of cell</li> <li>• Operating on undesired condition</li> </ul>	<ul style="list-style-type: none"> <li>• Replace or open the cylinder</li> <li>• Check the test procedure to run the test</li> <li>• Check the settings (channels &amp; values) in LabVIEW</li> <li>• Tighten the connections</li> <li>• Check the filters regularly</li> <li>• Check the functionality of solenoid valves and flow controllers</li> <li>• Check the power supplies</li> <li>• Check the pipework</li> <li>• Open manual line</li> </ul>
		More flow	<ul style="list-style-type: none"> <li>• Flow controller fault</li> <li>• Pressure regulator fault &amp; incorrect setting</li> </ul>	<ul style="list-style-type: none"> <li>• Operating on undesired condition</li> </ul>	<ul style="list-style-type: none"> <li>• See the section on No flow</li> </ul>
		Less flow	<ul style="list-style-type: none"> <li>• Flow controller fault</li> <li>• Pressure regulator fault &amp; incorrect setting</li> <li>• Leakage/blockage</li> </ul>	<ul style="list-style-type: none"> <li>• Oxidation of cell</li> <li>• Operating on undesired condition</li> </ul>	<ul style="list-style-type: none"> <li>• See the section on No flow</li> </ul>
	<b>Pressure</b>	No pressure	<ul style="list-style-type: none"> <li>• No flow (see the section on No flow)</li> <li>• Pressure meter fault</li> <li>• Pressure regulator fault</li> </ul>	<ul style="list-style-type: none"> <li>• Oxidation of cell</li> </ul>	<ul style="list-style-type: none"> <li>• Check the pressure regulators and meters</li> <li>• See the section on Flow</li> </ul>
		More pressure	<ul style="list-style-type: none"> <li>• Pressure regulator fault</li> <li>• Blockage</li> </ul>	<ul style="list-style-type: none"> <li>• Operating on undesired condition</li> </ul>	<ul style="list-style-type: none"> <li>• Check the pressure regulators and meters</li> <li>• See the section on Flow</li> </ul>
		Less pressure	<ul style="list-style-type: none"> <li>• Pressure regulator fault</li> <li>• Leakage/venting</li> <li>• Cylinder empty</li> </ul>	<ul style="list-style-type: none"> <li>• Oxidation of cell</li> </ul>	<ul style="list-style-type: none"> <li>• Check the pressure regulators and meters</li> <li>• See the section on Flow</li> </ul>

System	Fault		Cause	Effect	Solution
Humidifier	Flow		<ul style="list-style-type: none"> <li>• See the section on Flow(gas blender)</li> </ul>	<ul style="list-style-type: none"> <li>• See the section on Flow (gas blender)</li> </ul>	<ul style="list-style-type: none"> <li>• See the section on Flow (gas blender)</li> <li>• Check the sealing</li> </ul>
	Temperature	More or less	<ul style="list-style-type: none"> <li>• Temperature controller fault</li> <li>• Thermocouple fault</li> <li>• Heating element fault</li> </ul>	<ul style="list-style-type: none"> <li>• Diluted fuel (less power)</li> <li>• Operating on undesired condition</li> </ul>	<ul style="list-style-type: none"> <li>• Check the thermocouple</li> <li>• Check the controller</li> </ul>
Furnace	Flow		<ul style="list-style-type: none"> <li>• See the section on flow (gas blender)</li> <li>• Air leakage</li> </ul>	<ul style="list-style-type: none"> <li>• Oxidation of cell</li> <li>• Operating on undesired condition</li> </ul>	<ul style="list-style-type: none"> <li>• Check the air flow rate</li> <li>• Check the sealing</li> <li>• See the section on Flow</li> </ul>
	Pressure		<ul style="list-style-type: none"> <li>• See the section on Pressure (gas blender)</li> </ul>	<ul style="list-style-type: none"> <li>• See the section on Pressure (gas blender)</li> </ul>	<ul style="list-style-type: none"> <li>• See the section on Pressure (gas blender)</li> </ul>
	Temperature	More or less	<ul style="list-style-type: none"> <li>• Temperature controller fault</li> <li>• Thermocouple fault</li> <li>• Change in position of thermocouples</li> <li>• Heating element fault</li> <li>• Over-temperature controller fault</li> <li>• Furnace insulation fault</li> <li>• Temperature fluctuation</li> </ul>	<ul style="list-style-type: none"> <li>• Operating on undesired condition</li> </ul>	<ul style="list-style-type: none"> <li>• Check the controllers</li> <li>• Check the thermocouples position</li> <li>• Check the insulation</li> <li>• Check the mica cap position</li> <li>• Check the air inlet position</li> </ul>
	Fire		<ul style="list-style-type: none"> <li>• Leakage of hydrogen</li> </ul>	<ul style="list-style-type: none"> <li>• Damage to rig and operators</li> </ul>	<ul style="list-style-type: none"> <li>• Press emergency button</li> <li>• If safe to do so turn off gases at cylinders</li> </ul>
LabVIEW program	Crash		<ul style="list-style-type: none"> <li>• Software/computer problems</li> </ul>	<ul style="list-style-type: none"> <li>• Oxidation of cell</li> </ul>	<ul style="list-style-type: none"> <li>• Unload the cell</li> <li>• Restart the program/PC and control the gas blender through program</li> <li>• If the fault is permanent cool down the furnace using manual line</li> </ul>
	Accidental close of program		<ul style="list-style-type: none"> <li>• Operator mistake (signals are still being sent to devices)</li> </ul>	<ul style="list-style-type: none"> <li>• Operating on undesired condition</li> </ul>	<ul style="list-style-type: none"> <li>• Run the program in operating mode (signals are stopped)</li> <li>• Set the H2 and N2 flow rates first in program, then press “power switch”</li> </ul>

Fault		Cause	Effect	Solution
Voltage Current	No V/I Less More	<ul style="list-style-type: none"> <li>• Broken gold wire</li> <li>• Nickel diffuser fault</li> <li>• Broken or loose wires to LV kit</li> <li>• Load bank wrong setting</li> <li>• Power supply wrong setting</li> <li>• Lead wires wrong setting</li> <li>• Short circuit</li> <li>• No/less fuel flow rate</li> <li>• Loose springs, No compression force</li> </ul>	<ul style="list-style-type: none"> <li>• Operating on undesired condition</li> <li>• Damage to cell</li> </ul>	<ul style="list-style-type: none"> <li>• Measure the voltage using different gold wires</li> <li>• Check the wires to LV kit</li> <li>• Check the connection/setting of lead wires</li> <li>• Check the load bank setting</li> <li>• Check the power supply setting</li> <li>• Check the flow, see section on flow (gas blender)</li> <li>• Check the spring setting</li> </ul>
	Smell of H <sub>2</sub> S	<ul style="list-style-type: none"> <li>• High concentration of H<sub>2</sub>S in building</li> </ul>	<ul style="list-style-type: none"> <li>• Poisoning</li> </ul>	<ul style="list-style-type: none"> <li>• Use the detector to measure the concentration of H<sub>2</sub>S in building</li> <li>• Open the roller shutter door and switch on the fans in the building</li> <li>• if the concentration of H<sub>2</sub>S in the building is higher than 10 ppm evacuate the building</li> <li>• if the concentration does not decrease shut down the rig</li> </ul>
Safety	Operator faults	<ul style="list-style-type: none"> <li>• Extreme fatigue</li> <li>• Untrained operator</li> </ul>	<ul style="list-style-type: none"> <li>• Risk of making poor decisions</li> <li>• Operating on undesired condition</li> <li>• Oxidation of cell</li> <li>• Damage to the rig and people</li> <li>• Burning due to high temperature</li> <li>• Slips, trips, falls</li> <li>• Poisoning due to H<sub>2</sub>S</li> </ul>	<ul style="list-style-type: none"> <li>• 2 operators running the rig in shifts</li> <li>• Train the operators</li> </ul>

## **Appendix 2 Risk Assessment and COSHH Forms**

**Risk Assessment Form**

*please email a copy of the completed risk assessment form to*

*me-labsafety@shef.ac.uk*

Risk : (H) High (M) Medium (L) Low (O) No Risk			Environment : Beighton labs, SOFC test rig	
TASK or ACTIVITY : Commissioning sofc rig		INITIAL RISK		FINAL RISK RATING
SIGNIFICANT HAZARD	RISK	RATING	EXISTING CONTROL / PROPOSED CONTROL MEASURES	
Electricity	Shocks, burns, damage to equipments	M	Installation of instruments to be left to a qualified technician Disconnect all electrical sources when not in use	L
Hand tools	Cuts, abrasions hazards	L	Appropriate PPE should be worn at all times in addition to boots, stout gloves where appropriate	L
Heated and high temperature elements	Burns, overheat damage, fire	M	All insulation to be checked before test, Due care should be taken by staff	L
Components on rig	Fall	M	Wear safety boots, Place elements away from walk ways keep all walkways clear and have no items sticking out	L
High pressure gases	Damage to rig and people	L	Support the cylinders, tighten the connections	L
Flammable/explosive gases	Fire/explosion	L	Control the flow rate of hydrogen, ensure gas connections are correctly made, cylinders are connected up by people who are trained to make the connections and all connections are leak tested, including those to the cylinder as well all rig pipework	L
Asphyxiating gases	Damage to people	L	Control the flow rate of gases, ensure gas connections are correctly made, cylinders are connected up by people who are trained to make the connections and all connections are leak tested, including those to the cylinder as well all rig pipework	L
Poisonous gases	Poisoning effects	L	Ensure all gas connections are tightened and leak tested	L
Irritable materials (furnace insulation)	Damage to respiratory system and skin	L	Wear gloves and masks	L

**Risk Assessment Form**

*please email a copy of the completed risk assessment form to  
me-labsafety@shef.ac.uk*

<p>Extreme fatigue, Falling into sleep, Operator faults</p>	<p>Risk of making poor decisions, Operating on undesired condition, Damage to the rig and people, Burns, Slips, Trips, Falls, Poisoning due to H<sub>2</sub>S, Setting up gases incorrectly</p>	<p>M</p>	<p>2 operators running the rig in shifts Train the operators</p>	<p>L</p>	
<p>H<sub>2</sub>S leak from piping and flow controller</p>	<p>Risk of corrosion of pipes, valves and flow controller sealing</p>	<p>L</p>	<p>Regularly check the piping and valves, use suitable sealing for flow controller</p>	<p>L</p>	
				<p>Overall Risk :</p>	
<p>Comments :</p>					
<p>Additional References, Tasks etc :</p>					
<p>Undertaken By :</p>	<p>Status:</p>	<p>Date:</p>			
<p>Other Person(s) Consulted :</p>		<p>Reference No:</p>			
		<p>Revision Date:</p>			
<p><b>Before proceeding you must have read &amp; fully understood this risk assessment &amp; have signed the attached form This form is to be reviewed when any change is made &amp; annually. When allocating the reference number please mark up the apparatus accordingly</b></p>					

I have read & understood the attached Risk Assessment

Name	Signed	Date	Supervisor (if applicable)
------	--------	------	----------------------------



The  
University  
Of  
Sheffield.

## Department of Mechanical Engineering

### Risk Assessment Form

*please email a copy of the completed risk assessment form to  
[me-labsafety@shef.ac.uk](mailto:me-labsafety@shef.ac.uk)*




**COSHH Form**

Risk : (H) High (M) Medium (L) Low (O) No Risk			Environment : Beighton labs, SOFC test rig	
TASK or ACTIVITY : Commissioning SOFC rig		INITIAL RISK RATING	EXISTING CONTROL / PROPOSED CONTROL MEASURES	FINAL RISK RATING
SIGNIFICANT HAZARD	RISK			
Asphyxiating gases	Damage to people	L	Control the flow rate of gases, ensure gas connections are correctly made, cylinders are connected up by people who are trained to make the connections and all connections are leak tested, including those to the cylinder as well all rig pipework	L
Poisonous gases	Poisoning effects	L	Ensure all gas connections are tightened and leak tested	L
Components on rig	Fall	M	Wear safety boots, Place elements away from walk ways keep all walkways clear and have no items sticking out	L



## **Appendix 3 LabVIEW Hardware and Channels**

				Channel no.								
Module no	Card type	Break-out		0	1	2	3	4	5	6	7	
AI	SC1 Mod4	SCXI 1120	SCXI 1320	signal	-	CH <sub>4</sub> rate	CO <sub>2</sub> rate	O <sub>2</sub> rate	N <sub>2</sub> rate	H <sub>2</sub> rate	HS reading	HS TC
				gain	1	1	1	1	1	1	1	100
	SC1 Mod5	SCXI 1120	SCXI 1320	signal	-	V	Fur signal	FS	I	fur temp2	fur temp	HT TC
				gain	1	1	1	1	20	100	100	100
AO	PXI1 slot3	PXI 6713	TB 2705	-		CH <sub>4</sub> set rate	CO <sub>2</sub> set rate	O <sub>2</sub> set rate	N <sub>2</sub> set rate	H <sub>2</sub> set rate	HS volt out	
DO	SC1 Mod1	SCXI 1161	-	-	CH <sub>4</sub> line	CH <sub>4</sub> vent	CH <sub>4</sub> outlet	N <sub>2</sub> line	N <sub>2</sub> vent	N <sub>2</sub> outlet	H <sub>2</sub> line	H <sub>2</sub> vent
	SC1 Mod2	SCXI 1161	-	-	H <sub>2</sub> outlet	CO <sub>2</sub> line	O <sub>2</sub> line		Switch status			

## **Appendix 4 Test Procedure**

## Operation procedure

1. Refer to the "Fiaxell" manual to prepare the set up
2. Mount the SOFC set on the "Rohde" furnace
3. Connect the lead wires to the terminals, see figure 01
  - 3.1. Cathode: two pieces of gold wire for current, one piece for voltage
  - 3.2. Anode: fuel inlet for current, diffuser rod for voltage

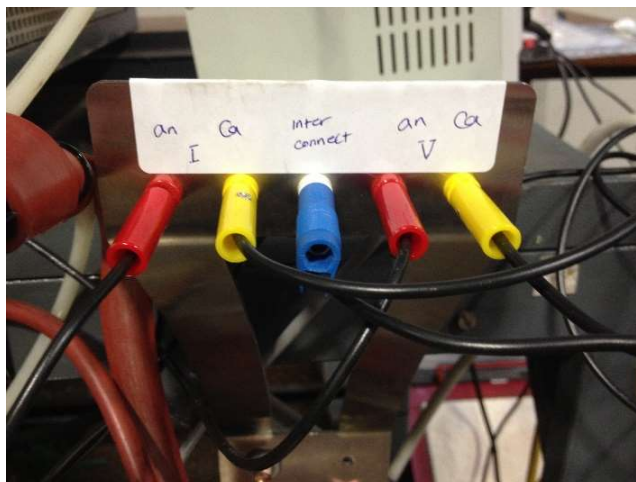
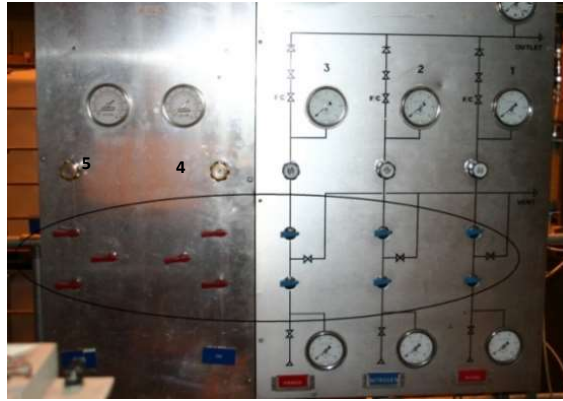


Figure 01: connection of lead wires to terminals

4. Make sure that the wires are kept separated and there are no short circuits between the connections
5. Connect the thermocouples
6. Connect the fuel inlet using Teflon ferrule
7. Put the outlet tubes on place (as heater) and connect the fuel outlet using the silicon tubes
8. Connect the air inlet using Teflon ferrule
9. Set the pressure on bottles and purge the lines from cylinder to gas panel
  - 9.1. Connect a bottle to each air actuator inlet
  - 9.2. Set the pressure on all regulators
  - 9.3. Do not change the pressure of bottles (do not turn the regulators volume/handle)
10. Make sure power supply and cell are arranged correctly
11. Close **all** the ball valves on gas panel (see figure 02)
12. Make sure the air compressor is ON



**Figure 02: gas panel ball valves**

13. Make sure that both emergency buttons are released (see figure 03)



**Figure 03: emergency buttons**

14. Switch on the flow controllers power supplies (on the power supplies and sockets panel)
15. Switch on the relays power supply (on the socket panel)
16. Close the ball valve and flow controller on the manual fuel line, see figure 04

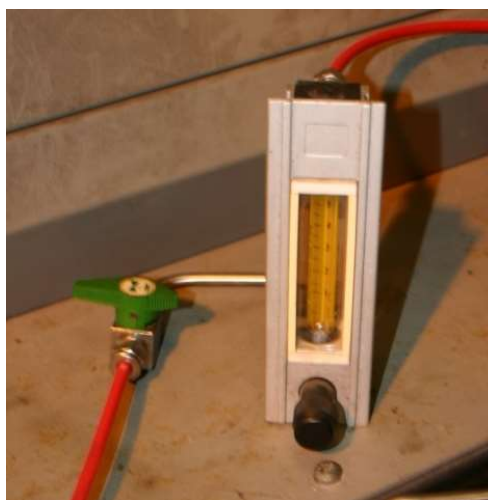


**Figure 04: manual fuel line**

17. Switch on the solenoid valves power supply, see figure 05



Figure 05: solenoid valves power supply

18. Turn on solenoid-valves air supply valve and set the pressure to 3.5 bars (see figure 06), 1<sup>st</sup> fuel line air-actuated valve opens (2<sup>nd</sup> one is normally open, thus, both valves – manual line – are open now).



Figure 06: solenoid air supply valve and pressure regulator

#### 19. Purge manual line

- 19.1. Make sure that the H<sub>2</sub> cylinder is open and pressure is **4** bars
- 19.2. Open the ball valve on manual fuel line, then slowly open the rotameter and set the flow to 1 l/min (figure 04)
20. Switch on the PC (national instruments chassis)
21. Run the controlling program (see figure 07), choose "Test Rig" then choose "Operation Mode" and confirm it, then **switch on the "Power Switch"** (see figure 08), 2<sup>nd</sup> fuel manual line air-actuated valve closes (manual line closes)
22. Make sure all the flow controllers' value is set to zero, see figure 09

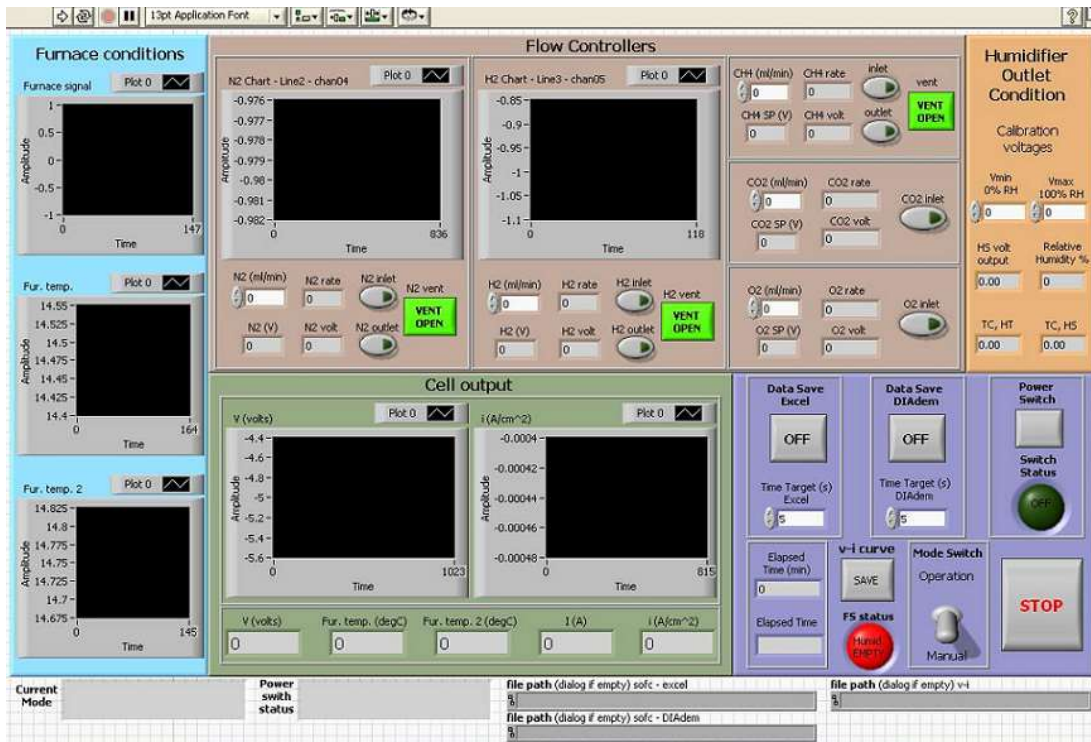


Figure 07: controlling program

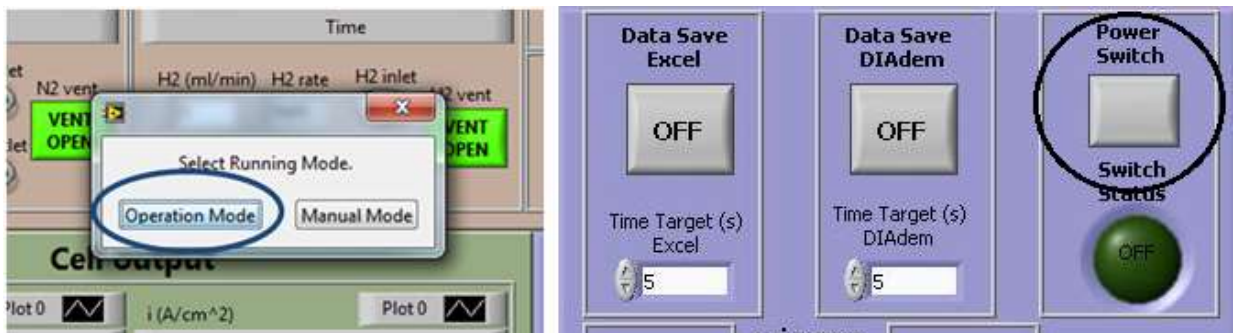


Figure 08: operation mode-power switch

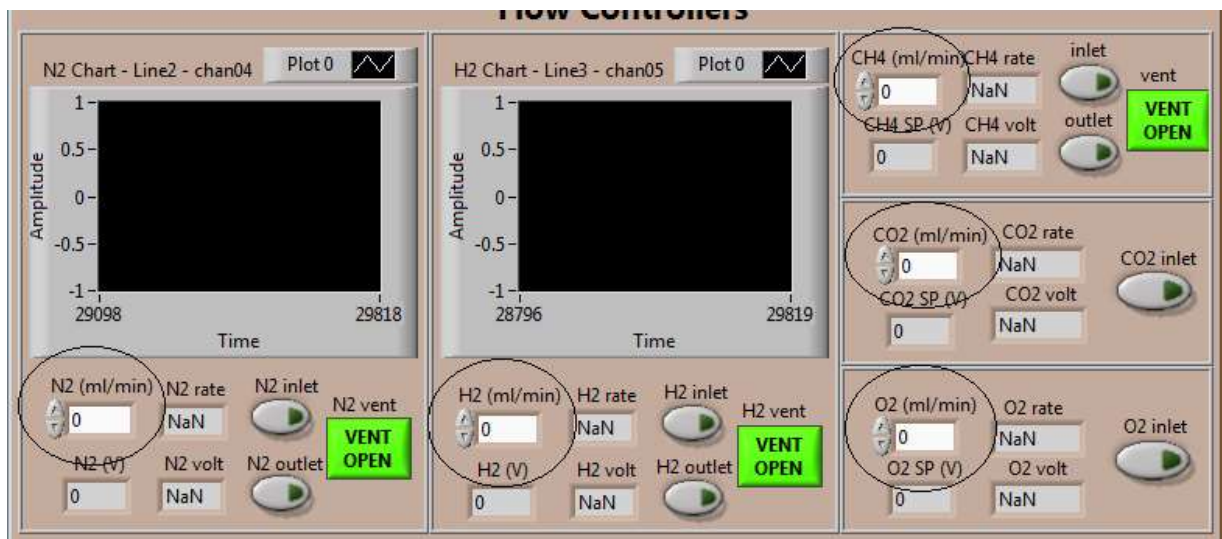


Figure 09: flow controllers set point

### 23. Set the humidifier

23.1. Check the humidifier status for level of water – add water through the filling port on the humidifier in case of alarm and afterwards ensure the filling port in sealed and leak checked, see figure 10

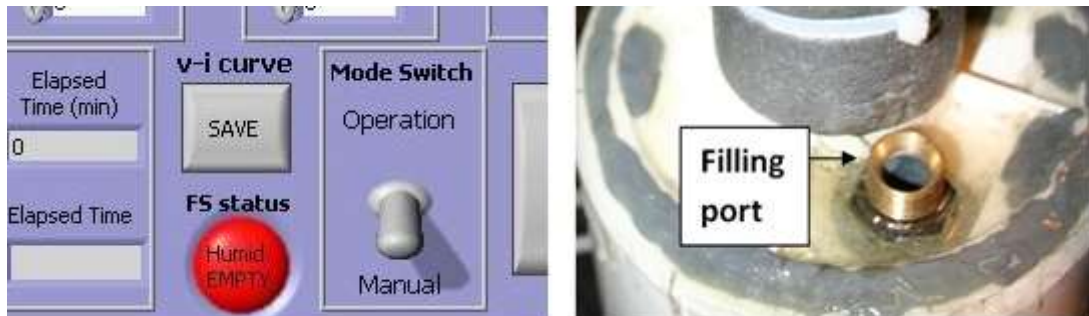


Figure 10: check the float switch alarm

23.2. Switch on the humidifier power supply (on sockets panel)

23.3. Set the temperature of humidifier to 25 °C for 3 % water content (see figure 11)



Figure 11: humidifier controller

23.4. Make sure that the fuel tubes above the humidifier is covered with heating tape

23.5. Cover the fuel outlet tubes with the second heating tape, see figure 12

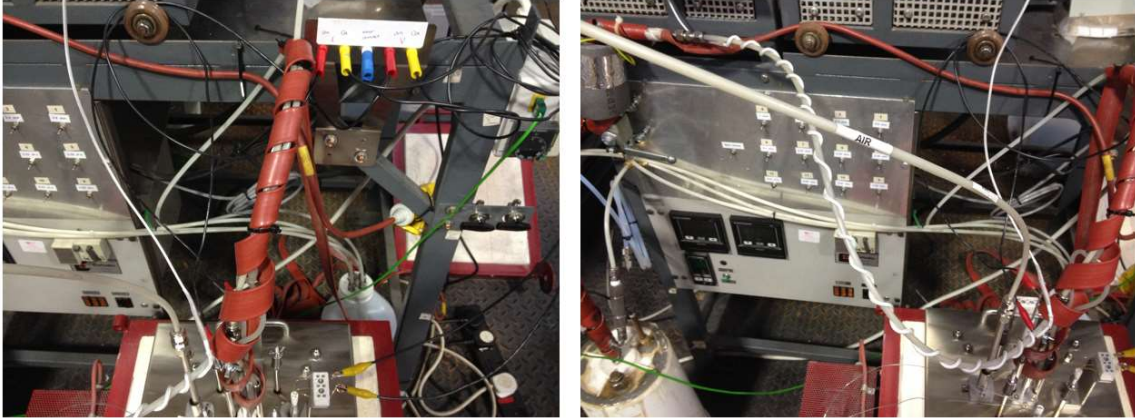


Figure 12: heating tape/wire to cover fuel inlet and outlet tubes

23.6. Switch on the heating tape and set the temperature (see figure 13) – the temperature should be smaller than 120°C

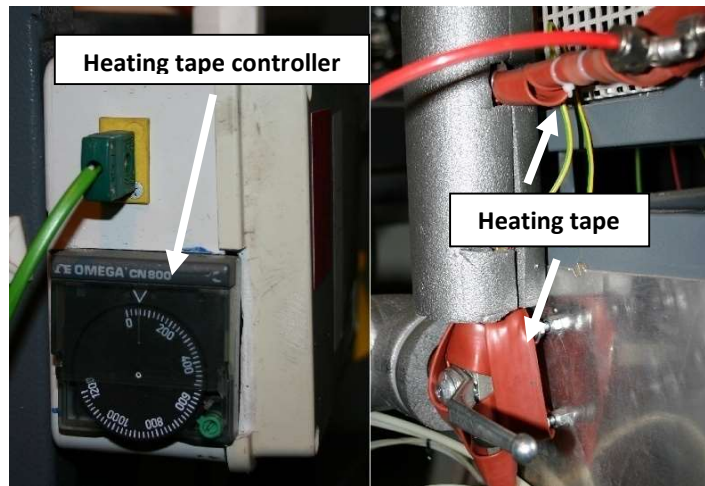


Figure 13: heating tape & controller

24. Put the heating wire around the fuel inlet hose and switch on/set the controller, see figure 12
25. Make sure **all** the switches on load bank panel are in OFF (middle) position, see figure 14

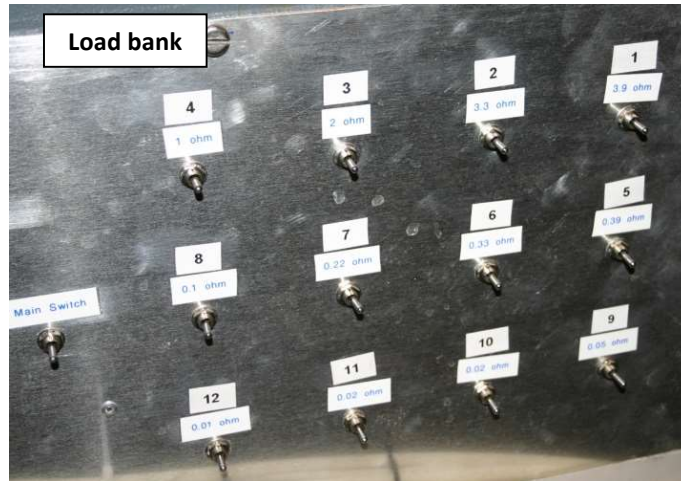


Figure 14: load bank

26. Make sure that the 1<sup>st</sup> 3-way valve is open to humidifier (handle up) and the 2<sup>nd</sup> is open to cell (handle down), see figure 15 and figure 16



Figure 15: 3-way valves – 1st mode

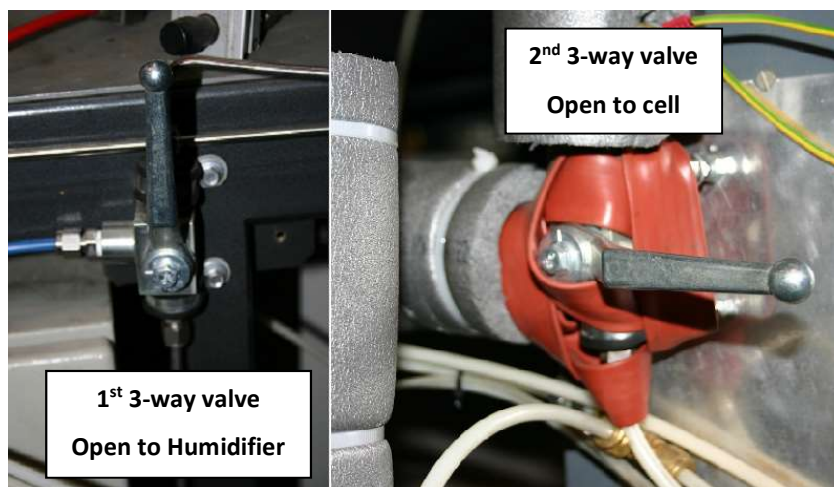


Figure 16: 3-way valve - 2nd mode

27. Ensure that the humidifier check valve is open (see figure 17)

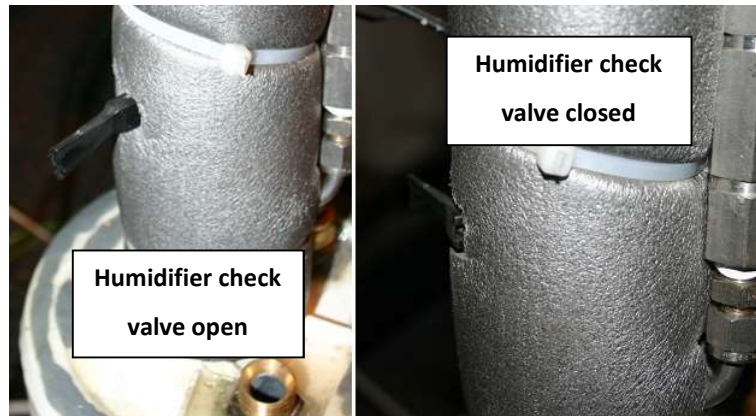


Figure 17: humidifier check valve

## 28. Set the furnace

- 28.1. Switch on the furnace controller
- 28.2. Select program 1 on the furnace controller
- 28.3. Set ramp1, ramp2 and ramp3 to 120°C
- 28.4. Set temp1 and temp2 to the operating temperature
- 28.5. Set t1 and t1 to hold
- 28.6. Change temp1 to change the operating temperature during the test
- 28.7. Press the “start” button on the furnace controller to start the program

## 29. Purge system

- 29.1. Make sure all the flow controller values are set to zero, (figure 09)
- 29.2. Open ball valves on N<sub>2</sub> line (line 2) and H<sub>2</sub> line (line 3), see figure 18
- 29.3. Set both N<sub>2</sub> and H<sub>2</sub> set point to 100 ml/min in LabVIEW, see figure 19
- 29.4. **Set the pressure of air flow to 3 bars and set the flow to 1 l/min**, see figure 20
- 29.5. Run N<sub>2</sub>, H<sub>2</sub> and air for 10 minutes (change the mode of valve on the inlet of the air actuators to purge both inlets), then set both N<sub>2</sub> and H<sub>2</sub> set points to zero in LabVIEW (see figure 19), let the air run
- 29.6. While H<sub>2</sub> and N<sub>2</sub> lines are being purged, for H<sub>2</sub>S line, connect a bottle of N<sub>2</sub> to inlet valve, set the pressure on regulator, open the ball valves on the inlet and line, set the set point to 100 ml/min in LabVIEW to purge the line for a few minutes. Close all the ball valves (inlet and line), disconnect the N<sub>2</sub> bottle, connect the H<sub>2</sub>S bottle to inlet, open the inlet ball valve, and loosen the connection on inlet ball valve. Run the gas for a few second then tighten the connection. Close the inlet ball valve



Figure 18: ball valves on N<sub>2</sub> and H<sub>2</sub> line

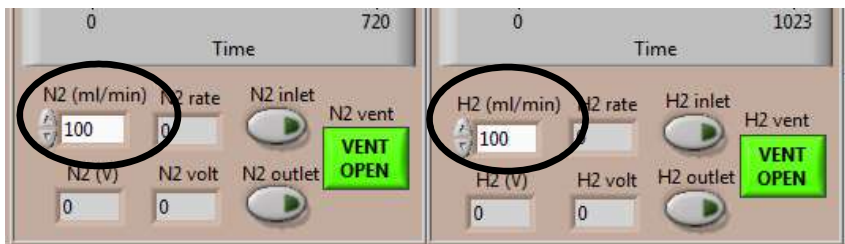


Figure 19: set N<sub>2</sub> and H<sub>2</sub> set points in LabVIEW to purge



Figure 20: air flow valve, pressure regulator and rotameter

30. Once the temp reached 100 °C

30.1. set the H<sub>2</sub> and N<sub>2</sub> set points to 50 and 100 ml/min respectively in LabVIEW to prevent oxidation of Ni, see figure 21

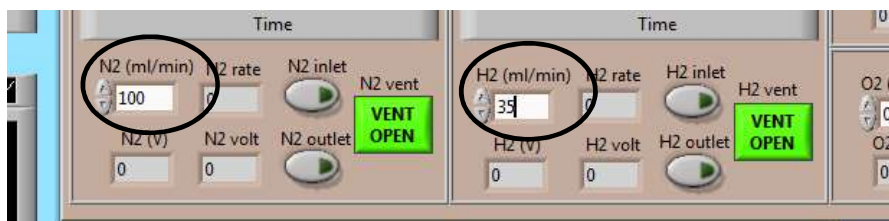


Figure 21: set N<sub>2</sub> and H<sub>2</sub> set points in LabVIEW

30.2. set the "Time Target (s) Excel" to 2 and "Time Target (s) DIAdem" to 0.5, then switch on "Data Save Excel" and "Data Save DIAdem" buttons, see figure 22

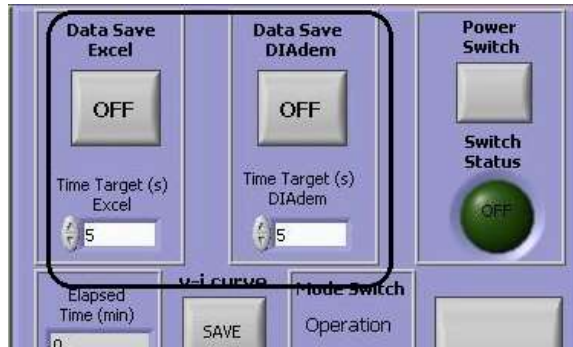


Figure 22: time target and data auto save

31. while heating up check the springs' length, make sure the wingnuts are not loose
32. Once the temperature reached the set point
  - 32.1. Re-adjust the wingnut again, turn each wingnut half a turn. If the voltage does not change do not turn the wingnuts anymore
  - 32.2. **Check that the air is still flowing at 1 l/min**, see figure 20
  - 32.3. Set the H<sub>2</sub> & N<sub>2</sub> set points to 100 & 566.67 ml/min respectively in LabVIEW
33. Wait 1 hour for voltage to stabilize, see figure 23

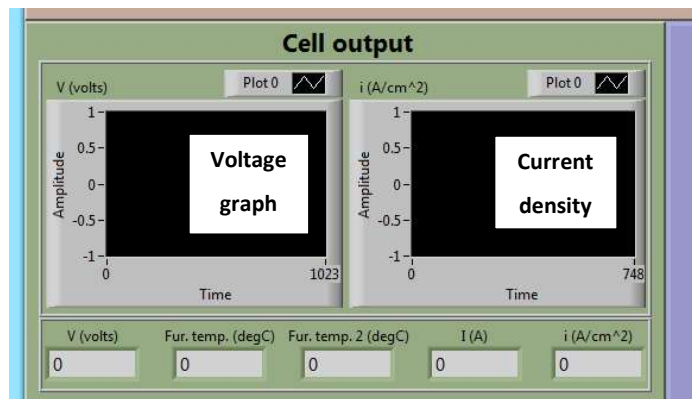


Figure 23: voltage graph in LabVIEW

34. Take the v-i curve
  - 34.1. Make sure all the switches on the LB including the "main switch" are off (in middle position; the circuit is open)
  - 34.2. On the power supply in series with cell set the current limit to the 5.2 A (maximum value)
    - 34.2.1. Switch on the power supply, see figure 24
    - 34.2.2. Bring all voltage and current knobs to zero.
    - 34.2.3. Use a short-circuit wire to short the current terminals (+) to (-).

- 34.2.4. Adjust the current knob until the CC indicator is on.
- 34.2.5. Adjust the current knob to the desired value (it may be necessary to increase the voltage a bit to be able to adjust the current).
- 34.2.6. Take off the short circuit wire and the limit is set.
- 34.2.7. When the unit is switched off, the limit will revert to the default value

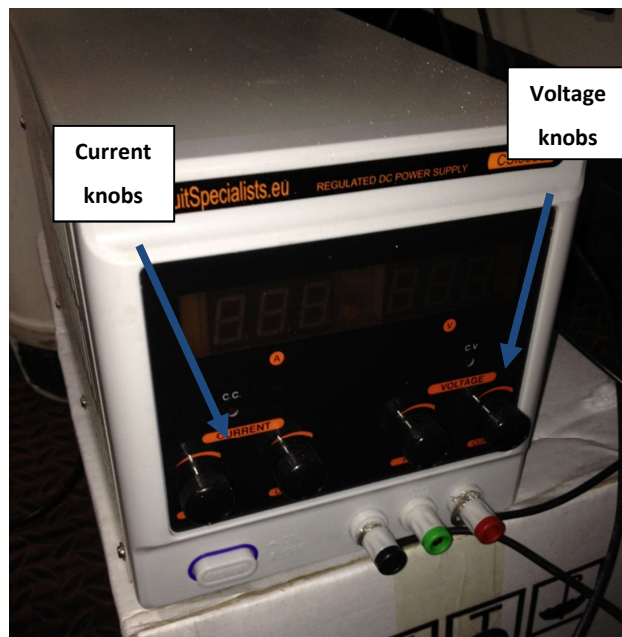


Figure 24: Power supply in series to the cell

- 34.3. Save v and i values (V=OCV, I=0) i.e. press “v-I curve” button to save data, see figure 25

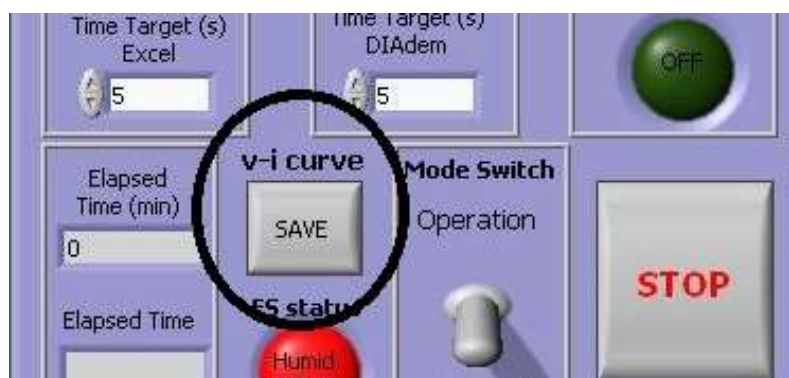


Figure 25: V-I curve button

- 34.4. Set the voltage of the power supply to 0.5 V
- 34.5. Switch on the “main switch” on LB, then save v & i after 20 s (expected current:  $I = [1 + 0.5] / 11.9 = 0.12$  A)

34.6. Increase  $V_{ps}$  in steps of 1.5 or 2 V up to 4 V and save  $v$  &  $i$  at each step after stabilization time of 20 s (expected current at  $V_{ps}=4$ :  $I = [1+4]/11.9=0.42$  A)

34.7. Once the  $V_{ps}$  is 4 V decrease the resistance on load bank according to table 01 (see figure 14), save  $v$  &  $i$  at each step after stabilization of 20 s

34.8. If the final current is less than 5.2 A, increase the voltage of the power supply slowly (in steps of 0.3 A) so that current reaches 5.2 A (maximum current).

Step	Resistor No.	1	2	3	4	5	6	7	8	9	10	11	12	Main switch
	1	ON	OFF											
2	ON	OFF	ON	ON	OFF	ON								
3	ON	ON	OFF	ON	OFF	ON								
4	ON	ON	OFF	ON	ON	ON	OFF	ON						
5	ON	ON	ON	OFF	ON									
6	ON	ON	ON	OFF	ON	OFF	ON							
7	ON	ON	ON	OFF	ON	OFF	ON	OFF	OFF	OFF	OFF	OFF	OFF	ON
8	ON	ON	ON	OFF	ON	ON	OFF	ON	OFF	OFF	OFF	OFF	OFF	ON
9	ON	ON	ON	ON	OFF	ON								
10	ON	ON	ON	ON	OFF	OFF	OFF	ON	OFF	OFF	OFF	OFF	OFF	ON
11	ON	ON	ON	ON	OFF	OFF	ON	OFF	OFF	OFF	OFF	OFF	OFF	ON
12	ON	ON	ON	ON	OFF	OFF	ON	OFF	ON	ON	OFF	OFF	OFF	ON
13	ON	ON	ON	ON	OFF	OFF	ON	ON	OFF	OFF	OFF	OFF	OFF	ON

Table 01: steps to decrease the resistance on load bank

35. take reverse  $v - i$  curve (if necessary)

35.1. Set the voltage of power supply back to 4 V and save  $v$  &  $i$  after stabilization time

35.2. Increase the resistance on LB according to table 01 (in reverse) and save  $v$  &  $i$  at each step after stabilization time

35.3. Decrease  $V_{ps}$  in steps of 1.5 V down to 0.5 V, save  $v$  &  $i$  at each step after stabilization time

35.4. Switch off the “main switch” on load bank and save  $v$  &  $i$  after stabilization time

36. Load the cell for durability test

36.1. Make sure that the cell is unloaded i.e. **all switches** on the LB are off (middle position)

36.2. On the power supply bring all current and voltage knobs to zero

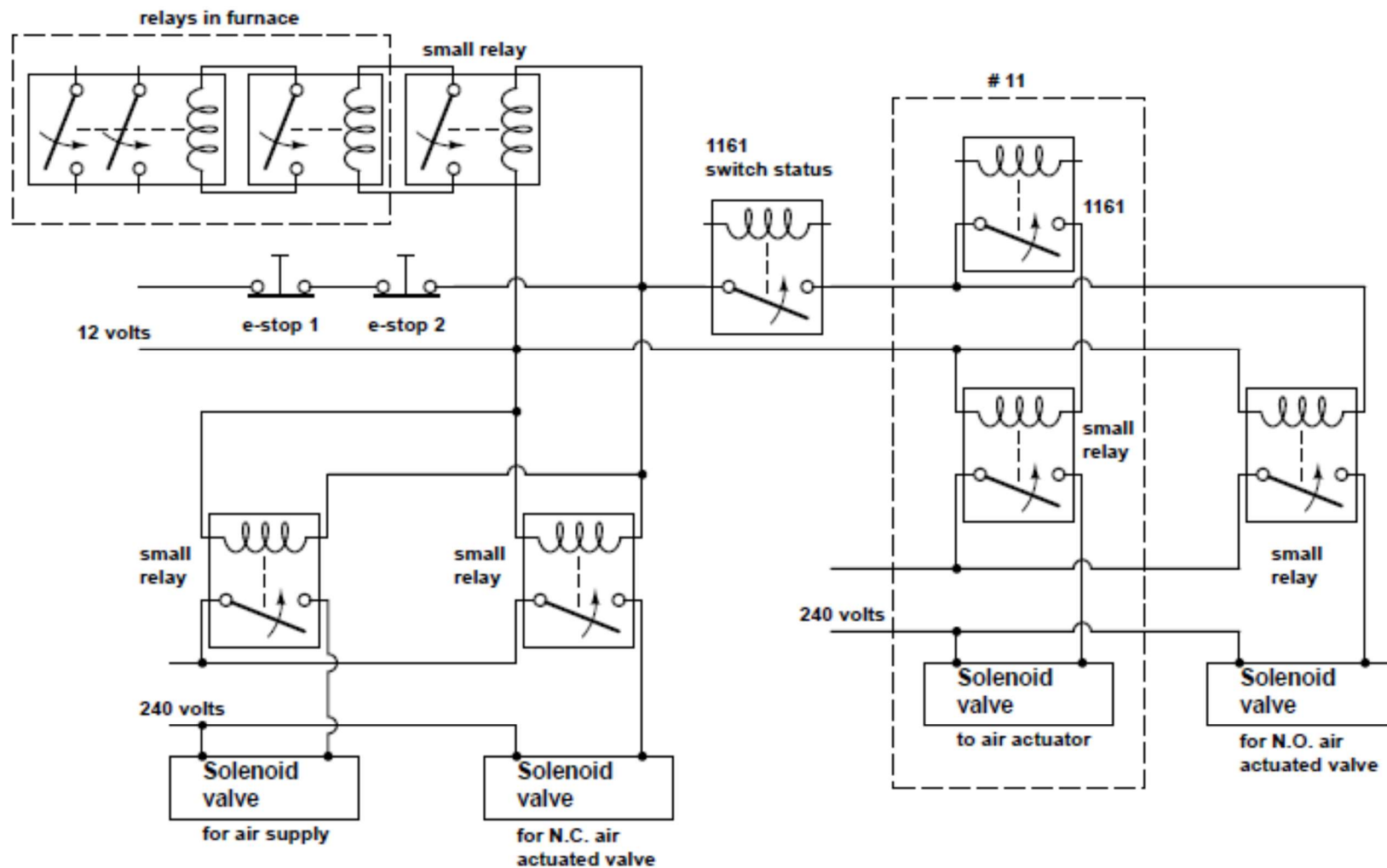
- 36.3. Set the current limit of power supply to 3.2 A (0.2 A/cm<sup>2</sup>), see section 34.2
- 36.4. Set the load bank as the step 7 of table 01
- 36.5. Increase the voltage of the power supply until the current reaches the limit (3.19 A)
- 36.6. Use the current fine knob to adjust the current density to 0.200 on LabVIEW
37. Take v-i and reverse v-i curves in the middle of durability test (if necessary)
  - 37.1. Decrease the voltage of power supply to zero
  - 37.2. Unload the cell i.e. switch off all the switches on the LB
  - 37.3. Repeat the steps 34 and 35
38. Introduce H<sub>2</sub>S – (the cell has been already loaded for durability test)
  - 38.1. Make sure that the current limit of power supply to 3.2 A (0.2 A/cm<sup>2</sup>) and the load bank has been set as the step 7 of table 01
  - 38.2. Change the temperature of humidifier according to the humidification calculation
  - 38.3. Open all the ball valves on the contamination line (inlet and line)
  - 38.4. Change the flow rates in LabVIEW according to the desired concentration, use auxiliary rates
    - 38.4.1. Set the new values in auxiliary rates
    - 38.4.2. Press the "Set new SPs" button (auxiliary rates are sent to FCs - main rates are idle)
    - 38.4.3. Change the main SPs according to level of contamination
    - 38.4.4. Press the "Set new SPs" button (main SPs are sent to FCs - aux. rates are idle)
  - 38.5. The voltage of cell will start to drop, to maintain the current turn on the voltage knob to make sure that the power supply will compensate for any drop in the voltage (see figure 24)
39. Recover the cell (run the cell on clean fuel)
  - 39.1. Set the flow rate of clean N<sub>2</sub> to 566.66 in LV and the flow rate of contamination line to zero in LV using auxiliary rates
  - 39.2. Close the inlet valve on H<sub>2</sub>S line
  - 39.3. Close the ball valves on H<sub>2</sub>S line
  - 39.4. Shut the H<sub>2</sub>S bottle off
40. Purge the H<sub>2</sub>S line on cooling down

- 40.1. Disconnect the H<sub>2</sub>S bottle and connect a pure N<sub>2</sub> cylinder to contamination line
- 40.2. Open all the ball valves on contamination line
- 40.3. Set the flow rate of contamination line to 500 in LV
- 40.4. Let N<sub>2</sub> run for a few minutes then set the set point to zero
- 40.5. Close the ball valves
41. Maintaining the temperature
  - 41.1. Press the “start/stop” button on the furnace controller to stop the program
  - 41.2. Adjust temp1 and temp2 a bit to set the furnace temperature
    - 41.2.1. Press temp1 or temp2 button
    - 41.2.2. Adjust the value using - + buttons
  - 41.3. Press the “start/stop” button on the furnace controller to start the program again

## Procedure to cool down

1. Switch off the resistance by-pass switches slowly to increase the resistance and finally switch off the main switch on load bank so that the voltage reaches the OCV
2. Set the H<sub>2</sub> and N<sub>2</sub> set points to 35 and 100 ml/min, respectively in LabVIEW
3. Set temp2 to 200 below operating temperature
4. Set t1 and t2 to 0.01 on furnace controller
5. Once temperature has fallen below **100°C**, (stop H<sub>2</sub> flow)
  - 5.1. set the H<sub>2</sub> set point to zero in LabVIEW
  - 5.2. close all the ball valves on H<sub>2</sub> line
  - 5.3. close the H<sub>2</sub> cylinder regulator
6. Let N<sub>2</sub> run for 5 minutes, then
  - 6.1. set the N<sub>2</sub> set point to zero in LabVIEW
  - 6.2. close all the ball valves on N<sub>2</sub> line
  - 6.3. close the N<sub>2</sub> cylinder regulator
7. Close the ball valve and rotameter on manual line
8. Switch off the “power switch” and make sure all the set points are set to zero in LabVIEW
9. Make sure all the ball valves on gas panel are closed
10. Let the cell cool down to ambient temperature
11. Switch off the humidifier power supply
12. Switch off the heating tape power supply
13. Switch off the furnace controller
14. Switch off solenoid valves power supply
15. Switch off relays power supply
16. Switch off Flow Controllers power supplies
17. Turn off the cell air flow rotameter
18. Turn off the air flow ball valve
19. Stop the LabVIEW program and switch off the computer
20. Open the filling port on humidifier and empty the water inside the humidifier

## **Appendix 5 Electrical Drawing of SOFC Test Rig**



## **Appendix 6 Test Sheet**

Start date/time:	Active area (cm <sup>2</sup> ):	LabVIEW file:
Durability current (A/cm <sup>2</sup> ):	Heating ramp (°C/min):	Data logging interval Diadem (s): Data logging interval Excel (s):

	H <sub>2</sub> line:		Clean N <sub>2</sub> line:			Humid. T °C	Fuel composition %		
	Sp (ml/min)	Rate (ml/min)	Sp (ml/min)	Output (v)	rate (ml/min)	sp	H <sub>2</sub>	N <sub>2</sub>	H <sub>2</sub> O
Heating									
v-i									

Time at which the set point is reached:

## References

1. Cheng, X., Shi, Z., Glass, N., Zhang, L., Zhang, J., Song, D., Liu, Z.S., Wang, H. and Shen, J., *A review of PEM hydrogen fuel cell contamination: Impacts, mechanisms, and mitigation*. Journal of power sources, 2007. **165**(2): p. 739-756.
2. Erwin, P. and Hardy, J., *Draft Climate Change Bill - Consultation Document*, 2007, Department for Environment, Food and Rural Affairs: London, GB.
3. Birnbaum, U., Haines, M., Hake, J.F. and Linssen, J. *Reduction of greenhouse gas emissions through fuel cell combined heat and power applications*. in *Proceedings of the 17th World Hydrogen Energy Conference*. 2008. Brisbane, Australia.
4. George, R.A., *Status of tubular SOFC field unit demonstrations*. Journal of power sources, 2000. **86**(1): p. 134-139.
5. Hoogers, G., *Fuel cell technology handbook*. 2003: CRC Press, New York.
6. Veyo, S.E., Shockling, L.A., Dederer, J.T., Gillett, J.E. and Lundberg, W.L., *Tubular solid oxide fuel cell/gas turbine hybrid cycle power systems: Status*. Journal of Engineering for Gas Turbines and Power, 2002. **124**: p. 845.
7. Blomen, L.J.M.J. and Mugerwa, M.N., *Fuel cell systems*. 1994: Springer.
8. Hirschenhofer, J., Stauffer, D., Engleman, R. and Klett, M., *Fuel cell handbook*. 4th ed. 1998: US Department of Energy, Office of Fossil Energy, Federal Energy Technology Center.
9. Larminie, J. and Dicks, A., *Fuel cell systems explained*. 2003: Wiley New York.
10. Steele, B.C.H. and Heinzel, A., *Materials for fuel-cell technologies*. Nature, 2001. **414**(6861): p. 345-352.
11. *Fuel Cells for Distributed Generation, A Technology and Marketing Summary*, 2000, Energy Center of Wisconsin.
12. *Water electrolysis and renewable energy systems*, 2013, Fuel cell today. p. 8-9.
13. Ferrero, D., Lanzini, A., Leone, P. and Santarelli, M., *Reversible operation of solid oxide cells under electrolysis and fuel cell modes: Experimental study and model validation*. Chemical Engineering Journal, 2015. **274**: p. 143-155.
14. Rayment, C. and Sherwin, S., *Introduction to fuel cell technology*. Department of Aerospace and Mechanical Engineering, University of Notre Dame. 2003.
15. Boyer, R. *Interactive Concepts in Biochemistry*. 2002], Available from: <http://www.wiley.com/college/boyer/0470003790/index.htm>.
16. Singhal, S.C. and Kendall, K., *High temperature Solid Oxide Fuel Cells: Fundamentals, Design and Applications*. 2003: Elsevier Science.
17. *NIST Chemistry WebBook*. [cited 2012], Available from: <http://webbook.nist.gov/chemistry>.
18. Sonntag, R.E., Borgnakke, C., Van Wylen, G.J. and Van Wyk, S., *Fundamentals of thermodynamics*. 1998: Wiley New York.
19. Bevc, F., *Advances in solid oxide fuel cells and integrated power plants*. Institution of Mechanical Engineers, Part A: Journal of Power and Energy, 1997. **211**(5): p. 359-366.
20. Minh, N.Q., *Solid oxide fuel cell technology—features and applications*. Solid State Ionics, 2004. **174**(1): p. 271-277.
21. Singhal, S., *Advances in solid oxide fuel cell technology*. Solid State Ionics, 2000. **135**(1): p. 305-313.
22. Brylewski, T., Nanko, M., Maruyama, T. and Przybylski, K., *Application of Fe–16Cr ferritic alloy to interconnector for a solid oxide fuel cell*. Solid State Ionics, 2001. **143**(2): p. 131-150.
23. Eguchi, K., *Ceramic materials containing rare earth oxides for solid oxide fuel cell*. Journal of Alloys and Compounds, 1997. **250**(1-2): p. 486-491.
24. Lin, B., Wang, S., Liu, X. and Meng, G., *Simple solid oxide fuel cells*. Journal of Alloys and Compounds, 2010. **490**(1): p. 214-222.

25. Lawlor, V., Griesser, S., Buchinger, G., Olabi, A., Cordiner, S. and Meissner, D., *Review of the micro-tubular solid oxide fuel cell: Part I. Stack design issues and research activities*. Journal of power sources, 2009. **193**(2): p. 387-399.
26. Yokokawa, H., Tu, H., Iwanschitz, B. and Mai, A., *Fundamental mechanisms limiting solid oxide fuel cell durability*. Journal of power sources, 2008. **182**(2): p. 400-412.
27. Achenbach, E. and Riensche, E., *Methane/steam reforming kinetics for solid oxide fuel cells*. Journal of power sources, 1994. **52**(2): p. 283-288.
28. Hofmann, P., Panopoulos, K., Fryda, L., Schweiger, A., Ouweltjes, J. and Karl, J., *Integrating biomass gasification with solid oxide fuel cells: effect of real product gas tars, fluctuations and particulates on Ni-GDC anode*. International Journal of Hydrogen Energy, 2008. **33**(11): p. 2834-2844.
29. Bao, J.E., Krishnan, G.N., Jayaweera, P., Perez-Mariano, J. and Sanjurjo, A., *Effect of various coal contaminants on the performance of solid oxide fuel cells: Part I. Accelerated testing*. Journal of power sources, 2009. **193**(2): p. 607-616.
30. Singhal, S., *Science and technology of solid-oxide fuel cells*. MRS bulletin, 2000. **25**(03): p. 16-21.
31. *University of Cambridge DoITPoMS website - Solid oxide fuel cells (SOFCs)*. [cited 2015], Available from: [http://www.doitpoms.ac.uk/tlplib/fuel-cells/high\\_temp\\_sofc.php](http://www.doitpoms.ac.uk/tlplib/fuel-cells/high_temp_sofc.php).
32. Matsuzaki, Y. and Yasuda, I., *The poisoning effect of sulfur-containing impurity gas on a SOFC anode: Part I. Dependence on temperature, time, and impurity concentration*. Solid State Ionics, 2000. **132**(3): p. 261-269.
33. Martinez, A., Gerdes, K., Gemmen, R. and Poston, J., *Thermodynamic analysis of interactions between Ni-based solid oxide fuel cells (SOFC) anodes and trace species in a survey of coal syngas*. Journal of power sources, 2010. **195**(16): p. 5206-5212.
34. Irshad, M., Siraj, K., Raza, R., Ali, A., Tiwari, P., Zhu, B., Rafique, A., Ali, A., Kaleem Ullah, M. and Usman, A., *A Brief Description of High Temperature Solid Oxide Fuel Cell's Operation, Materials, Design, Fabrication Technologies and Performance*. Applied Sciences, 2016. **6**(3): p. 75.
35. Wincewicz, K.C. and Cooper, J.S., *Taxonomies of SOFC material and manufacturing alternatives*. Journal of power sources, 2005. **140**(2): p. 280-296.
36. Martinez, A.S. and Brouwer, J., *Percolation modeling investigation of TPB formation in a solid oxide fuel cell electrode–electrolyte interface*. Electrochimica Acta, 2008. **53**(10): p. 3597-3609.
37. Ge, X., Fu, C. and Chan, S.H., *Three phase boundaries and electrochemically active zones of lanthanum strontium vanadate–yttria-stabilized zirconia anodes in solid oxide fuel cells*. Electrochimica Acta, 2011. **56**(17): p. 5947-5953.
38. Tao, Y., Shao, J., Wang, W.G. and Wang, J., *Optimisation and Evaluation of La<sub>0.6</sub>Sr<sub>0.4</sub>CoO<sub>3-δ</sub> Cathode for Intermediate Temperature Solid Oxide Fuel Cells*. Fuel Cells, 2009. **9**(5): p. 679-683.
39. Sarantaridis, D. and Atkinson, A., *Redox Cycling of Ni-Based Solid Oxide Fuel Cell Anodes: A Review*. Fuel Cells, 2007. **7**(3): p. 246-258.
40. Ormerod, R.M., *Solid oxide fuel cells*. Chem. Soc. Rev., 2002. **32**(1): p. 17-28.
41. Johnson, J. and Qu, J., *Effective modulus and coefficient of thermal expansion of Ni–YSZ porous cermets*. Journal of power sources, 2008. **181**(1): p. 85-92.
42. Basu, S., *Materials for Solid Oxide Fuel Cells*, in *Recent Trends in Fuel Cell Science and Technology*. 2007, Anamaya Publishers, New Delhi, India.
43. Kuhn, J.N., Lakshminarayanan, N. and Ozkan, U.S., *Effect of hydrogen sulfide on the catalytic activity of Ni-YSZ cermets*. Journal of Molecular Catalysis A: Chemical, 2008. **282**(1): p. 9-21.
44. Belyaev, V., Politova, T., Mar'ina, O. and Sobyenin, V., *Internal steam reforming of methane over Ni-based electrode in solid oxide fuel cells*. Applied Catalysis A: General, 1995. **133**(1): p. 47-57.

45. Takeguchi, T., Kani, Y., Yano, T., Kikuchi, R., Eguchi, K., Tsujimoto, K., Uchida, Y., Ueno, A., Omoshiki, K. and Aizawa, M., *Study on steam reforming of CH<sub>4</sub> and C<sub>2</sub> hydrocarbons and carbon deposition on Ni-YSZ cermets*. Journal of power sources, 2002. **112**(2): p. 588-595.
46. Weber, A., Sauer, B., Müller, A.C., Herbstritt, D. and Ivers-Tiffée, E., *Oxidation of H<sub>2</sub>, CO and methane in SOFCs with Ni/YSZ-cermet anodes*. Solid State Ionics, 2002. **152**: p. 543-550.
47. Balakos, M.W. and Chuang, S.S.C., *CO disproportionation on Ni-based catalysts*. Reaction Kinetics and Catalysis Letters, 1993. **49**(1): p. 7-12.
48. Li, Y., Wang, Y., Zhang, X. and Mi, Z., *Thermodynamic analysis of autothermal steam and CO<sub>2</sub> reforming of methane*. International Journal of Hydrogen Energy, 2008. **33**(10): p. 2507-2514.
49. Laurencin, J., Lefebvre-Joud, F. and Delette, G., *Impact of cell design and operating conditions on the performances of SOFC fuelled with methane*. Journal of power sources, 2008. **177**(2): p. 355-368.
50. Xu, J., Yeung, C.M.Y., Ni, J., Meunier, F., Acerbi, N., Fowles, M. and Tsang, S.C., *Methane steam reforming for hydrogen production using low water-ratios without carbon formation over ceria coated Ni catalysts*. Applied Catalysis A: General, 2008. **345**(2): p. 119-127.
51. Hofmann, P., Schweiger, A., Fryda, L., Panopoulos, K., Hohenwarter, U., Bentzen, J.D., Ouweltjes, J., Ahrenfeldt, J., Henriksen, U. and Kakaras, E., *High temperature electrolyte supported Ni-GDC/YSZ/LSM SOFC operation on two-stage Viking gasifier product gas*. Journal of power sources, 2007. **173**(1): p. 357-366.
52. Dicks, A., Pointon, K. and Siddle, A., *Intrinsic reaction kinetics of methane steam reforming on a nickel/zirconia anode*. Journal of power sources, 2000. **86**(1): p. 523-530.
53. Laosiripojana, N. and Assabumrungrat, S., *Catalytic steam reforming of methane, methanol, and ethanol over Ni/YSZ: The possible use of these fuels in internal reforming SOFC*. Journal of power sources, 2007. **163**(2): p. 943-951.
54. Koh, J.H., Yoo, Y.S., Park, J.W. and Lim, H.C., *Carbon deposition and cell performance of Ni-YSZ anode support SOFC with methane fuel*. Solid State Ionics, 2002. **149**(3): p. 157-166.
55. Kirtley, J., Eigenbrodt, B. and Walker, R., *In Situ Optical Studies of Oxidation Kinetics of Ni/YSZ Cermet Anodes*. ECS Transactions, 2011. **33**(40): p. 25-37.
56. Hofmann, P., Panopoulos, K., Aravind, P., Siedlecki, M., Schweiger, A., Karl, J., Ouweltjes, J. and Kakaras, E., *Operation of solid oxide fuel cell on biomass product gas with tar levels > 10 g Nm<sup>-3</sup>*. International Journal of Hydrogen Energy, 2009. **34**(22): p. 9203-9212.
57. Laurencin, J., Delette, G., Morel, B., Lefebvre-Joud, F. and Dupeux, M., *Solid oxide fuel cells damage mechanisms due to Ni-YSZ re-oxidation: Case of the anode supported cell*. Journal of power sources, 2009. **192**(2): p. 344-352.
58. Waldbillig, D., Wood, A. and Ivey, D., *Electrochemical and microstructural characterization of the redox tolerance of solid oxide fuel cell anodes*. Journal of power sources, 2005. **145**(2): p. 206-215.
59. Zhang, Y., Liu, B., Tu, B., Dong, Y. and Cheng, M., *Redox cycling of Ni-YSZ anode investigated by TPR technique*. Solid State Ionics, 2005. **176**(29): p. 2193-2199.
60. Faes, A., Hessler-Wyser, A. and Zryd, A., *A Review of RedOx Cycling of Solid Oxide Fuel Cells Anode*. Membranes, 2012. **2**(3): p. 585-664.
61. Fouquet, D., Müller, A., Weber, A. and Ivers-Tiffée, E., *Kinetics of oxidation and reduction of Ni/YSZ cermets*. Ionics, 2003. **9**(1): p. 103-108.
62. Waldbillig, D., Wood, A. and Ivey, D.G., *Thermal analysis of the cyclic reduction and oxidation behaviour of SOFC anodes*. Solid State Ionics, 2005. **176**(9): p. 847-859.
63. Eichler, A., *Tetragonal Y-doped zirconia: Structure and ion conductivity*. Physical Review B, 2001. **64**(17): p. 174103.
64. *University of Cambridge DoITPoMS website - Electrolyte*. [cited 2015], Available from: [http://www.doitpoms.ac.uk/tlplib/fuel-cells/sofc\\_electrolyte.php](http://www.doitpoms.ac.uk/tlplib/fuel-cells/sofc_electrolyte.php).
65. Kee, R.J., Zhu, H. and Goodwin, D.G., *Solid-oxide fuel cells with hydrocarbon fuels*. Proceedings of the Combustion Institute, 2005. **30**(2): p. 2379-2404.

66. Ivers-Tiffée, E., Weber, A. and Herbristrit, D., *Materials and technologies for SOFC-components*. Journal of the European Ceramic Society, 2001. **21**(10): p. 1805-1811.
67. Zhu, B., Liu, X., Zhou, P., Zhu, Z., Zhu, W. and Zhou, S., *Cost-effective yttrium doped ceria-based composite ceramic materials for intermediate temperature solid oxide fuel cell applications*. Journal of materials science letters, 2001. **20**(7): p. 591-594.
68. Minh, N.Q. and Takahashi, T., *Science and technology of ceramic fuel cells*. 1995: Elsevier Science.
69. Shi, Y. and Cai, N., *A general mechanistic model of solid oxide fuel cells*. Tsinghua Science & Technology, 2006. **11**(6): p. 701-711.
70. Yamamoto, O., *Solid oxide fuel cells: fundamental aspects and prospects*. Electrochimica Acta, 2000. **45**(15): p. 2423-2435.
71. Aguiar, P., Adjiman, C. and Brandon, N.P., *Anode-supported intermediate temperature direct internal reforming solid oxide fuel cell. I: model-based steady-state performance*. Journal of power sources, 2004. **138**(1): p. 120-136.
72. Campanari, S. and Iora, P., *Definition and sensitivity analysis of a finite volume SOFC model for a tubular cell geometry*. Journal of Power Sources, 2004. **132**(1): p. 113-126.
73. Moussa, H.B., Zitouni, B., Oulmi, K., Mahmah, B., Belhamel, M. and Mandin, P., *Hydrogen consumption and power density in a co-flow planar SOFC*. International journal of hydrogen energy, 2009. **34**(11): p. 5022-5031.
74. Hernández-Pacheco, E., Mann, M.D., Hutton, P.N., Singh, D. and Martin, K.E., *A cell-level model for a solid oxide fuel cell operated with syngas from a gasification process*. International Journal of Hydrogen Energy, 2005. **30**(11): p. 1221-1233.
75. Costamagna, P., Selimovic, A., Del Borghi, M. and Agnew, G., *Electrochemical model of the integrated planar solid oxide fuel cell (IP-SOFC)*. Chemical Engineering Journal, 2004. **102**(1): p. 61-69.
76. Yonekura, T., Tachikawa, Y., Yoshizumi, T., Shiratori, Y., Ito, K. and Sasaki, K., *Exchange Current Density of Solid Oxide Fuel Cell Electrodes*. ECS Transactions, 2011. **35**(1): p. 1007-1014.
77. Yakabe, H. and Sakurai, T., *3D simulation on the current path in planar SOFCs*. Solid State Ionics, 2004. **174**(1): p. 295-302.
78. Ding, X., Cui, C. and Guo, L., *Thermal expansion and electrochemical performance of La 0.7 Sr 0.3 CuO 3- $\delta$ -Sm 0.2 Ce 0.8 O 2- $\delta$  composite cathode for IT-SOFCs*. Journal of Alloys and Compounds, 2009. **481**(1): p. 845-850.
79. Hsiao, Y.C. and Selman, J.R., *The degradation of SOFC electrodes*. Solid State Ionics, 1997. **98**(1): p. 33-38.
80. Lin, C.-K., Chen, T.-T., Chyou, Y.-P. and Chiang, L.-K., *Thermal stress analysis of a planar SOFC stack*. Journal of Power Sources, 2007. **164**(1): p. 238-251.
81. Ryan, E.M., Xu, W., Sun, X. and Khaleel, M.A., *A damage model for degradation in the electrodes of solid oxide fuel cells: Modeling the effects of sulfur and antimony in the anode*. Journal of power sources, 2012.
82. Marina, O.A., Coyle, C.A., Thomsen, E.C., Edwards, D.J., Coffey, G.W. and Pederson, L.R., *Degradation mechanisms of SOFC anodes in coal gas containing phosphorus*. Solid State Ionics, 2010. **181**(8): p. 430-440.
83. Faes, A., Hessler-Wyser, A., Presvytes, D. and Vayenas, C., *Nickel-Zirconia Anode Degradation and Triple Phase Boundary Quantification from Microstructural Analysis*. Fuel Cells, 2009. **9**(6): p. 841-851.
84. Yürüm, Y., *Hydrogen energy system: production and utilization of hydrogen and future aspects*. 1995: Springer.
85. Lau, G.Y., Tucker, M.C., Jacobson, C.P., Visco, S.J., Gleixner, S.H. and DeJonghe, L.C., *Chromium transport by solid state diffusion on solid oxide fuel cell cathode*. Journal of power sources, 2010. **195**(22): p. 7540-7547.

86. Tucker, M.C., Kurokawa, H., Jacobson, C.P., De Jonghe, L.C. and Visco, S.J., *A fundamental study of chromium deposition on solid oxide fuel cell cathode materials*. Journal of power sources, 2006. **160**(1): p. 130-138.
87. *UK Biomass Strategy*, 2007, Department for Environment, Food and Rural Affairs.
88. Higman, C. and Burgt, M.J.v.d., *Gasification*. 2nd ed. 2008: Gulf professional publishing.
89. McKendry, P., *Energy production from biomass (part 2): conversion technologies*. Bioresource technology, 2002. **83**(1): p. 47-54.
90. Amos, W.A., *Analysis of two biomass gasification/fuel cell scenarios for small-scale power generation*. 1998: National Renewable Energy Laboratory.
91. Brown, R.C., Smeenk, J. and Steinfeld, G., *investigation of an integrated switchgrass gasification/fuel cell power plant*, 1998, U.S. Department of Energy Biomass Power Program.
92. Hernandez, J., Barba, J. and Aranda, G., *Combustion characterization of producer gas from biomass gasification*. Global Nest Journal, 2012. **14**(2): p. 125-132.
93. Bhawan, P. and Nagar, E.A., *Comprehensive industrial documents for producer gas plants and biomass gasifiers*, 2008, Central Pollution Control Board (Ministry of Environment & Forests, Govt. of India).
94. Baron, S., Brandon, N., Atkinson, A., Steele, B. and Rudkin, R., *The impact of wood-derived gasification gases on Ni-CGO anodes in intermediate temperature solid oxide fuel cells*. Journal of power sources, 2004. **126**(1): p. 58-66.
95. Giltrap, D., McKibbin, R. and Barnes, G., *A steady state model of gas-char reactions in a downdraft biomass gasifier*. Solar Energy, 2003. **74**(1): p. 85-91.
96. Vervaeke, P., Tack, F., Navez, F., Martin, J., Verloo, M. and Lust, N., *Fate of heavy metals during fixed bed downdraft gasification of willow wood harvested from contaminated sites*. Biomass and Bioenergy, 2006. **30**(1): p. 58-65.
97. Zainal, Z., Rifau, A., Quadir, G. and Seetharamu, K., *Experimental investigation of a downdraft biomass gasifier*. Biomass and Bioenergy, 2002. **23**(4): p. 283-289.
98. Aravind, P.V. and de Jong, W., *Evaluation of high temperature gas cleaning options for biomass gasification product gas for Solid Oxide Fuel Cells*. Progress in Energy and Combustion Science, 2012.
99. Aravind, P.V., J.P. Ouweltjes, E. De Heer, N. Woudstra and G. Rietveld. *Impact of Biosyngas and its components on SOFC Anodes*. in *Electrochemical Society Proceedings*. 2005.
100. Brandin, J., Tunér, M. and Odenbrand, I., *Swedish Energy Agency Report, Small Scale Gasification: Gas Engine CHP for Biofuels*, 2011, Linnaeus University.
101. Ciferno, J.P. and Marano, J.J., *Benchmarking biomass gasification technologies for fuels, chemicals and hydrogen production*. US Department of Energy. National Energy Technology Laboratory, 2002.
102. Aravind, P., Ouweltjes, J., Woudstra, N. and Rietveld, G., *Impact of biomass-derived contaminants on SOFCs with Ni/Gadolinia-doped ceria anodes*. Electrochemical and Solid-State Letters, 2008. **11**(2): p. B24-B28.
103. Lorente, E., Millan, M. and Brandon, N., *Use of gasification syngas in SOFC: Impact of real tar on anode materials*. International Journal of Hydrogen Energy, 2011.
104. Mermelstein, J., Millan, M. and Brandon, N., *The impact of steam and current density on carbon formation from biomass gasification tar on Ni/YSZ, and Ni/CGO solid oxide fuel cell anodes*. Journal of power sources, 2010. **195**(6): p. 1657-1666.
105. Mermelstein, J., Millan, M. and Brandon, N., *The interaction of biomass gasification syngas components with tar in a solid oxide fuel cell and operational conditions to mitigate carbon deposition on nickel-gadolinium doped ceria anodes*. Journal of power sources, 2011. **196**(11): p. 5027-5034.
106. Mermelstein, J., Millan, M. and Brandon, N., *The impact of carbon formation on Ni-YSZ anodes from biomass gasification model tars operating in dry conditions*. Chemical Engineering Science, 2009. **64**(3): p. 492-500.

107. Bao, J.E., Krishnan, G.N., Jayaweera, P., Lau, K.H. and Sanjurjo, A., *Effect of various coal contaminants on the performance of solid oxide fuel cells: Part II. ppm and sub-ppm level testing*. Journal of power sources, 2009. **193**(2): p. 617-624.
108. Cayan, F.N., Zhi, M., Pakalapati, S.R., Celik, I., Wu, N. and Gemmen, R., *Effects of coal syngas impurities on anodes of solid oxide fuel cells*. Journal of power sources, 2008. **185**(2): p. 595-602.
109. Veyo, S.E., *Evaluation of Fuel Impurity Effects on Solid Oxide Fuel Cell Performance*, 1998, Westinghouse Electric Company, a Subsidiary of CBS Corporation, Science & Technology Center, SOFC Power Generation.
110. Trembly, J., Gemmen, R. and Bayless, D., *The effect of coal syngas containing AsH<sub>3</sub> on the performance of SOFCs: Investigations into the effect of operational temperature, current density and AsH<sub>3</sub> concentration*. Journal of power sources, 2007. **171**(2): p. 818-825.
111. Demircan, O., Zhang, W., Xu, C., Zondlo, J. and Finklea, H.O., *The effect of overpotential on performance degradation of the solid oxide fuel cell Ni/YSZ anode during exposure to syngas with phosphine contaminant*. Journal of power sources, 2010. **195**(10): p. 3091-3096.
112. Trembly, J., Gemmen, R. and Bayless, D., *The effect of coal syngas containing HCl on the performance of solid oxide fuel cells: Investigations into the effect of operational temperature and HCl concentration*. Journal of power sources, 2007. **169**(2): p. 347-354.
113. Dekker, N. and Rietveld, G., *Highly efficient conversion of ammonia in electricity by solid oxide fuel cells*. Transactions of the ASME-U-Journal of Fuel Cell Science and Technology, 2006. **3**(4): p. 499.
114. Maskalisk, N. and Ray, E., *Contaminant effects in solid oxide fuel cells*, 1992, Westinghouse Electric Corp., Pittsburgh, PA (United States). Science and Technology Center.
115. Brightman, E., Ivey, D.G., Brett, D.J.L. and Brandon, N.P., *The effect of current density on H<sub>2</sub>S poisoning of nickel-based solid oxide fuel cell anodes*. Journal of Power Sources, 2011. **196**(17): p. 7182-7187.
116. Grgicak, C.M., Green, R.G. and Giorgi, J.B., *SOFC anodes for direct oxidation of hydrogen and methane fuels containing H<sub>2</sub>S*. Journal of power sources, 2008. **179**(1): p. 317-328.
117. Marquez, A.I., Ohrn, T.R., Trembly, J.P., Ingram, D.C. and Bayless, D.J., *Effects of coal syngas and H<sub>2</sub>S on the performance of solid oxide fuel cells: Part 2. Stack tests*. Journal of power sources, 2007. **164**(2): p. 659-667.
118. Trembly, J.P., Marquez, A.I., Ohrn, T.R. and Bayless, D.J., *Effects of coal syngas and H<sub>2</sub>S on the performance of solid oxide fuel cells: Single-cell tests*. Journal of power sources, 2006. **158**(1): p. 263-273.
119. Haga, K., Adachi, S., Shiratori, Y., Itoh, K. and Sasaki, K., *Poisoning of SOFC anodes by various fuel impurities*. Solid State Ionics, 2008. **179**(27): p. 1427-1431.
120. Li, T.S. and Wang, W.G., *The Mechanism of H<sub>2</sub>S Poisoning Ni/YSZ Electrode Studied by Impedance Spectroscopy*. Electrochemical and Solid-State Letters, 2011. **14**(3): p. B35-B37.
121. Lohsoontorn, P., Brett, D. and Brandon, N., *The effect of fuel composition and temperature on the interaction of H<sub>2</sub>S with nickel-ceria anodes for Solid Oxide Fuel Cells*. Journal of power sources, 2008. **183**(1): p. 232-239.
122. Rasmussen, J.F.B. and Hagen, A., *The effect of H<sub>2</sub>S on the performance of Ni-YSZ anodes in solid oxide fuel cells*. Journal of Power Sources, 2009. **191**: p. 534-541.
123. Feduska, W. and Isenberg, A., *High-temperature solid oxide fuel cell—technical status*. Journal of power sources, 1983. **10**(1): p. 89-102.
124. Cheng, Z. and Liu, M., *Characterization of sulfur poisoning of Ni-YSZ anodes for solid oxide fuel cells using in situ Raman microspectroscopy*. Solid State Ionics, 2007. **178**(13): p. 925-935.
125. Dong, J., Cheng, Z., Zha, S. and Liu, M., *Identification of nickel sulfides on Ni-YSZ cermet exposed to H<sub>2</sub> fuel containing H<sub>2</sub>S using Raman spectroscopy*. Journal of power sources, 2006. **156**(2): p. 461-465.

126. Cheng, Z., Zha, S. and Liu, M., *Influence of cell voltage and current on sulfur poisoning behavior of solid oxide fuel cells*. Journal of power sources, 2007. **172**(2): p. 688-693.
127. Smith, T.R., Wood, A. and Birss, V.I., *Effect of hydrogen sulfide on the direct internal reforming of methane in solid oxide fuel cells*. Applied Catalysis A: General, 2009. **354**(1): p. 1-7.
128. Lohsoontorn, P., Brett, D.J.L. and Brandon, N.P., *Thermodynamic predictions of the impact of fuel composition on the propensity of sulphur to interact with Ni and ceria-based anodes for solid oxide fuel cells*. Journal of power sources, 2008. **175**(1): p. 60-67.
129. Shariat, M.H. and Behgozin, S.A., *A new look at nickel-oxygen-sulfur diagrams*. Calphad, 1996. **20**(1): p. 47-67.
130. Lin, R.Y., Hu, D.C. and Chang, Y.A., *Thermodynamics and phase relationships of transition metal-sulfur systems: II. The nickel-sulfur system*. Metallurgical Transactions B, 1978. **9**(4): p. 531-538.
131. Sasaki, K., Haga, K., Yamamoto, J. and Dobuchi, K. *Impurity Poisoning of SOFCs: Towards Understanding Chemical Degradation Mechanisms*. in *Proceedings of the 8th European SOFC Forum 2008*. Lucerne, Switzerland.
132. Bartholomew, C., Agrawal, P. and Katzer, J., *Sulfur poisoning of metals*. Advances in catalysis, 1982. **31**: p. 135-242.
133. Gong, M., Liu, X., Trembly, J. and Johnson, C., *Sulfur-tolerant anode materials for solid oxide fuel cell application*. Journal of power sources, 2007. **168**(2): p. 289-298.
134. Lussier, A., Sofie, S., Dvorak, J. and Idzerda, Y., *Mechanism for SOFC anode degradation from hydrogen sulfide exposure*. International Journal of Hydrogen Energy, 2008. **33**(14): p. 3945-3951.
135. Zha, S., Cheng, Z. and Liu, M., *Sulfur poisoning and regeneration of Ni-based anodes in solid oxide fuel cells*. Journal of the Electrochemical Society, 2007. **154**(2): p. B201-B206.
136. Zhang, L., Jiang, S.P., He, H.Q., Chen, X., Ma, J. and Song, X.C., *A comparative study of H<sub>2</sub>S poisoning on electrode behavior of Ni/YSZ and Ni/GDC anodes of solid oxide fuel cells*. International Journal of Hydrogen Energy, 2010. **35**(22): p. 12359-12368.
137. Van Dijk, H., *Tail gas treatment of sour-SEWGS CO<sub>2</sub> product*. 2012.
138. Kröcher, O. and Elsener, M., *Hydrolysis and oxidation of gaseous HCN over heterogeneous catalysts*. Applied Catalysis B: Environmental, 2009. **92**(1): p. 75-89.
139. Jorcin, J.-B., Orazem, M.E., Pébère, N. and Tribollet, B., *CPE analysis by local electrochemical impedance spectroscopy*. Electrochimica Acta, 2006. **51**(8): p. 1473-1479.
140. Krishnan, V.V., McIntosh, S., Gorte, R.J. and Vohs, J.M., *Measurement of electrode overpotentials for direct hydrocarbon conversion fuel cells*. Solid State Ionics, 2004. **166**(1): p. 191-197.
141. *Gamry Instruments website - Basics of Electrochemical Impedance Spectroscopy* [cited 2015], Available from: <http://www.gamry.com/application-notes/EIS/basics-of-electrochemical-impedance-spectroscopy>.
142. Macdonald, J.R., *Impedance spectroscopy*. Annals of biomedical engineering, 1992. **20**(3): p. 289-305.
143. Meyer, Q., Ronaszegi, K., Pei-June, G., Curnick, O., Ashton, S., Reisch, T., Adcock, P., Shearing, P.R. and Brett, D.J., *Optimisation of air cooled, open-cathode fuel cells: Current of lowest resistance and electro-thermal performance mapping*. Journal of Power Sources, 2015. **291**: p. 261-269.
144. Goodhew, P.J., Humphreys, J. and Beanland, R., *Electron microscopy and analysis*. 2000: CRC Press.
145. *BOC website*. [cited 2011], Available from: <http://www.boconline.co.uk>.
146. *Brooks Instrument website*. [cited 2011], Available from: <http://www.brooksinstrument.com>.
147. *Scientific & Medical Products (SciMed) website*. [cited 2014], Available from: <http://www.scimed.co.uk>.

148. *Gamry Instruments website - Gamry Simplex Fit- Algorithm Details*. [cited 2015], Available from: <http://www.gamry.com/application-notes/software-scripting/simplex-fit-algorithm/>.
149. Haddad, L., *Solid oxide fuel cell test rig - operating procedures manual*, 1993, British Gas - Research and Technology: London.
150. *Resistalloy Trading Limited website*. [cited 2011], Available from: <http://www.resistalloytrading.co.uk>.
151. *Elcogen Fuel Cell Technology website*. [cited 2011], Available from: <http://www.elcogen.com>.
152. Paragreen, J., *Personal communication*, 2012, University of Sheffield.
153. *Fuel Cell Materials website - High Temperature Sealing Paste*. [cited 2011], Available from: <https://www.fuelcellmaterials.com/products/equipment/high-temperature-sealing-paste/>.
154. *Fiaxell SOFC Technologies website*. [cited 2014], Available from: <http://www.fiaxell.com>.